SOFT-THEN-HARD SUB-PIXEL MAPPING ALGORITHM FOR REMOTE SENSING IMAGES

WANG QUNMING

Ph.D

The Hong Kong Polytechnic University

2015

The Hong Kong Polytechnic University

Department of Land Surveying and Geo-Informatics

SOFT-THEN-HARD SUB-PIXEL MAPPING ALGORITHM FOR REMOTE SENSING IMAGES

WANG QUNMING

A thesis submitted in partial fulfilment of the requirements for the degree of Doctor of Philosophy

March 2015

CERTIFICATE OF ORIGINALITY

I hereby declare that this thesis is my own work and that, to the best of knowledge and belief, it reproduces no material previously published or written, nor material that has been accepted for the award of any other degree or diploma, except where due acknowledgement has been made in the text.

__________________________(Signed)

Qunming Wang (Name of student)

Abstract

Image classification, one of the most important techniques in remote sensing, is used widely to extract land cover information from remote sensing images. The inevitable mixed pixels in remote sensing images have brought a great challenge for traditional hard classification-based land cover mapping. To solve this mixed pixel problem, soft classification (e.g., spectral unmixing) has been developed to predict land cover proportions for land cover classes that have a spatial frequency higher than the interval between pixels. Soft classifiers exploit the spectral information of remote sensing images, but fail to predict the spatial location of classes within mixed pixels. To address this issue, sub-pixel mapping (SPM) has been developed, in which each mixed pixel is divided into multiple sub-pixels for which class labels are predicted. SPM, thus, transforms a soft classification into a finer resolution hard classification.

SPM is also termed super-resolution mapping in remote sensing. It has been receiving increasing attention in recent years. In this thesis, the soft-then-hard SPM (STHSPM) algorithms are summarized for the first time. STHSPM is a type of SPM algorithm consisting of soft class value (between 0 and 1) estimation at fine spatial resolution and hard class allocation for sub-pixels. The STHSPM algorithms provide a good opportunity to achieve SPM solutions quickly. Furthermore, they provide important insight into SPM and open doors to more alternatives.

This thesis focuses on the STHSPM algorithm and the main research includes developing new class allocation approaches for the STHSPM algorithms, using additional information in STHSPM to enhance SPM, developing new STHSPM algorithms and applying STHSPM in sub-pixel resolution change detection. Specifically, a new class allocation approach that allocates classes in units of class (UOC) is proposed and UOC is further extended with an adaptive scheme, called AUOC; The multiple shifted images are incorporated to the STHSPM algorithms to decrease the uncertainty in SPM; Two new STHSPM algorithms, radial basis function interpolation and naive indicator cokriging, are proposed; STHSPM is proposed for fast sub-pixel resolution change detection. The experimental results demonstrate the feasibilities of the proposed methods in this thesis.

List of publications

Published (*Corresponding author)

[1] **Wang Q.**, Shi W., Atkinson P. M., and Pardo-Iguzquiza E., 2015. A new geostatistical solution to remote sensing image downscaling. *IEEE Transactions on Geoscience and Remote Sensing*, DOI: 10.1109/TGRS.2015.2457672 (**SCI**, in press).

[2] **Wang Q.** *, Shi W. *, Atkinson P. M., and Zhao Y., 2015. Downscaling MODIS images with area-to-point regression kriging. *Remote Sensing of Environment*, 166, pp. 191–204 (**SCI**).

[3] Shi W. and **Wang Q.***, 2015. Soft-then-hard sub-pixel mapping with multiple shifted images. *International Journal of Remote Sensing*, 36(5), pp. 1329–1348 (**SCI**).

[4] **Wang Q.**, Atkinson P. M., and Shi W., 2015. Indicator cokriging-based subpixel mapping without prior spatial structure information. *IEEE Transactions on Geoscience and Remote Sensing*, 53(1), pp. 309–323 (**SCI**).

[5] **Wang Q.**, Atkinson P. M., and Shi W., 2015. Fast sub-pixel mapping algorithms for sub-pixel resolution change detection. *IEEE Transactions on Geoscience and Remote Sensing*, 53(4), pp. 1692–1706 (**SCI**).

[6] **Wang Q.**, Shi W., Atkinson P. M., and Li Z., 2015. Land cover change detection at sub-pixel resolution with a Hopfield neural network. *IEEE Journal of Selected Topics in Applied Earth Observation and Remote Sensing*, 8(3), pp. 1339–1352 (**SCI**).

[7] Li Z., Shi W., **Wang Q.**, and Miao Z., 2015. Extracting man-made objects from high spatial resolution remote sensing images via fast level set evolutions. *IEEE Transactions on Geoscience and Remote Sensing*, 53(2), pp. 883–899 **(SCI)**.

[8] **Wang Q.** *, Shi W. *, and Atkinson P. M., 2014. Sub-pixel mapping of remote sensing images based on radial basis function interpolation. *ISPRS Journal of Photogrammetry and Remote Sensing*, 92, pp. 1–15 **(SCI)**.

[9] **Wang Q.**, Shi W., and Wang L., 2014. Allocating classes for soft-then-hard subpixel mapping algorithms in units of class. *IEEE Transactions on Geoscience and Remote Sensing*, 52(5), pp. 2940–2959 **(SCI)**.

[10] **Wang Q.**, Shi W., and Zhang H., 2014. Class allocation for soft-then-hard subpixel mapping algorithms with adaptive visiting order of classes. *IEEE Geoscience and Remote Sensing Letters*, 11(9), pp. 1494–1498 **(SCI)**.

[11] **Wang Q.**, Shi W., and Wang L., 2014. Indicator cokriging-based subpixel land cover mapping with shifted images. *IEEE Journal of Selected Topics in Applied Earth Observation and Remote Sensing*, 7(1), pp. 327–339 **(SCI)**.

[12] Shi W., Zhao Y., and **Wang Q.***, 2014. Sub-pixel mapping based on BP neural network with multiple shifted remote sensing images. *Journal of Infrared and Millimeter Waves* (In Chinese with English Abstract), 33(5), pp. 527–532 (**SCI**).

[13] Shi W., Miao Z., and **Wang Q.**, Zhang Hua, 2014. Spectral-spatial classification and shape features for urban road centerline extraction. *IEEE Geoscience and Remote Sensing Letters*, 11(4), pp. 788–792 **(SCI)**.

[14] **Wang Q.** and Shi W., 2014. Utilizing multiple subpixel shifted image in subpixel mapping with image interpolation. *IEEE Geoscience and Remote Sensing Letters*, 11(4), pp. 798–802 **(SCI)**.

[15] **Wang Q.** and Shi W., 2013. Unsupervised classification based on fuzzy c-means with uncertainty analysis. *Remote Sensing Letters*, 4(11), pp. 1087–1096 **(SCI)**.

Submitted

[1] **Wang Q.**, Shi W., and Atkinson P. M.. Spatial-temporal sub-pixel mapping of time-series images. *IEEE Transactions on Geoscience and Remote Sensing* (**SCI**, under review).

[2] **Wang Q.**, Shi W., and Atkinson P. M.. Area-to-point regression kriging for pan-sharpening. *ISPRS Journal of Photogrammetry and Remote Sensing* (**SCI**, under review).

[3] **Wang Q.**, Shi W., and Atkinson P. M.. Approximate area-to-point regression kriging for fast hyperspectral image sharpening. *Remote Sensing of Environment* (**SCI**, under review).

Acknowledgments

First and foremost, I would like to sincerely thank my supervisor, Professor Wenzhong Shi. He provided me with this valuable opportunity to work toward the PhD degree. He has supported me throughout the thesis with his profound knowledge. No matter how busy he is, he can always spare time soon to have the face-to-face discussions when asked. His teaching affects me in many ways.

Many thanks to Professor Peter Atkinson of the University of Southampton, UK. The 6-month visiting study under his guidance in Southampton is a very enjoyable experience. The regular meeting once every two weeks has greatly affected my way of thinking. Thank him for all his important contributions to this thesis and his friendship.

My sincere thanks to the scholars who provided the remote sensing data in this thesis, including Dr. Feng Ling and Xiaodong Li of the Institute of Geodesy and Geophysics, Chinese Academy of Sciences, Dr. Hua Zhang of the China University of Mining and Technology, Xuzhou, Dr. Lefei Zhang of the Wuhan University, Dr. Yong Xu of the Chinese University of Hong Kong, Dr. Andrew J. Tatem of the University of Southampton, Dr. Anuar M. Muad of the Universiti Kebangsaan Malaysia, Dr. Huiran Jin of the State University of New York College of Environmental Science and Forestry, and Prof. Paolo Gamba of the University of Pavia. I also thank them for their kind discussion and patience.

I would like to thank all of my friends in LSGI and PolyU: Zelang Miao, Zhongbin Li, Bin Wang, Xing Yan, Anshu Zhang, Cheng Yang, Yuanling Zhao, Ming Hao, Yiliang Wan, Rui Jin, Xiaoliang Fang, Dr. Chang Li, Dr. Hao Wu…

I would like to thank my friends in Southampton: Julio, Iytzia, Radhika, Caio, Nabaz, Adam, Jay, Ying Wang, Rong Wang, Lingquan Zhou, Ke Zhang…

The PhD study is funded by the 3-year Hong Kong PhD Fellowship Scheme of the Research Grants Council of Hong Kong. Many thanks to the great support.

Last but not least, I thank my parents and all the other family members. Their love and encouragement give me continuous impetus to move forward.

Table of contents

List of Abbreviations

AUOC	a class allocation method that allocates classes in units of class with adaptive visiting order of classes
BPNN	back-propagation neural network
CD	change detection
ETM+	enhanced thematic mapper plus
FRM	fine spatial resolution land cover map
HAVF	a class allocation method that assigns sub-pixels with highest soft attribute values first
HC	hard classification
HNN	Hopfield neural network
HNNB	HNN-based SPM
HNNB_MSI	HNN-based SPM with MSI
HYDICE	Hyperspectral Digital Imagery Collection Experiment airborne
ICK	indicator cokriging
ICKB	ICK-based SPM
ICKB_MSI	ICK-based SPM with MSI
LOT	linear optimization technique
LSMA	linear spectral mixture analysis
MERIS	Medium Resolution Imaging Spectrometer
MLC	maximum likelihood classifier
MODIS	Moderate Resolution Imaging Spectroradiometer
MSI	multiple shifted images
NICK	naiive indicator cokriging
NLCD	National Land Cover Database
OA	overall accuracy
PCC	the overall accuracy in terms of the percentage of correctly classified pixels
PSA	pixel swapping algorithm
RBF	radial basis function
RMSE	root mean square error
ROSIS	Reflective Optics System Imaging Spectrometer sensor
SPM	sub-pixel mapping
SPSAM	sub-pixel/pixel spatial attraction model
SRBF	revised RBF that considers the change of scale
STHSPM	soft-then-hard sub-pixel mapping
UOC	a class allocation method that allocates classes in units of class
UOS	a class allocation method that allocates classes in units of sub-pixel

1. Introduction

1.1. Background

Man has extended to space his view of the land by using remote sensing images, hence greatly improving the observation depth of the earth. Land cover classification is an important technique to extract land cover information from remote sensing images. It has been a key issue in remote sensing domain for many years. Conventional classification techniques allocate each pixel to a single land cover class. This type of technique is known as hard classification. It is not sufficient for hard classification to provide the detailed information concerning the spatial distribution of land cover classes, as mixed pixels exist widely in remote sensing images. Mixed pixel contains more than one class. Fisher (1997) and Foody (2006) illustrated some common origins of mixed pixel problems. Whatever the spatial resolution of the sensor, mixed pixels are unavoidable in remote sensing images and usually the aim of investigators is to extract information that is smaller than pixel size (Fisher, 1997).

Soft classification has been developed to extract land cover information from remote sensing images in an attempt to solve mixed pixel problems. Commonly used instances include linear spectral mixture analysis (Heinz and Chang, 2001), fuzzy c-means classifiers (Bastin, 1997), artificial neural networks (Carpenter et al., 1999), k-nearest neighbor classifiers (Schowengerdt, 1996), support vector machines (Brown et al., 2000; Wang and Jia, 2009) and non-linear unmixing (Halimi et al., 2011). The outputs of soft classification, however, are proportions (also termed fractions) of the classes within the mixed pixels. Soft classification fails to predict the spatial locations of the classes.

Sub-pixel mapping (SPM, also termed super-resolution mapping and downscaling in the remote sensing literature) (Atkinson, 1997, 2009, 2013) is a new technique to address the mixed pixel problem. It divides each mixed pixel into multiple sub-pixels and then predicts their hard class values. The number of sub-pixels belonging to each class depends on the outputs of soft classification. SPM results in an increase in spatial resolution above the conventional hard classification of the input remote sensing images. In nature, SPM transforms the soft classification into a finer scaled hard classification. Using SPM, spatial distribution of land cover can be displayed at finer spatial resolution and provides investigators more detailed and reliable information for decision.

1.2. Overview of SPM algorithms

After Atkinson mentioned that SPM can be considered as the post-processing of soft classification based on the spatial dependence theory (Atkinson, 1997), many SPM algorithms have been continuously developed. Verhoeye and De Wulf (2002) adopted Kriging to characterize spatial dependence and adopted linear optimization techniques (LOT) to maximize the dependence. Considering each sub-pixel as a neuron, Tatem et al. (2001a,b,c, 2002, 2003) set up an energy function for a Hopfield neural network (HNN). This function increases the spatial correlation between neighboring sub-pixels, taking account of class constraints. The energy function is minimized iteratively to generate SPM results. Mertens et al. (2003a) constructed a goal function evaluating the sum of the neighboring values of all sub-pixels and used a genetic algorithm to search for the most possible configuration. According to the defined attractiveness in Atkionson (2005), a pixel swapping algorithm (PSA) was introduced that exchanged two sub-pixel classes most in need of swapping within coarse pixel and SPM results were approached iteratively. Mertens et al. (2006) applied sub-pixel/pixel spatial attraction models (SPSAM) to calculate the spatial attractions between sub-pixels and their neighboring pixels. Ge et al. (2009, 2014) utilized the fractions in the neighboring coarse pixels to draw a linear boundary for each class inside each center coarse pixel. This geometric method is analogous to the contouring method presented in Foody et al. (2005) and Su et al. (2012). In addition, Wang et al. (2012a) studied the essence of the pixel swapping algorithm and introduced the particle swarm optimization to maximize the correlation between sub-pixels after the application of the sub-pixel/pixel spatial attraction models-based SPM process. In Wang et al. (2012b) and Ling et al. (2014), multi-scale spatial dependence was considered simultaneously for SPM.

Using the prior spatial structure information from available high spatial resolution images, some learning-based SPM methods were developed, including the back-propagation neural network (BPNN), two-point histogram and indicator cokriging (ICK). This type of SPM algorithm is able to decrease the inherent uncertainty in SPM to some extent, especially when the spatial distribution of classes is complex or in the L-resolution case (Atkinson, 2009). Specifically, Mertens et al. (2003b, 2004), Wang et al. (2006), Zhang et al. (2008), and Nigussie et al. (2011) presented a BPNN-based SPM approach which extract the relationship between fine class labels and coarse fractions from the training image (i.e., a high spatial resolution image). Atkinson (2004) introduced a two-point histogram-based method, which optimized the randomly initialized sub-pixel maps with maintained class fractions by swapping sub-pixel classes within pixels to gradually match the two-point histogram extracted from the training image. Boucher and Kyriakidis (2006, 2008), Boucher et al. (2008), and Boucher (2009) proposed an ICK-based SPM model. In this model, the prior spatial structure of each class can be utilized by extracting the indicator semivariogram from fine spatial resolution images.

1.3. The soft-then-hard SPM algorithm

As the post-processing of soft classification, there are two basic types of SPM algorithms (see Figure 1.1).

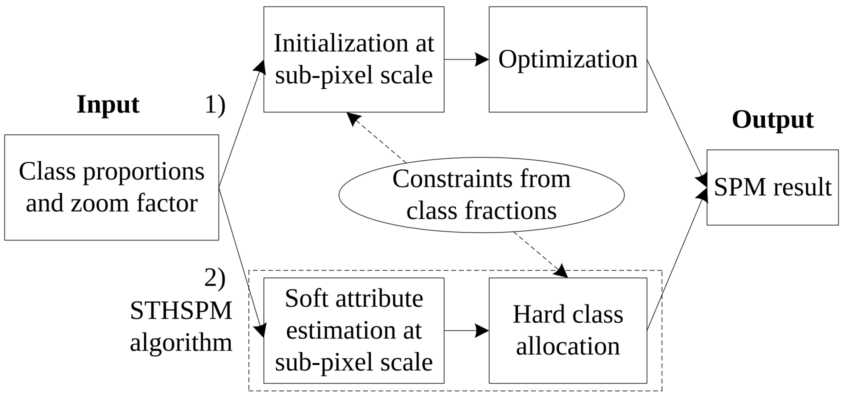

Figure 1.1. Two types of SPM algorithms as the post-processing of soft classification, where "constraints from class fractions" means the class fractions are used to determine the number of sub-pixels for each class.

1) For the first type, the sub-pixels for each class are first allocated randomly (or by using some fast SPM algorithms (Shen et al., 2009; Wang et al., 2012 a,b)) under the condition of maintaining class fractions. Then, the initialized sub-pixel map is optimized by changing the spatial arrangement of sub-pixels inside coarse pixels to gradually approach a certain objective, such as maximizing the attraction between neighboring sub-pixels in PSA (Atkinson, 2005; Makido and Shortridge, 2007; Wang et al., 2012a), the neighboring value (Mertens et al., 2003), the Moran's I of the image (Makido et al., 2007), multi-scale spatial dependence (Wang et al., 2012b; Ling et al., 2014), ratio of

connectivity to directivity (Ai et al., 2014), or minimizing the perimeter of the area belonging to each class (Villa et al., 2011). In addition, the objective of optimization can be to match the two-point histogram (Atkinson, 2004, 2008; Muslim et al., 2007) or landscape structure (Lin et al., 2011) extracted from training image. The optimization can be realized by employing artificial intelligence algorithms to solve the relevant models, including particle swarm optimization in Wang et al. (2012a) and Li et al. (2015), simulating annealing in Makido et al. (2007), Atkinson (2008), Lin et al. (2011), and Villa et al. (2011), genetic algorithms in Mertens et al. (2003) and Wang et al. (2012b). During the optimization process, only the spatial locations of the sub-pixels can vary and the number of sub-pixels for each class within each coarse pixel is fixed.

2) The second type of SPM algorithm, called soft-then-hard SPM (STHSPM) algorithm, consists of two steps. First, the soft attribute values (between 0 and 1) of all classes for all sub-pixels are estimated and a set of soft classified images for all classes at fine spatial resolution are generated in this way. This step is also termed sub-pixel sharpening (Mertens et al., 2004). The second step is to allocate hard attribute values for sub-pixels according to the soft attribute values of each class and constraints from class fractions. Algorithms falling into this type include SPSAM (Mertens et al., 2006), BPNN (Mertens et al., 2003, 2004; Wang et al., 2006; Nigussie et al., 2011), HNN (Tatem et al., 2001a,b,c, 2003; Muad and Foody, 2012a), Kriging (Verhoeye and De Wulf, 2002) and ICK (Boucher and Kyriakidis, 2006, 2008; Boucher et al., 2008; Boucher, 2009; Jin et al., 2012). A general framework of STHSPM is shown in Figure 1.2, where a map in Tatem (2002) is used for illustration. The map covers an area in Bath, UK, and has 360 by 360 pixels with a pixel size of 0.6 m by 0.6 m.

Additionally, SPM can also be performed by the one-stage methods that do not need soft classification process and take as input the raw image in units of reflectance (Kasetkasem et al., 2005; Tolpekin and Stein, 2009; Li et al., 2012a,b, 2014a; Ling et al., 2012a; Wang and Wang, 2013). These methods consider spectral and spatial information simultaneously to achieve SPM, which can also be considered as spatial-spectral methods. This type of SPM methods can be applied to multi-/hyperspectral remote sensing images directly. Figure 1.3 shows the difference between spatial-spectral SPM and the two types of methods summarized in Figure 1.2. The estimation of the parameter controlling the contributions from spatial and spectral terms is always a case-by-case problem: the choice of the optimum parameter depends upon the spatial pattern of study area and spectral variation of the remote sensing image. The spatial-spectral SPM methods also require iterations to approach a satisfactory solution and much time is always needed in the optimization process.

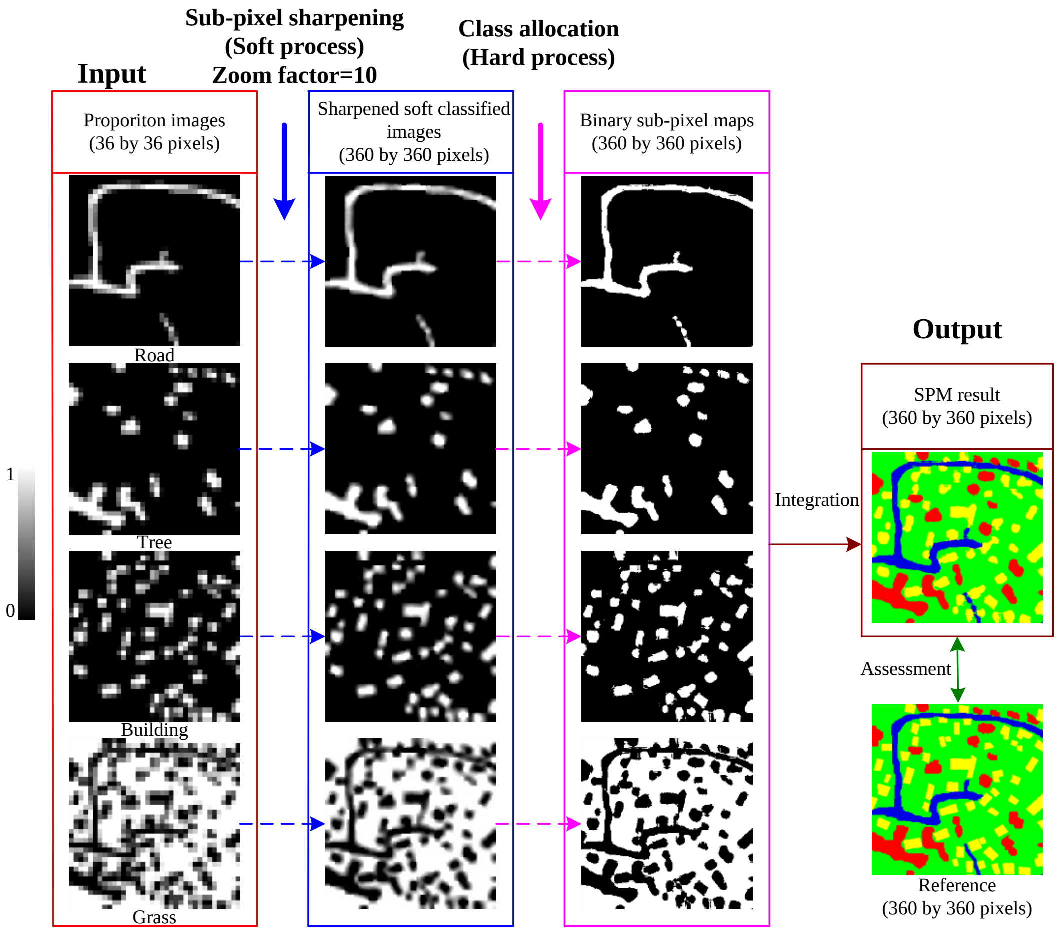

Figure 1.2. Framework of STHSPM.

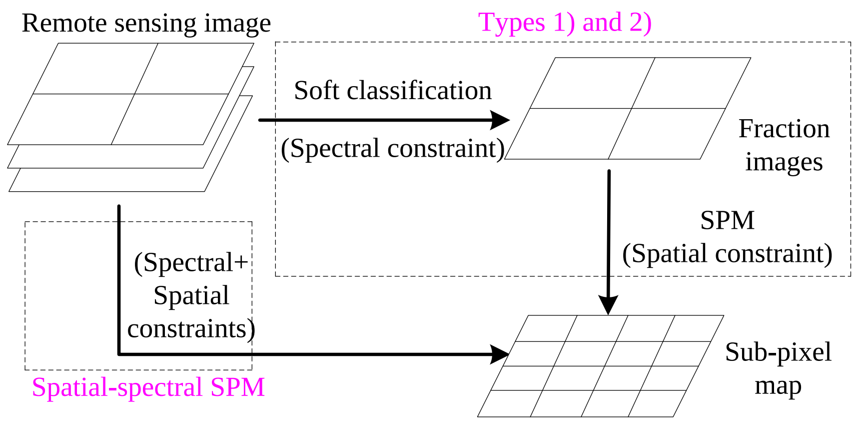

Figure 1.3. Spatial-spectral SPM and the two types of methods in Figure 1.2.

For most STHSPM algorithms, including BPNN, SPSAM, Kriging and ICK, SPM solutions can be achieved without iterations. Note the iterations in the training process in a BPNN are not considered, since the training process is always off-line. Hence, SPM can be realized quickly for the STHSPM algorithm. Moreover, as observed from Figure 1.2, the sub-pixel sharpening process can be potentially achieved by many existing super-resolution algorithms and, thus, the framework of STHSPM opens the door to new options for SPM. This study, therefore, was carried out focusing on the STHSPM algorithm.

1.4. Class allocation for STHSPM algorithms

How to allocate classes for STHSPM algorithms is a critical issue that directly affects the performance of STHSPM and needs in-depth study. When HNN-based SPM was initially proposed, a simple class allocation approach was applied: each sub-pixel is assigned to the class with the highest soft attribute value. This approach is easy to realize, since it does not take the constraints from class fractions into account and is carried out by only comparing the soft attribute values for sub-pixels. The approach was also applied for some other STHSPM algorithms, such as BPNN in Mertens et al. (2003, 2004) and Nigussie et al. (2011), ICK in Boucher and Kyriakidis (2008). However, the experiments in the related literature showed that this allocation approach does not guarantee coarse proportion reproduction and the SPM results are over smooth. It is insufficient to reproduce land cover objects smaller than a coarse pixel (Muad and Foody, 2012b).

In Verhoeye and De Wulf (2002), linear optimization technique (LOT) was introduced to allocate classes. In that work, Kriging was applied to estimate the soft attribute value for each class at each location. A mathematical model was then constructed to maximize the sum of soft attribute values of all sub-pixels in SPM results while satisfying a set of equality constraints from class fractions. The model was solved using LOT. LOT can obtain the theoretically optimal solution in terms of maximizing the objective function in the mathematical model. However, LOT involves numbers of iterations to gradually approach the optimal solution. Especially, when the zoom scale or the number of classes is large, much time will be consumed. Computational burden is a key issue in LOT-based class allocation method (Verhoeye and De Wulf, 2002).

A sequential assignment based class allocation method was also adopted for class allocation in Boucher and Kyriakidis (2006), Boucher et al. (2008), and Boucher

(2009). It assigns classes in units of sub-pixel (UOS). With UOS, the hard classified sub-pixel map is generated along a randomly predefined path that determines the order of visited sub-pixels. According to the path, each visited sub-pixel is assigned to the class with the highest soft attribute value, on condition that the sub-pixels of the dominant class have not been completely exhausted. In this way, the sub-pixel class labels within coarse pixels reproduce exactly the corresponding coarse fractions. This class allocation method involves no iteration and is fast. However, many speckle artifacts appear in the SPM results when using UOS-based class allocation method (Boucher, 2009).

Another sequential assignment based class allocation method was applied in Mertens et al. (2004, 2006) and Jin et al. (2012), where sub-pixels with the highest soft attribute values are assigned first (HAVF). With HAVF-based method, among soft attribute values for all sub-pixels and all classes within each coarse pixel, the highest one is found out during each comparison and the corresponding sub-pixel of this value is allocated to the dominant class if the sub-pixels of this class have not been completely exhausted. The already exhausted classes and allocated sub-pixels do not involve in the subsequent comparisons. The main difference between HAVF and UOS is that the visiting order of sub-pixels in HAVF is not randomly determined, instead, each sub-pixel in the path is specified by comparison of all soft attribute values. Even though, the performance of HAVF based class allocation method is not satisfying. Therefore, it is necessary to develop a more effective and efficient class allocation approach for STHSPM algorithms.

1.5. Using additional information in SPM

In order to produce more detailed and accurate sub-pixel land cover maps, some SPM techniques have been developed for use of supplementary information. Foody (1998) sharpened fraction images with additional finer spatial resolution image of the same scene to provide a more informative representation of the classes within coarse pixels. Aplin and Atkinson (2001) introduced a per-field classification-based SPM method by using auxiliary land-line vector boundaries to refine the distribution of classes within each polygon. In Atkinson (2008), the two-point histogram-based SPM model was enhanced by adding proportion constraints obtained from intermediate spatial resolution panchromatic images to the objective function of this model. Nguyen et al. (2005) applied the elevation data from LIDAR data to add a height function to HNN. Ling et al. (2008) and Huang et al. (2014)

obtained the terrain of land cover from digital elevation models and modified the waterline mapping results according to such elevations. Aiming at SPM for urban buildings, Ling et al. (2012) employed an anisotropic model by incorporating the prior shape information and enhancing the spatial dependence in some directions.

Based on HNN, Nguyen et al. (2006, 2011), Ling et al. (2010), and Muad and Foody (2010) presented some methods to provide additional proportion constraints for the energy function of HNN. In detail, Nguyen et al. (2006) obtained the fraction of each class at intermediate spatial resolution from panchromatic images. Similarly, Nguyen et al. (2011) fused panchromatic and multispectral images to obtain a multispectral image at the spatial resolution of the panchromatic image, and soft classification of the fused image was implemented to obtain the fractions at intermediate spatial resolution. Usually, observation satellites capture images of the same area at different times. Due to the slight orbit translations and the earth's rotation, these images are shifted at the sub-pixel level (Lu and Inamura, 2003; Ling et al., 2010; Muad and Foody, 2012b; Xu et al., 2013; Zhong et al., 2014). Ling et al. (2010) and Muad and Foody (2010) added soft classification outputs of multiple shifted images (MSI) to HNN.

1.6. SPM-based change detection

Change detection (CD) in remote sensing is a process in which multitemporal datasets are used to analyze and quantify temporal changes in Earth surface properties (Lu et al., 2004a; Hussain et al., 2013). Since remote sensing data can cover the same scene periodically and the digital format is suitable for further computer processing, they are a major source of information for CD. As one of the most important objectives in remote sensing, CD is applied in ecosystem monitoring, damage assessment, disaster monitoring, urban expansion, planning and land management (Lu et al., 2004a). Further details of CD applications using remote sensing technologies and existing CD methods can be found in reviews in Singh (1989), Coppin e al (2004), Lu et al. (2004a), Hussain et al. (2013) and Bruzzone and Bovolo (2013).

With increasing change on the Earth's surface (especially due to land cover, in highly developed areas, and as a function of changes in climate), timely CD is becoming increasingly important. Sensors such as the Moderate Resolution Imaging Spectroradiometer (MODIS) can cover the same area on a daily basis and have been in operation for over 10 years. However, a problem is that MODIS provides images with coarse spatial resolutions only, ranging from 250 to 1000 m. It is usually desirable to monitor changes at a fine spatial resolution to provide as much detailed information as possible. There is always a tradeoff between spatial resolution and temporal resolution. For example, although the Landsat sensors can provide remote sensing images at a finer spatial resolution (30 m) than MODIS, it can only revisit the same area every 16 days. Note that some satellites are able to capture fine spatial resolution images with relatively short revisit time (on a daily basis), such as WorldView and GeoEye, but the high budget and narrow swath hamper their application in timely CD to some extent, especially for large areas. Therefore, it is of great interest to apply CD at both fine spatial and temporal resolutions (such as at Landsat spatial resolution and MODIS temporal resolution) with computer technologies. Note that here we considered the Landsat spatial resolution (30 m) as "fine" relative to the MODIS spatial resolution (250 to 1000 m) and not in the absolute sense.

1.6.1. Spatiotemporal fusion

Spatiotemporal fusion techniques (Gao et al., 2006; Hilker et al., 2009; Zhu et al., 2010; Huang and Song, 2012; Song and Huang, 2013) have been developed to blend fine spatial but coarse temporal resolution images with coarse spatial but fine temporal resolution images to generate an image with both fine spatial and temporal resolution. Gao et al. (2006) proposed a spatial and temporal adaptive reflectance fusion model (STARFM) to blend fine temporal resolution information from a MODIS image and fine spatial resolution information from a Landsat image. To enhance the performance of STARFM for heterogeneous landscapes, an enhanced STARFM was developed in Zhu et al. (2010). For mapping forest disturbance, STARFM was extended with a spatial and temporal adaptive algorithm for mapping reflectance change that uses multiple Landsat images and a temporally dense stack of spatially coincident MODIS images (Hilker et al., 2009). In Huang and Song (2012), sparse representation was applied to characterize the corresponding relationship between structures in the known fine spatial resolution Landsat images and the corresponding coarse spatial resolution MODIS images, and the unknown fine spatial resolution image was reconstructed through sparse coding. Song and Huang (2013) superresolved a coarse spatial resolution MODIS image with sparse representation first, which was then fused with a known Landsat image by high-pass modulation to obtain a Landsat image on the prediction date.

The outputs of spatiotemporal fusion are remote sensing images in units of reflectance which can act as an intermediate step towards CD: the resulting fused images can be further processed by existing CD techniques in Singh (1989), Coppin e al (2004), Lu et al. (2004a), Hussain et al. (2013) and Bruzzone and Bovolo (2013) to monitor changes at a fine spatial and temporal resolution. Nevertheless, these spatiotemporal fusion models are usually built under different assumptions or for particular applications (e.g., mapping forest disturbance in Hilker et al. (2009)). They are performed with the hypothesis that there is fixed correspondence between the known fine spatial resolution image and the corresponding coarse spatial resolution image in the same area and such correspondence is used to predict the unknown fine resolution image on other days. However, because of differences in the weather, atmosphere and some other factors (e.g., uncertain natural changes and human activities) during data acquisition, it is sometimes difficult to obtain a reliable relationship between the fine and coarse resolution images, and in other cases the relationship may not be constant over a long period (i.e., is temporally non-stationary).

1.6.2. Spectral unmixing-based CD

For the coarse spatial resolution image, each pixel covers a large area and generally contains more than one type of land cover class, that is, constitutes a mixed pixel. Mixed pixels are a common problem caused by limited spatial resolution. Mixed pixel analysis techniques, such as spectral unmixing, have been studied for decades to extract land cover information within mixed pixels. Spectral unmixing is a technique to estimate the proportions of land cover classes within each mixed pixel and it has already been applied to CD (Haertel et al., 2004; Lu et al., 2004b, 2011). With spectral unmixing, the proportions of each class in the coarse spatial but fine temporal resolution images can be estimated. The unmixing outputs derived from time-series images can inform users of by how much the proportion of each land cover class increases or decreases during a given period (Anderson et al., 2005). Employing spectral unmixing straightforwardly for CD, however, one can only obtain quantitative information about the changes at the pixel-level (i.e., coarse spatial resolution) and cannot determine detailed change information at a finer spatial resolution, that is, changes in the sub-pixel classes.

Note that with the availability of fine spatial resolution land-use database LGN5, Zurita-Milla et al. (2009) introduced an unmixing-based data fusion approach to produce images with the temporal resolution of Medium Resolution Imaging Spectrometer (MERIS) and the spatial resolution of Landsat. Different from the standard spectral unmixing, however, the objective of such unmixing is to estimate endmembers (with the spectral resolution of MERIS) for each Landsat pixel which can be assumed to be pure. This unmixing-based fusion produces fine spatial resolution images in units of reflectance and it is essentially a type of spatiotemporal fusion technique.

1.6.3. SPM-based CD

SPM is a promising technique for CD and can provide fine spatial resolution thematic maps of land cover changes. It enables land cover changes between coarse spatial, but fine temporal resolution images to be monitored at a finer spatial resolution and, thus, enables CD to be performed at both fine spatial and temporal resolution. In recent years, several studies have been conducted on this topic. Foody and Doan (2007) studied forest cover changes in Brazil at 30 m Landsat spatial resolution, using two MERIS-like images (300 m). Specifically, the Hopfield neural network was employed for SPM of the two 300 m coarse spatial resolution images and the two resulting 30 m fine spatial resolution maps were compared for change analysis.

With the aid of a former fine spatial resolution land cover map, Ling et al. (2011) and Xu et al. (2014) utilized a pixel swapping algorithm to predict the land cover change at the sub-pixel resolution between bitemporal images. However, both the HNN and PSA are optimization-based algorithms, which are iterative and time-consuming. Using bitemporal Landsat and MODIS images, Li et al. (2014b) proposed a new Markov random field model for sub-pixel resolution CD of forests in the Brazilian Amazon basin. In this model, a temporal energy function characterized by transition probabilities during the studied period was added to the original Markov random field for SPM (Kasetkasem et al., 2005; Tolpekin and Stein, 2009). This model is also iterative, and moreover, determination of the weights for the spatial and temporal energy functions is an open problem. Thus, there is a need for the development of fast SPM algorithms for sub-pixel resolution CD in practical applications (e.g., CD at Landsat spatial resolution and MODIS temporal resolution).

1.7. Objectives

This thesis aims to study STHSPM for remote sensing images. The objectives are as follows.

1) To develop new class allocation methods for STHSPM algorithms, as presented in Chapter 2.
2) To use additional information (e.g., MSI) in STHSPM algorithms to enhance SPM accuracy, as presented in Chapter 3.
3) To develop new STHSPM algorithms, as presented in Chapters 4 and 5.
4) To develop fast STHSPM algorithms for fast sub-pixel resolution CD, as presented in Chapter 6.

2. Class allocation for STHSPM algorithms

2.1. Allocating classes for STHSPM algorithms in units of class

(This section is based on Wang *et al.* (2014b))

2.1.1. Introduction

In Section 2.1, a novel sequential assignment based class allocation method is proposed for STHSPM algorithms, which allocates classes in units of class (UOC). Different from three existing class allocation schemes (i.e., linear optimization technique (LOT), sequential assignment in units of sub-pixel (UOS) and a method that assigns sub-pixels with highest soft attribute values first (HAVF)), UOC allocates classes for sub-pixels along a predefined path that determines the order of visited class. The visiting order of all classes can be obtained from Moran's *I* (Makido et al., 2007), an index of intraclass spatial correlation. The proposed UOC approach holds several characteristics and advantages:

1) Similar to UOS and HAVF, UOC is free of any iteration. UOC is a very fast method (especially in comparison with LOT).
2) Similar to LOT, UOS and HAVF, UOC is implemented under the condition of reproducing exactly the coarse fraction data.
3) The unique advantage of UOC over LOT, UOS and HAVF is that UOC is processed on each soft classified image at fine spatial resolution in turn. In STHSPM algorithms, intraclass spatial dependence is taken into consideration in the first step. As a result, within each coarse pixel, sub-pixels staying together tend to have close soft attribute values for the same class and each generated soft classified image at fine spatial resolution encapsulates intraclass spatial correlation. During class allocation in UOC, autocorrelation for each class can be maximized and hence the proposed method is able to produce more satisfactory SPM results.

2.1.2. The STHSPM algorithms

The STHSPM algorithms contain two steps: 1) sub-pixel sharpening: computing soft attribute values for each class at fine pixels and 2) class allocation: allocating classes for these fine pixels according to the soft attribute values and class fractions. The outputs of the first and second step are a set of soft classified images and a set of hard classified images for all classes at fine spatial resolution, respectively. The first step can be accomplished by existing SPM methods including back-propagation neural network (BPNN), Hopfield neural network (HNN), sub-pixel/pixel spatial attraction model (SPSAM), Kriging and Indicator CoKriging (ICK). The first steps of these five STHSPM algorithms are briefly introduced in this section.

Suppose S is the zoom scale factor (i.e., each coarse pixel is divided into S^2 sub-pixels), P_t ($t = 1, 2, ..., M$, M is the number of pixels in the coarse image) is a coarse pixel, p_i (i=1,2,...,MS^2) is a sub-pixel and $Z_k(p_i)$ denotes the soft attribute value for the k-th ($k = 1, 2, ..., K$, K is the number of classes) class at sub-pixel p_i. The outputs of the first step of STHSPM algorithm are $\{Z_k(p_i) | i=1,2,...,MS^2; k = 1, 2, ..., K\}$. Define $x_k(p_i)$ as the binary class indicator for the k-th class at sub-pixel p_i:

$$x_k(p_i) = \begin{cases} 1, \text{ if sub-pixel } p_i \text{ belongs to class } k \\ 0, \text{ otherwise} \end{cases} \quad (2.1)$$

2.1.2.1. BPNN-based SPM

Mertens et al. (2003b, 2004), Wang et al. (2006), Zhang et al. (2008), and Nigussie et al. (2011) presented a BPNN-based SPM method. This method first extracts training samples from available high spatial resolution images, which are used as training images. The input of each training sample is a vector composed of coarse fractions for the k-th class at all coarse pixels within a local window while the output is a vector composed of $x_k(p_i)$ for all sub-pixels within the center coarse pixel. The training samples are then used to fit a BPNN. During the training process, the connection weightings between neurons of different layers are obtained iteratively. The trained BPNN is used to predict the outputs of test samples subsequently, of which the inputs are extracted from the fraction images for SPM.

2.1.2.2. HNN-based SPM

In HNN-based SPM, each sub-pixel is considered as a neuron and HNN is set up to minimize an energy function which comprises a goal and constraints (Tatem et al., 2001a,b,c, 2003; Atkinson, 2005; Nguyen et al., 2005, 2006, 2011; Muad and Foody, 2012a):

$$E = \alpha_1 G + \alpha_2 C \tag{2.2}$$

where α_1 and α_2 are weightings, the term G is to increase the spatial correlation between neighboring sub-pixels, and C are the constraints from fraction data and sum-to-one condition (i.e., the sum of soft attribute values for all classes at each neuron is equal to 1). The HNN is an optimization tool in nature. In this model, the attribute value (between 0 and 1) per sub-pixel per class is pushed iteratively toward 0 or 1 (Atkinson, 2009). The output of each neuron, $Z_k(p_i)$, is an attribute value either close to 0 or 1, however, not completely equal to 0 or 1.

2.1.2.3. SPSAM-based SPM

Mertens et al. (2006) applied SPSAM to directly calculate the spatial correlation between sub-pixels and their neighboring pixels by attractions. Suppose sub-pixel p_i's neighboring coarse pixels are $P_1, P_2, ..., P_N$ (N is the number of neighboring coarse pixels). In SPSAM, each p_i is assumed to be attracted by its neighboring coarse pixels. The soft attribute value $Z_k(p_i)$ can be calculated by the attraction from the k-th class to p_i:

$$Z_k(p_i) = \frac{1}{N}\sum_{n=1}^{N}\frac{F_k(P_n)}{d(P_n, p_i)} \tag{2.3}$$

where $d(P_n, p_i)$ is the Euclidean distance between geometric centers of pixel P_n and sub-pixel p_i, and $F_k(P_n)$ is the coarse fraction of the k-th class at the n-th neighboring pixel P_n.

2.1.2.4. Kriging-based SPM

The Kriging-based SPM developed by Verhoeye and De Wulf (2002) was based on the assumption that the soft attribute value for each class at each location (i.e., sub-pixel) is a weighted linear combination of N_0 observed values:

$$Z_k(p_i) = \sum_{n=1}^{N_0}\beta_n Z_k(P_n) \tag{2.4}$$

where β_n is a weight and $Z_k(P_n)$ denotes a continuous variable for the *k*-th class at pixel P_n. $Z_k(P_n)$ can be depicted by fraction of the *k*-th class at P_k and β_n are estimated by solving the kriging system (Goovaerts, 1997). The semivariance in the kriging system can be derived from the coarse images, which does not require any prior information.

2.1.2.5. ICK-based SPM

Let all fractions for the *k*-th class be arranged in a $(M \times 1)$ vector $\boldsymbol{F}_k$ and π_k be the mean of all elements in vector $\boldsymbol{F}_k$. Suppose there are *H* informed (i.e., the class labels are known) fine pixels available and the *H* indicators for the *k*-th class are arranged in a $(H \times 1)$ vector $\boldsymbol{j}_k$. Then, the soft attribute value $Z_k(p_i)$ can be estimated by:

$$Z_k(p_i) = \boldsymbol{\eta}_k(p_i)^{\mathrm{T}} \boldsymbol{F}_k + \boldsymbol{\lambda}_k(p_i)^{\mathrm{T}} \boldsymbol{j}_k + \pi_k[1 - sum(\boldsymbol{\eta}_k(p_i)^{\mathrm{T}}) - sum(\boldsymbol{\lambda}_k(p_i)^{\mathrm{T}})] \quad (2.5)$$

where the $(M \times 1)$ vector $\boldsymbol{\eta}_k(p_i)$ and $(H \times 1)$ vector $\boldsymbol{\lambda}_k(p_i)$ are ICK weightings for the *k*-th class. The function *sum*(•) takes the sums of all the elements in vector •. The weightings $\boldsymbol{\eta}_k(p_i)$ and $\boldsymbol{\lambda}_k(p_i)$ are calculated by solving the ICK system (Boucher and Kyriakidis, 2006, 2008; Boucher et al., 2008; Boucher, 2009; Jin et al., 2012). The semivariance in the ICK system needs to be extracted from available fine spatial resolution images.

The soft attribute value $Z_k(p_i)$ estimated by STHSPM algorithms can be understood as the probability of the *k*-th class occurrence at sub-pixel p_i. Usually, the preliminarily obtained soft attribute value, denoted as $Z_k^{'}(p_i)$, may be less than 0 or not satisfy the sum-to-one condition (especially for BPNN). Taking account of the physical meaning, two extra steps for adjustments are applied. The first is to revise the attribute values to 0 if they are less than 0 and the second is to normalize the soft attribute values by:

$$Z_k(p_i) = \frac{Z_k^{'}(p_i)}{\sum_{k=1}^{K} Z_k^{'}(p_i)} \quad (2.6)$$

so that $Z_k(p_i) \in [0,1]$ and $\sum_{k=1}^{K} Z_k(p_i) = 1$.

2.1.3. Three class allocation methods for STHSPM algorithms

The ultimate goal of SPM is to generate hard classified maps at sub-pixel level. After $\{Z_k(p_i) | i=1,2,...,MS^2; k=1,2,...,K\}$ are obtained by any STHSPM algorithm introduced in Section 2.1.2, they are used to allocate hard attribute values for sub-pixels along with the class fractions. This section describes three existing class allocation methods, LOT, UOS and HAVF.

To facilitate description in this section, all sub-pixels in the coarse image that has M pixels are divided into M groups, i.e., $\{p_i | i=1,2,...,MS^2\}$ is re-denoted as $\{p_i^t | i=1,2,...,S^2; t=1,2,...,M\}$, where p_i^t denote the sub-pixels within coarse pixel P_t and S is the zoom scale factor. The objective of class allocation is to acquire binary class indicators $\{x_k(p_i^t) | i=1,2,...,S^2; t=1,2,...,M; k=1,2,...,K\}$ and a sub-pixel map R (i.e., SPM result) having K gray values, can be produced by:

$$R(p_i^t) = \sum_{k=1}^{K} k x_k(p_i^t),\ i=1,2,...,S^2; t=1,2,...,M \tag{2.7}$$

As can be concluded from (2.1) and the principle that each sub-pixel belongs to only one class, $R(p_i^t) = 1,2,...,K$.

2.1.3.1. LOT

LOT was introduced in Verhoeye and De Wulf (2002) for Kriging-based SPM, which is to maximize an objective function while meeting a set of equality constraints. In the constructed mathematical model, for each coarse pixel P_t in the coarse image, J_t is maximized:

$$\begin{aligned} &\max \quad J_t = \sum_{i=1}^{S^2}\sum_{k=1}^{K} x_k(p_i^t) Z_k(p_i^t) \\ &s.t. \quad \sum_{k=1}^{K} x_k(p_i^t) = 1, \quad i=1,2,...,S^2 \\ &\qquad\ \ \sum_{i=1}^{S^2} x_k(p_i^t) = F_k(P_t)S^2, \quad k=1,2,...,K \end{aligned} \tag{2.8}$$

where $F_k(P_t)$ is the coarse fraction of the k-th class at pixel P_t and $\sum_{k=1}^{K} F_k(P_t) = 1$. $Z_k(p_i^t)$ were originally obtained by Kriging in Verhoeye and De Wulf (2002), but we know now they can also be calculated by any STHSPM algorithm introduced in Section 2.1.2. The two types of equality constraints in (2.8) can be written as the two corresponding expressions:

$$\boldsymbol{X}\boldsymbol{1}_K = \boldsymbol{1}_{S^2} \tag{2.9}$$

$$\boldsymbol{X}^{\mathrm{T}}\boldsymbol{1}_{S^2} = S^2\boldsymbol{F} \tag{2.10}$$

where $\boldsymbol{X}$ is a ($S^2 \times K$) matrix:

$$\boldsymbol{X} = \begin{bmatrix} x_1(p_1^t) & x_2(p_1^t) & \dots & x_K(p_1^t) \\ x_1(p_2^t) & x_2(p_2^t) & \dots & x_K(p_2^t) \\ \dots & \dots & \dots & \dots \\ x_1(p_{S^2}^t) & x_2(p_{S^2}^t) & \dots & x_K(p_{S^2}^t) \end{bmatrix}$$

and $\boldsymbol{F} = \left[F_1(P_t), F_2(P_t), \ldots, F_K(P_t)\right]^{\mathrm{T}}$. $\boldsymbol{1}_K$ and $\boldsymbol{1}_{S^2}$ denote, respectively, a ($K \times 1$) and a ($S^2 \times 1$) vector of ones.

Constraints in (2.9) means that each sub-pixel should be assigned to only one class while constraints in (2.10) means that the number of sub-pixels belonging to each class should be consistent with the coarse fraction data. In all, this mathematical model is to maximize the sum of soft attribute values of all sub-pixels in the resulting SPM map in the meanwhile fixing the number of sub-pixels for each class according to the coarse fractions. The linear problem in (2.8) can be solved by LOT and the classical simplex algorithm (Kolman and Beck, 1995) can be employed for this purpose.

Using LOT, the optimal solution to (2.8) will be generated. The whole process, however, requires numbers of iterations and is time consuming. It can be observed that for each coarse pixel, there are KS^2 variables and $K+S^2$ equality constraints in (2.8), and correspondingly KS^2 elements in matrix $\boldsymbol{X}$. Therefore, the computing complexity is closely related to M, K and S. When K or S increases, the computing complexity will increase noticeably. Computational limitations prevent further research into finer spatial resolutions and more classes (Verhoeye and De Wulf, 2002).

2.1.3.2. UOS

The sequential assignment based class allocation method, UOS, is also performed under the conditions of meeting the equality constraints in (2.8) or (2.9)-(2.10) and the basic principle of UOS is the same as the objective function in (2.8). The class allocation process of UOS, however, is different from LOT. UOS is performed by direct comparison of K soft attribute values for each sub-pixel.

UOS first determines the number of sub-pixels for each class according to the coarse fractions. To satisfy the constraints in (2.8), during the allocation process, each sub-pixel has to be assigned to only one class and the sub-pixels for each class have to be completely exhausted. A visiting path is then defined that determines the order of visited sub-pixels. Along this path, for a sub-pixel being visited, say p_i, the K soft attribute values $Z_1(p_i), Z_2(p_i), ..., Z_K(p_i)$ are compared and ranked in a descending order. If the sub-pixels for the class with the highest soft attribute value, say class k_0, have not been completely exhausted, then p_i is allocated to class k_0 (i.e., $x_{k_0}(p_i)=1, x_{k \neq k_0}(p_i)=0$); if the sub-pixels for k_0 have already been exhausted, p_i is allocated to the class whose sub-pixels have not been completely exhausted as well as having the highest soft attribute value, and for the remaining sub-pixels, the soft attribute values for class k_0 are not considered in the comparisons any more.

UOS is a single-pass method and thus it involves no iteration (Boucher and Kyriakidis, 2006). The visiting order of sub-pixels in UOS method is determined randomly. The visiting path has direct influence on the SPM performance and different paths may result in different SPM results. There is much randomness when the path is determined randomly as there are S^2! paths for each coarse pixel in all. The experimental results in the literature on UOS revealed that many speckle artifacts appear in the SPM results (Boucher, 2009).

2.1.3.3. HAVF

Similar to UOS, another sequential assignment based class allocation method, HAVF, is also realized by direct comparison of soft attribute values. HAVF has been applied to BPNN (Mertens et al., 2004), SPSAM (Mertens et al., 2006) and ICK (Jin et al., 2012). In each comparison, however, HAVF does not only compare K soft attribute values for a sub-pixel, but also KS^2 values for all S^2 sub-pixels and K classes within a particular coarse pixel. The highest soft attribute value is found out and the corresponding sub-pixel is also selected out meanwhile. The selected sub-pixel is allocated to its dominant class, on condition that the sub-pixels for this class have not been completely exhausted; otherwise, all S^2 soft attribute values for this class are set to a value less than 0 to be excluded in the following comparisons. When the selected sub-pixel is successfully allocated to a class, the K soft attribute values for this sub-pixel are also set to a value less than 0. The process is terminated when all S^2 sub-pixels within each coarse pixel are allocated.

HAVF is also non-iterative and reproduces exactly the coarse fraction data. Different from UOS, for each coarse pixel, each sub-pixel in the visiting path in HAVF method is found by comparison of all KS^2 values. Therefore, for each coarse pixel, the visiting path is unique, rather than a random one (as in UOS). Note that for UOS and HAVF, a normalization procedure is suggested (Mertens et al., 2004, 2006; Shen et al., 2009). Specifically, within each coarse pixel, each soft attribute value is divided by the sum of S^2 attribute values from the same class. This adjustment is advantageous in cases where sub-pixels are surrounded by small fractions of a certain class and soft attribute values for this class are small (Mertens et al., 2004, 2006). This normalization procedure is performed previously to that in (2.6).

2.1.4. UOC

From LOT, UOS and HAVF, it can be concluded that three tasks should be completed during class allocation process for STHSPM algorithms.

1) For each sub-pixel, it should be assigned to one and only one class.
2) For each class, the number of sub-pixels belonging to it should be consistent with the coarse fraction data and they should be completely exhausted during class allocation process.
3) Attempt to maximize the objective function in (2.8).

Based on these three aspects, a new class allocation method, UOC, is proposed. In UOC, sub-pixels for each class are allocated in turn. Actually, UOS and HAVF start with 1) whereas the proposed UOC starts with 2).

2.1.4.1. Implementation of UOC

The implementation of UOC includes the following 6 steps.

Step 1: Define a visiting order of K classes: $k_1, k_2, \cdots, k_K$. This order can be defined randomly or by Moran's I, see Section 2.1.4.2 for details.

Step 2: For the being visited class, say k_r, the number of sub-pixels belonging to it in coarse pixel P_t is determined as $F_{k_r}(P_t)S^2$.

Step 3: At the current coarse pixel P_t, rank the S^2 soft attribute values $Z_{k_r}(p_1^t), Z_{k_r}(p_2^t), ..., Z_{k_r}(p_{S^2}^t)$ that have been obtained by any STHSPM algorithm in Section 2.1.2 in a decreasing order and a new sequence is generated: $Z_{k_r}(p^t_{D_1}), Z_{k_r}(p^t_{D_2}),..., Z_{k_r}(p^t_{D_{S^2}})$.

Step 4: According to aforementioned tasks 2) and 3) in Section 2.1.4, the first NCr (NCr=$F_{k_r}(P_t)S^2$) sub-pixels in the new sequence, $p^t_{D_1}, p^t_{D_2},..., p^t_{D_{NCr}}$, are allocated to class k_r.

Step 5: According to task 1), the already allocated sub-pixels should not be considered in the allocation for remaining classes. To guarantee that, all soft attribute values for the next visited class k_{r+1} are adjusted by:

$$Z_{k_{r+1}}(p^t_i) = Z_{k_{r+1}}(p^t_i) - c\sum_{j=1}^{r} x_{k_j}(p^t_i) \tag{2.11}$$

where $c > 1$ is a coefficient. After adjustment, at any already allocated sub-pixel p_a:

$$\left.\begin{aligned} &\sum_{j=1}^{r} x_{k_j}(p_a) = 1 \\ &Z_{k_{r+1}}(p_a) \in [0,1] \end{aligned}\right\} \Rightarrow \left[Z_{k_{r+1}}(p_a) - c\sum_{j=1}^{r} x_{k_j}(p_a) \right] \in [-c, 1-c] \tag{2.12}$$

which indicates with (2.11), the soft attribute values for the next visited class k_{r+1} at already allocated sub-pixels are automatically suppressed to be less than 0 (1-c<0). On the other hand, at any unallocated sub-pixel p_{ua}:

$$\left.\begin{aligned} &\sum_{j=1}^{r} x_{k_j}(p_{ua}) = 0 \\ &Z_{k_{r+1}}(p_{ua}) \in [0,1] \end{aligned}\right\} \Rightarrow Z_{k_{r+1}}(p_{ua}) - c\sum_{j=1}^{r} x_{k_j}(p_{ua}) = Z_{k_{r+1}}(p_{ua}) \in [0,1] \tag{2.13}$$

which indicates that the soft attribute values at unallocated sub-pixels do not make any change using adjustment in (2.11). From (2.12) and (2.13), it can be concluded after adjustment (2.14) holds:

$$Z_{k_{r+1}}(p_a) < Z_{k_{r+1}}(p_{ua}) \tag{2.14}$$

As the number of sub-pixels for class k_{r+1} is less than the number of unallocated sub-pixels, adjustment in (2.11) ensures the already allocated sub-pixels will not be allocated to class k_{r+1} any more. Therefore, the adjustment in (2.11) is an adaptive and simple scheme that does not need to artificially find out the already allocated sub-pixels or specially exclude them during class allocation process. Using (2.11), only one simple command is needed to exclude the already allocated sub-pixels for class allocation, as shown in the last sentence in the pseudocode given below.

Note that c can take any value greater than 1 to ensure 1-c<0, and it does not have any influence on the following class allocation process as it does not change the soft attribute values at unallocated sub-pixels at all.

Step 6: The whole process is terminated when all MS^2 sub-pixels are allocated.

Algorithm: Class allocation based on UOC

Inputs:

Soft attribute values $\left\{Z_k(p_i^t) \middle| i=1,...,S^2; t=1,...,M; k=1,...,K\right\}$;

Class fractions $\left\{F_k(P_t) \middle| t=1,2,...,M; k=1,2,...,K\right\}$ and zoom scale factor S.

Define a visiting order of K classes: $k_1, k_2, \cdots, k_K$

for r = 1: K

  for t = 1: M

    Rank sequence $Z_{k_r}(p_1^t), Z_{k_r}(p_2^t), ..., Z_{k_r}(p_{S^2}^t)$ in a decreasing order:

    $Z_{k_r}(p_{D_1}^t), Z_{k_r}(p_{D_2}^t), ..., Z_{k_r}(p_{D_{S^2}}^t)$

    for i = 1: $F_{k_r}(P_t)S^2$

      $x_{k_r}(p_{D_i}^t) = 1$

    end

    for i = $F_{k_r}(P_t)S^2 + 1$: S^2

      $x_{k_r}(p_{D_i}^t) = 0$

    end

  end

  Image $Z_{k_{r+1}}$ is updated by $Z_{k_{r+1}} = Z_{k_{r+1}} - c\sum_{j=1}^{r} x_{k_j}$

end

Outputs:

Binary class indicators $\left\{x_k(p_i^t) \middle| i=1,...,S^2; t=1,...,M; k=1,...,K\right\}$.

Without the adjustment in (2.11), some sub-pixels would be allocated to more than one class and some sub-pixels would not be allocated to any class as a result. This conflicts with the aforementioned task 1). An example in Figure 2.1 is used to illustrate the necessity of the adjustment in (2.11). Suppose a coarse pixel covers three land cover classes, class 1, 2 and 3, and the fraction of three classes are 50%, 25% and 25%. With a zoom scale S=2, there should be two, one and one sub-pixels assigned to class 1, 2 and 3, respectively. Let the visiting order of the three classes be 1-2-3. According to the soft attribute values of class 1, sub-pixels p_4 and p_3 are allocated to this class first. Without the adjustment, however, when class 2 is visited, p_3 is again allocated to class 2 as 0.5 is the largest value among the four soft attribute values of class 2. Consequently, p_2 will be allocated to class 3 and p_1 will not be allocated to any class. If adjustment in (2.11) is applied (c is set to 2), when class 2 is visited after class 1, the four soft attribute values of class 2 are adjusted to $Z_2(p_1)=0.3$, $Z_2(p_2)=0.2$, $Z_2(p_3)=-1.5$ and $Z_2(p_4)=-1.9$. $Z_2(p_3)$ and $Z_2(p_4)$ are very small after adjustment and p_4 and p_3 will not be considered in the allocation for class 2. Instead, p_1 will be allocated to class 2 and p_2 will be allocated to class 3 as a result.

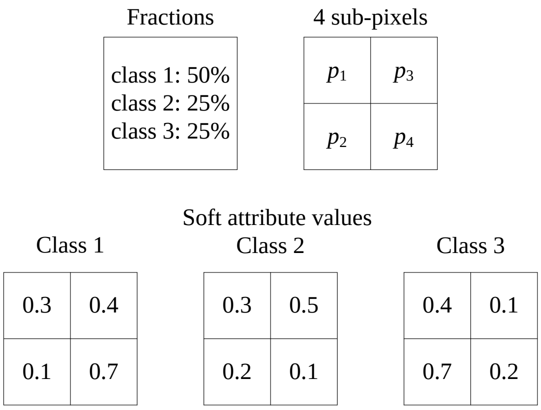

Figure 2.1. Illustration of the necessity of the adjustment in (2.11).

2.1.4.2. Visiting order of classes specified by Moran's I

In UOC, there are $K!$ visiting orders of classes in all and different orders may lead to different SPM results. This can also be illustrated by the example in Figure 2.1. Along two different visiting orders, such as 1-2-3 and 2-1-3, different SPM results are generated (see Figure 2.2). The visiting order in UOC, therefore, should be specified reasonably.

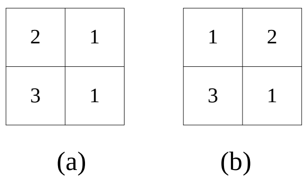

Figure 2.2. Follow-up to Figure 2.1. Two different SPM results generated along two different visiting orders of classes in UOC. (a) Class order: 1-2-3. (b) Class order: 2-1-3

Moran's I is an index of spatial autocorrelation for the landscape (Makido et al., 2007). In Makido et al. (2007), Moran's I was used to determine the order of input classes for pixel swapping algorithm that was extended to multiple classes. Here, it is employed to determine a reasonable visiting order of classes in UOC. The index can be estimated from an available high spatial resolution land cover map. The map needs to be representative of the study area for SPM. Moran's *I* for the *k*-th class, I_k, is calculated as:

$$I_k = \frac{V\sum_{i=1}^{V}\sum_{j=1}^{V}W_{ij}\left[x_k(p_i)-\overline{x_k}\right]\left[x_k(p_j)-\overline{x_k}\right]}{\left(\sum_{i=1}^{V}\sum_{j=1}^{V}W_{ij}\right)\sum_{i=1}^{V}\left[x_k(p_i)-\overline{x_k}\right]^2} \tag{2.15}$$

where

$$W_{ij} = \begin{cases} 1, \text{ if } p_i \text{ and } p_j \text{ are neighbors} \\ 0, \text{ otherwise} \end{cases} \tag{2.16}$$

and *V* is the number of pixels in the high spatial resolution map. $\overline{x_k}$ is the mean of all binary class indicator for the *k*-th class. In this study, 8-nearest neighbors are considered in (2.16).

If the high spatial resolution map is available, it can be readily used for Moran's *I* estimation. A critical issue, however, is that such high spatial resolution images are not obtainable in general. For this reason, a novel method to calculate Moran's *I* without high spatial resolution map is proposed, which estimates the index by directly using the fraction image of each class. Although the fraction images are in coarse spatial resolution, they contain spatial distribution characteristics for land cover classes. With the novel method, I_k is calculated as:

$$I_k = \frac{M\sum_{i=1}^{M}\sum_{j=1}^{M}W_{ij}\left[F_k(P_i)-\overline{F_k}\right]\left[F_k(P_j)-\overline{F_k}\right]}{\left(\sum_{i=1}^{M}\sum_{j=1}^{M}W_{ij}\right)\sum_{i=1}^{M}\left[F_k(P_i)-\overline{F_k}\right]^2} \tag{2.17}$$

where $\overline{F_k}$ is the mean of all fractions for the *k*-th class in fraction image F_k. I_k take values in the range [-1, 1], and -1 and 1 indicate the weakest and the strongest autocorrelation, respectively. After the indices of *K* classes are calculated, they are ranked in a decreasing order and the classes with higher indices are visited first.

2.1.4.3. Comparison with UOS, HAVF and LOT

Similar to UOS and HAVF, UOC is also a sequential assignment based class allocation method. All of them are single-pass methods that are free of iteration and thus are fast. Moreover, all three methods are performed under the condition of reproducing exactly the coarse fractions. The core difference between UOS and UOC is that comparisons of soft attribute values are implemented in different units, see Figure 2.3. More precisely, UOS compares K soft attribute values of K classes at the being visited sub-pixel while UOC compared S^2 soft attribute values for the being visited class within each coarse pixel. UOS and UOC allocate classes for sub-pixels along paths which determine the order of visited sub-pixels and classes.

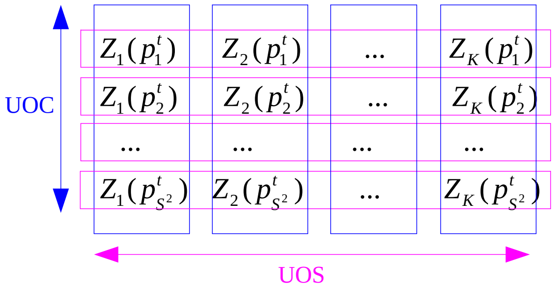

Figure 2.3. Difference between UOC and UOS: comparisons in different units.

Compared with LOT, a significant advantage of UOC is its little computing complexity. For each coarse pixel, LOT solves a linear problem involving KS^2 variables and $K+S^2$ equality constraints, as listed in (2.8). The optimal solution is obtained after numbers of iterations. When K or S, or even M is large, the whole process will be considerably CPU-demanding. As for UOC, for each coarse pixel, only K comparisons need to be carried out and the output of each comparison is a sequence, which is used to select out the sub-pixels for the corresponding class, as shown in Step 3 in Section 2.1.4.1. The comparisons in UOC require little time, far less than LOT does.

Table 2.1 summarizes the soft attribute value comparison for three sequential assignment based class allocation methods: UOS, HAVF and UOC. As shown in the table, for each coarse pixel, UOS and UOC need S^2 and K comparisons, and K and S^2 elements are involved in each comparison for the two methods; HAVF sometimes need more than S^2 comparisons, because the sub-pixels for the class, to which the highest soft attribute value corresponds, may have been exhausted and the selected sub-pixel will not be allocated to any class for that comparison. For HAVF, KS^2 elements are compared each time. Obviously, HAVF requires more time than UOS to complete class allocation. Similar to UOC, the consuming time of UOS and HAVF is generally less than that of LOT, since the value comparison is easy and fast for computers to realize.

UOC is processed on K soft classified images at fine spatial resolution one-by-one. Each soft classified image encapsulates spatial continuity for the corresponding class. That is, within each coarse pixel, sub-pixels with large soft attribute values for the same class tend to stay together. Using UOC, sub-pixels staying together are more likely to be allocated to the same class than distant ones. In this way, autocorrelation for each class can be maximized by Step 4 in Section 2.1.4.1, which is not the case in LOT, UOS and HAVF. According to spatial dependence principle that underpins SPM, the intraclass spatial correlation are expected to be maximized, which can just been done by UOC. For UOC, this is the unique advantage over LOT, UOS and HAVF when it is applied to STHSPM algorithms.

Table 2.1 Statistics of soft attribute value comparison during class allocation process for UOS, HAVF and UOC (analyzed for a single coarse pixel)

	Comparison times	Elements involved in each comparison
UOS	S^2	K
HAVF	$[S^2, K+S^2)$	KS^2
UOC	K	S^2

After description of five STHSPM algorithms, existing LOT, UOS, HAVF and the proposed UOC, the systemic framework of STHSPM algorithms are shown in Figure 2.4.

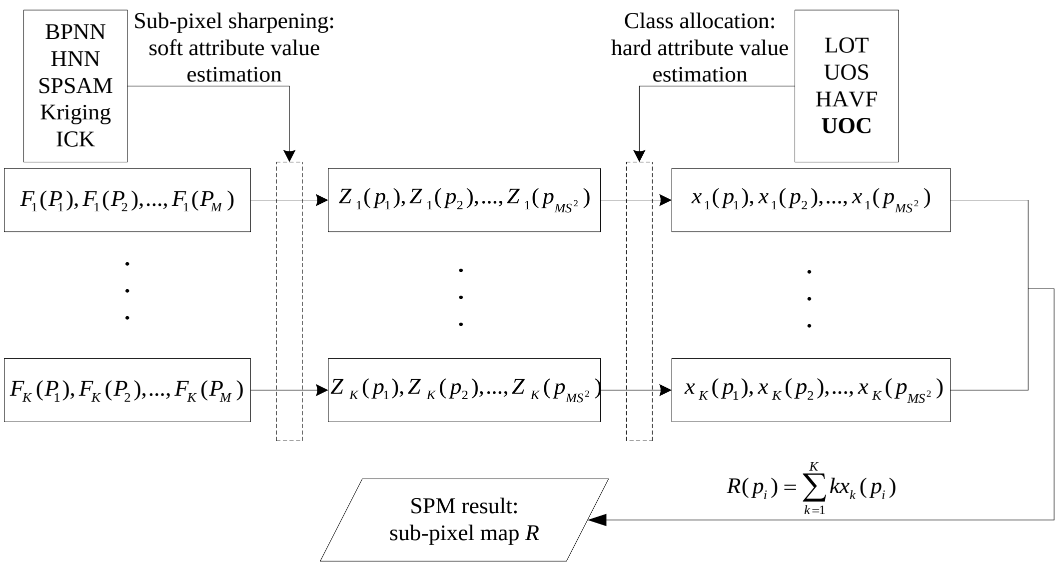

Figure 2.4. Systemic framework of STHSPM algorithms, where the proposed class allocation method UOC is in bold.

2.1.5. Experiments and Analysis

2.1.5.1. Experimental setup and accuracy assessment

To demonstrate the effectiveness and advantages of the proposed UOC-based class allocation method for STHSPM algorithms, experiments on three remote sensing images were implemented. UOC was applied to all the five STHSPM algorithms introduced in Section 2.1.2: BPNN, HNN, SPSAM, Kriging and ICK. UOC was also compared to LOT, UOS and HAVF-based class allocation methods. All experiments were tested on an Intel Core 2 Processor (1.80-GHz Duo central processing unit, 2.00-GB random access memory) with MATLAB 7.1 version. For BPNN, a 3×3 local window was used to extract the inputs of both training and test samples, and the parameters involved in this method were set to the same values as in Wang et al. (2006). The parameters in HNN were the same as in Wang and Wang (2013).

To objectively evaluate and solely concentrate on the performance of the proposed UOC, in the first and second experiments the studied coarse images were produced by degrading hard classified reference land cover maps using an $S \times S$ mean filter. The synthetic coarse images were considered as outputs of soft classification. SPM algorithms were processed on the coarse images to yield land cover maps having the same spatial resolution as the corresponding reference maps, by zooming in the coarse images with the scale factor S. The advantages of using such synthetic coarse images include: 1) errors from soft classification and some other processes (e.g., registration) are avoided (Xu et al., 2013) and the test is directed at the SPM algorithm itself (Atkinson, 2009); 2) the reference land cover maps are completely reliable for accuracy assessment. In the third experiment, a coarse image was produced by degrading a Landsat TM image. Soft classification was then implemented on the coarse image to generate fractions, with SPM subsequent to that. By such setup, inherent uncertainty in soft classification was taken into consideration (Atkinson, 2009) and the fractions were more similar to those in real applications in comparison with those in the first two experiments.

SPM is essentially a hard classification technique carried out at sub-pixel level. The accuracy of hard classification algorithms is usually evaluated quantitatively by the overall accuracy in terms of the percentage of correctly classified pixels (PCC). Due to that, PCC was used for accuracy assessment on SPM results in all three experiments. To evaluate the statistical significance in accuracy for different

STHSPM algorithms and class allocation methods, McNemar's test (Foody, 2004) was also applied. The significance of difference between two classification results is determined by:

$$z_{01} = \frac{f_{01} - f_{10}}{\sqrt{f_{01} + f_{10}}} \tag{2.18}$$

where f_{01} are the number of pixels that are correctly classified in result 0 but incorrectly classified in result 1 and f_{10} vice versa. Using the 95% degree of confidence level, the difference between two classification results is considered to be statistically significant if $|z_{01}|$>1.96.

2.1.5.2. Experiment 1

In the first experiment, a land cover map of an area in Bath, UK was studied, as shown in Figure 2.5 (provided by Dr. A. J. Tatem). The land cover map was obtained by manual digitization of the aerial photograph in Tatem et al. (2001c). The map contains 360×360 pixels and covers four classes: roads, trees, buildings and grass. The roads and buildings mainly appear as straight lines and right-angles, respectively. The spatial pattern of trees is more complex and irregular. The map was degraded with two scales, S=5 and 10, to generate two coarse images. The fraction images of four classes in the coarse image generated with S=10 are shown in Figure 2.6. From these fraction images, it can be seen clearly that the coarse proportion information is insufficient to represent the spatial distribution of land cover classes, which indicates the necessity of SPM in land cover information extraction.

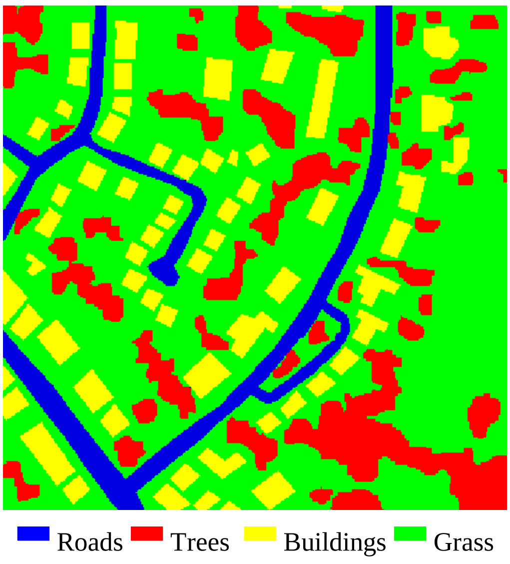

Figure 2.5. Reference land cover map in the first experiment.

The five STHSPM algorithms, BPNN, HNN, SPSAM, Kriging and ICK, were then processed on the two coarse images generated with *S*=5 and 10 to reconstruct the land cover maps having the same spatial resolution as that of Figure 2.5. The reference map in Figure 2.5 was used to extract training samples for BPNN and indicator semivariogram for ICK. Table 2.2 lists the Moran's *I* of the four classes in different spatial resolution images and the corresponding specified visiting orders of four classes. Here, *S*=1 means the indices were calculated using (2.15), based on the assumption that the required high spatial resolution map (i.e., Figure 2.5) is available. For two coarse images, the indices of classes were calculated using our proposed method in (2.17). As shown in the table, in this experiment, the orders specified by two approaches at three scales are the same.

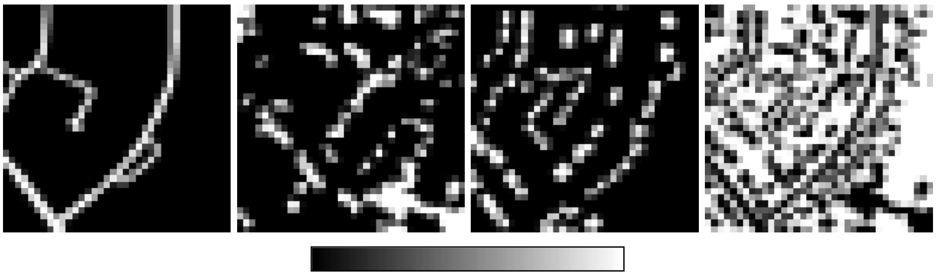

(a) (b) (c) (d)

Figure 2.6. Fraction images produced by degrading the reference land cover map in the first experiment with *S*=10. (a) Roads. (b) Trees. (c) Buildings. (d) Grass.

Table 2.2 Moran's *I* of four classes at different scales in the first experiment

	S=1	*S*=5	*S*=10
Roads	0.9243	0.7227	0.5034
Trees	0.9130	0.7123	0.4919
Buildings	0.8961	0.6577	0.3590
Grass	0.8731	0.5715	0.2850
Specified order	Roads-Trees -Buildings-Grass	Roads-Trees -Buildings-Grass	Roads-Trees -Buildings-Grass

Figure 2.7 shows the SPM results for the coarse fraction images in Figure 2.6. The five STHSPM algorithms were combined with UOS, HAVF, LOT and UOC based class allocation methods. The results of UOC shown in Figure 2.7 were produced with specified order at *S*=10 (i.e., Roads-Trees-Buildings-Grass), as listed in Table 2.2. For UOS, results generated with a random visiting order of sub-pixels for five STHSPM algorithms are shown in the first column in Figure 2.7. As can be

seen from the maps, there are many speckle artifacts in SPM results while using UOS for class allocation. In comparison with UOS, much less speckle artifacts are generated by HAVF and LOT, and both of them can obviously obtain better results than UOS. Focusing on maps yielded by the proposed UOC, the boundaries of classes are clearer than those in UOS, HAVF and LOT results. There are fewer isolated pixels in UOC results, which is particularly well illustrated by the restoration of roads in five maps in the last column. Among four class allocation methods, UOC produces the most satisfactory fine spatial resolution maps.

(a)
(b)
(c)
(d)
(e)

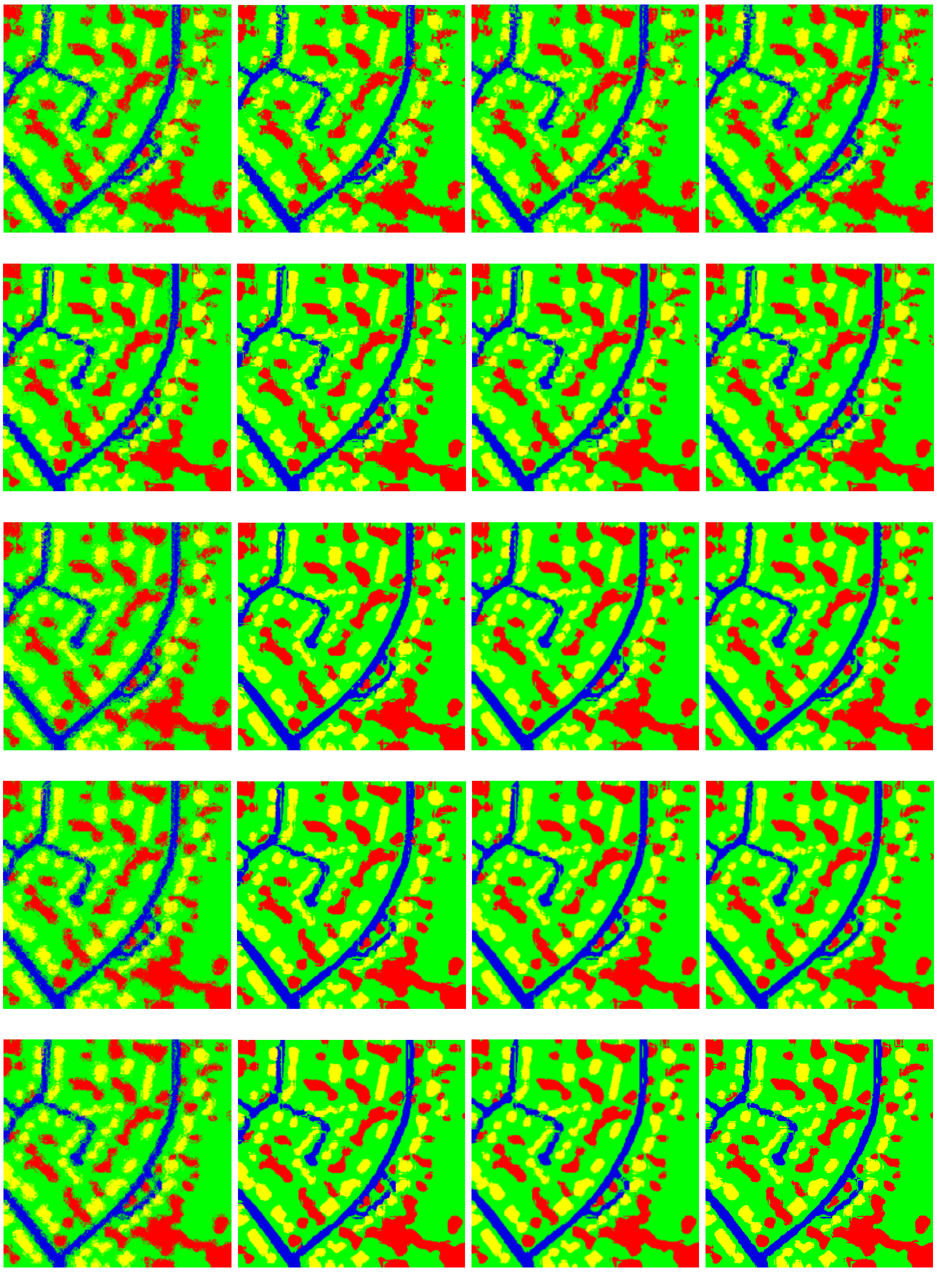

Figure 2.7. SPM results of five STHSPM algorithms combined with UOS, HAVF, LOT and UOC based class allocation methods in the first experiment (S=10). (a) BPNN. (b) HNN. (c) SPSAM. (d) Kriging. (e) ICK. From left to right: UOS (a random realization), HAVF, LOT and UOC (visiting order specified by Moran's I).

The SPM results were also assessed quantitatively by PCC. As can be observed in the fraction images in Figure 2.6, there are some pure coarse pixels containing only one land cover class. In SPM, all sub-pixels within the pure pixel are allocated to the same class to which the pure pixel belongs. This simple copy process only raises PCC without providing useful information about the SPM algorithms' prediction abilities (Mertens et al., 2003; Wang et al., 2012a,b; Zhong and Zhang, 2012, 2013). To eliminate the influence brought by the pure pixels, sub-pixels within them were excluded in the accuracy statistics in this experiment. Figure 2.8 shows PCC of five STHSPM algorithms combined with HAVF, LOT and UOC at S=5 and 10, corresponding to 10 sub-figures in all. To clearly exhibit the differences between lines of LOT and HAVF, the PCC of UOS is not shown in Figure 2.8 but in Table 2.3 instead. Because in UOS different visiting paths of sub-pixels lead to different SPM results, 100 random paths were tested for UOS. In all 10 cases, the PCC of UOS is lower than that of HAVF, LOT and UOC. The PCC of UOC with all 24 (4!=24) visiting orders are also displayed in Figure 2.8. The labels for corresponding visiting orders are illustrated in Table 2.4. As shown in Table 2.2, Moran's *I* estimated from both high and low spatial resolution images specify the same visiting order of classes in UOC in this experiment. We therefore only consider UOC+MoranIL case, which means UOC with specified order by Moran's *I* estimated from low spatial resolution fraction images.

Table 2.3 PCC (%) of UOS method in experiment 1 (averages of 100 runs ± standard deviation)

	S=5	S=10
BPNN	87.77±0.09	81.36±0.06
HNN	90.35±0.06	83.21±0.04
SPSAM	81.64±0.12	79.61±0.09
Kriging	83.00±0.14	80.33±0.07
ICK	83.72±0.11	80.84±0.06

Table 2.4 Labels of 24 visiting orders (C1-C4 denote roads, trees, buildings and grass, respectively)

1	C4-C3-C2-C1	2	C4-C3-C1-C2	3	C4-C2-C3-C1
4	C4-C2-C1-C3	5	C4-C1-C2-C3	6	C4-C1-C3-C2
7	C3-C4-C2-C1	8	C3-C4-C1-C2	9	C3-C2-C4-C1
10	C3-C2-C1-C4	11	C3-C1-C2-C4	12	C3-C1-C4-C2
13	C2-C3-C4-C1	14	C2-C3-C1-C4	15	C2-C4-C3-C1
16	C2-C4-C1-C3	17	C2-C1-C4-C3	18	C2-C1-C3-C4
19	C1-C3-C2-C4	20	C1-C3-C4-C2	21	C1-C2-C3-C4
22	C1-C2-C4-C3	23	C1-C4-C2-C3	24	C1-C4-C3-C2

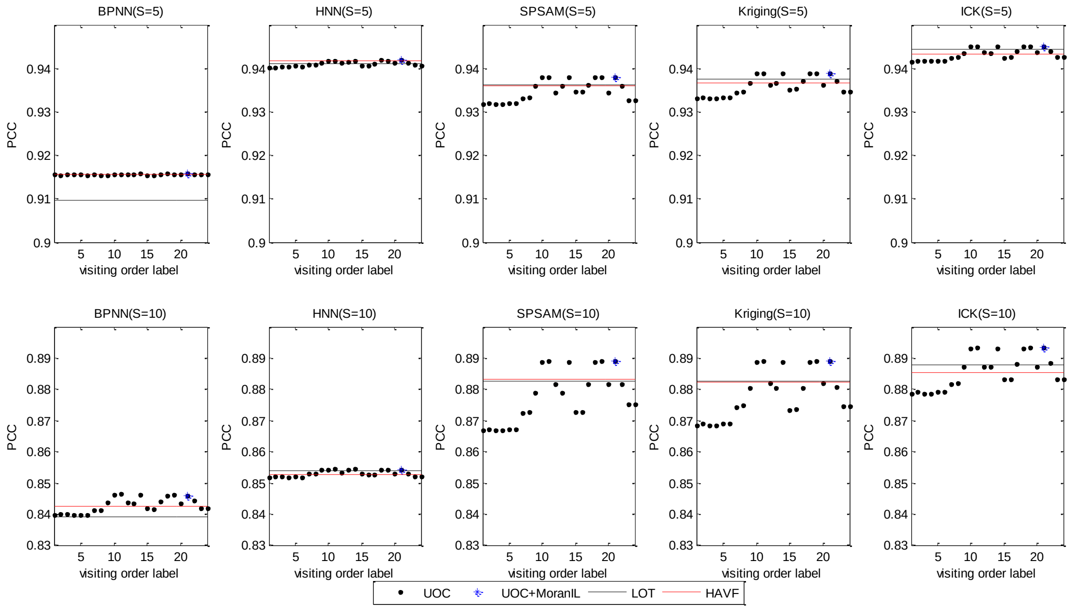

Figure 2.8. PCC of five STHSPM algorithms combined with HAVF, LOT and UOC at S=5 and 10 in the first experiment. UOC+MoranIL means UOC with Moran's I estimated from low spatial resolution fraction images.

Comparing PCC at different scale factors, we can see clearly as the scale factor increases, the accuracies of SPM decrease. The reason is that the SPM problem becomes more complicated with higher scale factors, as for each coarse pixel the spatial locations of more sub-pixels need to be estimated and uncertainty increases (Mertens et al., 2004). More precisely, at S=5 and 10, locations of 25 and 100 sub-pixels need to be predicted within each coarse pixel. While observing the data for UOC in each sub-figure, it can be found that different visiting orders of classes result in different SPM accuracies, which is particularly obvious in SPSAM, Kriging and ICK results. Hence, the visiting order in UOC has direct influence on SPM accuracy. When Moran's I is applied in UOC (i.e., UOC +MoranIL) in each STHSPM algorithm, the highest accuracy is achieved among all 24 orders, which indicates Moran's I is able to select out the best visiting order in UOC and also validates the effectiveness of using Moran's I gained from coarse fraction images in UOC. Furthermore, from the comparison of PCC of UOC+MoranIL, HAVF and LOT, we can conclude UOC+MoranIL is capable of producing higher accuracy than HAVF and LOT in all cases.

Table 2.5 lists the McNemar's test results for UOS, HAVF, LOT and UOC+MoranIL that were applied to five STHSPM algorithms. The statistically insignificant values at the 95% confidence level are underlined. As can be concluded from these values, UOC+MoranIL produces significantly higher accuracy than other three class allocation methods in nearly all cases. This reveals the intraclass spatial correlation is more important than the objective function in (2.8) in this experiment. With reasonably specified visiting order of classes, UOC maximized the spatial autocorrelation of each class, which was not well taken into consideration in UOS, HAVF and LOT.

Table 2.5 McNemar's test for different class allocation methods in the first experiment (0: UOC+MoranIL; 1: UOS; 2: HAVF; 3: LOT)

		z_{01}	z_{02}	z_{03}
S=5	BPNN	[27.0416, 29.7322]	<u>0.8752</u>	8.4650
	HNN	[31.3720, 33.4408]	<u>0.6266</u>	3.7311
	SPSAM	[63.2862, 65.9140]	8.0641	7.2449
	Kriging	[59.4212, 62.0354]	8.7551	7.2638
	ICK	[59.8257, 62.3790]	7.8893	4.3911
S=10	BPNN	[27.6674, 29.8159]	10.6104	11.0707
	HNN	[24.1120, 26.2680]	3.4411	<u>1.7018</u>
	SPSAM	[66.6251, 69.4362]	16.4369	16.4028
	Kriging	[62.9627, 64.9855]	18.0859	17.2707
	ICK	[63.2382, 65.4879]	21.0428	16.8453

In addition, the running time of four class allocation methods in this experiment is given in Table 2.6. Note that for each method, the hard class labels of sub-pixels within pure coarse pixels were determined by the simple copy process. The consuming time of three soft attribute comparison-based methods, UOS, HAVF and UOC, has the same order of magnitudes, which is less than 10 seconds and much less than that of LOT. More precisely, LOT needs several minutes to complete the class allocation process at both scales. The running time of LOT increases from 135s to 380s when *S* increases from 5 to 10, as at *S*=5, the optimization problem in LOT contains 100 variables and 29 equality constraints at each coarse pixel whereas at *S*=10, the corresponding number of variables and equality constraints increase to 400 and 104, respectively. However, for UOS, HAVF and UOC, within 10 seconds were consumed because only comparisons of soft attribute values were carried out and no complex processes are involved.

Table 2.6 Running time (seconds) of each class allocation method in the first experiment

	LOT	UOS	HAVF	UOC
S=5	135	2	3	2
S=10	380	4	7	2

2.1.5.3. Experiment 2

A land cover map of an area in Nanjing, China was used for test in the second experiment (see Figure 2.9). This map was derived from a 30m spatial resolution image at http://www.ceode.cas.cn/txzs/dxyy/, using a maximum likelihood classifier (MLC) along with a modal filter removing the noises in MLC results. The study area contains 360×360 pixels and was assigned to four classes, namely, C1, C2, C3 and C4. Comparing Figure 2.9 with Figure 2.5, one can find the distribution of the classes in this experiment is more random and more complex than that in the first experiment. The reference land cover map was degraded with S=8 and 12, producing two different coarse spatial resolution images. Figure 2.10 displays the fraction images of four land cover classes for S=8. Table 2.7 lists the Moran's I of the four classes in different spatial resolution images and the corresponding specified visiting orders of four classes. Comparing the values at S=1 in Table 2.7 to those at S=1 in Table 2.2, we can find that the indices of the four classes in this experiment are generally lower than those in the first experiment, as the spatial continuity of classes in Figure 2.9 is weaker than that in Figure 2.5. In addition, specified orders using Moran's I estimated from high spatial resolution map and low spatial resolution fraction images are different in this experiment.

The 20 SPM results for coarse fraction images in Figure 2.10 are shown in Figure 2.11, which were produced by combining five STHSPM algorithms with UOS, HAVF, LOT and UOC. For UOC, the visiting order of classes used was determined by Moran's I at S=8. Again, many speckle artifacts appear in UOS results. HAVF obtains sub-pixel maps with much fewer speckle artifacts than UOS. However, the performance of HAVF is still poorer than that of LOT and UOC. For example, the boundaries of C4 in five HAVF results are rougher than those in LOT and UOC results. SPM results obtained with LOT and UOC look nearly the same and both of them produce more satisfactory SPM results than UOS and HAVF.

In this experiment, sub-pixels within pure pixels were also excluded in quantitative assessment. PCC of five STHSPM algorithms combined with four class allocation methods at S=8 and 12 is shown in Figure 2.12. In each sub-figure, PCC of UOS is the average of 100 runs. As for UOC, all 24 visiting orders of classes in UOC were tested and labels for visiting orders are similar to those in Table 2.3. UOC+MoranIH and UOC+MoranIL mean that the visiting orders of classes in UOC were specified by Moran's I estimated from high spatial resolution map and low spatial resolution fraction images, respectively.

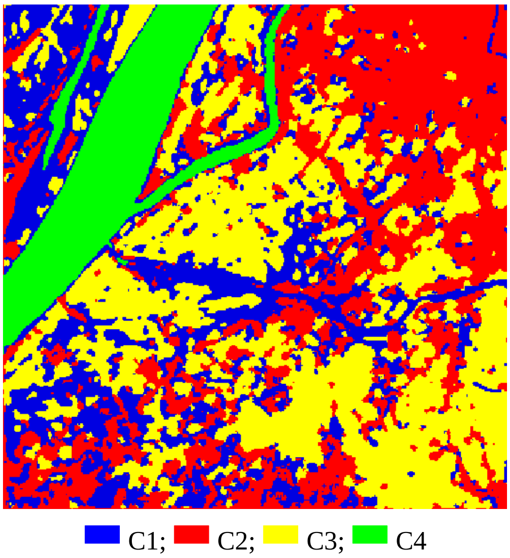

Figure 2.9. Reference land cover map in the second experiment.

Table 2.7 Moran's *I* of four classes at different scales in the second experiment

	S=1	*S*=8	*S*=12
C1	0.7355	0.5505	0.5406
C2	0.8229	0.6558	0.6628
C3	0.8410	0.6224	0.5914
C4	0.9622	0.8470	0.8038
Specified order	C4-C3-C2-C1	C4-C2-C3-C1	C4-C2-C3-C1

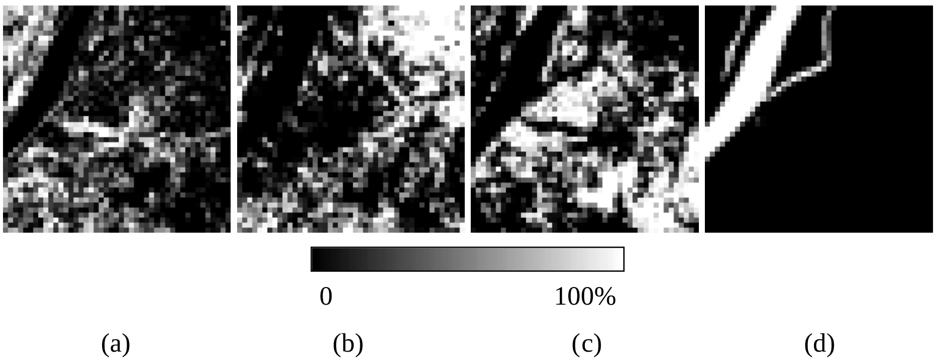

Figure 2.10. Fraction images of the four classes produced by degrading the reference land cover map in the second experiment with *S*=8. (a) C1. (b) C2. (c) C3. (d) C4.

As can be seen from the data in all 10 sub-figures, the performances of HAVF and LOT in five STHSPM algorithms are obviously superior to UOS. Compared to HAVF, LOT obtains higher accuracy. From the comparison between UOC and LOT, it is found when Moran's *I* is used in UOC, including both UOC+MoranIH and UOC+MoranIL, UOC is capable of producing slightly higher accuracy than

LOT in nearly all cases. In addition, accuracies of UOC+MoranIL are generally slightly lower than those of UOC+MoranIH. For BPNN at S=12, the accuracies of both UOC+MoranIH and UOC+MoranIL are lower than that of LOT. This is because the output of the first step (i.e., sub-pixel sharpening result) in BPNN is not as accurate as those in other four STHSPM algorithms, due to the inherent error in BPNN model itself. In this case, the spatial continuity of each class encapsulated in sub-pixel sharpening result of BPNN is not strong and the thus performances of UOC+MoranIH and UOC+MoranIL are a little poorer than LOT.

(a)
(b)
(c)
(d)
(e)

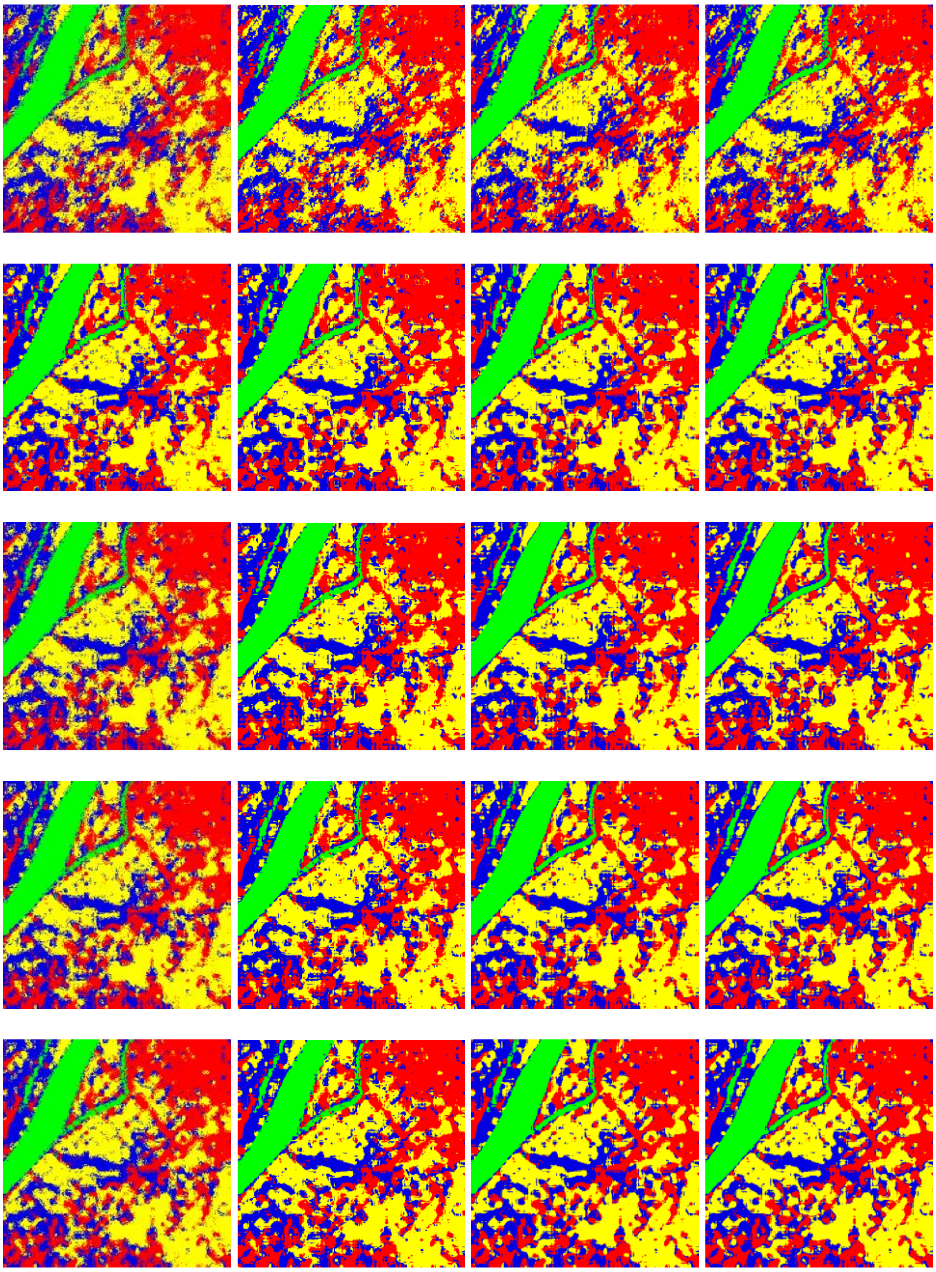

Figure 2.11. SPM results of five STHSPM algorithms combined with UOS, HAVF, LOT and UOC based class allocation methods in the second experiment (S=8). (a) BPNN. (b) HNN. (c) SPSAM. (d) Kriging. (e) ICK. From left to right: UOS (a random realization), HAVF, LOT and UOC (visiting order specified by Moran's I that was estimated from fraction images at S=8).

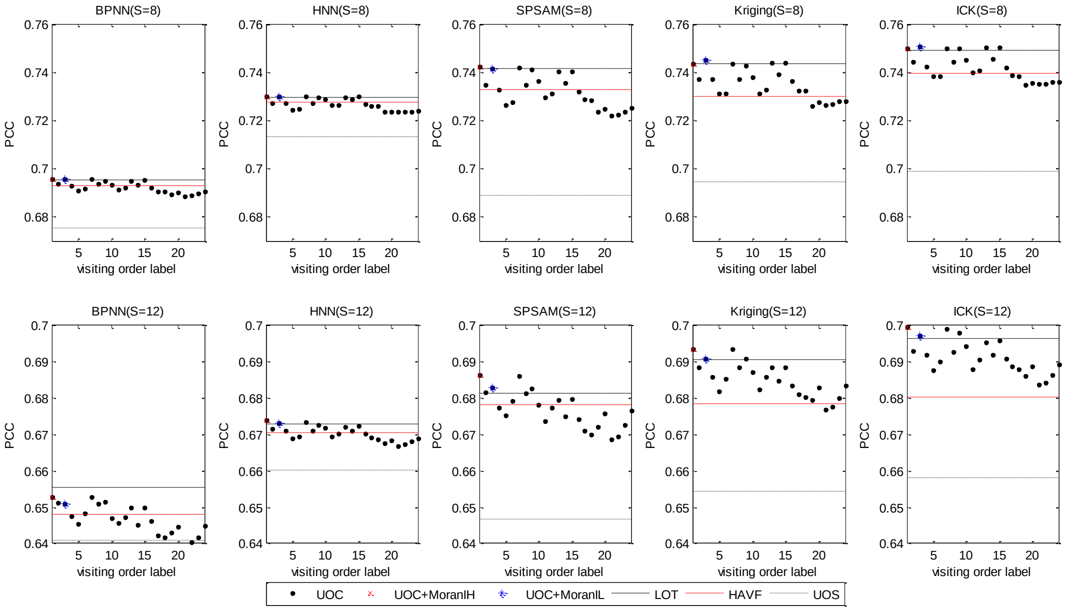

Figure 2.12. PCC of five STHSPM algorithms combined with UOS, HAVF, LOT and UOC at *S*=8 and 12 in the second experiment. PCC of UOS is the average of 100 runs; UOC+MoranIH and UOC+MoranIL mean UOC with Moran's *I* estimated from high spatial resolution map and low spatial resolution fraction images, respectively.

Table 2.8 McNemar's test for different class allocation methods in the second experiment (0: UOC+MoranIL; 1: UOS; 2: HAVF; 3: LOT)

		z_{01}	z_{02}	z_{03}
S=8	BPNN	[13.1000, 15.9465]	4.0308	*0.8109*
	HNN	[14.7358, 17.4458]	3.4283	*1.2672*
	SPSAM	[35.3203, 37.7278]	9.7576	*0.0781*
	Kriging	[34.1852, 37.0153]	16.4837	2.1078
	ICK	[35.2192, 37.9695]	21.1905	*1.9010*
S=12	BPNN	[5.7561, 8.8621]	2.7497	-4.0589
	HNN	[10.7939, 13.6949]	3.5008	0.5605
	SPSAM	[25.3217, 27.4000]	5.2029	1.9778
	Kriging	[26.0298, 28.6448]	12.8207	0.7635
	ICK	[27.8429, 30.7404]	16.9686	1.2814

The McNemar's test results for UOS, HAVF, LOT and UOC+MoranIL in five STHSPM algorithms are displayed in Table 2.8. Likewise, 100 random paths for UOS were tested and the statistically insignificant values at the 95% confidence level are underlined. In this experiment, UOC+MoranIL obtains significantly higher accuracy than UOS and HAVF for all five STHSPM algorithms. However, PCC of UOC+MoranIL is insignificantly higher than that of LOT in most cases. This is because the intraclass spatial correlation in the study area in this experiment is not very strong, as can be seen from the Moran's *I* at *S*=1 in Table 2.7, and thus in terms of SPM accuracy, the advantage of UOC+MoranIL over LOT is not obvious.

However, UOC has significant advantage over LOT in terms of computing complexity. As shown in Table 2.9, at *S*=8 and 12, LOT needs 360s and 700s to complete class allocation for each STHSPM algorithm. For the proposed UOC, it only consumes 2s, much less than LOT does. Additionally, UOS and HAVF also need little time for class allocation process.

Table 2.9 Running time (seconds) of each class allocation method in the second experiment

	LOT	UOS	HAVF	UOC
S=8	360	4	7	2
S=12	700	5	10	2

2.1.5.4. Experiment 3

In the third experiment, a 30m spatial resolution multispectral Landsat TM image (180×120 pixels) located in Xuzhou City, China, was used for test. The Landsat TM image was acquired in September, 2000 and mainly covers four classes: building, woodland, water and farmland. Bands 1-5 and 7 were used in this experiment. The image and its reference land cover map are shown in Figure 2.13. The reference land cover map in Figure 2.13(b) was obtained with the aid of a 1:2000 land use map that was produced around the same date as the Landsat TM image. To consider the inherent uncertainty in soft classification and simulate SPM in real cases, coarse image for SPM was generated by degrading the Landsat TM image with *S*=6 and Figure 2.13(b) can then be used for supervised accuracy assessment.

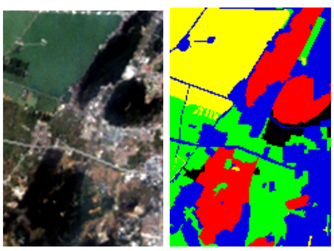

(a) (b)

Figure 2.13. The Landsat TM image in experiment 3. (a) Color image (bands 3, 2 and 1 as RGB). (b) Reference land cover map (Building; Woodland; Water; Farmland; Unclassified).

Table 2.10 Moran's *I* of four classes at different scales in third second experiment

	S=1	S=6
Building	0.8318	0.5094
Woodland	0.9224	0.7353
Water	0.9369	0.8951
Farmland	0.8431	0.6153
Specified order	Water-Woodland -Farmland-Building	Water-Woodland -Farmland-Building

First, soft classification was implemented on the coarse image to generate fractions. Linear spectral mixture analysis (LSMA) (Heinz and Chang, 2001) is widely used, appreciating its simple physical meaning and its convenience in application (Wang and Wang, 2013). Here, LSMA was used for soft classification. The fraction images of four land cover classes are displayed in Figure 2.14. SPM was then carried out to obtain land cover map that has the same spatial resolution as that of Figure 2.14. The Moran's I of the four classes obtained with high spatial resolution map in Figure 2.13(b) and fraction images in Figure 2.14 are listed in Table 2.10. As shown in the table, in this experiment, the specified order by two approaches are the same. Since the effectiveness of using Moran's I in UOC has been demonstrated in the first and second experiments, in this experiment only the visiting order of class specified by Moran's I was used for test of UOC method.

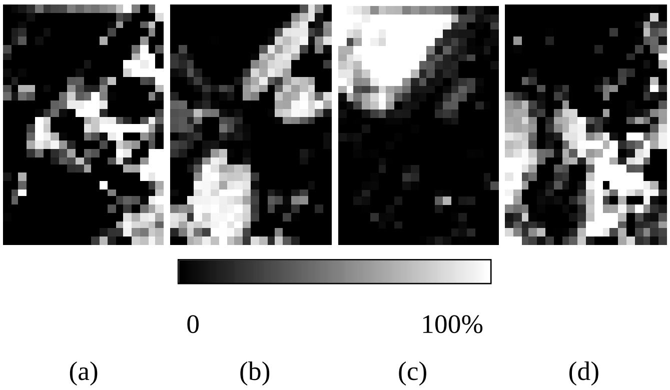

Figure 2.14. Fraction images of the 4 classes in the degraded Landsat TM image. (a) Building. (b) Woodland. (c) Water. (d) Farmland.

The SPM results of five STHSPM algorithms combined with UOS, HAVF, LOT and UOC are shown in Figure 2.15. Due to the errors from soft classification, some pixels are unavoidably misclassified in the results. For instance, in all 20 maps, some pixels are misclassified as water class within the area of woodland class, which conflicts with the distribution of woodland in the reference map in Figure

2.13(b). Errors from soft classification adversely affect the overall performance of SPM. Similar to the corresponding results in the first and second experiments, speckle artifacts were produced when UOS was applied for class allocation. From visual inspection, the results of HAVF, LOT and UOC are close to each other, and all of them are evidently superior to UOS results.

(a)
(b)
(c)
(d)
(e)

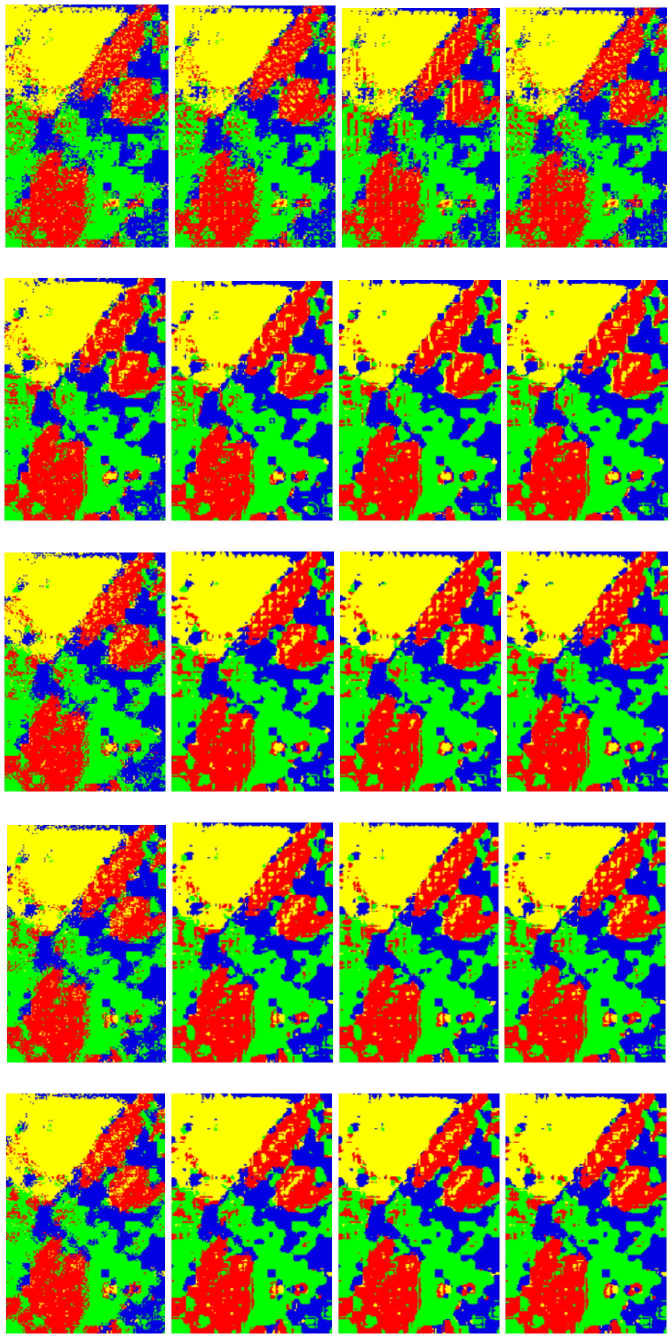

Figure 2.15. SPM results of five STHSPM algorithms combined with UOS, HAVF, LOT and UOC based class allocation methods in the third experiment (S=6). (a) BPNN. (b) HNN. (c) SPSAM. (d) Kriging. (e) ICK. From left to right: UOS (a random realization), HAVF, LOT and UOC (visiting order specified by Moran's I).

Table 2.11 lists the PCC of five STHSPM algorithms combined with UOS, HAVF, LOT and UOC. In this experiment, PCC was calculated taking account of all 180×120 pixels (except the unclassified ones in Figure 2.13) in each SPM result. The pure pixels in fraction images were not excluded in the accuracy statistics as whether a pixel is pure or not is determined by the soft classifier LSMA. We also consider the performance of soft classifier when multispectral coarse image is studied for SPM. This is different from the first and second experiments, where synthetic fraction images were studied and no soft classifier was applied in fact. UOS was also tested using 100 random paths. As can be concluded from the data in Table 2.11, the accuracies of HAVF, LOT and UOC for each STHSPM algorithm are higher than those of UOS.

Table 2.11 PCC (%) of four class allocation methods for five STHSPM algorithms (The data for UOS are averages of 100 runs ±standard deviation and the visiting order of class specified by Moran's *I* was used for UOC)

	UOS	HAVF	LOT	UOC
BPNN	70.54±0.09	71.11	71.23	71.08
HNN	71.01±0.06	71.25	71.43	71.38
SPSAM	70.08±0.07	71.09	71.27	71.24
Kriging	70.22±0.08	71.16	71.28	71.34
ICK	70.26±0.09	71.22	71.39	71.49

Table 2.12 McNemar's test for different class allocation methods in the third experiment (0: UOC; 1: UOS; 2: HAVF; 3: LOT)

	z_{01}	z_{02}	z_{03}
BPNN	[1.1173, 3.3433]	-0.2739	-0.9261
HNN	[1.2835, 3.2513]	0.9365	-0.7581
SPSAM	[4.0758, 6.1144]	1.4888	-0.2466
Kriging	[3.9939, 5.5421]	1.6537	0.7278
ICK	[4.3572, 6.3084]	2.4283	1.0721

In Table 2.12, the McNemar's test results for four class allocation methods in five STHSPM algorithms are displayed. In 100 random realizations of UOS, PCC values of SPSAM, Kriging and ICK are all significantly lower than those of UOC; for BPNN and HNN, 78% and 63% of the PCC values are significantly lower than those of UOC. Focusing on values in the last two columns in Table 2.12, it can be concluded that the advantage of UOC over HAVF is obvious than that over LOT. Especially, in comparison with HAVF, when UOC is applied to ICK, UOC achieves significantly higher accuracy. For all five STHSPM algorithms, however, the differences between UOC and LOT in accuracy are statistically insignificant. The main reason is that errors from soft classification were propagated to SPM results (Ge, 2013) and suppressed the performances of UOC. In this experiment, UOC is considered to produce comparable SPM accuracy to LOT.

The running time of LOT, UOS, HAVF and UOC in this experiment is 40s, 2s, 3s and 1s, respectively. Again, UOC spends much less time than LOT. Through this experiment, the effectiveness and advantages of the proposed UOC is further demonstrated.

2.1.5.5. Inter-comparison of five STHSPM algorithms

It is worth doing inter-comparison of SPM algorithms, as expected in Atkinson (2009). Here, the five STHSPM algorithms are compared visually and quantitatively. As the effectiveness and advantages of the proposed UOC has been demonstrated by three experiments, we compare the results of five STHSPM algorithms when UOC is applied in class allocation, with visiting order of classes specified by Moran's *I* that was estimated from coarse fraction images.

For visual comparison, we focus on the results in the second experiment (i.e., the last column in Figure 2.11). It can be seen that ICK is able to generate the best results among five STHSPM algorithms. Specifically, there are evident jagged boundaries in BPNN result. As for HNN, the distribution of classes looks more reasonable than that in BPNN result. However, the boundary of C4 is relatively rough when compared to ICK. Observing SPSAM result, we can find some cone-shaped objects in the map, especially for those belonging to C2. Kriging provides more satisfactory result than BPNN, HNN and SPSAM, but there are some linear artifacts. Compared to Kriging result, in the map yield by ICK there are less linear artifacts and the continuity of each class is stronger.

The quantitative comparison of five STHSPM algorithms is studied for the first and second experiment. The McNemar's test results for five STHSPM algorithms in the two experiments are shown in Table 2.13 and Table 2.14, and the PCC of each STHSPM algorithm is also given in the two tables. Similar to the conclusion drawn from visual comparison, the accuracy of ICK is found to be the highest among five STHSPM algorithms at each scale. ICK generates significantly higher accuracies than other four STHSPM algorithms in all cases. The reason is attributed to the fact that indicator geostatistics-based ICK method extracts prior spatial structure information of each class from additional fine spatial resolution images. Therefore, ICK is advantageous while dealing with complex spatial patterns. However, for another learning based-SPM method, BPNN, it does not obtain satisfactory accuracies, which indicates BPNN still needs an additional training data set (Zhong and Zhang, 2012). As for three STHSPM algorithms that need no prior spatial structure information, HNN gives the highest accuracy at small scale *S*=5 in experiment 1 while Kriging is advantageous at large scales. In HNN, the spatial dependence is expressed at the sub-pixel scale level and the spatial relation between sub-pixel and its nearest 8 neighboring sub-pixels is considered. On the one hand, this character enables HNN produce more continuous and better SPM results at small scale than do SPSAM and Kriging that consider dependence between sub-pixel and its neighboring coarse pixel. On the other hand, due to this character of HNN, spatial locations of sub-pixels for each class vary after each mapping and iterations are needed to acquire SPM results. It is easy to fall into local optimum, especially for complex SPM problems at large zoom scales. This is similar to the case in pixel swapping algorithm (Atkinson, 2005; Makido and Shortridge, 2007; Makido et al., 2007), which also considers dependence at the sub-pixel scale level. Consequently, Kriging could be a promising SPM approach for the large scale situation when prior spatial structure information is unavailable.

Table 2.13 McNemar's test for STHSPM algorithms in experiment 1

		BPNN vs	HNN vs	SPSAM vs	Kriging vs	ICK vs
S=5	BPNN (91.58%)		21.1843	18.0989	19.0711	23.7284
	HNN (94.19%)			-4.8908	-3.7968	4.8900
	SPSAM (93.79%)				<u>1.2009</u>	8.2348
	Kriging (93.89%)					7.8360
	ICK (94.51%)					
S=10	BPNN (84.60%)		6.3056	34.6841	35.0997	38.5479
	HNN (85.43%)			31.3589	35.4653	42.1081
	SPSAM (88.90%)				<u>0.1069</u>	4.9997
	Kriging (88.90%)					5.8163
	ICK (89.33%)					

Table 2.14 McNemar's test for STHSPM algorithms in experiment 2

		BPNN vs	HNN vs	SPSAM vs	Kriging vs	ICK vs
S=8	BPNN (69.58%)		21.6263	29.0998	31.2864	34.9863
	HNN (73.00%)			8.9742	13.0703	19.1045
	SPSAM (74.14%)				3.6298	7.9308
	Kriging (74.50%)					5.9101
	ICK (75.05%)					
S=12	BPNN (65.10%)		13.6655	19.9154	25.1336	28.8840
	HNN (67.31%)			7.6262	15.3039	21.1230
	SPSAM (68.30%)				8.5525	12.5661
	Kriging (69.10%)					7.0524
	ICK (69.72%)					

2.1.5.6. Analysis of scale factor *S*

In this section, scale factor *S* is analyzed for UOS, HAVF, LOT and UOC. The bar charts of PCC with various scales are shown in Figure 2.16 for the land cover maps in the first and second experiments. The four class allocation methods were applied to the STHSPM algorithm ICK. In the bar charts, PCC of UOS is the average of 100 random runs. The visiting order for UOC is determined by Moran's *I*, which was calculated from fraction images. Five scales, 5, 8, 10, 12 and 15, were discussed for each land cover map.

Due to the complex land cover pattern in the map of Nanjing, SPM accuracy of each method in Figure 2.16(b) is much lower than that in Figure 2.16(a). Precisely, for the same scale, the PCC of each method in Figure 2.16(b) is at least 12% lower than that in Figure 2.16(a). As the scale increases, the PCC of all class allocation methods in the two sub-figures takes on the tendency of descension. Furthermore, compared to the other three class allocation methods, the proposed UOC achieve higher SPM accuracy for nearly all scales. The McNemar's test results in Table 2.15 indicate that UOC generates significantly different results in comparison with UOS and HAVF for both land cove maps. The difference between UOC and LOT is significant for the land cover map of Bath, but becomes insignificant for *S*=5, 8 and 12 for the land cover map of Nanjing. We can find that the spatial dependence of the land cover in the map of Bath is stronger than that in the map of Nanjing. Hence the difference between UOC and LOT illustrates UOC is more advantageous when the spatial autocorrelation in the study area is stronger.

(a)

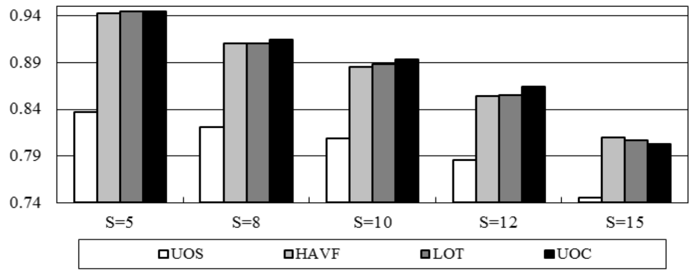

(b)

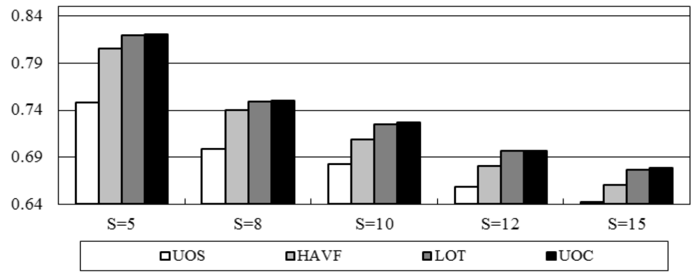

Figure 2.16. PCC of ICK combined with different class allocation methods for various scale factor *S*. (a) Land cover map of Bath, UK in experiment 1. (b) Land cover map of Nanjing, China in experiment 2.

Table 2.15 McNemar's test for results in Figure 2.16 (0: UOC; 1: UOS; 2: HAVF; 3: LOT)

		z_{01}	z_{02}	z_{03}
Bath	*S*=5	[59.8257, 62.3790]	7.8893	4.3911
	S=8	[63.8370, 66.5983]	13.4000	12.4416
	S=10	[63.2382, 65.4879]	21.0428	16.8453
	S=12	[59.9077, 62.2882]	21.8308	22.1929
	S=15	[44.0706, 47.3966]	-10.5289	-8.0895
Nanjing	*S*=5	[45.0977, 47.8272]	18.4676	<u>*1.7748*</u>
	S=8	[35.2192, 37.9695]	21.1905	<u>*1.9010*</u>
	S=10	[31.5941, 34.5169]	18.7045	2.0944
	S=12	[27.8429, 30.7404]	16.9686	<u>*1.2814*</u>
	S=15	[26.5480, 28.9816]	17.5462	2.6954

2.2. Allocating classes for STHSPM algorithms with adaptive visiting order of classes

(This section is based on Wang *et al.* (2014c))

2.2.1. Introduction

In the UOC-based class allocation method, different visiting orders of classes lead to different SPM results and the order needs to be specified reasonably. As presented in Section 2.1.4.2, the visiting order of classes can be determined by comparing the intra-class spatial correlation quantified by the Moran index, and the classes with stronger autocorrelation need to be visited first. In Section 2.1.4.2, the Moran index of each class was calculated using the entire proportion image generated by soft classification, which does not need any prior class information. In that way, however, the visiting order of classes is fixed for each coarse spatial resolution pixel. It is known that the spatial structure of land cover varies from area to area and the spatial autocorrelation of a class is usually not the same in all areas of an image. For example, in a local area of the studied image, the spatial continuity of a certain class may be the greatest among all classes and that class should be visited first for the coarse pixels, but in another area the Moran index of that same class may be the lowest and the class should be visited last. Therefore, using the Moran index calculated from the entire proportion image, the globally specified visiting order may not be the most suitable for all coarse pixels.

Section 2.2 aims to extend UOC with an adaptive scheme. In the proposed class allocation method, called the adaptive UOC (AUOC), the spatial correlation is quantified using the local structure information and AUOC is implemented on a per-coarse pixel basis.

2.2.2. Methods

Let S be the zoom factor, P_t ($t=1,2,...,M$, M is the number of pixels in the coarse spatial resolution image) be a coarse pixel and p_i (i=1,2,...,MS^2) be a sub-pixel. Suppose $F_k(P_t)$ is the proportion of the kth ($k=1,2,...,K$, K is the number of classes) class in coarse pixel P_t and $F_k(p_i)$ is the soft class value for the kth class at sub-pixel p_i.

2.2.2.1. Soft class value estimation for the STHSPM algorithm

The first step of the STHSPM algorithm is to estimate the soft class value for each sub-pixel which indicates the probability of a sub-pixel belonging to each class. The algorithms that can be used for this step have been introduced in detail in Section 2.1.4.2. Image interpolation algorithms can also estimate soft class values

(Ling et al., 2013) and can be developed into STHSPM algorithms. In Section 2.2, we focus on five fast STHSPM algorithms, including bilinear interpolation, bicubic interpolation, SPSAM, kriging and ICK, which are employed to predict $\left\{F_k(p_i)\middle| i=1,2,...,MS^2; k=1,2,...,K\right\}$.

2.2.2.2. UOC-based class allocation for the STHSPM algorithm

The second step of the STHSPM algorithm is class allocation. Based on the UOC method, within a coarse pixel, sub-pixels for the visited class (e.g., class *k*) are determined by comparison of soft class values $F_k(p_i)$ of all S^2 sub-pixels. The sub-pixels with larger soft values of class *k* are more likely to be allocated to class *k*. The number of sub-pixels for class *k* within a coarse pixel P_t, denoted as $E_k(P_t)$, is determined as

$$E_k(P_t) = F_k(P_t)S^2 \tag{2.19}$$

Once a sub-pixel is allocated to a class, it will not be considered in the class allocation process for the remaining classes. Generally, the classes with greater spatial autocorrelation are desired to be visited before those with weaker autocorrelation. The Moran index is used to quantify the spatial autocorrelation such that a larger index corresponds to greater autocorrelation. The index of class *k*, denoted as I_k, is calculated using the entire proportion image.

$$I_k = \frac{M\sum_{i=1}^{M}\sum_{j=1}^{M} W_{ij}\left[F_k(P_i) - \overline{F_k}\right]\left[F_k(P_j) - \overline{F_k}\right]}{\left(\sum_{i=1}^{M}\sum_{j=1}^{M} W_{ij}\right)\sum_{i=1}^{M}\left[F_k(P_i) - \overline{F_k}\right]^2} \tag{2.20}$$

where $\overline{F_k}$ is the mean of all *M* proportions for the *k*th class in proportion image F_k and

$$W_{ij} = \begin{cases} 1, \text{ if } P_i \text{ and } P_j \text{ are neighbors} \\ 0, \text{ otherwise} \end{cases} \tag{2.21}$$

After all *K* indices are calculated, they are ranked in a decreasing order and the classes with the larger indices are visited first.

2.2.2.3. AUOC-based class allocation for the STHSPM algorithm

It can be seen from UOC that using the entire class proportion image, the Moran index of each class is computed only once. In this way, a single visiting order is defined for all classes and is applied to determine the class allocation process for every coarse pixel. In the entire coarse image, however, the spatial structure of land cover is always complex and the spatial autocorrelation of a class in the entire study area cannot be characterized adequately by a fixed Moran index in general. The autocorrelation of a class may be the greatest in some local areas but may also be the weakest in other local areas. Consequently, the single visiting order is unlikely to be universally satisfactory for all coarse pixels. To overcome this shortcoming of the UOC-based class allocation method, the autocorrelation needs to be quantified in a spatially adaptive way and AUOC is proposed for this purpose.

In AUOC, the Moran index is calculated on a per-coarse pixel basis and the visiting order of classes within each coarse pixel is determined according to the spatial autocorrelation in the local area, which is centred at the coarse pixel. More precisely, a local window with a size of *N* by *N* pixels is selected for each coarse pixel. Using the Moran index, the spatial autocorrelation of class *k* in the local area for a coarse pixel (e.g., P_t) is quantified as

$$I_k^t = \frac{N^2 \sum_{i=1}^{N^2} \sum_{j=1}^{N^2} W_{ij} \left[F_k(P_i^t) - \overline{F_k^t} \right] \left[F_k(P_j^t) - \overline{F_k^t} \right]}{\left(\sum_{i=1}^{N^2} \sum_{j=1}^{N^2} W_{ij} \right) \sum_{i=1}^{N^2} \left[F_k(P_i^t) - \overline{F_k^t} \right]^2} \tag{2.22}$$

where P_i^t and P_j^t denote any coarse pixel in the local window centered at P_t, and $\overline{F_k^t}$ is the mean of all proportions for the *k*th class in the local window. The visiting order of *K* classes within P_t is specified by comparing all *K* indices (i.e., $I_1^t, I_2^t, ..., I_K^t$). As done in UOC, the classes with larger indices are given priority in AUOC-based class allocation.

As the local proportion image varies from window to window, the calculated Moran indices for all coarse pixels are different. Hence, in the AUOC method, the specified visiting order of classes is a function of the location of the coarse pixel. This is different from UOC that specifies the visiting order based on a per-global image basis. The advantages of the proposed AUOC are as follows.

1) Similar to UOC, AUOC also takes the intra-class spatial dependence into account during class allocation process.
2) As can be seen from (2.22), AUOC does not need any prior class information to determine the visiting order of classes. This is also the same as UOC.
3) AUOC behaves adaptively and selects the most suitable visiting order of classes within a coarse pixel according to the surrounding pixels.

2.2.2.4. Implementation of AUOC

The implementation of AUOC consists of the following steps.

Step 1: Select a coarse pixel P_t from the coarse spatial resolution image.

Step 2: Find the local window with a size of N by N pixels that is centered at P_t.

Step 3: Calculate the Moran indices of K classes, i.e., $I_1^t, I_2^t, ..., I_K^t$, according to (2.22).

Step 4: Determining the visiting order of classes by comparison of the K indices: $I_1^t, I_2^t, ..., I_K^t$.

Step 5: According to the specified visiting order, sub-pixels for each class are determined class-by-class. The class allocation process is implemented with soft class values that have been predicted by the STHSPM algorithm, under the constraints presented in (2.19). Readers may refer to Section 2.1 for details.

Step 6: The whole process is terminated when all sub-pixels within all coarse pixels are allocated to a class. Figure 2.17 is the flowchart of the AUOC-based class allocation method.

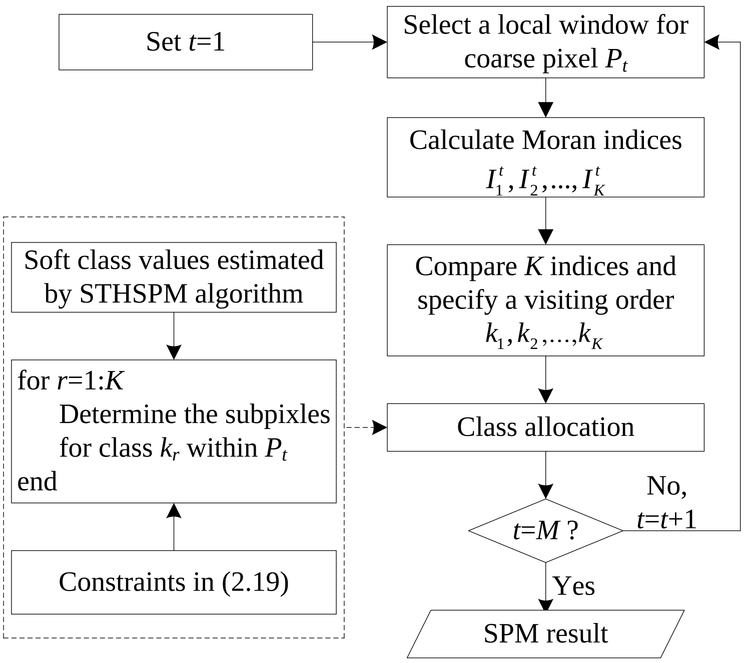

Figure 2.17. Flowchart of the proposed AUOC-based class allocation method.

2.2.3. Experiments

Experiments were conducted using three remote sensing images to test the AUOC method. To avoid the uncertainty in soft classification and concentrate only on the performance of SPM, synthetic proportion images were used. Specifically, the original images were classified with a hard classifier to yield land cover maps. Each land cover map was decomposed into K binary land cover maps and then proportion images were simulated by degrading the binary land cover maps with an S by S mean filter. SPM was performed to reproduce the fine spatial resolution land cover map with zoom factor S and the original fine resolution map was used for accuracy assessment of SPM. Since SPM is essentially a hard classification technique (but at the sub-pixel scale), the accuracy of SPM was evaluated quantitatively by the overall accuracy in terms of the percentage of correctly classified pixels (PCC). Note that the non-mixed pixels were not included in the accuracy statistics, because they will only increase the PCC without providing any useful information on the performance of SPM (Mertens et al., 2003; Wang et al., 2012a,b; Zhong and Zhang, 2012, 2013). Five STHSPM algorithms were implemented: bilinear interpolation, bicubic interpolation, SPSAM, kriging and ICK. The proposed AUOC was applied to the five STHSPM algorithms and also compared to UOC for validation.

2.2.3.1. Data

The first image is provided by Hyperspectral Digital Imagery Collection Experiment (HYDICE) airborne hyperspectral data. The data cover an area in Washington, DC Mall (191 bands with a spatial resolution of 3 m). The selected study area is covered by 240 by 296 pixels and the corresponding hyperspectral data were classified with an algorithm based on tensor discriminative locality alignment (Zhang et al., 2013). The obtained land cover map contains seven classes: shadow, water, road, tree, grass, roof and trail. The second and third images are two 0.61 m QuickBird images containing 480 by 480 pixels and three multispectral bands, which were acquired in August 2005. One covers the suburb of Xuzhou City, China while the other covers the urban center area of that city. The two images were classified with an algorithm that first integrated spatial features of pixel shape feature set, grey level co-occurrence matrix and Gabor transform with spectral information and then used a support vector machine for classification. Each generated land cover map contains seven classes: shadow, water, road, tree, grass, roof and bare soil. Figure 2.18 shows the three images as well as the classified maps.

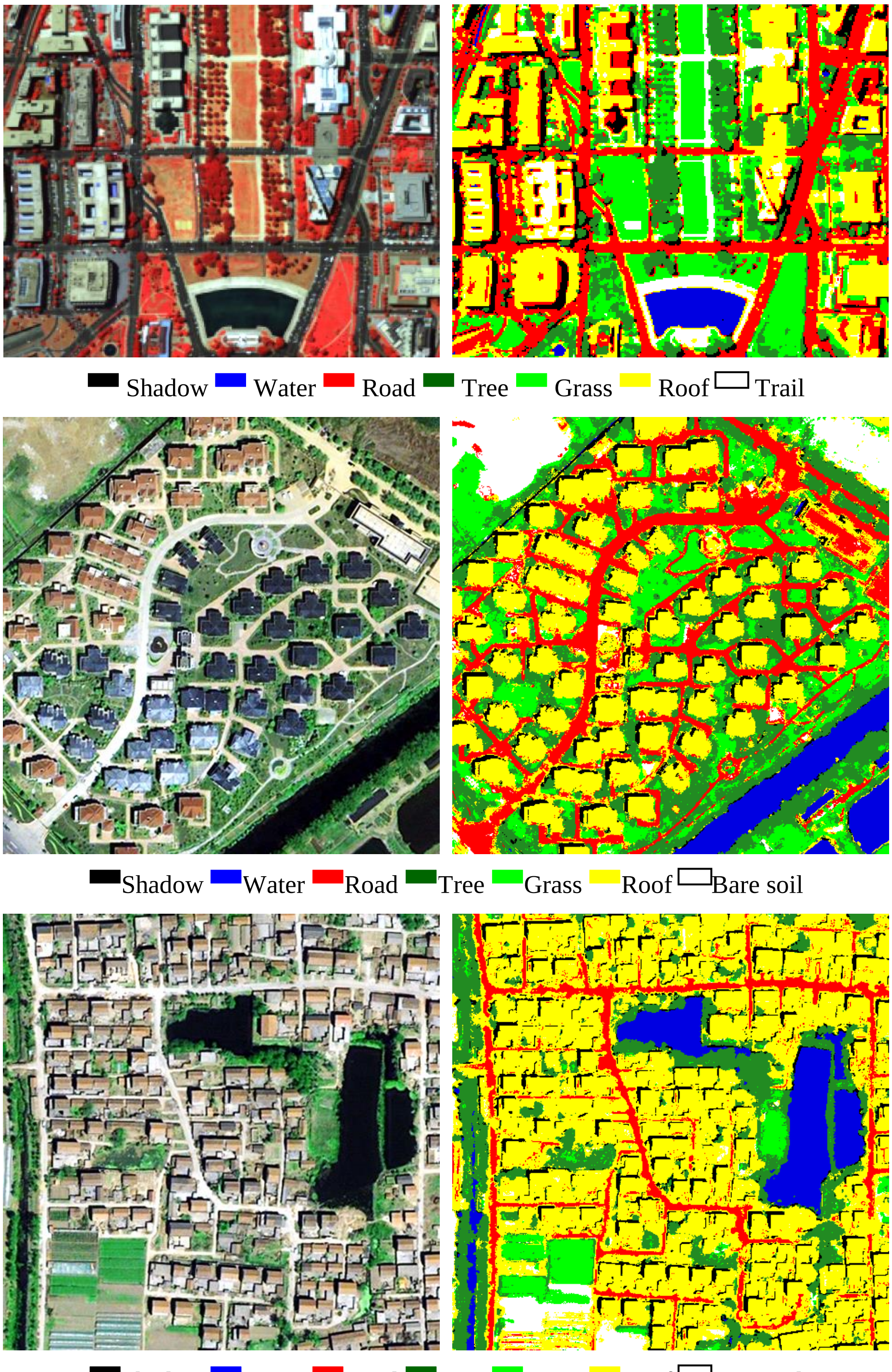

Figure 2.18. Three remote sensing images used for testing the proposed AUOC method. Left: Color images; Right: Classified land cover maps used as reference for SPM. Line 1: Washington, DC map; Line 2: Xuzhou suburb map; Line 3: Xuzhou urban center map.

2.2.3.2. Analysis of local window size

The Washington, DC and Xuzhou urban center land cover maps in Figure 2.18 were degraded using three zoom factors, S= 3, 5 and 8, to simulate the coarse proportion images. Using the corresponding three zoom factors, the five STHSPM algorithms (bilinear, bicubic, SPSAM, kriging and ICK) were then implemented to reproduce the fine spatial resolution maps, using the AUOC-based class allocation method. Here, three local window sizes, 3 by 3, 5 by 5 and 7 by 7 (i.e., N=3, 5 and 7), were tested for AUOC. For two maps, the PCC values of the five STHSPM algorithms with different window sizes and zoom factors are shown in Figure 2.19. From the bar charts, it can be seen that in most cases, the largest PCC was obtained for each STHSPM algorithm when N=3. Guided by the results in Figure 2.19, N was set to 3 for the AUOC in the following tests.

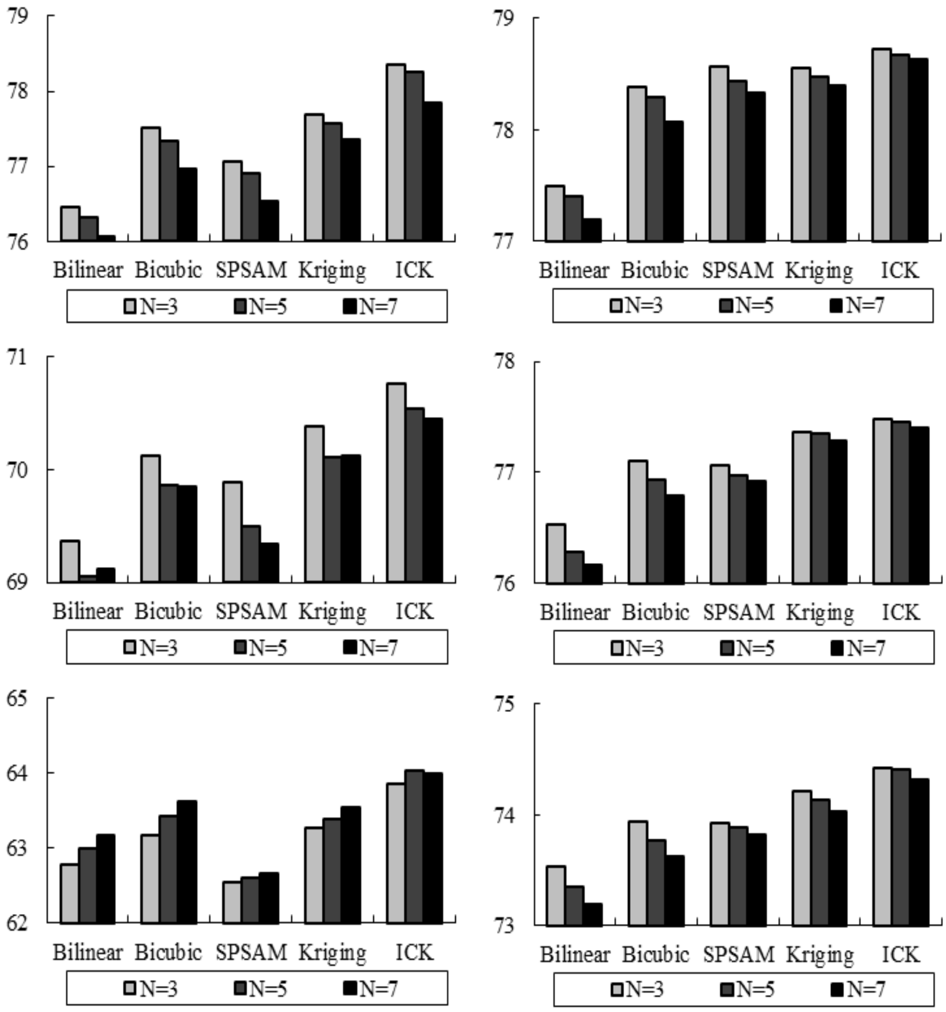

Figure 2.19. PCC (%) of the new AUOC method with three local window sizes: N=3, 5 and 7. Left: Washington, DC map; Right: Xuzhou urban center map. Line 1: S=3; Line 2: S=5; Line 3: S=8.

2.2.3.4. Results and analysis

Each reference land cover map in Figure 2.18 was degraded with six zoom factors, S= 3, 4, 5, 6, 8 and 12, to produce six groups of proportion images. The five STHSPM algorithms were then applied, coupled with the UOC and AUOC-based class allocation methods.

Figure 2.20 shows the SPM results of two STHSPM algorithms, bicubic and SPSAM, using UOC and AUOC for the Washington, DC map with S=4. As seen from the resulting maps, using the AUOC method the boundaries of classes are smoother and the spatial continuity is greater than for UOC. Focusing on the two marked subareas in the results, we can see clearly that in the UOC results some pixels for the roof class, which appear as noise or block artifacts, are incorrectly allocated to places that should be the road class. Using the AUOC method, however, this phenomenon is alleviated greatly and the spatial distribution of the classes is highly similar to that in the reference map. The visual comparison demonstrates that AUOC is capable of obtaining more accurate SPM results than UOC.

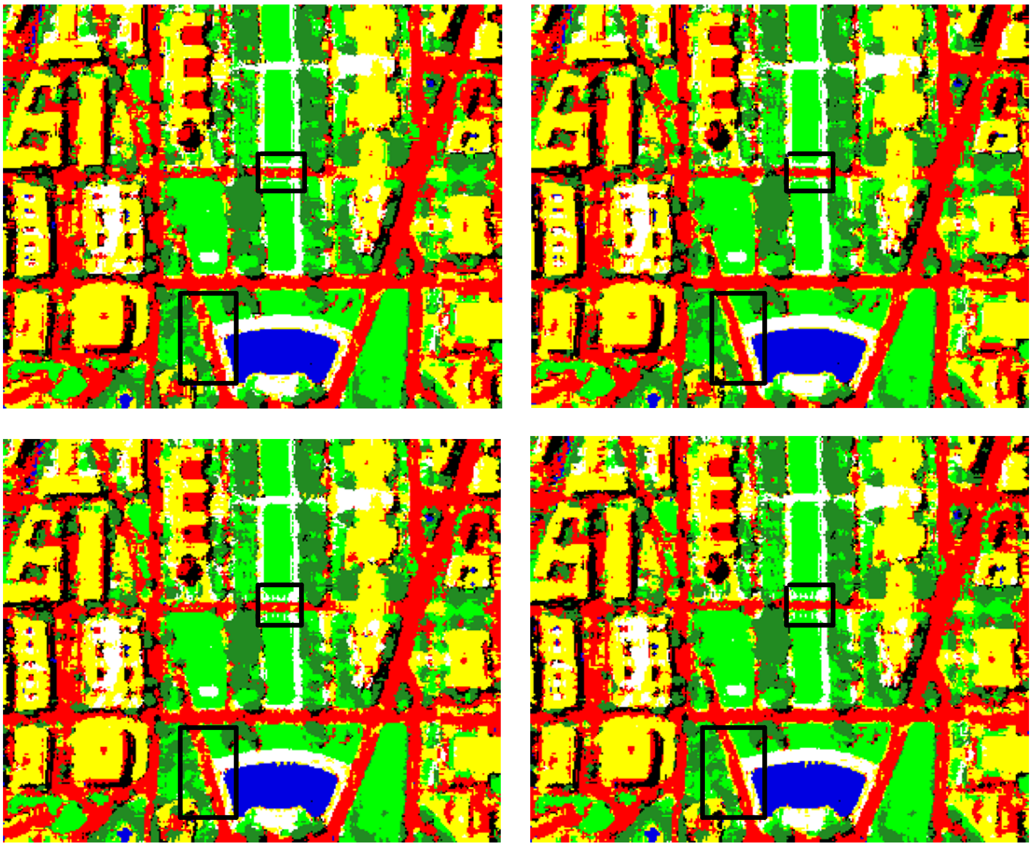

Figure 2.20. SPM results of the Washington, DC map (S=4). Left: UOC; Right: AUOC. Line 1: Bicubic results; Line 2: SPSAM results.

For each land cover map in Figure 2.18, the PCC of ten methods (five STHSPM algorithms with two class allocation methods) for each zoom factor S is shown in Figure 2.21. From the figure, three observations can be made.

First, consistent with visual inspection, comparison between UOC and AUOC reveals that using the adaptive visiting order of classes, all five STHSPM algorithms produce greater SPM accuracy, particularly for a small zoom factor.

Second, the increase in accuracy from UOC to AUOC is not very obvious for a large zoom factor. More precisely, in the experiments for the three studied images, when S is larger than 6, the difference between AUOC and UOC in terms of PCC is small. This is because both of them are performed based on spatial dependence: They compare the spatial autocorrelation of each class and determine sub-pixels for class with greater spatial autocorrelation first. When the reference land cover map is degraded with large factor S, a number of coarse pixels may be larger than some land cover objects, which is referred to as the L-resolution case in Atkinson (2009). In the L-resolution case, however, spatial dependence-based methods usually cannot reproduce objects accurately at a fine spatial resolution. Therefore, the proposed AUOC can enhance UOC when the zoom factor is small, but for large zoom factor the increase in accuracy may not be so obvious.

Third, the accuracy gain decreases from bilinear to ICK in each row in the figure. The accuracy of STHSPM algorithm is not only related to class allocation, but also the soft class value estimation. When the soft class values estimated by the STHSPM algorithms (such as kriging and ICK) are more reliable, the produced SPM result is more accurate, no matter whether UOC or AUOC is used for class allocation. In this case, applying AUOC to such STHSPM algorithms, the room for an increase in accuracy is small.

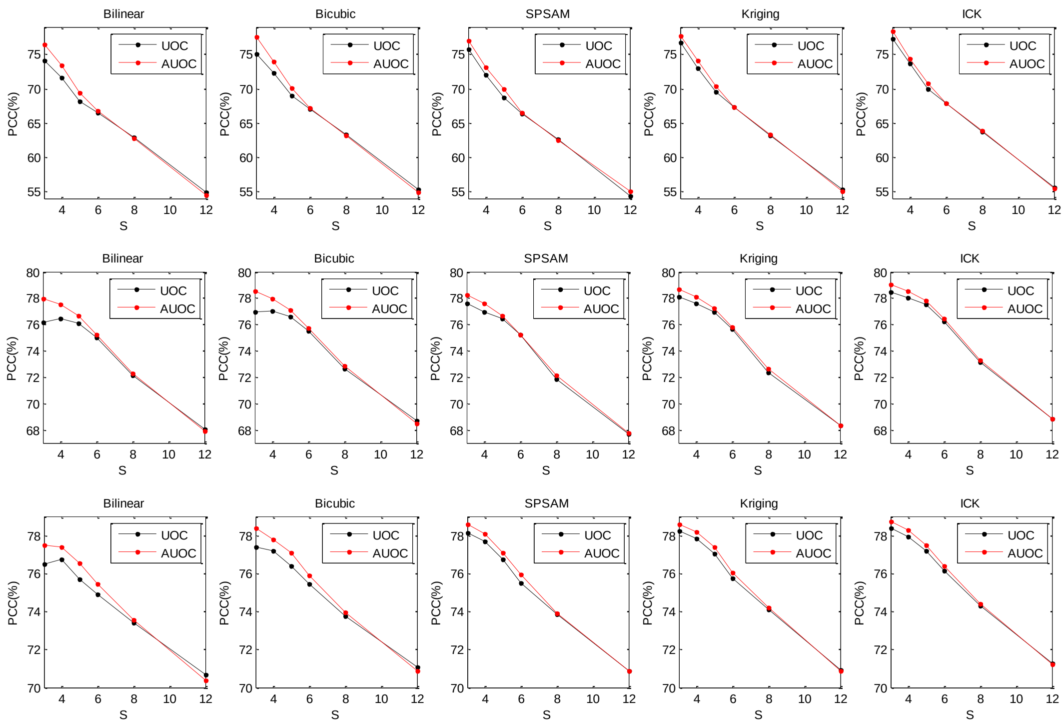

Figure 2.21. PCC of five STHSPM algorithms with UOC and AUOC. Line 1: Washington, DC map; Line 2: Xuzhou suburb map; Line 3: Xuzhou urban center map.

Table 2.16 gives the computing time of UOC and AUOC for the Xuzhou suburb map. We can see AUOC took more time than UOC. This is because in AUOC, the Moran indices of classes are calculated *M* times. In UOC, however, the Moran indices are calculated only once. Therefore, AUOC usually requires more computing time than UOC. This is the cost of enhancing SPM accuracy for AUOC. Note that only for small zoom factors, the accuracy improvement merits the extra computational load.

Table 2.16 Computing time (s) of UOC and AUOC for the Xuzhou suburb map

	S=3 (160×160)	S=4 (120×120)	S=5 (96×96)	S=6 (80×80)
UOC	8.4	7.1	6.4	5.7
AUOC	33	19	12	9.1

2.3. Summary

This chapter proposes two new class allocation methods for STHSPM algorithms: UOC and AUOC. Section 2.1 presents UOC for STHSPM algorithms. With UOC-based class allocation method, sub-pixels for each class are allocated in turn. The visiting order of classes can be specified by Moran's *I*, which can be estimated from either available high spatial resolution land cover map or coarse fraction images. UOC has the unique advantage of taking account of the intraclass spatial correlation in the second step of STHSPM algorithms. In the experiments on three remote sensing images, the proposed UOC was applied to five STHSPM algorithms, BPNN, HNN, SPSAM, Kriging and ICK, and compared with the existing class allocation methods, UOS, HAVF and LOT. The conclusions in Section 2.1 are summarized as follows.

1) The visiting order of classes in UOC can be reasonably determined by comparing Moran's *I* of each class. When spatial structure information of classes at fine spatial resolution is available, they can be readily utilized for calculating Moran's *I* of classes. However, when such prior information is unavailable, our proposed method that uses fraction images to calculate Moran's *I* can also be selected out a reasonable order.
2) UOC was successfully applied to five STHSPM algorithms. For all five STHSPM algorithms, with Moran's *I* that was estimated from fraction images, UOC is capable of obtaining more accurate SPM results than UOS and HAVF and achieving at least comparable SPM accuracy in comparison with LOT.

When the intraclass spatial correlation in the study area is stronger, the advantage of UOC in terms of SPM accuracy, especially over LOT, is more obvious. This is because UOC considers the intraclass spatial dependence in the second step of STHSPM algorithms.

3) Similar to UOS and HAVF, the computing complexity of UOC is much less than that of LOT. Therefore, UOC shows its great potential in real-time applications.
4) The inter-comparison of five STHSPM algorithms reveals that ICK is able to obtain the highest SPM accuracy among five algorithms, based on the proposed UOC with Moran's *I* estimated from fraction images. However, this advantage of ICK is based on the existence of prior spatial structure information of land cover that is representative of the study area.

In Section 2.2, AUOC is proposed for STHSPM algorithms. Different from the UOC method that determines the visiting order of classes based on the global proportion image, the AUOC method uses the local proportion image (i.e., local window) instead. According to the spatial autocorrelation quantified by the Moran index in the local window, AUOC specifies an adaptive visiting order for each coarse resolution pixel and ensures sub-pixels for the classes with greater indices are determined first. AUOC inherits the advantages of UOC: it accounts for the intra-class spatial dependence in class allocation and does not require prior class information to calculate the Moran index. In experiments, both UOC and AUOC were applied to five STHSPM algorithms (bilinear, bicubic, SPSAM, kriging and ICK) and tested on three remote sensing images with multiple zoom factors. Results show that for all five STHSPM algorithms, the proposed AUOC method leads to an increase in accuracy over the existing UOC method for SPM with small zoom factors (e.g., S<6 in this study). When the zoom factor increases, the advantage of AUOC over UOC in terms of PCC becomes less obvious. Hence, AUOC is recommended as a suitable class allocation method for SPM problems involving a relatively small zoom factor.

3. STHSPM algorithms with multiple shifted images

3.1. ICK-based SPM with MSI

(This section is based on Wang *et al.* (2014d))

3.1.1. Introduction

The back-propagation neural network-based SPM first extracts training samples from available high spatial resolution images, which are used as training images. The performance of back-propagation neural network, however, relies on the training sample numbers and highly accurate SPM results are more likely to be generated with sufficient training data. Actually, acquiring sufficient training data is a challenge in practical application. Furthermore, in the fitting of the model, many parameters need to be determined, such as the number of iterations, the number of hidden layers and nodes for each hidden layer, the learning rate and the momentum rate. Atkinson (2004) introduced a two-point histogram-based method, which optimized the randomly initialized sub-pixel maps with maintained class fractions by swapping sub-pixel classes within pixels to gradually match the two-point histogram extracted from the training image. This algorithm involves a number of iterations and much time is consumed in the optimization. Boucher and Kyriakidis (2006, 2008), Boucher et al. (2008), and Boucher (2009) proposed an Indicator CoKriging (ICK)-based SPM model. In this model, the prior spatial structure of each class can be utilized by extracting the indicator semivariogram from fine spatial resolution images. This model contains two steps: 1) computing conditional probabilities of class occurrence at fine pixels and 2) allocating classes for these fine pixels. Different from the learning-based back-propagation neural network that requires as much prior spatial structure information as possible to train the network, ICK-based SPM also works well when limited prior information is available. This is well illustrated by Jin et al. (2012), which extracted indicator semivariogram from a representative local area (2% of the entire study area) for ICK-based SPM. By using the limited target resolution reference data, ICK-based SPM produced

SPM results of comparable accuracy, with those using a globally derived spatial structure.

ICK is a typical STHSPM algorithm and has several characteristics and advantages:

- The additional information of informed fine spatial resolution pixels (i.e., the class labels of these pixels are known from prior information) can be coded easily into the model by ICK. These fine pixels can be selected randomly and are not necessarily to locate together, as long as these class labels and their locations are available.
- It is free of any iteration process as the conditional probabilities are obtained by solving a system of equations via ICK and the class allocation is a single-pass method. This is quite different from the SPM methods in Tatem et al. (2001 a,b,c, 2003), Mertens et al. (2003), Atkinson (2005), Kasetkasem et al. (2005), Tolpekin and Stein (2009), and Wang et al. (2012 a,b) and the learning-based two-point histogram Atkinson (2004), in which the algorithms evolve gradually to convergence to a stable solution. Hence, by using ICK-based SPM, time spent on iterations can be saved and the uncertainty introduced by random initialization and stochastic processes during the iterations can also be avoided.
- Few parameters are involved in this model. For ICK-based SPM, often a neighbourhood window is considered for each coarse pixel for computational efficiency reasons (Boucher and Kyriakidis, 2006). Many available SPM models have their own parameters, such as the control parameter in the Markov random field model (Tolpekin and Stein, 2009), the non-linear parameter in the distance dependent weightings in the pixel swapping algorithm (Makido, 2006; Makido and Shortridge, 2007) and the pseudotemperature (Collins and Jong, 2004) and the weightings in the energy function of Hopfield neural network (HNN). Certainly, much extra work would be done to estimate the optimum parameters and the change of them may lead to the uncertainty in SPM results. But these would not be the cases if the ICK-based SPM method is used.

The SPM problem is under-determined, in which it has multiple plausible solutions and many fine spatial resolution land cover maps can lead to an equally good reproduction of the input coarse imagery (Boucher and Kyriakidis, 2006). Although the ICK-based SPM is able to make use of the spatial structure information from fine spatial resolution images and informed fine pixels, it may still not be sufficient to deal with the uncertainty in SPM, especially when the zoom scale is large. The accuracy of SPM will certainly be limited by the large uncertainty involved. The additional information from other data can be useful in addressing the under-determined problem.

Ling et al. (2010) and Muad and Foody (2010) added soft classification outputs of multiple shifted images (MSI) to HNN. As observation satellites have multi-observation capability, they can capture images of the same area once every several days. For instance, the revisit interval of QuickBird is 1-6 days and MODIS covers the earth on a daily basis (Atkinson, 2013). These images are similar to each other but they are not completely identical. Because of the slight orbit translations and the earth's rotation, these images are usually shifted at the sub-pixel level (Lu and Inamura, 2003; Ling et al., 2010; Muad and Foody, 2012b, Xu et al., 2013). Ling et al. (2010) and Muad and Foody (2010). MSI have been widely used for super-resolution image reconstruction in the field of digital image processing, medical imaging, etc (Park et al., 2003). Super-resolution reconstruction is different from SPM studied in this chapter: continua are predicted in the former while categories are predicted in the latter. Further details on the differences between the two types of super-resolution algorithms can be found in Lu and Inamura (2003) and Ling et al. (2010). MSI can be obtained from time series images in remote sensing. Evidently, the accuracy of SPM based on a single date image can be enhanced by borrowing information from images before and after it in time (Atkinson, 2013).

The shifted observed images in the SPM model, are also coarse spatial resolution images that are usually acquired by the same type of senor. Therefore, the MSI are easily acquired and the geometric correction and reflectance retrievals between different spatial resolution images can be avoided. For this reason and the advantages of ICK-based SPM, Section 3.1 presents a new SPM method that uses the additional information from MSI to produce more accurate SPM results using ICK. For MSI, the corresponding multiple conditional probability maps are obtained with ICK and then the ICK-derived probabilities are integrated for each sub-pixel. The integrated probabilities are finally used to determine the sub-pixel class labels. Similar to ICK-based SPM, the proposed algorithm is performed based on the existence of prior spatial structure information of land cover that is representative of the study area. It inherits all the advantages of the ICK-based SPM:

it is able to incorporate the information from the informed fine pixels, no parameters except the neighborhood window size are involved and it is free of iteration.

3.1.2. Methods

3.1.2.1. ICK-based SPM

The ICK-based SPM model consists of two steps: computing conditional probabilities and allocating classes, which are briefly described below (Boucher and Kyriakidis, 2006).

Let Y be the observed coarse spatial resolution image with N pixels and X be the sub-pixel map at the target spatial resolution with M pixels. Here, $M/N=S^2$ where S is the zoom scale factor (i.e., each coarse pixel is divided into S^2 sub-pixels). Suppose $c(v)$ denotes the class label of a sub-pixel v and $c(v)=k$, $k=1,2,\ldots,K$, where K is the total number of classes in the area studied. Define the binary class indicator for the k-th class $i_k(v)$ as:

$$i_k(v)=\begin{cases}1, \text{ if } c(v)=k \\ 0, \text{ otherwise}\end{cases} \tag{3.1}$$

In the ICK model, the spatial pattern of the k-th class at the fine spatial resolution is characterized by the corresponding k-th class indicator semivariogram, $\gamma_k(\boldsymbol{h})$, which is defined as:

$$\gamma_k(\boldsymbol{h})=\frac{1}{2N(\boldsymbol{h})}\sum_{p=1}^{N(\boldsymbol{h})}[i_k(v_p)-i_k(v_p+\boldsymbol{h})]^2 \tag{3.2}$$

where $N(\boldsymbol{h})$ is the number of paired pixels at a specific lag $\boldsymbol{h}$ from the centre pixel v_p. The indicator semivariogram for each land cover class is usually obtained from the prior spatial structure.

Let $a_k(V)$ be the k-th class fraction in a coarse pixel V. The fine-to-coarse spatial resolution semivariogram between the k-th class indicator $i_k(v_m)$ at the fine pixel v_m and the k-th class fraction $a_k(V_n)$ at the coarse pixel V_n is calculated as:

$$\gamma_k(v_m,V_n)=\frac{1}{S^2}\sum_{m'=1}^{S^2}\gamma_k(\boldsymbol{h}_{mm'}) \tag{3.3}$$

where $\boldsymbol{h}_{mm'}$ denotes the separation vector between the centroid of v_m and the centroid of any fine pixel $v_{m'}$ within V_n. Similarly, the coarse-to-coarse spatial resolution semivariogram between any two coarse pixels V_n and $V_{n'}$ can be calculated as:

$$\gamma_k(V_n, V_{n'}) = \frac{1}{S^4} \sum_{m=1}^{S^2} \sum_{m'=1}^{S^2} \gamma_k(\boldsymbol{h}_{mm'}) \quad (3.4)$$

where $\boldsymbol{h}_{mm'}$ denotes the separation vector between the centroid of any fine pixel v_m within V_n and the centroid of any fine pixel $v_{m'}$ within $V_{n'}$.

The semivariogram models in (3.2)-(3.4) are used to estimate the conditional probabilities of class occurrence at fine pixels, and ICK is utilized for this purpose. Let all fractions for the k-th class be arranged in a $(N\times1)$ vector $\boldsymbol{a}_k=[a_k(V_n), n=1,2,...,N]^{\mathrm{T}}$. Define the k-th global class fraction π_k as the mean of all elements in vector $\boldsymbol{a}_k$. Suppose there are G informed fine pixels v_g available and the G indicators for the k-th class are arranged in a $(G\times1)$ vector $\boldsymbol{j}_k=[i_k(v_g), g=1,2,...,G]^{\mathrm{T}}$. The ICK-derived probability $p_k(v_m)$, which denotes the probability of the k-th class occurrence at fine pixel v_m (m=1,2,…,M), can be computed as:

$$p_k(v_m) = \boldsymbol{\eta}_k(v_m)^{\mathrm{T}}\boldsymbol{a}_k + \boldsymbol{\lambda}_k(v_m)^{\mathrm{T}}\boldsymbol{j}_k + \pi_k[1 - sum(\boldsymbol{\eta}_k(v_m)^{\mathrm{T}}) - sum(\boldsymbol{\lambda}_k(v_m)^{\mathrm{T}})] \quad (3.5)$$

where $\boldsymbol{\eta}_k(v_m)$ and $\boldsymbol{\lambda}_k(v_m)$ denotes the ICK weights for the k-th class, which are $(N\times1)$ and $(G\times1)$ vectors of weights for the N coarse pixels and G informed fine pixels, respectively. The function $sum(\bullet)$ takes the sums of all the elements in vector $\bullet$. The weights $\boldsymbol{\eta}_k(v_m)$ and $\boldsymbol{\lambda}_k(v_m)$ are calculated by solving the ICK system of equations:

$$\begin{bmatrix} \boldsymbol{\Gamma}_k^{VV} & \boldsymbol{\Gamma}_k^{Vv} \\ \boldsymbol{\Gamma}_k^{vV} & \boldsymbol{\Gamma}_k^{vv} \end{bmatrix} \begin{bmatrix} \boldsymbol{\eta}_k(v_m) \\ \boldsymbol{\lambda}_k(v_m) \end{bmatrix} = \begin{bmatrix} \boldsymbol{\gamma}_k^{vV}(v_m) \\ \boldsymbol{\gamma}_k^{vv}(v_m) \end{bmatrix} \quad (3.6)$$

where $\boldsymbol{\Gamma}_k^{VV}$ is a $(N\times N)$ matrix of coarse-to-coarse spatial resolution semivariogram values between all pairs of coarse pixels [see (3.4)], $\boldsymbol{\Gamma}_k^{vV}$ is a $(G\times N)$ matrix of fine-to-coarse spatial resolution semivariogram values between all pairs of informed fine and coarse pixels [see (3.3)], $\boldsymbol{\Gamma}_k^{vv}$ is a $(G\times G)$ matrix of indicator semivariogram values between all pairs of informed fine pixels, and $\boldsymbol{\Gamma}_k^{Vv} = [\boldsymbol{\Gamma}_k^{vV}]^{\mathrm{T}}$. The term $\boldsymbol{\gamma}_k^{vV}(v_m)$ denotes a $(N\times1)$ vector of fine-to-coarse semivariogram values between the uninformed fine pixel v_m and all N coarse pixels, and $\boldsymbol{\gamma}_k^{vv}(v_m)$ denotes a $(G\times1)$ vector of semivariogram values between v_m and all G informed fine pixels.

After the ICK-derived probabilities are predicted, the sub-pixels for each class can be decided in units of class (UOC), as introduced in Chapter 2.

3.1.2.2. Using MSI as additional information for ICK-based SPM

The essence of class allocation in the ICK-based SPM is the comparison of ICK-derived probabilities in order to find the highest one during each comparison. Sub-pixel class labels are then predicted according to rank and number of sub-pixels for each class is constrained by the coarse fractions in the process. This process would be smooth if the highest probability is consistently unique during the comparisons. Sometimes, however, there is more than one highest probability value to consider. In this case, it is difficult to determine which to select.

A simple example is provided in Figure 3.1, see Example I. Suppose the fraction of a class, denoted as a gray class, is 50%, and the scale factor S=2. The ICK-derived conditional probabilities of the gray class in a coarse pixel are shown in Figure 3.1(a). Amongst the four fine pixels, two should be allocated to the gray class. As 0.9 is the highest probability among the four sub-pixels, the sub-pixel at (1, 1) is first assigned to the gray class. The second sub-pixel of gray class should be selected among the remaining three sub-pixels by comparing of the three corresponding probabilities. However, the two next highest probabilities of 0.7 are at (1, 2) and (2, 2), respectively. It is impossible to determine which one should be selected as the gray class when there is only one observed coarse image.

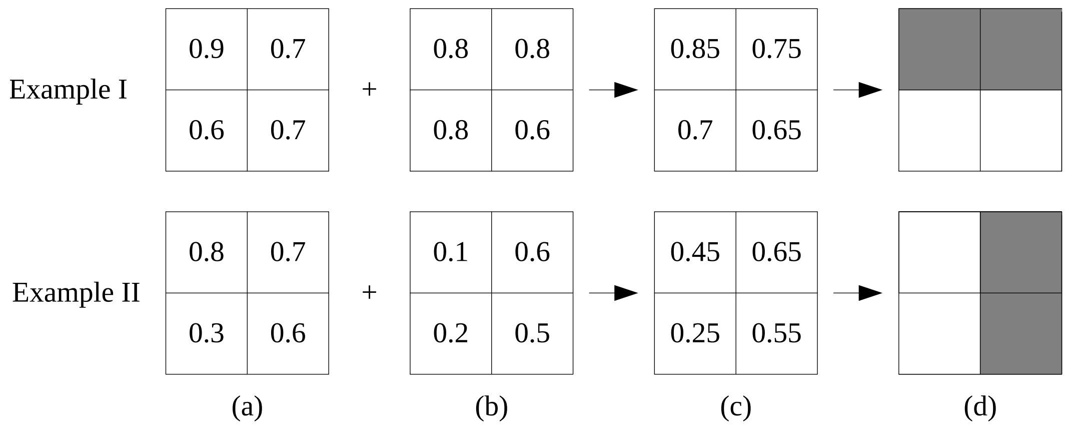

Figure 3.1. ICK-derived conditional probabilities of the gray class in a coarse pixel with 2×2 fine pixels. (a) A conditional probability map. (b) Another conditional probability map obtained from additional information. (c) Integration of the two maps in (a) and (b). (d) Using (c) for class allocation given the condition that the fraction of gray class is 50%.

If there is some supplemental information, however, such as another ICK-derived conditional probability map containing this coarse pixel, the second gray class sub-pixel may be selected out. For example, Figure 3.1(b) shows the conditional probabilities of the gray class for the same four sub-pixels. As can be seen in Figure 3.1(b), the probability of the sub-pixel at (1, 2) is greater than that at (2, 2), and hence the sub-pixel at (1, 2) should be the one assigned to the gray class. A convenient and reasonable way to integrate multiple probability maps of each class, is to average these probabilities at each sub-pixel and a single probability map of each class is generated in this way. Figure 3.1(c) shows the integrated probabilities of the gray class for the four fine pixels that can be used for the subsequent class allocation shown in Figure 3.1(d).

Errors are also unavoidable during the process of ICK-based probability estimation and the ICK-derived probabilities from single observed coarse image may therefore not be absolutely dependable. Integration of the multiple probabilities acquired from the additional information could be an effective way to alleviate errors and the derived integrated probability map for each class would be more accurate. Example II in Figure 3.1 illustrates this problem. Again, the fraction of gray class and S are supposed to be 50% and 2. The reference gray class distribution is the same as that displayed in (d) in this example. The probability at sub-pixel (1, 1) from probability map (a), i.e., 0.8, is generated with some inherent error from the ICK model itself. Using only (a), because of the error at sub-pixel (1, 1), the sub-pixel will be assigned to the gray class. If, however, there exists another probability map (b) obtained from additional information where the probability at sub-pixel (1, 1) is 0.1, with much less error than (a). Then by integration in (c), the error from (a) will be alleviated to a large degree and the expected sub-pixel map will be generated, as in (d).

In this section, MSI are used to obtain multiple probability maps. Suppose there are R shifted images, and the sub-pixel shift between the r-th (r=1,2,…,R) and the first observed coarse image is (x_r, y_r), which means the rightward and the downward shift are x_r and y_r sub-pixels, respectively. If (a_m, b_m) is the coordinate of sub-pixel v_m in the first image, then the coordinate of its corresponding sub-pixel v_m^r in the r-th image is ($a_m - x_r, b_m - y_r$).

Figure 3.2 provides an example to illustrate the relationship between the shifted images. In Figure 3.2(a), there are two coarse images A (solid line) and B (dashed line) and the sub-pixel shift is (1, 1). Each coarse pixel in the two images is divided into 2×2 sub-pixels, as shown in Figure 3.2(b) and (c). The black sub-pixel in A is at (3, 3), falling within the coarse pixel at (2, 2) while in B it is at (2, 2), falling within the coarse pixel at (1, 1). The probability of the k-th class occurrence at the black sub-pixel in A is related to fractions $\boldsymbol{a}_k^A$=[$a_k(V_n^A)$, n=1,2,...,N_A]$^{\mathrm{T}}$ while in B it is related to fractions $\boldsymbol{a}_k^B$=[$a_k(V_n^B)$, n=1,2,...,N_B]$^{\mathrm{T}}$, where N_A and N_B are the number of coarse pixels in A and B, respectively. Therefore, with two images A and B, the probability of the k-th class for black sub-pixel relies on $\boldsymbol{a}_k^A$ and $\boldsymbol{a}_k^B$ simultaneously. Due to the sub-pixel shift, $a_k(V_n^A)$ and $a_k(V_n^B)$ for the coarse pixels at the same grid n in two images are usually different from each other. The differences actually reflect the great significance of MSI.

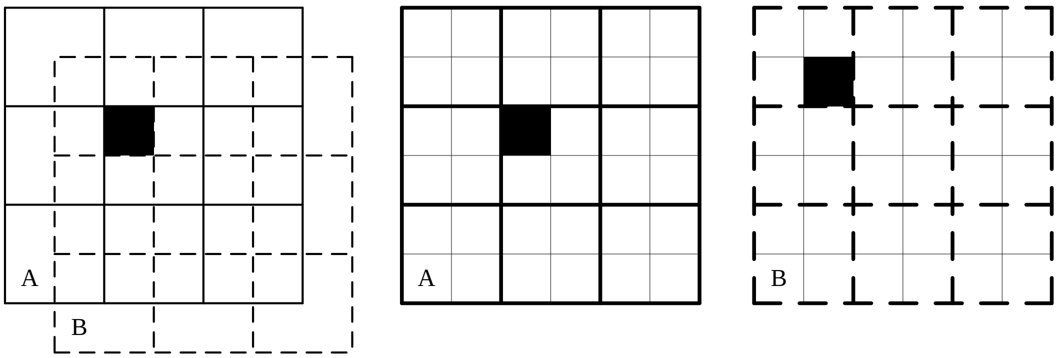

(a) (b) (c)

Figure 3.2. (a) Two coarse images A and B with sub-pixel shift (1, 1). (b) and (c) The black sub-pixel is at (3, 3) in A and (2, 2) in B.

When MSI are used, the probability of the k-th class occurrence at v_m's corresponding sub-pixel v_m^r in the r-th (r=1,2,…,R) image, denoted as $p_k(v_m^r)$, can be calculated as:

$$p_k(v_m^r) = \boldsymbol{\eta}_k(v_m^r)^{\mathrm{T}}\boldsymbol{a}_k^r + \boldsymbol{\lambda}_k(v_m^r)^{\mathrm{T}}\boldsymbol{j}_k + \pi_k[1 - sum(\boldsymbol{\eta}_k(v_m^r)^{\mathrm{T}}) - sum(\boldsymbol{\lambda}_k(v_m^r)^{\mathrm{T}})] \quad (3.7)$$

where $\boldsymbol{a}_k^r$=[$a_k(V_n^r)$, n=1,2,...,N_r]$^{\mathrm{T}}$ is a (N_r ×1) vector and N_r is the number of coarse pixels in the r-th image. Similarly, the ICK weights $\boldsymbol{\eta}_k(v_m^r)$ and $\boldsymbol{\lambda}_k(v_m^r)$ are computed by expression (3.6). The R ICK-derived probabilities of the k-th class are then integrated by:

$$p_k^o(v_m) = \frac{1}{R}\sum_{r=1}^{R} p_k(v_m^r) \quad (3.8)$$

An extra step is to normalize the K integrated probabilities by:

$$p_k(v_m) = \frac{p_k^o(v_m)}{\sum_{k=1}^{K} p_k^o(v_m)} \tag{3.9}$$

so that $\sum_{k=1}^{K} p_k(v_m) = 1$. Figure 3.3 displays the flowchart of the proposed ICK-based SPM with MSI.

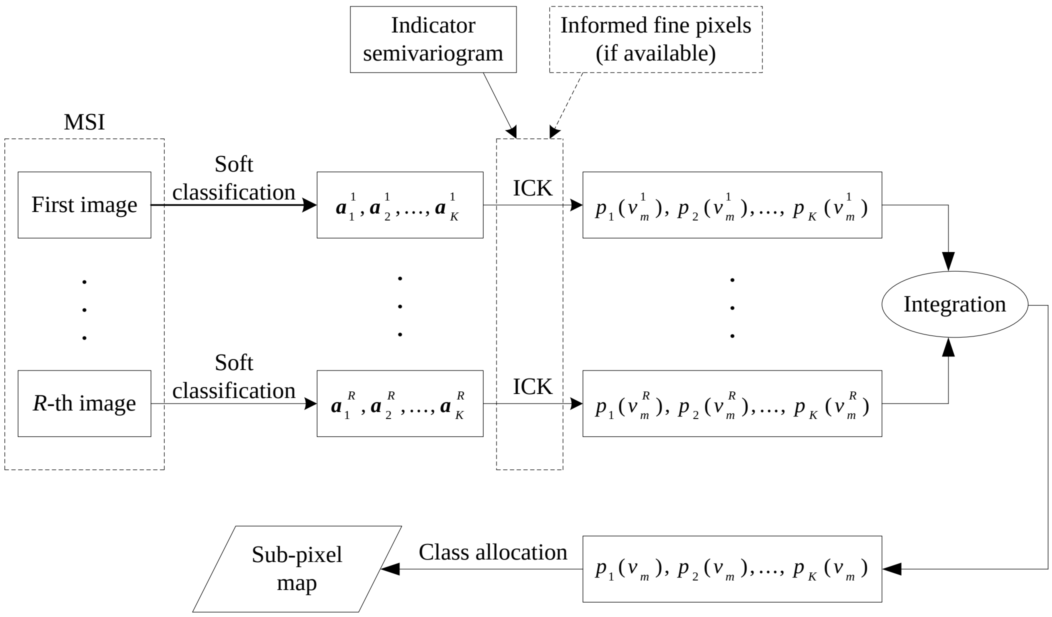

Figure 3.3. Flowchart of the proposed algorithm.

Note that when the R ICK-derived probabilities are integrated by expression (3.8), the sub-pixel shifts (x_r, y_r) (r=1,2,…,R) should be estimated in advance to locate v_m's corresponding sub-pixel v_m^r in the r-th image. Usually, the MSI are obtained by a sensor taking images over the same area at different times. Though these images are from the same site, they are not completely identical, due to the slight relative translations between the satellite and earth. In section 3.1, these images were assumed to be translated horizontally and vertically at sub-pixel level, ignoring rotation and deformation. Phase correlation is a widely used technique for image registration and is capable of measuring the relative shift between two images at sub-pixel level (Manuel et al., 2008). This technique was applied for MSI sub-pixel shift estimation.

3.1.3. Experiments

In this section, three experiments on different types of remote sensing images were carried out to demonstrate the effectiveness and advantages of the proposed

SPM method. Four SPM methods were compared: HNN-based SPM (HNNB), HNN-based SPM with MSI (HNNB_MSI), ICK-based SPM (ICKB) and ICK-based SPM with MSI (ICKB_MSI). All experiments were tested on an Intel Core i7 Processor at 3.40-GHz with MATLAB 7.1 version. For ICKB and ICKB_MSI, a set of 5×5 coarse pixel neighbors were chosen for each coarse pixel, as did in Boucher and Kyriakidis (2006). The parameters in HNNB and HNNB_MSI were the same as those in Wang and Wang (2013): all the weighting constants in the network energy function were set to 1, the steepness of the *tanh* function was set to 10, the time step was set to 0.001 and the number of iterations was set to 1000.

3.1.3.1. Experimental setup

In the first two experiments synthetic coarse images were studied, in order to avoid the errors due to soft classification and coregistration, and solely concentrate on the performance of the proposed SPM method. The coarse images were created by degrading the reference land cover maps via an $S\times S$ mean filter and considered as outputs of soft classification (i.e., fractions). The task of SPM methods is to generate land cover maps having the same spatial resolution as the reference maps, by zooming in the degraded images with scale factor S. This has also been a popular approach in many existing SPM literature. In addition, the MSI were generated by shifting the fine spatial resolution land cover maps and the sub-pixels shifts were therefore known, which can avoid the errors caused by sub-pixel shift estimation. In each experiment, four shifted images were used and the sub-pixel shifts at the scale factor S were assumed to be (0, 0), ($floor(S/2)$, 0), (0, $floor(S/2)$) and ($floor(S/2)$, $floor(S/2)$), where $floor(\bullet)$ is a function that takes the integer nearest to $\bullet$ but not larger than it. Note that in the two experiments on synthetic coarse images, the number of sub-pixels for each class is strictly maintained (for all four SPM methods) according to the coarse fraction data. This is because there is no error in the synthetic coarse fraction data. The used class allocation method is UOC.

In the last experiment, real image data were used for tests: a Landsat ETM+ image and a time series of MODIS images of the same site. Four MODIS images obtained on different dates were used as MSI. Soft classification was implemented on the MODIS images and SPM was conducted subsequent to that. The task of SPM in this experiment was to predict the distribution of land cover classes at the spatial resolution of the Landsat ETM+ image for the coarse spatial resolution

MODIS images. The hard classified map of the Landsat ETM+ image was used as a reference map for accuracy assessment.

SPM is essentially a hard classification technique, which is carried out at sub-pixel level. The accuracy of hard classification algorithms is usually evaluated quantitatively by the overall accuracy in terms of the percentage of correctly classified pixels (PCC). Therefore, this index was used for accuracy assessment on SPM in the experiments. To evaluate the statistical significance in accuracy for different SPM algorithms, McNemar's test (Foody, 2004) was also used. Using the 95% degree of confidence level, the difference between two classification results is considered to be statistically significant if $|z|>1.96$.

3.1.3.2. Experiment 1: synthetic coarse image of a land cover map in Bath, UK

In the first experiment, a land cover map of an area in Bath, UK was studied. It is shown in Figure 3.4 (provided by Dr. A. J. Tatem). Contained are 360×360 pixels with a pixel size of 0.6m×0.6m, covering the following four classes: roads (with global fraction 8.77%), trees (with global fraction 17.07%), buildings (with global fraction 13.43%) and grass (with global fraction 60.73%). The roads and buildings have regular spatial distribution with linear features, which mainly appear as straight lines and right-angles, respectively. As for the trees, the spatial pattern is more complex and irregular. The fine spatial resolution map was degraded by a mean filter with scale 10, to produce the fraction maps of four classes shown in Figure 3.5(a), where white indicates a fraction of 100% and black indicates 0%. That is, each coarse pixel has a size of 6m×6m and each fraction map contains 36×36 pixels. These fraction maps were then used as input of SPM.

Using the fractions in the first column in Figure 3.5 and the indicator semivariogram extracted from the fine spatial resolution land cover map in Figure 3.4, the ICK-derived conditional probability map with 360×360 pixels of each class was generated, as shown in the second column in Figure 3.5. The third column in Figure 3.5 presents the ICK-derived probability maps produced by the proposed ICKB_MSI model. From visual comparison, we can conclude that the probability maps generated by ICKB_MSI provide more detailed information and the boundaries of land cover objects are clearer. This phenomenon indicates that ICKB_MSI can produce more accurate probabilities than ICKB. After computing the probabilities, class allocation was then implemented to generate hard classified sub-pixel maps by comparing these probabilities.

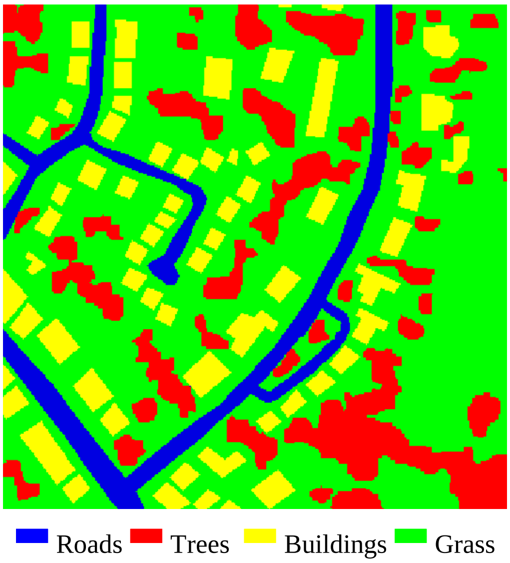

Figure 3.4. Reference land cover map in experiment 1.

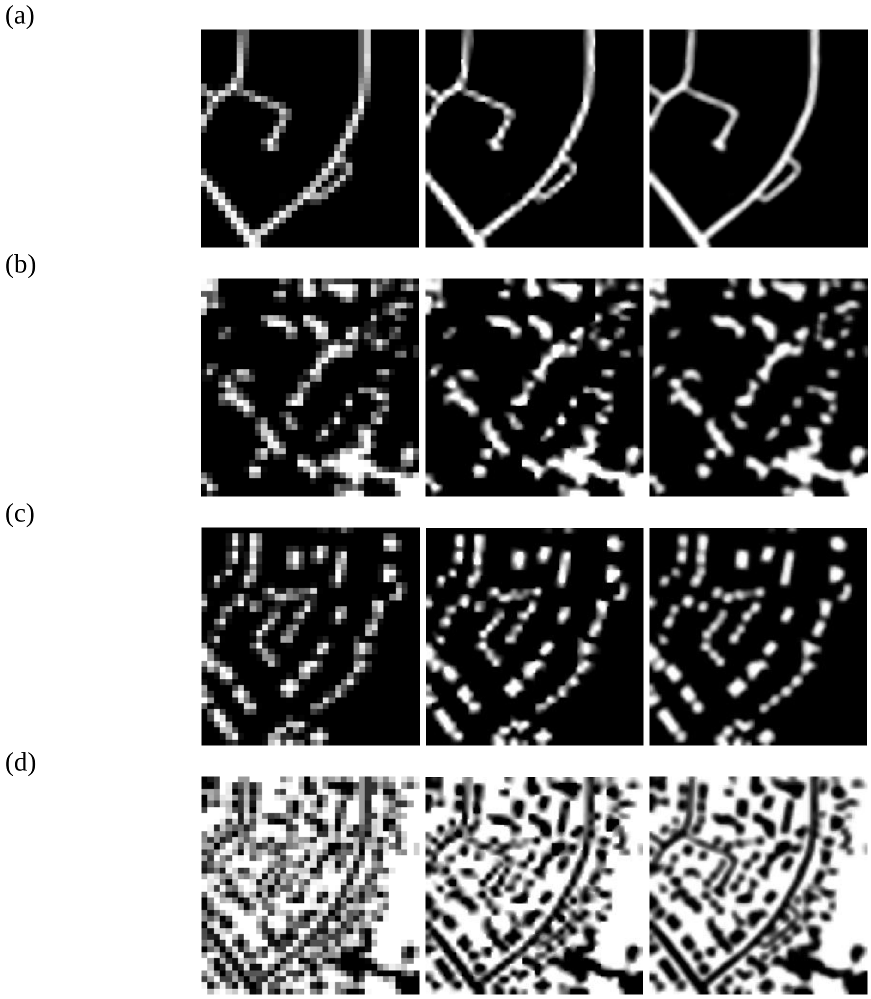

Figure 3.5. From left to right: Fraction maps, ICK-derived probability maps from ICKB and ICK-derived probability maps from ICKB_MSI. (a) Roads. (b) Trees. (c) Buildings. (d) Grass.

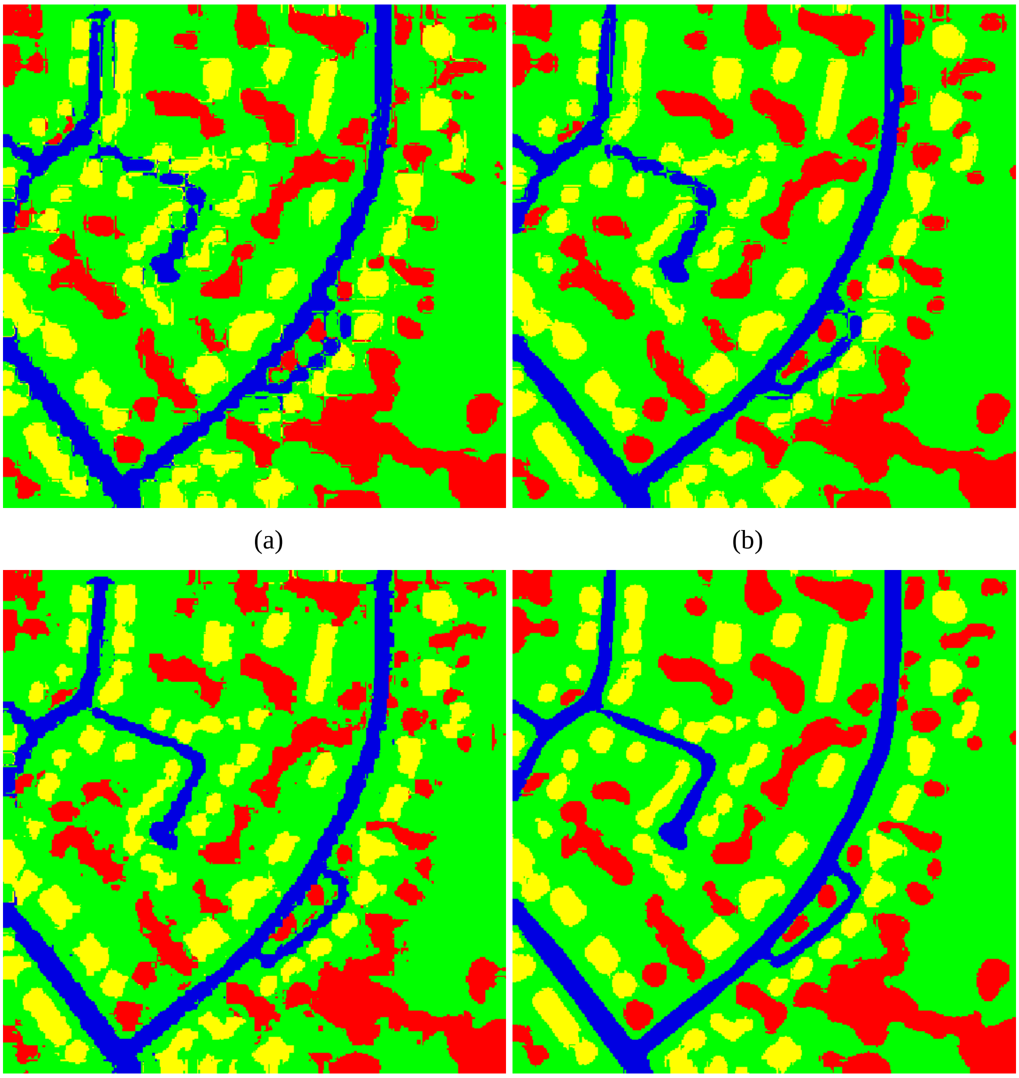

(a) (b) (c) (d)

Figure 3.6. SPM results in experiment 1 produced by (a) HNNB, (b) ICKB, (c) HNNB_MSI and (d) ICKB_MSI.

Figure 3.6(b) and (d) show the SPM results of the ICKB and ICKB_MSI. To fully demonstrate the advantages of the proposed method, SPM results of the HNNB and HNNB_MSI are also exhibited in Figure 3.6(a) and (c). From the visual comparison of the four sub-pixel maps, we can see clearly that with MSI, both HNN and ICK models are capable of producing more satisfying SPM results than does the single observed coarse image. Specifically, many linear artifacts are yielded by conventional HNNB and ICKB. The result yielded by ICKB, also, looks smoother and more continuous than that by HNNB and there are fewer linear artifacts in the ICKB result. This is because prior spatial structure information is incorporated into ICKB to alleviate the uncertainty in SPM and thus the result will be much closer to the reference land cover map, as mentioned above in the introduction. In the HNNB_MSI result, some speckle artifacts appear and the boundary between each class is relatively rough. Inheriting the advantage of using prior spatial structure information in ICKB, in the ICKB_MSI result, most of the land objects are recovered effectively and the improvement is considerably pronounced when MSI are used. Among the four SPM methods, ICKB_MSI produces the most satisfying sub-pixel map.

Table 3.1 PCC (%) of the four SPM methods in experiment 1

	HNNB	ICKB	HNNB_MSI	ICKB_MSI
Including pure pixels	89.69	92.45	92.11	**95.54**
Excluding pure pixels	85.43	89.33	88.84	**93.70**

Table 3.2 McNemar's test for SPM methods in experiment 1

	ICKB vs	HNNB_MSI vs	ICKB_MSI vs
HNNB	42.1081	25.3082	71.0868
ICKB		-3.9533	48.7943
HNNB_MSI			46.3061
ICKB_MSI			

Table 3.1 displays the PCC of each SPM method. In a coarse image, there are always some pure pixels containing only one land cover class. SPM assigns all sub-pixels within the pure pixel to the same class to which the pure pixel belongs. This simple copy process raises accuracy without providing any useful information about the SPM algorithms' performances (Mertens et al., 2003; Wang et al., 2012a,b; Zhong and Zhang, 2012, 2013). To eliminate the influence brought by the pure pixels, we also evaluated the accuracy when pure pixels are excluded in the statistics. Values in bold indicate the highest accuracy. Similar to the visual comparison, more accurate SPM results can be obtained with MSI. The ICK model outperforms HNN model, no matter whether MSI are applied in HNN in this experiment. Using MSI, the ICK model is able to generate the most accurate SPM result among the four methods. More precisely, the accuracy for each class of ICKB_MSI is the highest and the PCC of it is 5.85%, 3.09% and 3.43% greater than those of HNNB, ICKB and HNNB_MSI when considering all pixels for accuracy statistics. Excluding pure pixels, the differences in accuracy between the four

methods are more distinct: the PCC of ICKB_MSI is 8.27%, 4.37% and 4.86% greater than that of HNNB, ICKB and HNNB_MSI, respectively. The advantages of the proposed ICKB_MSI can also be confirmed by the McNemar's test results in Table 3.2. One can see from Table 3.2 that using MSI, both HNNB_MSI and ICKB_MSI have significantly higher PCC than does the single observed coarse image. Moreover, ICKB_MSI achieves significantly higher accuracy than other three SPM methods.

In addition, Figure 3.7 presents the PCC of the four SPM methods with S=5, 10, 15 and 20 when excluding pure pixels for accuracy statistics. It can be concluded from the bar chart that as the scale increases, the accuracy of all four methods decreases. The reason for this phenomenon is that the SPM process becomes more complicated with higher scale factors, as for every coarse pixel the locations of more sub-pixels need to be estimated and uncertainty increases. Because of the use of MSI, the accuracy of both HNNB and ICKB increases greatly, except for scale 5 as at this scale, SPM is relatively simple and HNNB is able to produce highly accurate result. In fact, as the scale increases, the advantage of the proposed ICKB_MSI method becomes more obvious, generating the most accurate SPM results at all four scales. At scale 20, especially, the PCC of ICKB_MSI still reaches about 85% while the PCC of other three methods is much less than 80%. This reveals that ICKB_MSI could be a promising approach for the large scale situation.

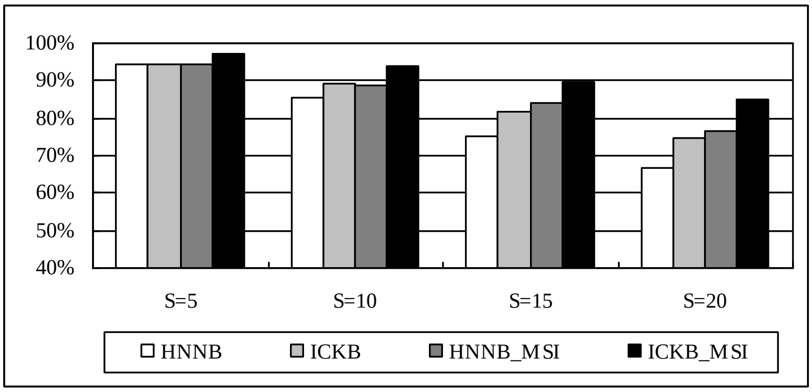

Figure 3.7. PCC (excluding pure pixels) of the four SPM methods at four scales: 5, 10, 15 and 20.

3.1.3.3. Experiment 2: synthetic coarse image of a land cover map in Washington, DC

The second experiment is to test the proposed method for area with large number of classes and complex land cover patterns. A part of Hyperspectral Digital Imagery Collection Experiment airborne hyperspectral data from the Washington, DC Mall

(191 bands with 3m spatial resolution) was used for test (Landgrebe, 2003). The study area has a size of 240×296 pixels with seven classes: shadow, water, road, tree, grass, roof and trail. The reference land cover map of the studied site is shown in Figure 3.8, which was obtained with the tensor discriminative locality alignment-based classification of the hyperspectral data in Zhang et al. (2013). The synthetic coarse image was generated by degrading the reference land cover map with S=8, as shown in the first column in Figure 3.9. The second and third columns of Figure 3.9 show the ICK-derived conditional probability maps of seven classes with ICKB and ICKB_MSI, respectively. The indicator semivariogram used in ICK model was extracted from Figure 3.8. It can be observed that the seven probability maps derived by ICKB_MSI provide visually clearer information of land cover.

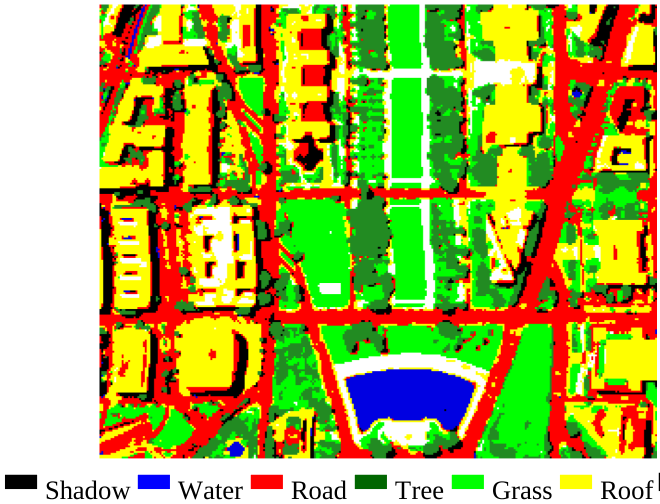

Figure 3.8. Reference land cover map in experiment 2.

Figure 3.10(a)-(d) show the SPM results of HNNB, ICKB, HNNB_MSI and ICKB_MSI. As can be concluded from visual comparison of the four maps, the proposed ICKB_MSI generated the best result. For example, the continuity of the trail class in the centre of Figure 3.10(d) is the strongest and is the closest to that in the reference map in Figure 3.8; The reconstruction of the boundaries of water and road class in Figure 3.10(d) is more satisfying in comparison with Figure 3.10(a)-(c). Table 3.3 gives the PCC of the four SPM methods. Similar to the conclusion of visual comparison, ICKB_MSI achieves the highest accuracy among the four methods. The McNemar's test results in Table 3.4 indicate that the PCC of ICKB_MSI is significantly higher than that of HNNB, ICKB, HNNB_MSI.

(a)

(b)

(c)

(d)

(e)

(f)

(g)

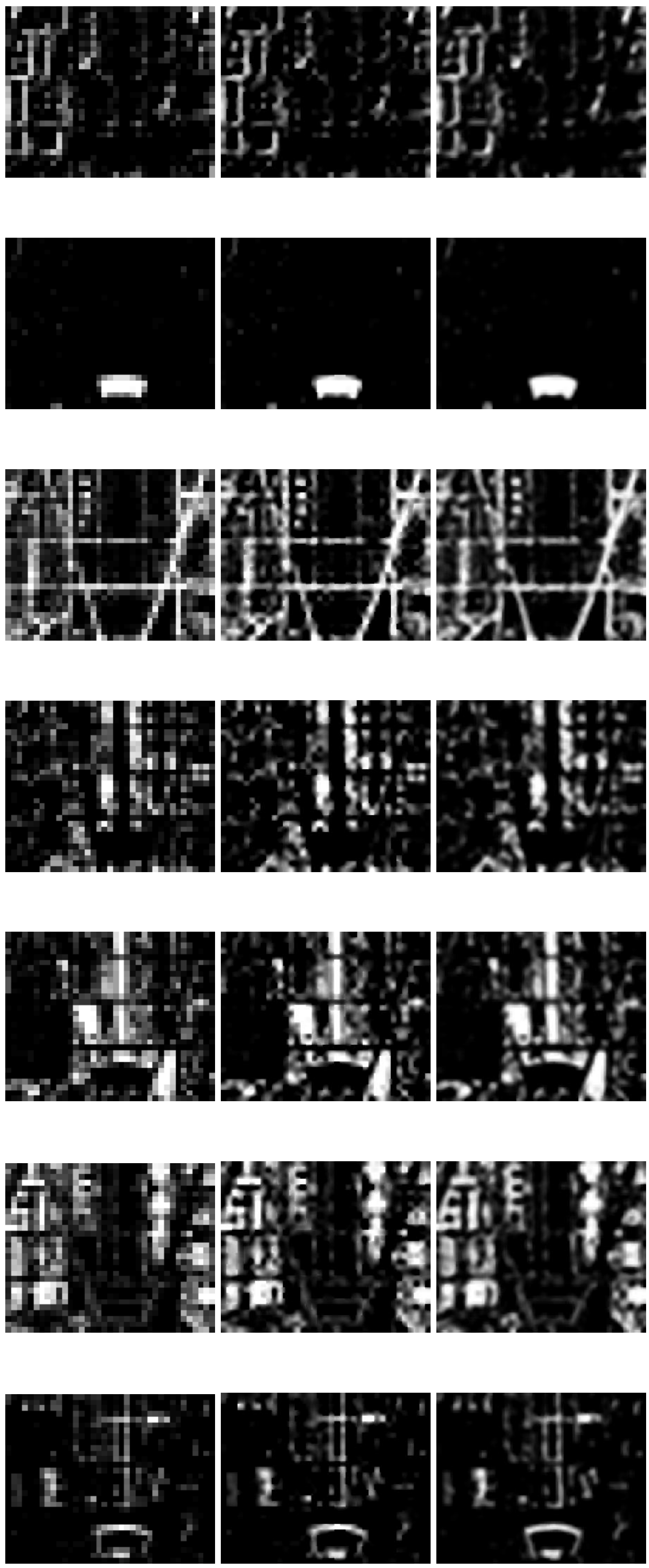

Figure 3.9. From left to right: Fraction maps, ICK-derived probability maps from ICKB and ICK-derived probability maps from ICKB_MSI. (a) Shadow. (b) Water. (c) Road. (d) Tree. (e) Grass. (f) Roof. (g) Trail.

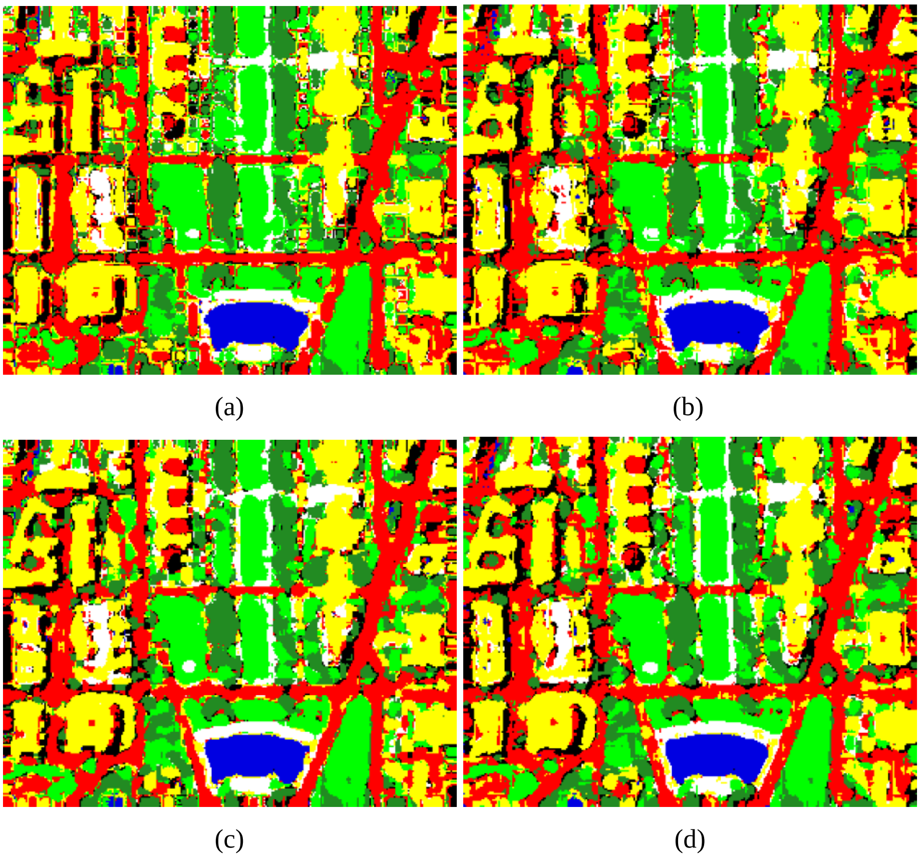

Figure 3.10. SPM results in experiment 2 produced by (a) HNNB, (b) ICKB, (c) HNNB_MSI and (d) ICKB_MSI.

Table 3.3 PCC (%) of the four SPM methods in experiment 2

	HNNB	ICKB	HNNB_MSI	ICKB_MSI
Including pure pixels	64.98	66.64	70.92	**72.54**
Excluding pure pixels	61.85	63.66	68.32	**70.08**

Table 3.4 McNemar's test for different SPM methods in experiment 2

	ICKB vs	HNNB_MSI vs	ICKB_MSI vs
HNNB	10.7968	33.3190	44.0003
ICKB		24.2095	40.1149
HNNB_MSI			10.7551
ICKB_MSI			

3.1.3.4. Experiment 3: real data

To further validate the advantages of the proposed SPM method, tests on real data were implemented in the third experiment. Two sets of image data were used, including a time series of MODIS images and a Landsat ETM+ image. They cover an area located in Quebec province, Canada, mainly made up of lakes and land. Four MODIS 250m spatial resolution images on four close days in 2002 were acquired: 21 June, 30 June, 5 July and 6 August. The Landsat ETM+ image with a spatial resolution of 30m obtained on 10 July 2002 was used to provide ground truth data. Only the images acquired in the near infrared band of the two sets of data were used because the land cover classes were highly separable in this band. The MODIS image obtained on 5 July was used as a reference image for sub-pixel shift estimation of MSI. Further details on the description of site and data can be found in Muad (2011). The sub-pixel shifts of the images measured by a phased correlation technique are (5, 6), (4, 7) and (1, 5) sub-pixels (i.e., (156m, 188m), (125m, 219m) and (31m, 156m)) for images acquired on 21 June, 30 June and 6 August.

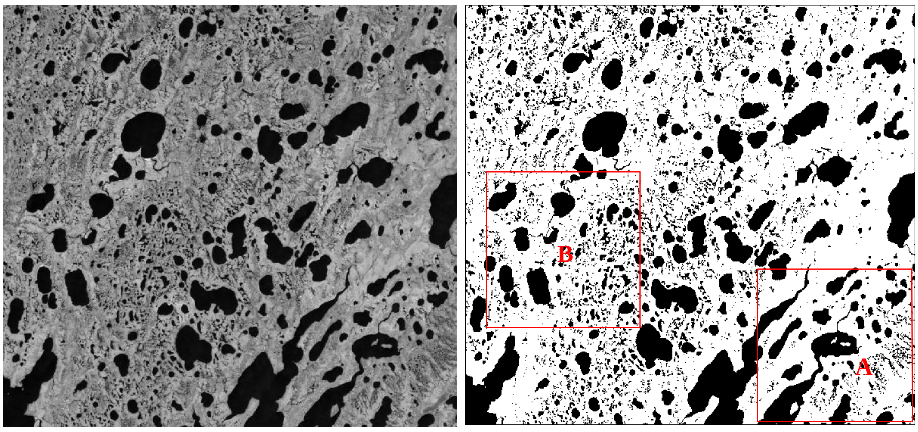

(a) (b)

Figure 3.11. The Landsat ETM+ image. (a) Near infrared band image. (b) Hard classified map, where white and black pixels denote land and water, respectively.

The original Landsat ETM+ image has a size of 865×927 pixels. Using nearest neighbour interpolation, it was interpolated to 872×936 pixels, 8×8 times of the size of MODIS images (109×117 pixels). The pixels in the Landsat ETM+ image were supposed to be pure materials, and an unsupervised *k*-means classifier (Duda et al., 2001) was employed to generate the hard classified ground truth map from this image. Without ground survey, it is difficult to conduct a rigorous evaluation of the accuracy of reference data. Through visual interpretation, however, the generated reference map looks highly similar to the Landsat ETM+ image (see Figure 3.11(a) and (b)). A sub-site was selected for test, labelled as sub-site A in Figure 3.11(b). It has a size of 320×320 pixels. The classified map at sub-site B was used as prior spatial structure information and the indicator semivariogram was extracted from it for ICKB and ICKB_MSI. This process was based on the assumption that the distribution of classes at sub-site B was available and the spatial pattern of this area was similar to sub-site A.

The MODIS images were soft classified by an unsupervised fuzzy *c*-means algorithm (c=2). The weighting parameter that determines the degree of fuzziness was set to 2. After that, four SPM methods were carried out on the fraction images, with a zoom factor S=8. When the estimated fractions were used to strictly maintain the sub-pixels of each class during the class allocation process, a large number of isolated pixels were produced in the SPM results. In this way, the generated sub-pixel maps appeared to be dominated by a speckled pattern, which greatly suppressed the performances of the SPM methods. This phenomenon was caused by the errors in the soft classification. For example, suppose in the coarse image there is a pure pixel covering the class, water. By SPM, all 8×8 sub-pixels within this pixel should be allocated to water. However, if the estimated fraction of water for this pixel is 12.5%, by class allocation, 8 sub-pixels should be allocated to water. In this case, these 8 sub-pixels are produced by errors from soft classification and are quite likely to appear as noise in the SPM result. For sub-site A, the PCC values (considering all pixels) of four SPM methods are between 80% and 81% when coarse fractions were strictly maintained. To alleviate the influence of such errors from soft classification, in this experiment the fractions were used in probability estimation but not in the pivotal class allocation process. Instead, a simple class allocation method was applied whereby each sub-pixel was allocated to the class with the highest probability. The SPM results for the two sub-sites are shown in Figure 3.12.

As can be seen from the results in Figure 3.12, there are some jagged boundaries in the HNNB and ICKB results, appearing as right-angle shape, as shown in Figure 3.12(a) and (b). This phenomenon conflicts with the class distribution in the ground reference maps (Figure 3.11(b)). With MSI, the performances of both HNNB and ICKB were enhanced. The boundaries in Figure 3.12(c) and (d) looks smoother and more places were correctly classified, such as those places with small lakes. While focusing on Figure 3.12(c), it is found that in HNNB_MSI result, some block objects classified as land lie within some large lakes. In the ground truth maps, however, these large lakes are of hole-shape, as shown in Figure 3.11(b). Therefore, places covered by these block objects in Figure 3.12(c) were misclassified. This is not the case, however, in ICKB_MSI result. Among the four methods, the proposed method generated the SPM result that is the closest to the reference maps.

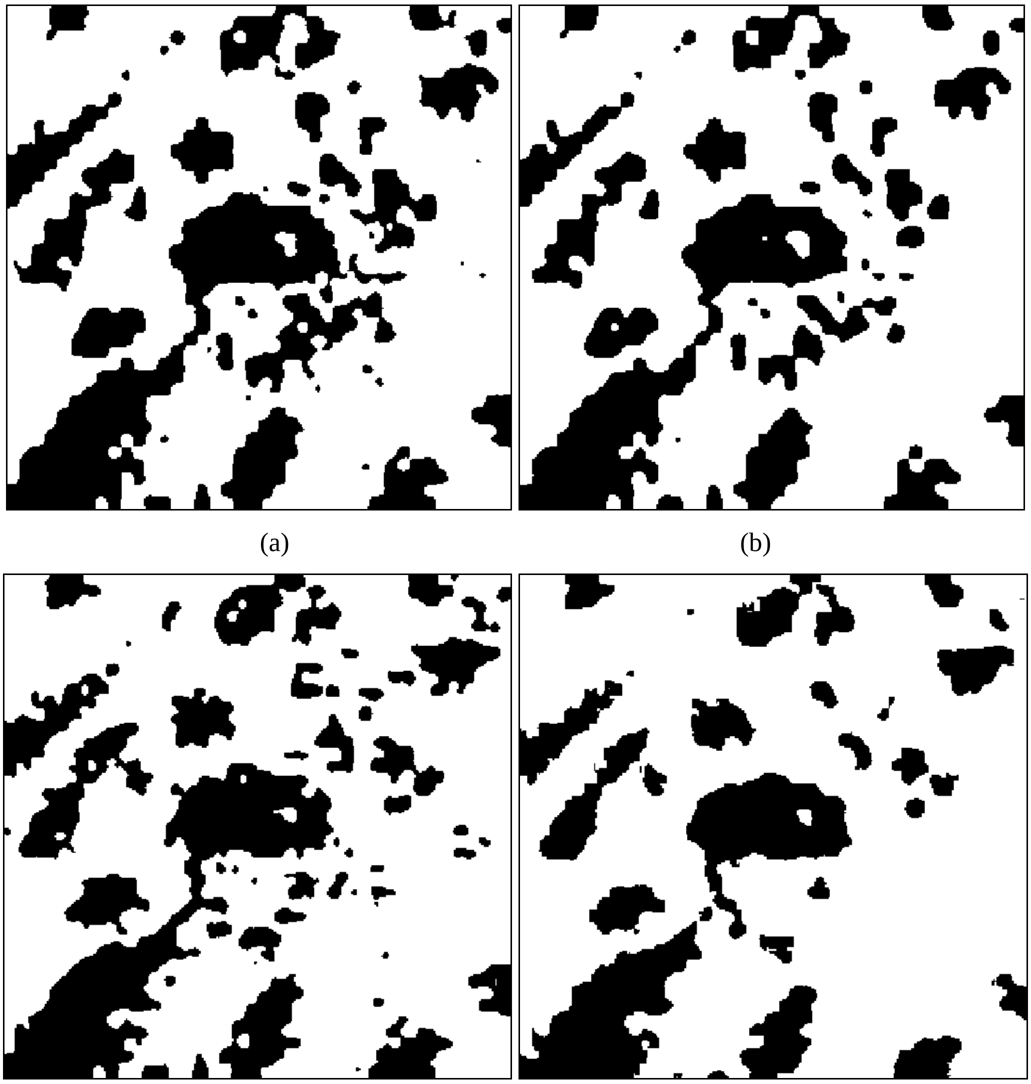

(a) (b) (c) (d)

Figure 3.12. SPM results of the real MODIS data produced by (a) HNNB, (b) ICKB, (c) HNNB_MSI and (d) ICKB_MSI. White and black pixels denote land and water, respectively.

Table 3.5 lists the PCC of the four SPM approaches. Note that PCC in this experiment was calculated taking account of all pixels in SPM results. The pure pixels in coarse images were not excluded as whether a pixel is pure or not is determined by the soft classifier (fuzzy *c*-means algorithm in this experiment). We are also concerned about the performance of soft classifier when real coarse images are studied for SPM. This is different from the previous two experiments, where synthetic coarse images were studied and no soft classifier was applied and hence no error exists in soft classification in fact. The PCC of the proposed method is 84.15%, about 2%, 1.2% and 1% greater than that of HNNB, ICKB and

HNNB_MSI. In all, the proposed method produced the highest SPM accuracy. The McNemar's test results are shown in Table 3.6. It can be observed that ICKB obtains significantly higher accuracy than HNNB because ICKB makes use of prior spatial structure information. Similar to the conclusions drawn from the previous two experiments on synthetic coarse images, HNNB_MSI obtains significantly higher accuracy than HNNB while ICKB_MSI obtains significantly higher accuracy than ICKB; The accuracy of proposed ICKB_MSI is significantly higher than other three SPM methods.

Table 3.5 PCC (%) of the four SPM methods in experiment 3

HNNB	ICKB	HNNB_MSI	ICKB_MSI
82.18	82.98	83.20	**84.15**

Table 3.6 McNemar's test for different SPM methods in experiment 3

	ICKB vs	HNNB_MSI vs	ICKB_MSI vs
HNNB	14.0072	10.3767	17.0608
ICKB		2.2357	10.6082
HNNB_MSI			9.5271
ICKB_MSI			

3.1.4. Discussion

From the results in three experiments, we can obtain a general rank of the four SPM methods in terms of SPM accuracy: HNNB, ICKB, HNNB_MSI and ICKB_MSI. From HNNB to ICKB_MSI, the overall performances become better in this study. The reason for the advantages of ICK-based SPM methods (i.e., ICKB and ICKB_MSI) over HNN-based methods (i.e., HNNB and HNNB_MSI) is that the former utilize prior spatial structure information while the latter are based on spatial dependence and thus fail to deal with complex spatial patterns, as mentioned in the introduction. With the aid of MSI, however, HNN is able to produce better SPM results than does ICKB. This reveals the great potentiality of MSI in SPM.

The computational efficiency is also an important factor to evaluate the four SPM methods. In each experiment, HNNB and HNNB_MSI took several hours for 1000 iterations. However, both ICKB and ICKB_MSI took less than 2 minutes. The considerably low computational burden in ICKB and ICKB_MSI is mainly due to the fact no iterations are involved in them. Therefore, the proposed method will be promising for a real-time system.

The proposed algorithm is different from the HNN-based SPM with MSI, except that the proposed algorithm is learning-based while the HNN model is based on spatial dependence assumption. For HNN-based SPM with MSI, each fine pixel also falls within multiple coarse pixels in MSI, and the fractions of classes within the corresponding multiple coarse pixels are added into the constraint term of the HNN's energy function, to provide multiple fraction constraints. Essentially, the HNN used for SPM is an optimization tool. In this model, the attribute value of each class for each sub-pixel (between zero and one) is changed after each iteration and the energy function is minimized iteratively to approach a solution. With multiple fraction constraints from MSI, therefore, a large number of iterations (usually over 1000) for the conventional HNN model are still required to generate attribute values. However, this is not the case in the proposed algorithm based on the ICK model. In the ICK-based SPM, for each sub-pixel v_m, fractions (those from all coarse pixels in the observe image, not only the one, v_m falls within) are used in linear combination, see (3.5), and their weights are calculated by solving the equations in (3.6). No iterations are involved in the whole process. With MSI, for each sub-pixel v_m, all fractions in the shifted images are used and a set of ICK-derived probabilities are also calculated in the same way and without iterations. Besides, from expression (3.6) we can also see that no parameters are involved and the information from informed fine pixels can also be readily coded into the new model. Consequently, the proposed algorithm inherits all the advantages of the ICK-based SPM.

As can be found from Table 3.1 and Table 3.3, the PCC of the proposed algorithm decreases from around 94% in Table 3.1 to 70% in Table 3.3. This is because the number of classes increases from four in experiment 1 to seven in experiment 2. Furthermore, the complexity of land cover pattern is also different in the two experiments. In Figure 3.4, the roads and buildings have regular spatial distribution with linear features, which can be well recreated by the proposed SPM method. In Figure 3.8, however, there are many linear and elongated features, which are more difficult to be restored in comparison with the features in Figure 3.4. We can conclude that the performance of the proposed SPM algorithm is influenced by the number of classes and spatial complexity of land cover pattern in the study area.

Focusing on Figure 3.7, it is concluded that the performance of the proposed SPM algorithm deteriorates when the zoom scale factor increases. Compared with the other three SPM methods, the proposed method is relatively less sensitive to the scale factor, suggesting the new SPM method is potential for the large scale cases.

As a pre-processing step, the soft classification has a direct influence on the SPM and errors from the former can be propagated to the latter (Villa et al., 2011). In real word cases, the uncertainty in soft classification needs further study. The selection of MSI is also a critical issue. In different periods, the land cover from the same area may be different due to the human activities (e.g., buildings construction) and natural changes (e.g., changes of rainfall and vegetation in different seasons) and so on. Additionally, illumination and angular effects sometimes plays an important role in MSI. It makes a huge difference to an image whether it is acquired in the morning or afternoon or if the viewing angle is from the right, left, or nadir. The uncertainty in MSI data certainly has an impact on the proposed method that uses MSI as additional information. It necessitates the consideration of acquired time, illumination and angular while selecting MSI for the proposed SPM method.

3.2. Image Interpolation -based SPM with multiple shifted images

(This section is based on Wang and Shi (2014))

3.2.1. Introduction

As can be seen from Section 3.1, the advantageous STHSPM algorithm (i.e., ICK-based SPM) requires prior spatial structure information, which limits the applications in real world. Actually, the critical step one of STHSPM can also be realized by some image super-resolution algorithms and in Section 3.2 the classical bilinear and bicubic interpolation algorithms are used for this purpose. The advantages of bilinear and bicubic interpolation are that both of them are non-parametric, non-iterative and fast algorithms. Moreover, they do not need prior spatial structure information on classes. In this section, MSI are used in SPM with image interpolation-based STHSPM algorithms. Unlike the methods in Ling et al. (2010), Wang and Wang (2013), Xu et al. (2013), Zhong et al. (2014) and Section

3.1, which are iteration-based or need prior information, the methods studied in Section 3.2 inherit the advantages of bilinear and bicubic interpolation.

3.2.2. Methods

Suppose the soft classification results of a coarse spatial resolution image are K (K is the number of land cover classes) fraction images $\boldsymbol{F_1}, \boldsymbol{F_2}, ..., \boldsymbol{F_K}$, and each coarse pixel is divided into $S \times S$ sub-pixels. Let P_j (j=1,2,…,M, M is the number of pixels in the coarse image) be a coarse pixel, p_i (i=1,2,...,MS^2) be a sub-pixel, and $F_k(P_j)$ is the fraction of the k-th class for pixel P_j.

3.2.2.1. Bilinear and bicubic interpolation-based STHSPM

Let $Z_k(p_i)$ be the soft attribute value for the k-th class at sub-pixel p_i. Taking the fraction images $\boldsymbol{F_1}, \boldsymbol{F_2}, ..., \boldsymbol{F_K}$ as inputs, both bilinear and bicubic interpolation can produce super-resolution images $\boldsymbol{Z}_1, \boldsymbol{Z}_2, ..., \boldsymbol{Z}_K$ quickly, each of which are composed of MS^2 soft attribute values.

In the SPM problem, the fractions and zoom factor S are used to determine the number of sub-pixels belonging to each class. More specifically, within each coarse pixel P_j, the number of sub-pixels for the k-th class, $NC_k(P_j)$, is

$$NC_k(P_j) = \text{round}(F_k(P_j)S^2) \tag{3.10}$$

where round(•) is a function that takes the integer nearest to •.

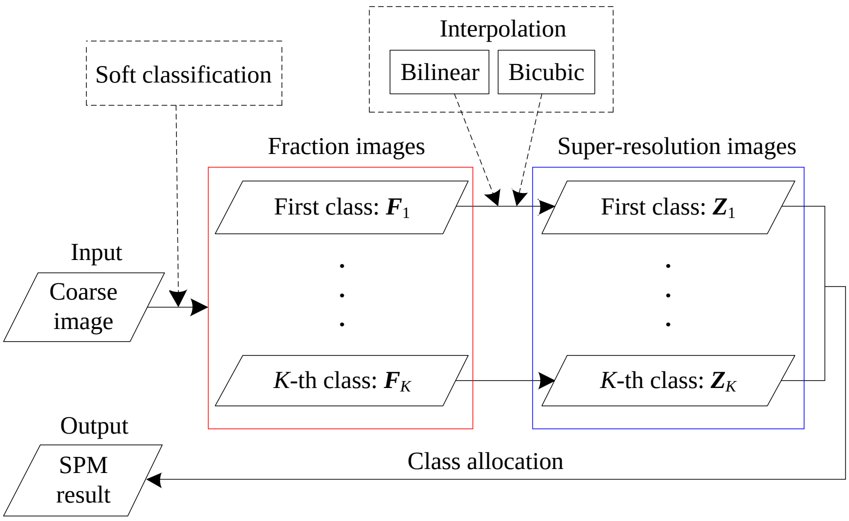

Figure 3.13. Flowchart of the bilinear and bicubic interpolation-based STHSPM.

Along with the constraints in (3.10), $\boldsymbol{Z}_1, \boldsymbol{Z}_2, ..., \boldsymbol{Z}_K$ are used to allocate hard class labels to sub-pixels. The UOC-based class allocation method is employed, with which sub-pixels for each class are allocated in turn. For each class, sub-pixels with larger soft attribute values are allocated before those with smaller ones. Using this method, the autocorrelation for each class can be maximized. The visiting order of all classes can be decided by comparing Moran's I (Makido et al., 2007) of K classes and the classes with higher indices are visited first. Figure 3.13 is the flowchart describing the bilinear and bicubic interpolation-based SPM methods.

3.2.2.2. Using MSI in bilinear and bicubic interpolation-based STHSPM

MSI can be acquired by a satellite taking images over the same area at different times. The images usually have the same spatial resolution. Due to the slight relative translations between the satellite and Earth, these images will not be completely identical and will usually be shifted from each other. In this section, the MSI are assumed to be translated horizontally and vertically at the sub-pixel level.

Suppose the number of MSI is R, and the sub-pixel shift between the r-th (r=1,2,…,R) and the first coarse image is (x_r, y_r), which indicates that the rightward and the downward shifts are x_r and y_r sub-pixels. If the coordinate of a sub-pixel, say p_i, in the first image is (a_m, b_m), the coordinate of its corresponding sub-pixel p_i^r in the r-th coarse image should be ($a_m - x_r, b_m - y_r$). An example is given in Figure 3.14 to illustrate the sub-pixel shifts. There are two 3×3 coarse images A (black) and B (red). Suppose each coarse pixel in the two images is divided into 2×2 sub-pixels (S=2). The sub-pixel shift from A to B is (1, 1). If a sub-pixel, labelled in blue in the figure, is at (3, 3) in A, then it should be at (2, 2) in B.

In the proposed bilinear and bicubic interpolation-based SPM with MSI, the soft attribute value for the k-th class at sub-pixel p_i is determined by integration of R attribute values:

$$Z_k(p_i) = \frac{1}{R}\sum_{r=1}^{R} Z_k(p_i^r) \tag{3.11}$$

where $Z_k(p_i^r)$ indicates the soft attribute value for the k-th class at p_i's corresponding sub-pixel p_i^r in the r-th coarse image. $Z_k(p_i^r)$ is estimated by bilinear or bicubic interpolation, taking the k-th class fraction image for the r-th coarse image as input.

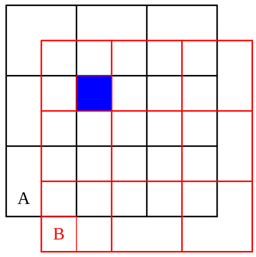

Figure 3.14. Two coarse images A and B with sub-pixel shift (1, 1)

3.2.2.3. Implementation of the proposed methods

The implementation of the bilinear and bicubic interpolation-based SPM with MSI includes five steps.

Step 1: Estimation of sub-pixel shifts (x_r, y_r) (r=1,2,…,R). Many existing algorithms can be applied to estimate the sub-pixel shift, such as phase correlation and cross-correlation matching.

Step 2: Soft classification of MSI. All R coarse images are soft classified. The results for each coarse image are K class fraction images. Correspondingly, there are R fraction images for each class.

Step 3: Image interpolation of fraction images. With bilinear or bicubic interpolation, all RK coarse images are super-resolved to the desired fine spatial resolution. The outputs are RK super-resolution images.

Step 4: Integration of interpolated images. For each class, its R interpolated super-resolution images are integrated, see (3.11). In this way, K fine spatial resolution images will be generated.

Step 5: Class allocation for each sub-pixel. Under the constraints in (3.10), K fine spatial resolution images generated in Step (4) are used for allocation of hard class labels, and sub-pixels for each class are allocated in turn. Details of the class allocation method can be found in Chapter 2.

In Section 3.2, the method for utilizing MSI for enhancement of SPM is different from that in Ling et al. (2010), Wang and Wang (2013), Xu et al. (2013), and Zhong et al. (2014), where additional information from MSI is used at coarse spatial resolution. Specifically, R (the number of MSI) constraints at original coarse pixel scale, such as those in terms of class fraction (Ling et al., 2010; Xu et al., 2013; Zhong et al., 2014) or spectral reflectance of the coarse pixel (Wang and Wang, 2013), are incorporated into the relevant SPM models. In the SPM process, each sub-pixel corresponds to R coarse pixels in MSI and has to satisfy R constraints when its class attribute is predicted. As the class attribute of each sub-pixel varies after each prediction, iterations are required to approach optimal SPM results. The whole process is always time consuming. In the proposed methods, however, information from MSI is exploited at sub-pixel scale, by up-sampling all fraction images of MSI to the desired fine spatial resolution in advance (see Step 3). The interpolated images for MSI are then straightforwardly integrated, which is a non-iterative and very fast scheme.

Super-resolution for each image of MSI is accomplished by bilinear or bicubic interpolation. The two interpolation algorithms are well-known for their simplicity and high computational efficiency. They are non-parametric, non-iterative and can process coarse spatial resolution images without prior spatial structure information. Based on bilinear and bicubic interpolation, therefore, the new SPM methods inherit all their advantages and MSI data are utilized efficiently.

3.2.3. Experiments

Experiments on two remote sensing images were carried out to validate the proposed SPM methods. Five SPM methods were tested and compared: PSA, bilinear, bicubic, bilinear with MSI and bicubic with MSI. All experiments were tested on an Intel Core 2 Processor (1.80-GHz Duo central processing unit, 2.00-GB random access memory) with MATLAB 7.1 version.

For supervised assessment of SPM methods, fine spatial resolution images were degraded via a mean filter to simulate coarse images. The task of SPM was to restore the fine spatial resolution map. Since many algorithms can be used for image registration of MSI, the estimation of sub-pixel shifts is beyond the scope of Section 3.2. To solely concentrate on the performance of the proposed SPM methods, in each experiment, the fine spatial resolution image was first shifted and then degraded to generate the MSI. In experiment 1 and experiment 2, four shifted images were considered and the sub-pixel shifts were assumed to be (0, 0), (0.5, 0), (0, 0.5) and (0.5, 0.5) coarse pixel. The number of MSI is further discussed in Section 3.2.3.2.

The accuracy of SPM was evaluated quantitatively by the overall accuracy in terms of the percentage of correctly classified pixels (PCC). McNemar's test was also applied to determine whether the difference between the SPM results is statistically significant. Using the 95% degree of confidence level, the difference is considered to be statistically significant if the calculated z-value is greater than 1.96.

3.2.3.1. Experiment 1

In the first experiment, an aerial image covering an area in Bath, UK was used for test. Figure 3.15(a) shows the image while Figure 3.15(b) shows the reference land cover map, which was provided by Dr. A. J. Tatem. The image has 360 by 360 pixels with a pixel size of 0.6m by 0.6m, and covers four classes: road, tree, building and grass. The reference map in Figure 3.15(b) was degraded with a 10 by 10 mean filter to generate fraction images for classes, each of which have 36 by 36 coarse pixels.

The SPM results of bilinear, bicubic, bilinear with MSI and bicubic with MSI are shown in Figure 3.15(c)-Figure 3.15(f). As can be seen in Figure 3.15(c) and Figure 3.15(d), with respect to the restoration of the road class, there are obvious disconnected shapes; as for trees and buildings, many burrs occur on their boundaries, which seem rough. With the aid of MSI, the performance of both bilinear and bicubic interpolation-based SPM methods are noticeably improved. In Figure 3.15(e) and Figure 3.15(f), the spatial continuity of each class is greater, the boundaries of the classes are smoother and the results are closer to the reference map in Figure 3.15(b).

Table 3.7 gives the accuracy of each class and the overall accuracy in terms of PCC for five SPM methods. In this experiment, the non-mixed pixels were not considered in the accuracy statistics. As shown in Table 3.7, PSA produces a greater PCC than both bilinear and bicubic methods in experiment 1. Comparing the accuracy of the four interpolation-based methods, using MSI, the SPM accuracy of bilinear and bicubic methods is evidently enhanced and also higher than for PSA. For the proposed two methods with MSI, the SPM accuracy of road, tree, building and grass increases by around 2.5%, 1.5%, 3% and 2%, respectively when compared to the bilinear and bicubic methods. For the two classes, road and building, they are regularly distributed and mainly appear within objects which have straight lines and right-angles in the study area. Hence increases in the accuracy with which they are predicted are more obvious than for the other two classes. The PCC of the bilinear method increases from 90.44% to 92.96% when MSI are used, and for the bicubic method, the PCC increases from 90.87% to 93.27% when MSI are used. The McNemar’s test indicates that the PCC of both bilinear with MSI and bicubic with MSI are significantly higher than for the PSA, bilinear and bicubic methods. In addition, bicubic with MSI achieves significantly higher accuracy than the other four SPM methods.

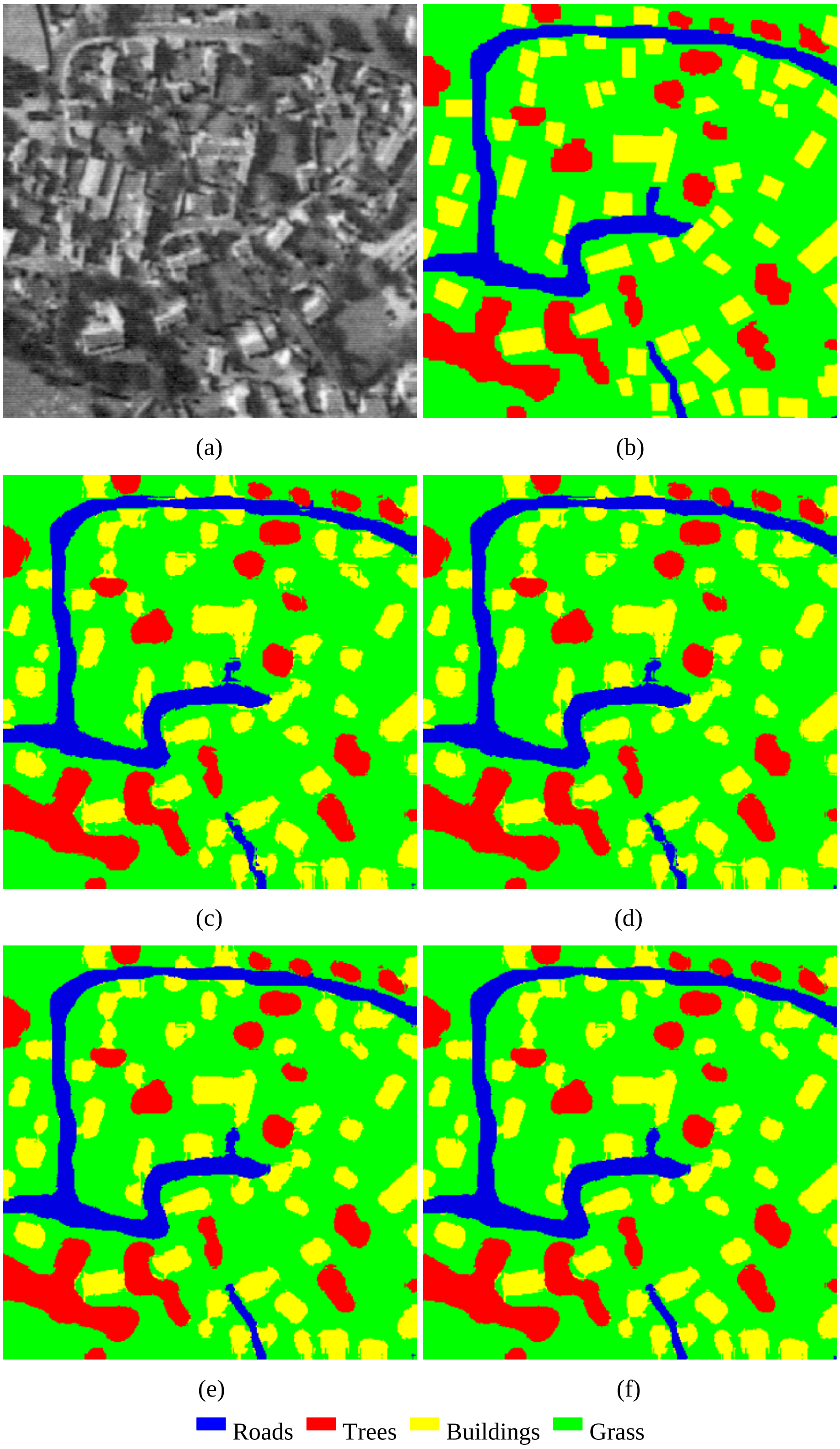

Figure 3.15. SPM results for the aerial image. (a) The aerial image. (b) The reference land cover map. (c) Bilinear result. (d) Bicubic result. (e) Bilinear with MSI result. (f) Bicubic with MSI result.

Table 3.7 Accuracy (%) of SPM methods for the aerial image (S=10)

	PSA	Bilinear	Bicubic	Bilinear with MSI	Bicubic with MSI
Road	93.94	94.17	94.44	96.88	96.98
Tree	92.71	92.60	92.90	94.05	94.31
Building	87.79	86.45	87.12	89.86	90.34
Grass	91.46	90.96	91.35	93.28	93.58
PCC	91.01	90.44	90.87	92.96	93.27

3.2.3.2. Experiment 2

In this experiment, a hyperspectral image was studied. The image was acquired by the Reflective Optics System Imaging Spectrometer (ROSIS) sensor during a flight campaign over Pavia, northern Italy. It has a spatial resolution of 1.3 m with 102 bands. The tested region has 384 by 384 pixels and mainly covers six classes: shadow, water, road, tree, grass and roof. The false color image is shown in Figure 3.16(a). Figure 3.16(b) gives the reference land cover map of the 1.3 m hyperspectral image, which was obtained with the tensor discriminative locality alignment-based classifier in Zhang et al. (2013). A 10m spatial resolution image was created by degrading the original 1.3 m hyperspectral image band by band via an 8 by 8 mean filter. The fine spatial resolution land cover map in Figure 3.16(b) was used for both visual and quantitative assessment, which has an overall accuracy of 96.42% for 5343 test samples and provides a reliable reference data set.

Soft classification was implemented on the 10m coarse image first to obtain the fraction images. Fully constrained least squares linear spectral mixture analysis (Wang et al., 2013) was employed for soft classification, considering its simple physical meaning and convenience in application. The predicted fraction is compared to the reference fraction by means of the correlation coefficient (CC), as exhibited in Table 3.8. The reference fraction data were acquired by degrading Figure 3.16(b) with an 8 by 8 pixel mean filter. We can observe that the water, tree and roof classes have higher CC than the other three classes, suggesting that the soft classification of water, tree and roof is more accurate.

Table 3.8 CC of soft classification results for the degraded 10m ROSIS image

Shadow	Water	Road	Tree	Grass	Roof
0.7668	0.9617	0.8518	0.9426	0.8797	0.8854

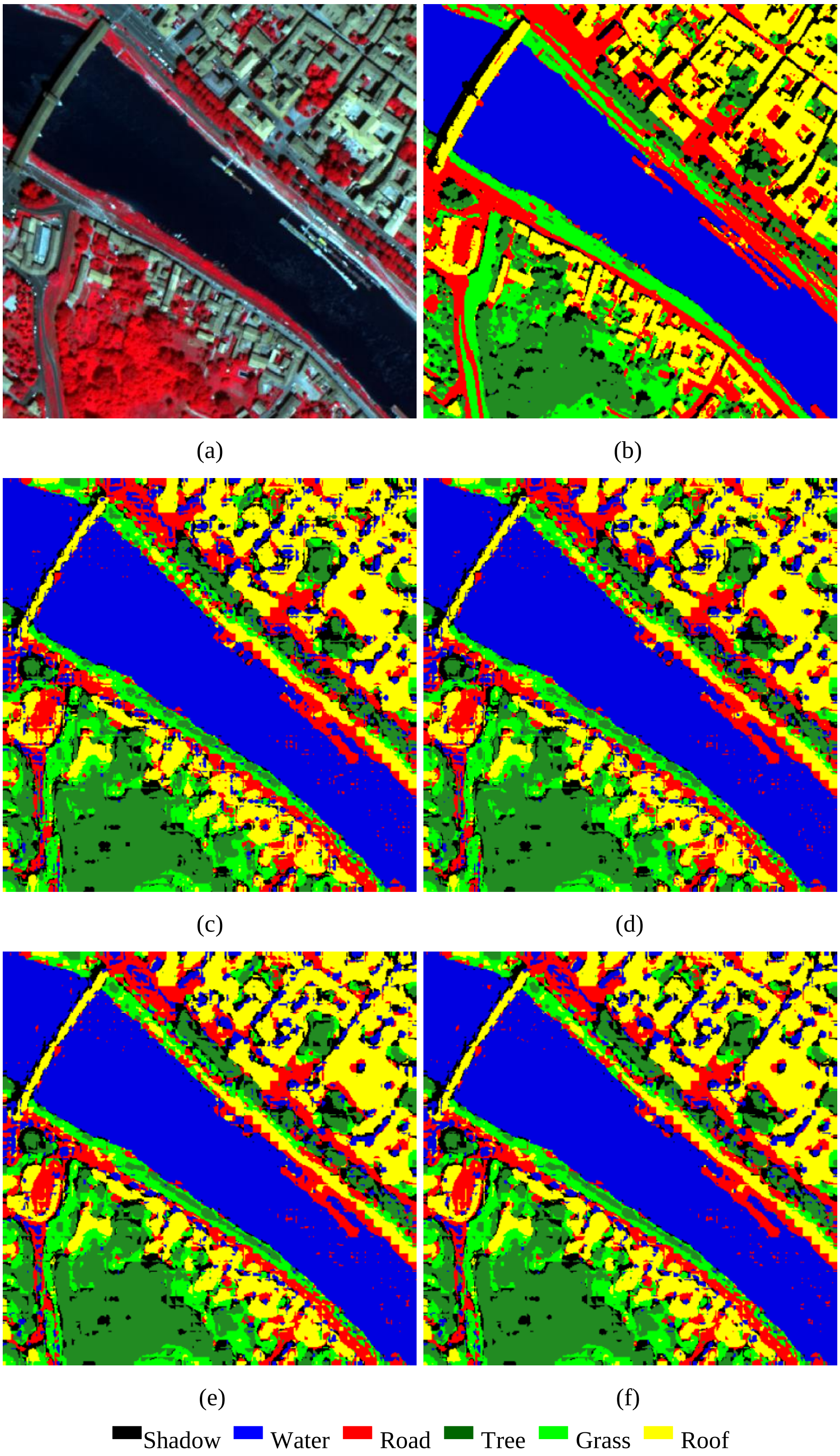

Figure 3.16. SPM results for the ROSIS image. (a) The three-band color image of the ROSIS hyperspectral dataset (bands 102, 56, and 31 as RGB). (b) The reference land cover map. (c) Bilinear result. (d) Bicubic result. (e) Bilinear with MSI result. (f) Bicubic with MSI result.

The bilinear, bicubic, bilinear with MSI and bicubic with MSI methods were applied to the predicted fraction images, with S=8, generating the 1.3m land cover maps shown in Figure 3.16(c)-Figure 3.16(f). It can be observed that many linear artefacts exist in the bilinear and bicubic results. Using MSI, the phenomenon is alleviated and the SPM results are more in agreement with the reference map in Figure 3.16(b). The SPM accuracy of the four methods as well as PSA is listed in Table 3.9. Due to the low soft classification accuracy of shadow, road and grass, as seen in Table 3.8, the SPM accuracy of these three classes is relatively lower in comparison with the other three classes. When compared to the SPM accuracy in the first experiment, the accuracy of all five methods is much lower in this experiment. This is attributed to the errors from soft classification as well as the more complex spatial pattern in the study area. Inter-comparison of the values in Table 3.9 reveals that with MSI, both bilinear and bicubic methods achieve higher SPM accuracy for all six classes than the PSA, bilinear and bicubic methods. The McNemar's test suggests that bilinear with MSI and bicubic with MSI methods have significantly higher PCC than the PSA, bilinear and bicubic methods.

Table 3.9 Accuracy (%) of SPM methods for the ROSIS image (S=8)

	PSA	Bilinear	Bicubic	Bilinear with MSI	Bicubic with MSI
Shadow	34.68	34.33	34.82	37.37	37.99
Water	96.22	96.28	96.32	96.45	96.52
Road	48.51	48.57	48.86	50.99	51.39
Tree	76.07	75.67	76.07	77.61	77.90
Grass	54.48	53.27	53.51	56.06	56.33
Roof	76.20	76.43	76.74	78.89	79.21
PCC	70.09	69.91	70.17	71.75	72.04

In experiment 1, the bilinear and bicubic methods took around 2 seconds while the proposed methods took less than 5 seconds. In experiment 2, the bilinear and bicubic methods took less than 4 seconds whereas the proposed methods took less than 8 seconds. For PSA running with 20 iterations, however, it took 90 and 138 seconds in experiment 1 and experiment 2.

3.2.3.3. Analysis of the number of MSI

The proposed SPM methods were tested with different numbers of MSI. We discussed four numbers: 2, 4, 6 and 9. The corresponding sub-pixel shifts are shown in Table 3.10. Note that when four images were discussed here, the sub-pixel shifts are different from those in the previous two experiments. The impact of the number of MSI can be seen in Figure 3.17. For both aerial and ROSIS images, when the number of MSI increases from 1 to 9, the PCC of both the bilinear and bicubic methods increases. Moreover, the bicubic method consistently obtains a higher PCC than the bilinear method.

Table 3.10 Sub-pixel shifts for discussion on the number of MSI

Number of images	Sub-pixel shifts
2	(0,0) (3,0)
4	(0,0) (3,0) (0,3) (3,3)
6	(0,0) (3,0) (6,0) (0,3) (3,3) (6,3)
9	(0,0) (3,0) (6,0) (0,3) (3,3) (6,3) (0,6) (3,6) (6,6)

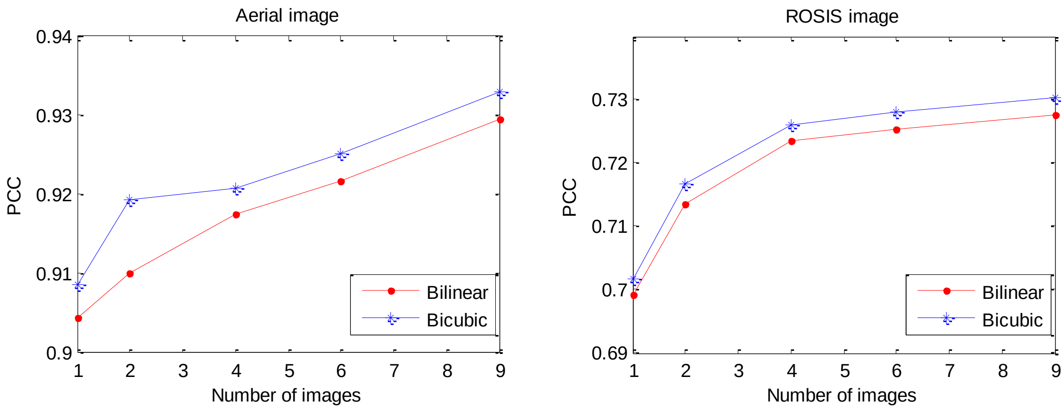

Figure 3.17. Influence of the number of sub-pixel shifted images for bilinear and bicubic interpolation-based SPM.

3.3. Summary

SPM is always an under-determined problem. In this chapter, MSI are used as additional data in STHSPM to enhance the accuracy of SPM. The MSI are sub-pixel shifted from each other, situation replicated by sensors taking images over the same area at different times.

In Section 3.1, an STHSPM algorithm based on ICK with MSI is proposed. The algorithm utilizes MSI to provide additional constraints for the ICK-based STHSPM model to increase the accuracy. In detail, with extracted prior structure information, the MSI are used to obtain multiple ICK-derived conditional probability maps for each class. Then according to the sub-pixels shifts of MSI, the multiple probabilities are integrated. The integrated probabilities are then used for class allocation to yield sub-pixel maps meeting a target spatial resolution. This new method inherits all the advantages of the ICK-based STHSPM model, which is capable of making use of prior spatial structure information and incorporating the information from the informed fine pixels. In addition, no parameters (except the neighborhood window size) and iterations are involved in the new model. Experiments based on three synthetic coarse images and a set of real MODIS images demonstrated the effectiveness and advantages of the proposed algorithm. From both visual and quantitative assessments, the conclusion can be drawn that the proposed ICK with MSI can produce more satisfying and accurate sub-pixel maps than conventional ICK as well as HNN-based SPM, whether or not MSI are applied in HNN.

The ICK method in Section 3.1 requires prior spatial structure information, which may be unavailable in practice. In Section 3.2, MSI are used in STHSPM that is achieved by fast and simple bilinear and bicubic interpolation. In contrast to the ICK method in Section 3.1, they do not need prior spatial structure information. Moreover, they are free of iteration and very fast. Two remote sensing images were tested in the experiments for validation of the proposed SPM methods. Both visual and quantitative assessment showed that the new methods can noticeably increase the accuracy of conventional bilinear and bicubic interpolation-based SPM. The SPM results of the new methods are visually more continuous and smoother than those obtained without MSI. The PCC of the new methods is significantly higher than that of conventional methods. Furthermore, the proposed SPM methods took only several seconds for the two studied images. The considerably low computational burden fully indicates the proposed methods are fast methods to utilize MSI in SPM. Therefore, the proposed methods show their great potential in real-time applications, particular in cases where prior spatial structure information is unavailable.

4. Radial basis function interpolation-based STHSPM

(This chapter is based on Wang *et al.* (2014a))

4.1. Introduction

The outputs of sub-pixel sharpening in the STHSPM algorithm are continuous values between 0 and 1, which indicate the probabilities of class occurrence at each sub-pixel. Actually, the task of sub-pixel sharpening can be viewed as downscaling the coarse spatial resolution proportion images to the target spatial resolution. This task can also be accomplished by super-resolution reconstruction when the proportion images are taken as input. It would be worth employing super-resolution reconstruction algorithms for the purpose of sub-pixel sharpening.

In this chapter, for the first time, a SPM algorithm based on radial basis function (RBF) interpolation is proposed. Interpolation-based super-resolution algorithms have been used widely for image downscaling. They can process a single coarse spatial resolution image by exploiting the spatial information encapsulated in the input image. As a powerful tool for modeling a non-linear function from given input-output data, RBFs have attracted considerable attention in many areas, such as neural networks (González et al., 2003), solution of differential equations (Pollandt, 1997), scattered data interpolation (Torres and Barba, 2009), and structure optimization (Wang et al., 2007). A detailed overview of RBFs and their applications can be found in Buhmann (2003). RBFs are known widely as a versatile tool for image interpolation (Magoules et al., 2007; Lee and Yoon, 2010). In RBF-based image interpolation, a system of equations is solved to obtain the RBF coefficients that characterize the input-output mapping (Fuji et al., 2012). The matrices described by the basis function are always uniquely solvable for most stencils in two-dimensional space (Lee and Yoon, 2010). RBF interpolation has been shown to be a highly accurate super-resolution reconstruction algorithm (Magoules et al., 2007; Lee and Yoon, 2010), both theoretically and practically, and has gained a wide range of successful applications, including medical image processing (Carr et al., 1997) and computer graphics (Carr et al., 2001). These properties and advantages of RBFs allow their application in SPM. In the proposed

RBF interpolation-based SPM, the coarse proportion images are used as input and soft class values at sub-pixels are estimated by RBF interpolation. Conditional upon the original class proportions constraint that fixes the number of sub-pixels allocated to each class per pixel, the estimated soft class values are then hardened to generate a hard classified land cover map at the sub-pixel scale.

The proposed RBF interpolation-based SPM belongs to the aforementioned STHSPM algorithm. Similar to SPSAM-, back-propagation neural network-, Kriging- and Indicator CoKriging-based SPM, the proposed algorithm is a non-iterative method, and the uncertainty introduced by random initialization and stochastic processes involved in the iterations of the first type of SPM can also be avoided. On the other hand, compared to back-propagation neural network- and Indicator CoKriging-based SPM, the proposed SPM algorithm has the advantage of not relying on any prior model of land cover spatial structure. The RBF interpolation-based SPM is performed by exploiting fully the spatial information in the input proportion images.

4.2. The SPM problem

The SPM approach in this chapter represents a post-processing step following soft classification. In SPM, each mixed pixel is divided into multiple sub-pixels and then their class labels are predicted. The coarse proportion data and the zoom factor are used to calculate the number of sub-pixels for each class. The details are given below.

4.2.1. Calculation of the number of sub-pixels for each class

Suppose S is the zoom factor (i.e., each coarse pixel is divided into $S \times S$ sub-pixels), P_j ($j = 1, 2, ..., M$, M is the number of pixels in the coarse image) is a coarse pixel and $F_k(P_j)$ is the coarse proportion of the k-th ($k = 1, 2, ..., K$, K is the number of classes) class for pixel P_j. Considering the physical meaning, the coarse proportions estimated by soft classification (e.g., spectral unmixing (Bioucas-Dias et al., 2012)) usually meet the abundance sum-to-one constraint and the abundance non-negativity constraint, i.e.,

$$\begin{aligned} & \sum_{k=1}^{K} F_k(P_j) = 1, \quad j = 1, 2, ..., M \\ & F_k(P_j) \geq 0, \quad k = 1, 2, ..., K; \; j = 1, 2, ..., M \end{aligned} \tag{4.1}$$

For a particular pixel, say P_j, the number of sub-pixels for the k-th class, $E_k(P_j)$, is calculated by

$$E_k(P_j) = \text{round}(F_k(P_j)S^2) \tag{4.2}$$

where round(•) is a function that takes the integer nearest to •. The sum of the numbers of sub-pixels for all K classes are S^2.

4.2.2. Prediction of class labels for sub-pixels

Let p_i (i=1,2,...,MS^2) be a sub-pixel and $B_k(p_i)$ be the binary class indicator for the k-th class at sub-pixel p_i

$$B_k(p_i) = \begin{cases} 1, \text{ if sub-pixel } p_i \text{ belongs to class } k \\ 0, \text{ otherwise} \end{cases} \tag{4.3}$$

In the SPM result, each sub-pixel should be assigned to only one class and the number of sub-pixels for each class should be consistent with the coarse proportion data, which are described as

$$\begin{aligned} &\sum_{k=1}^{K} B_k(p_{j,i}) = 1, \quad i = 1,2,...,S^2;\ j = 1,2,...,M \\ &\sum_{i=1}^{S^2} B_k(p_{j,i}) = E_k(P_j), \quad k = 1,2,...,K;\ j = 1,2,...,M \end{aligned} \tag{4.4}$$

where sub-pixel $p_{j,i}$ falls within coarse pixel P_j.

The critical task of SPM is to obtain the binary class indicators for all classes at each sub-pixel. In this chapter they are predicted according to the soft class values at each sub-pixel estimated by RBF interpolation. The principle is introduced in the following Section 4.3.

4.3. RBF interpolation-based SPM

4.3.1. Estimation of soft class values at the sub-pixel scale using RBF interpolation

The RBF interpolation discussed in this chapter involves area-to-point prediction (Atkinson, 2013), which refers to the super-resolution of continua (proportion images in this chapter) though interpolation and is different from the common interpolation task of predicting between sparsely distributed points (Buhmann, 2003). In area-to-point prediction, the input variable (at a coarse resolution) is the same as the output variable (at a fine resolution) and both are generally continuous variables (Atkinson, 2013).

Let $F_k(p_i)$ be the soft class value for the k-th class at sub-pixel p_i. The task of RBF interpolation is to predict $\left\{F_k(p_i)\middle| i=1,2,...,MS^2; k=1,2,...,K\right\}$ at the target fine spatial resolution. The variables in Section 4.3 that have been mentioned in Section 4.2 have the same meaning as in Section 4.2.

In RBF interpolation, the soft class value $F_k(p_i)$ is predicted by

$$F_k(p_i) = \sum_{n=1}^{N} \lambda_k(P_n)\phi(P_n, p_i) \tag{4.5}$$

where N is the number of observed coarse pixels that are usually in a local window, $\lambda_k(P_n)$ is the coefficient of the k-th class for coarse pixel P_n, and $\phi(P_n, p_i)$ is a basis function that describes the spatial relation between sub-pixel p_i and coarse pixel P_n. The estimated soft class value is a weighted linear combination of N values calculated by the basis function. Correspondingly, two terms are needed for RBF interpolation: basis function values and their coefficients.

1) Basis function values. Suppose $d(P_n, p_i)$ is the Euclidean distance between the geometric centers of pixel P_n and sub-pixel p_i. A commonly used basis function in RBF interpolation is the Gaussian function (Lee and Yoon, 2010)

$$\phi(P_n, p_i) = e^{-d^2(P_n, p_i)/a^2} \tag{4.6}$$

in which a is a parameter. The larger the distance, the smaller the basis function value (i.e., the weaker the spatial relation). An example is provided in Figure 4.1 to illustrate the calculation of $d(P_n, p_i)$. Suppose there are N observed coarse pixels in a $N_0 \times N_0$ (N_0=3 in Figure 4.1) local window and each coarse pixel is divided into S by S sub-pixels (S=4 in Figure 4.1); coarse pixel P_n is in the R_n-th row and C_n-th $(R_n, C_n = 1, 2, ..., N_0)$ column in the local window; sub-pixel p_i is in the r_i-th row and c_i-th $(r_i, c_i = 1, 2, ..., S)$ column in the coarse pixel that it falls within. The coordinates of P_n and p_i, denoted as (X_n, Y_n) and (x_i, y_i), are calculated as

$$\begin{aligned} X_n &= (R_n - 0.5)S \\ Y_n &= (C_n - 0.5)S \\ x_i &= 0.5(N_0 - 1)S + r_i - 0.5 \\ y_i &= 0.5(N_0 - 1)S + c_i - 0.5 \end{aligned} \tag{4.7}$$

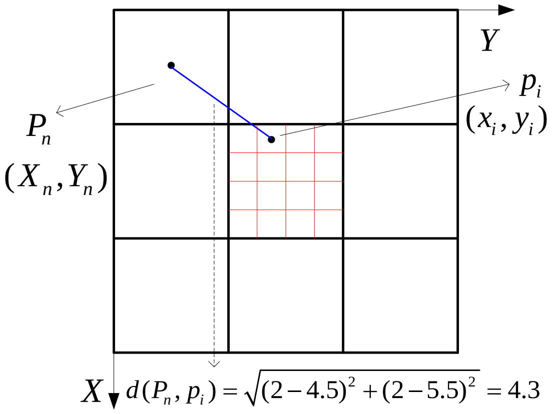

Figure 4.1. Illustration of distance calculation between pixel P_n and sub-pixel p_i.

The distance between them is

$$d(P_n, p_i) = \sqrt{(X_n - x_i)^2 + (Y_n - y_i)^2} \tag{4.8}$$

2) Coefficients. With respect to the coefficient $\lambda_k(P_n)$, it indicates the contribution from neighboring coarse pixel P_n. The coefficients are determined by exploiting the available information in the input proportion images. For each observed coarse pixel P_j, (4.9) holds

$$F_k(P_j) = \sum_{n=1}^{N} \lambda_k(P_n)\phi(P_n, P_j), \;\; j = 1, 2, ..., N \tag{4.9}$$

where $\phi(P_n, P_j)$ is the quantified spatial relation between pixel P_n and pixel P_j. It is calculated in the same way as that in (4.6). Combining all N equations, we can compute the coefficient sets $\boldsymbol{\lambda_k} = [\lambda_k(P_1), \lambda_k(P_2), ...\lambda_k(P_N)]^{\mathrm{T}}$ by solving the following equation

$$\boldsymbol{\Phi\lambda_k} = \boldsymbol{F_k} \tag{4.10}$$

in which

$$\boldsymbol{F_k} = [F_k(P_1), F_k(P_2), ...F_k(P_N)]^{\mathrm{T}} \tag{4.11}$$

The superscript T denotes a matrix transposition, and

$$\boldsymbol{\Phi} = \begin{bmatrix} \phi(P_1, P_1) & \phi(P_2, P_1) & ... & \phi(P_N, P_1) \\ \phi(P_1, P_2) & \phi(P_2, P_2) & ... & \phi(P_N, P_2) \\ ... & ... & ... & ... \\ \phi(P_1, P_N) & \phi(P_2, P_N) & ... & \phi(P_N, P_N) \end{bmatrix} \tag{4.12}$$

As can be seen from (4.12), $\boldsymbol{\Phi}$ is a matrix with $N \times N$ elements and the computing complexity in (4.10) scales quadratically with N. Moreover, for each mixed pixel, (4.10) is computed once and hence in the whole image the computation time of (4.10) is equal to the number of mixed pixels, which is always very large. Last but not least, the spatial dependence decreases when the distance between pixels increases. For these reasons, it is unrealistic to use a large number of observed coarse pixels in RBF interpolation-based SPM, and a neighborhood window is used for each sub-pixel.

The soft class value prediction in RBF interpolation is different from that in the existing SPSAM-based SPM method. More precisely, in the latter, the soft class value is a weighted linear combination of the class proportions in neighboring coarse pixels, and the weights are quantified straightforwardly by the distances. In RBF interpolation, however, the soft class value is a weighted linear combination of the basis function values. The weights in RBF interpolation (i.e., coefficient sets $\boldsymbol{\lambda_k}$) are calculated by using not only proportions in neighboring coarse pixels, but also the available information about spatial dependence in the neighborhood window: When calculating the coefficients, the spatial autocorrelation between coarse pixels in the neighborhood window is accounted for, as can be found from (4.10) and (4.12). This is the unique advantage of RBF interpolation.

The pseudocode of RBF interpolation is given below, where $p_{j,i}$ denotes any sub-pixel that falls within coarse pixel P_j.

RBF interpolation for prediction of soft class values at the sub-pixel scale

Inputs: $\{F_k(P_j) \mid j=1,2,...,M; k=1,2,...,K\}$ and *S*.

```
for k = 1: K
    for j = 1: M
        Select a neighborhood window with N coarse pixels
        Computation of coefficient vector λk using (4.10)
        for i = 1: S^2
            Calculation of N basis function values using (4.6)
            Estimation of Fk(pj,i) using (4.5)
        end
    end
end
```

Outputs: $\{F_k(p_{j,i}) \mid i=1,...,S^2; j=1,...,M; k=1,...,K\}$.

4.3.2. Estimation of hard class values at the sub-pixel scale by class allocation

SPM is essentially an algorithm for hard classification at the sub-pixel scale and its outputs are hard attribute values. After the $\{F_k(p_i) | i=1,2,...,MS^2; k=1,2,...,K\}$ are estimated by RBF interpolation, with the constraints in (4.4), they are used to predict hard class labels $\{B_k(p_i) | i=1,2,...,MS^2; k=1,2,...,K\}$, as defined in (4.3). In this chapter, classes are allocated to sub-pixels class-by-class, using a UOC-based class allocation method.

The flowchart of the proposed SPM method is shown in Figure 4.2.

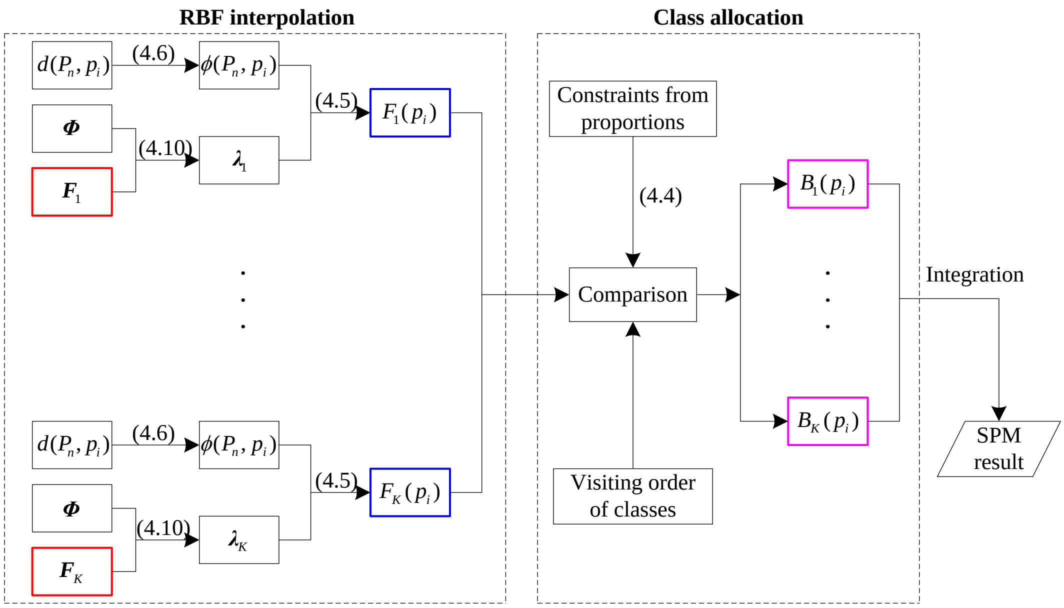

Figure 4.2. Flowchart of the proposed RBF interpolation-based SPM.

4.4. Experiments

4.4.1. Experimental setup

Three experiments were carried out for validation of the proposed RBF interpolation-based SPM method. The proposed method was compared to SPSAM and Kriging-based SPM methods in the experiments. The other two STHSPM algorithms, back-propagation neural network and Indicator CoKriging, were not compared in experiments because they need prior spatial structure information. As suggested by the principle of the proposed SPM method, other image interpolation methods are also expected to have potential in SPM. Hence, two well-known image interpolation algorithms, bilinear and bicubic, were also applied to SPM for comparison with the RBF interpolation-based SPM method. Specifically, bilinear and bicubic interpolation were used to predict the soft class values at each sub-pixel, and then UOC-based class allocation method was employed for hard class value prediction. In total, five SPM methods were tested: bilinear-, bicubic-, SPSAM-, Kriging- and RBF-based SPM algorithms. The accuracy of SPM was evaluated quantitatively by the overall accuracy in terms of the percentage of correctly classified pixels (PCC). For the proposed SPM method, the parameter a in the basis function was set to 10 and the window size N was set to 5. All experiments were run on an Intel Core 2 Processor (1.800-GHz Duo central processing unit, 2.00-GB random access memory) with MATLAB 7.1 version.

In the first experiment, three synthetic coarse spatial resolution images were used for testing, to avoid the errors from soft classification and solely concentrate on the performance of the proposed SPM method. More specifically, land cover maps were obtained by hard classification of the remote sensing images and these maps were used as reference. The reference maps were then degraded by an S by S mean filter (i.e., every S by S fine pixels were degraded to a coarse pixel) to generate the coarse proportion images. Finally, SPM methods were implemented to yield land cover maps with the same spatial resolution as the reference maps, by zooming in the proportion images with a scale factor S. Using synthetic coarse images, the input proportions contain no uncertainty and the reference land cover maps are completely reliable for accuracy assessment.

In the second experiment, a hyperspectral image in the first experiment was degraded band by band with two scales to generate two coarse spatial resolution hyperspectral images. Soft classification was then performed to yield proportion images and SPM methods were implemented subsequently. Similarly to the first experiment, the hard classification result of the fine spatial resolution hyperspectral image was used as reference for SPM evaluation. This experiment was used to consider the inherent uncertainty in soft classification (Atkinson, 2009).

In the last experiment, the five SPM methods were tested with multiple zoom factors, in order to further validate the effectiveness and advantages of the proposed SPM method and also test the influence of S on its performance. Moreover, the influence of parameter a in the basis function (4.6) and window size N were tested for the proposed SPM method.

4.4.2. Data description

Three images were used in the experiments in all, including an aerial image and two hyperspectral images. Detailed information on the three datasets is now provided.

The Aerial image. An aerial image in Tatem (2002) was used for testing. The image covers an area in the city of Bristol, UK and for the purposes of this experiment can be considered to contain five land cover classes: grass, road, river, soil and tree. The image has 170 by 170 pixels with a pixel size of 4 m by 4 m. Figure 4.3(a) shows the image while Figure 4.3(b) shows the reference land cover map. The land cover pattern in Figure 4.3(b) is relatively simple and the five classes appear mainly as large objects.

The Reflective Optics System Imaging Spectrometer (ROSIS) dataset. This dataset was acquired by the ROSIS sensor during a flight campaign over Pavia, northern Italy. The hyperspectral image has a spatial resolution of 1.3 m and 102 bands. A region with 400 by 400 pixels was studied, which covers six classes of interest: shadow, water, road, tree, grass and roof. The three-band color image (bands 102, 56, and 31 for RGB) is shown in Figure 4.4(a). The corresponding reference land cover map is shown in Figure 4.4(b), which was obtained with the tensor discriminative locality alignment-based classification of the hyperspectral data in Zhang et al. (2013).

The QuickBird dataset. The 0.61 m QuickBird image covers an area of the suburb of Xuzhou City, China, containing 480 by 480 pixels and three multispectral bands (RGB). The image was classified with an algorithm that first integrated spatial features of pixel shape feature set, grey level co-occurrence matrix and Gabor transform with spectral information and then used a support vector machine for classification. The generated land cover map contains seven classes: shadow, water, road, tree, grass, roof and bare soil. Figure 4.5(a) shows the RGB image and Figure 4.5(b) shows the hard classified land cover map. Through visual comparison, one can find that the land cover patterns in Figure 4.4(b) and Figure 4.5(b) are more complex than those in Figure 4.3(b).

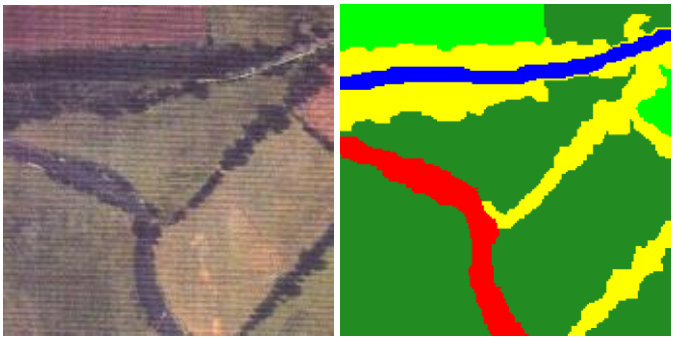

(a) (b)

Grass Road River Soil Tree

Figure 4.3. (a) The aerial image. (b) The reference land cover map.

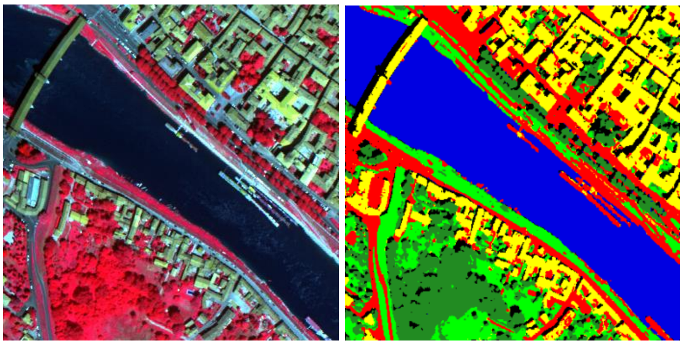

(a) (b)

Shadow Water Road Tree Grass Roof

Figure 4.4. (a) The three-band color image of the ROSIS hyperspectral dataset. (b) The reference land cover map.

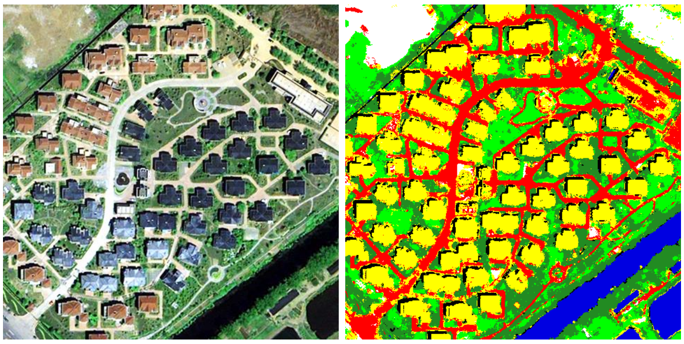

(a) (b)

Shadow Water Road Tree Grass Roof Bare soil

Figure 4.5. (a) The QuickBird image. (b) The reference land cover map.

4.4.3. Experiment 1-Synthetic coarse images

The three maps in Figure 4.3(b), Figure 4.4(b) and Figure 4.5(b) were degraded with an 8 by 8 mean filter. Figure 4.6 shows the produced proportion images. The sizes of the coarse spatial resolution images in the three lines for the three corresponding maps are 21 by 21, 50 by 50 and 60 by 60. As can be seen from the proportion images, the boundaries of classes are blurred, which necessitates SPM techniques. For SPM of the three coarse images in this experiment, the zoom factor was set to S=8 to restore the fine spatial resolution images. The five SPM methods (i.e., bilinear, bicubic, SPSAM, Kriging and RBF-based SPM) were applied to the three groups of coarse proportion images. Table 4.1 gives the Moran's I estimated from the class proportion images and the specified visiting order of classes for class allocation process.

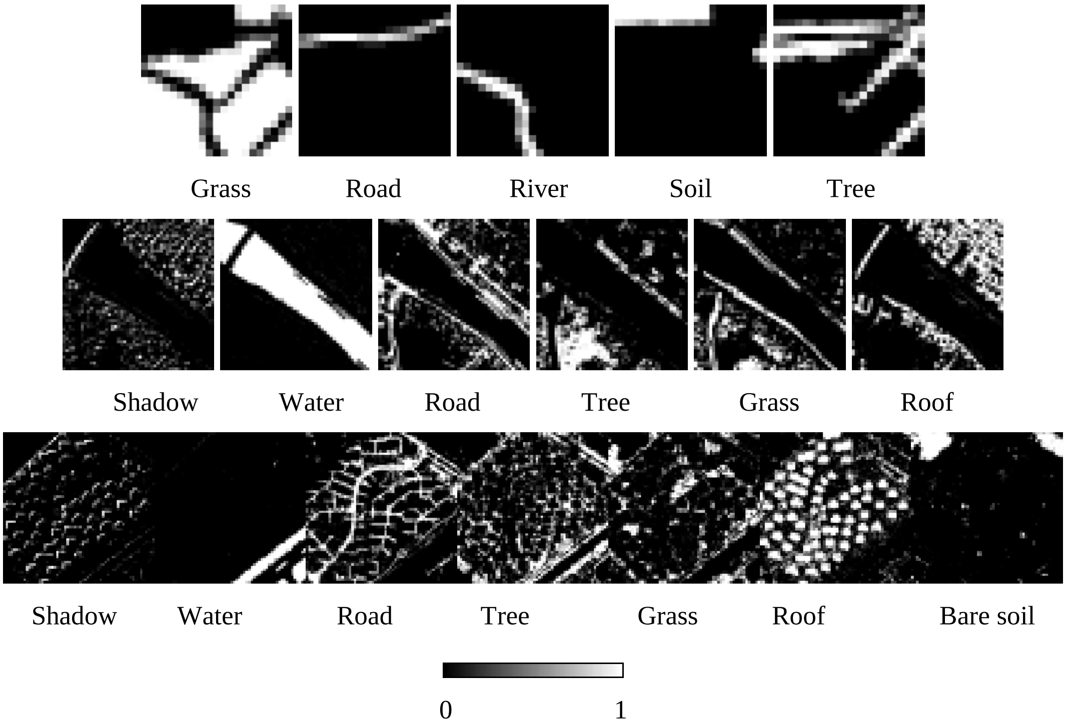

Figure 4.6. Proportion images of the classes in the degraded land cover maps of three images. Line 1: Aerial image; Line 2: ROSIS image; Line 3: QuickBird image.

Table 4.1 Visiting order of classes for class allocation

Aerial image	Class	Grass	Road	River	Soil	Trees		
	Moran's I	0.7181	0.3244	0.6083	0.8042	0.5033		
	Order	2	5	3	1	4		
ROSIS image	Class	Shadow	Water	Road	Tree	Grass	Roof	
	Moran's I	0.3087	0.9212	0.5706	0.7427	0.5540	0.6449	
	Order	6	1	4	2	5	3	
QuickBird image	Class	Shadow	Water	Road	Tree	Grass	Roof	Bare soil
	Moran's I	0.2540	0.8505	0.4725	0.4728	0.5829	0.6044	0.8908
	Order	7	2	6	5	4	3	1

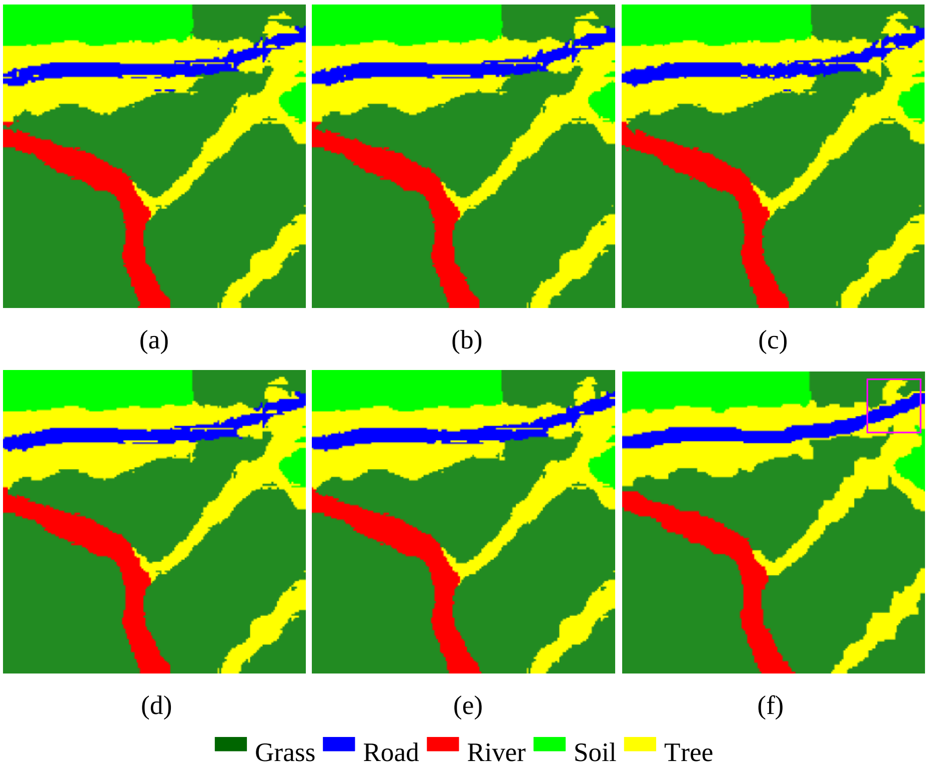

Figure 4.7. SPM results of the five methods for the degraded land cover map of the aerial image (S=8). (a) Bilinear. (b) Bicubic. (c) SPSAM. (d) Kriging. (e) RBF. (f) Reference with marked area.

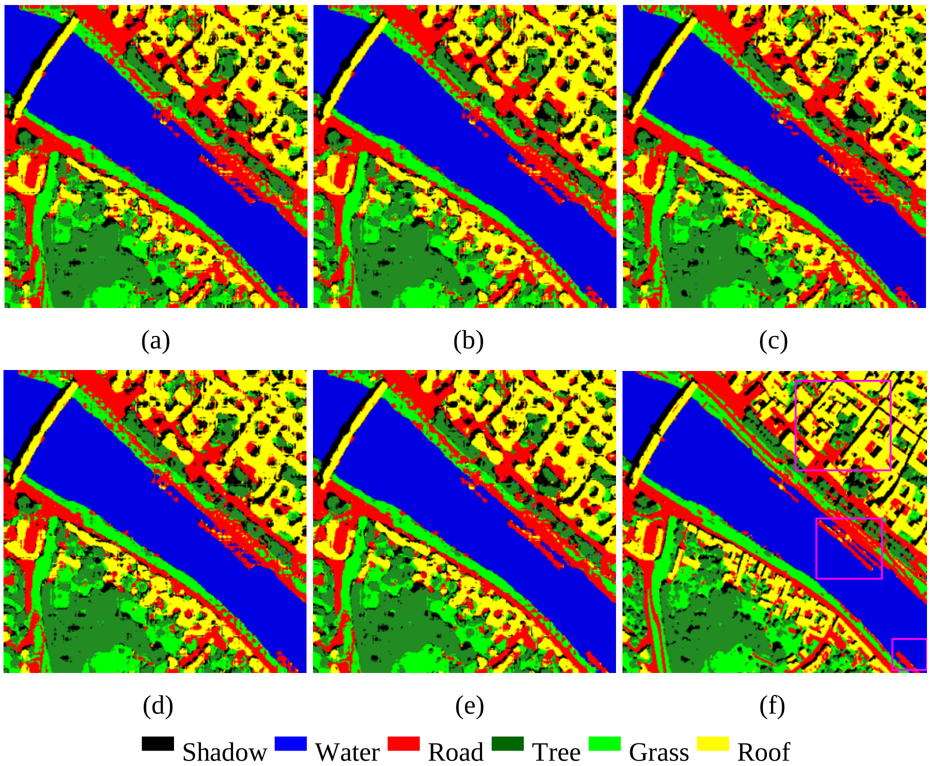

Figure 4.8. SPM results of the five methods for the degraded land cover map of the ROSIS image (S=8). (a) Bilinear. (b) Bicubic. (c) SPSAM. (d) Kriging. (e) RBF. (f) Reference with marked areas.

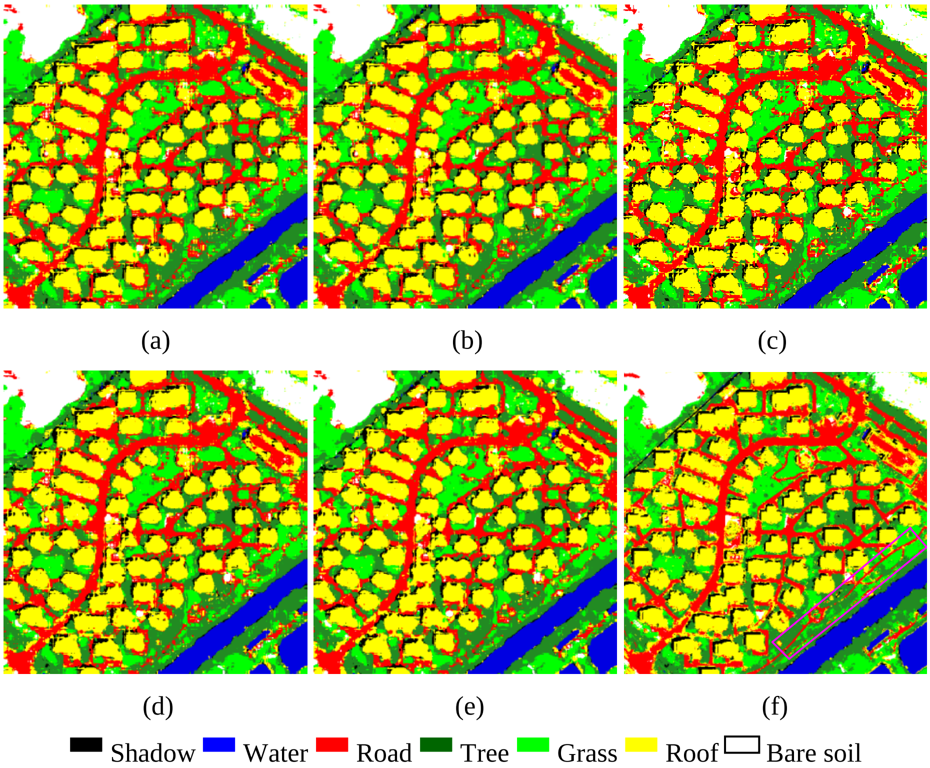

Figure 4.9. SPM results of the five methods for the degraded land cover map of the QuickBird image (S=8). (a) Bilinear. (b) Bicubic. (c) SPSAM. (d) Kriging. (e) RBF. (f) Reference with marked area.

Figure 4.7-Figure 4.9 display the SPM results for three images. Visual comparison of the five SPM results in each group in Figure 4.7-Figure 4.9 reveals that the proposed method can be usefully applied to the SPM of coarse images. Furthermore, the proposed method provides the most satisfactory SPM results among the five methods. Specifically, with respect to the results in Figure 4.7(a)-(e) for the aerial image, the boundaries of classes are the smoothest in Figure 4.7(e), and it is the closest to the reference map in Figure 4.3(b). As an example, the boundaries of the road and tree classes in the top right of the image (marked by the pink rectangle in Figure 4.7(f)) in the bilinear, bicubic and Kriging results are quite rough. For the SPSAM method, the restoration of the tree class in the same site is more satisfactory when compared to the bilinear, bicubic and Kriging methods, but still less acceptable than that of the proposed method. While examining Figure 4.8(a)-(d) for the ROSIS image, one can see that there are many linear artifacts and the spatial continuity of each class is weak, especially in the bilinear and SPSAM results. Using the proposed SPM method, however, the predicted map in Figure 4.8(e) has less linear artifacts and the distribution of classes is more continuous. This is particularly well illustrated by the results of mapping the roof and road classes (see the areas marked by the pink rectangles in Figure 4.8(f)). Consistent

with the results for the aerial and ROSIS images, for the QuickBird image, RBF result in Figure 4.9(e) is found to have more continuous boundaries of classes than the other four maps in Figure 4.9(a)-Figure 4.9(d).

Tables 4.2-4.4 list the classification accuracies of each class as well as the overall accuracy in terms of PCC for the SPM results of the three coarse images. To illustrate the gain of using SPM technique for land cover mapping, traditional pixel-level hard classification (HC) was performed, in which all sub-pixels within a coarse pixel are assigned to the dominated class. Note that the pure coarse pixels in Figure 4.6 were not considered in the accuracy statistics. Comparison of the PCC values of HC and the five SPM methods in Tables 4.2-4.4 reveals that SPM can produce obviously greater accuracy than HC method. For the aerial image, the accuracy gain of SPM over HC is around 15% and for the other two images, the gain is around 5%. As can be seen from Table 4.2, the Kriging method provides the greatest accuracy of classification for the river class. For the other four classes, the classification accuracy in the RBF result is the highest among the five SPM methods. The PCC of the RBF result reaches 92.63%, which is also higher than that of the other four SPM methods. In Table 4.3, the proposed RBF interpolation-based method achieves the greatest accuracy for all six classes in the ROSIS image. For example, the classification accuracy of the road class in the RBF result is 74.64%, which is 2.43%, 1.72%, 1.54% and 1.18% more than for the bilinear, bicubic, SPSAM and Kriging results; the classification accuracy of the roof class in the RBF result is 81.91%, which is greater by 1.53%, 1.04%, 1.15% and 0.86%, respectively. The high accuracy for the proposed method may be attributed mainly to the fact that the predicted map has fewer linear artifacts and a more continuous distribution of classes, as mentioned in the above visual inspection for Figure 4.8. Regarding the overall accuracy, the PCC of the proposed method is 74.89%, with gains of 1.99%, 1.34%, 1.55% and 1.03% over the bilinear, bicubic, SPSAM and Kriging methods. Focusing on Table 4.4, for the proposed method based on RBF interpolation, the classification of the roof class is less accurate than for the bicubic method, but the classification of the other six classes is the most accurate among the five SPM methods and the overall accuracy of the RBF method is the highest. More precisely, the SPSAM method has the lowest PCC, 71.88%, among the five SPM methods. For another three methods, bilinear, bicubic and Kriging, the PCC increased to 72.10%, 72.67% and 72.38%. However, their accuracies were still lower than that of the RBF method which produced a PCC of 73.24%.

Table 4.2 Accuracy (%) of the HC and five SPM methods for the aerial image

	HC	Bilinear	Bicubic	SPSAM	Kriging	RBF
Grass	76.59	92.69	92.86	92.83	93.12	**93.27**
Road	81.39	86.55	88.93	88.36	88.74	**91.13**
River	80.74	95.75	95.75	95.82	**96.10**	95.89
Soil	83.29	91.97	91.97	92.50	92.50	**92.89**
Trees	72.13	89.68	90.43	90.15	90.48	**91.23**
PCC	76.33	91.36	91.91	91.79	92.08	**92.63**

Table 4.3 Accuracy (%) of the HC and five SPM methods for the ROSIS image

	HC	Bilinear	Bicubic	SPSAM	Kriging	RBF
Shadow	38.77	55.17	56.06	55.18	56.08	**57.90**
Water	74.76	86.14	86.11	86.24	86.46	**87.29**
Road	67.99	72.21	72.92	73.10	73.46	**74.64**
Tree	75.12	74.52	75.19	74.46	75.35	**75.92**
Grass	65.75	70.19	71.01	71.01	71.56	**72.52**
Roof	80.79	80.38	80.87	80.76	81.05	**81.91**
PCC	68.51	72.90	73.55	73.34	73.86	**74.89**

Table 4.4 Accuracy (%) of the HC and five SPM methods for the QuickBird image

	HC	Bilinear	Bicubic	SPSAM	Kriging	RBF
Shadow	33.18	51.67	52.51	50.92	51.80	**53.34**
Water	83.80	91.23	91.46	91.04	90.93	**91.62**
Road	73.46	74.19	74.88	74.24	74.77	**75.81**
Tree	67.99	71.99	72.79	71.93	72.54	**73.52**
Grass	64.36	70.74	71.22	70.76	71.33	**72.04**
Roof	68.55	73.67	**73.93**	72.79	73.25	73.81
Bare soil	71.09	76.55	77.11	78.17	77.28	**78.04**
PCC	67.16	72.10	72.67	71.88	72.38	**73.24**

4.4.4. Experiment 2-Degraded hyperspectral images

In this experiment, the ROSIS hyperspectral image used in the first experiment was degraded band by band with *S*=4 and 8. In this way, two coarse hyperspectral images with spatial resolutions of 5 m and 10 m were produced. Prior to SPM, soft classification was essential to obtain the proportions of land cover classes within coarse pixels. Here, linear spectral mixture analysis (LSMA) (Heinz and Chang, 2001) was employed for soft classification, appreciating its simple physical meaning and its convenience in application (Wang and Wang, 2013). The generated proportion images for six classes at *S*=8 are shown in Figure 4.10. Figure 4.11(a)-(e) displays SPM results of the five methods for these coarse proportion images. The reference map in Figure 4.4(b) was used for both visual and quantitative assessment of the five SPM methods, which has an overall accuracy of 96.42% and hence provides a useful reference data set.

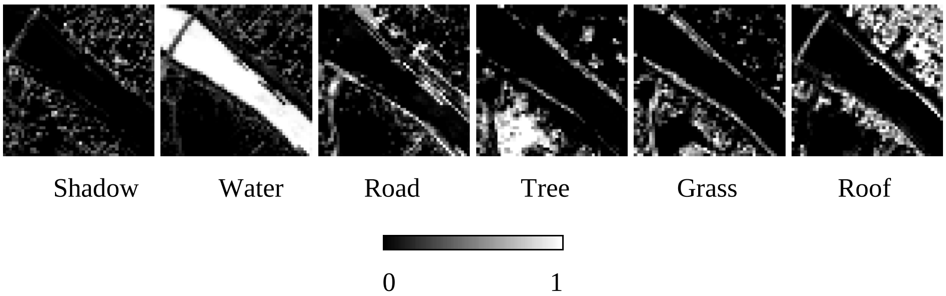

Figure 4.10. Proportion images of the 6 classes in the degraded ROSIS hyperspectral image.

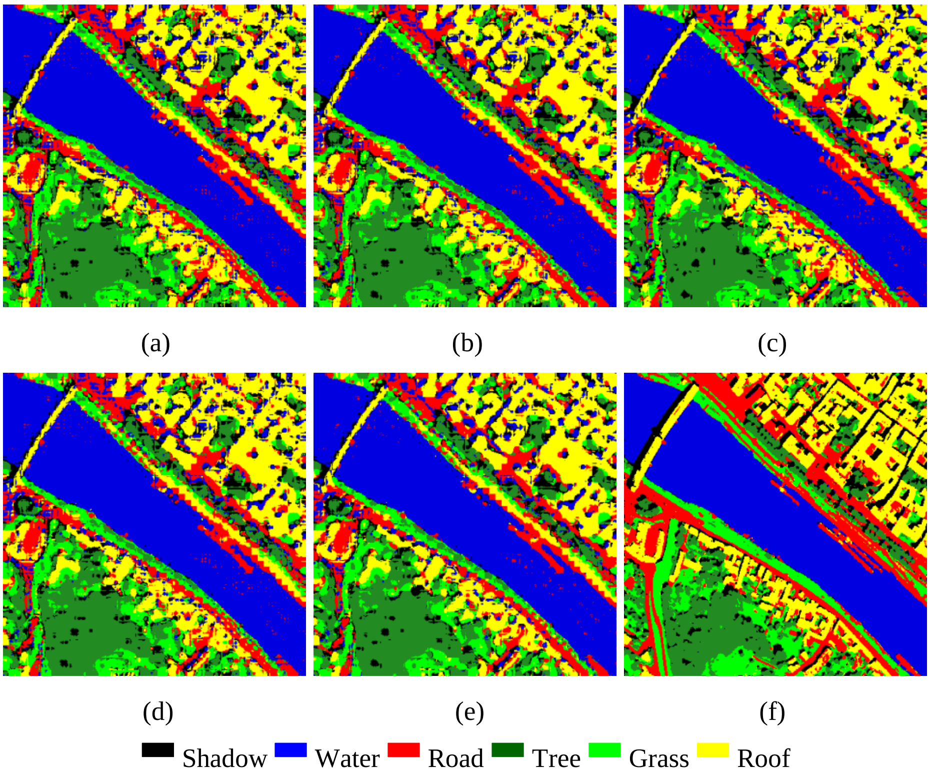

Figure 4.11. SPM results of the five methods for the degraded ROSIS hyperspectral image (S=8). (a) Bilinear. (b) Bicubic. (c) SPSAM. (d) Kriging. (e) RBF. (f) Reference.

It is worth noting that some scattering of pixels exists in the resulting maps (Figure 4.11). For example, some pixels that should belong to the water class were classified as the road class. The reason for this phenomenon is that there were inherent errors in the outputs of LSMA and they were propagated to the SPM results (Ge, 2013). Similar to the results in the first experiment, the distribution of land cover classes in Figure 4.11(e) is the closest to that in the reference map in Figure

4.11(f). As an instance, at the right bottom in Figure 4.11(a)-Figure 4.11(d), some pixels near the water class should be of the road class, but were misclassified as the roof class. In the RBF result, however, these pixels were almost always correctly classified and the road class within it seems more continuous than in the other four resulting maps.

The quantitative assessment results for both *S*=4 and *S*=8 are listed in Table 4.5. Note that in this experiment all coarse pixels in Figure 4.10 were included in the accuracy statistics, because errors in soft classification need to be considered. One can observe from the table that the bilinear method provides the lowest accuracy at both scales. Although bicubic and SPSAM methods can produce a more accurate SPM than the bilinear method, the PCC of them is still less than that of the Kriging method. For the proposed RBF method, it is able to achieve the highest accuracy for each class in nearly all cases. As for the overall accuracy, the RBF obtains a PCC of 75.08% at *S*=4 and 70.45% at *S*=8, both of which are the highest among the five methods.

Table 4.5 Accuracy (%) of the five SPM methods for the degraded ROSIS hyperspectral images

		Bilinear	Bicubic	SPSAM	Kriging	RBF
S=4	Shadow	49.46	49.75	50.15	50.21	**50.86**
	Water	97.72	97.74	97.66	97.74	**97.79**
	Road	51.96	52.37	52.70	52.91	**53.23**
	Tree	82.33	82.50	82.33	82.54	**82.62**
	Grass	58.21	58.45	59.10	59.04	**59.13**
	Roof	81.35	81.54	81.28	81.35	**81.68**
	PCC	74.48	74.67	74.76	74.86	**75.08**
S=8	Shadow	33.59	34.08	34.10	34.49	**35.18**
	Water	96.18	96.21	96.11	96.20	**96.29**
	Road	49.41	49.64	49.50	49.83	**50.11**
	Tree	75.45	75.87	75.89	76.14	**76.44**
	Grass	54.71	54.87	55.62	**55.68**	55.56
	Roof	76.66	76.90	76.46	76.63	**77.20**
	PCC	69.80	70.02	69.99	70.18	**70.45**

4.4.5. Experiment 3-Influences of parameter in the basis function, zoom factor and window size

1) Influence of zoom factor. The five SPM methods were tested with different zoom scale factors using three groups of synthetic coarse images. The coarse images were produced by degrading the maps in Figure 4.3(b), Figure 4.4(b) and Figure 4.5(b) with four different scales. In detail, the reference map in Figure 4.3(b) was degraded with S=5, 8, 10 and 15 while the reference maps in Figure 4.4(b) and Figure 4.5(b) were both degraded with S=4, 6, 8 and 12. Figure 4.12(a)-(c) exhibits the PCC (pure pixels were excluded for accuracy statistics) of the five SPM methods for three groups of coarse images. It is worth noting that as the scale increases, the accuracy of all five methods decreases. Precisely, the PCC of the five methods decreases by about 10% from S=5 to S=15 for the aerial image, 15% from S=4 to S=12 for the ROSIS image and 10% from S=4 to S=12 for the QuickBird image.

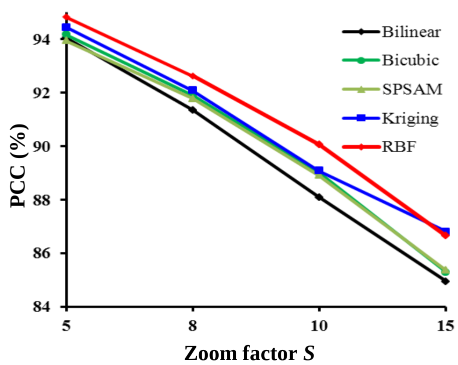

(a)

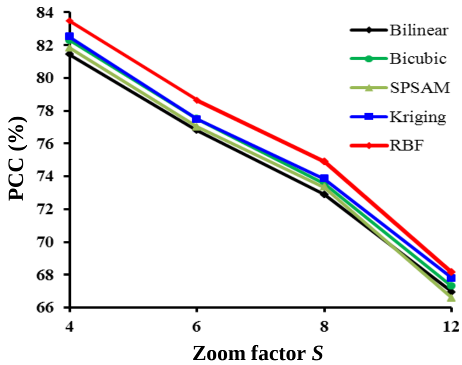

(b)

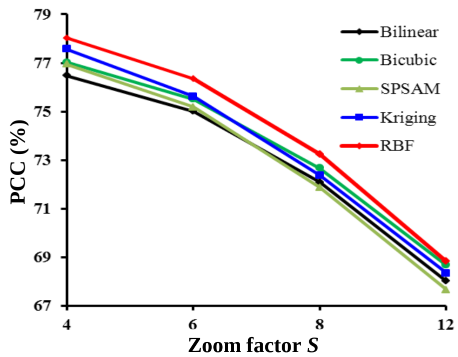

(c)

Figure 4.12. Performance of the five SPM methods with four different zoom factors. (a) Aerial image. (b) ROSIS image. (c) QuickBird image.

Table 4.6 summarizes the comparison of SPM accuracy between the five methods in Figure 4.12. From the results for all 12 cases in the table, we can see that the SPSAM and bilinear methods are competent in SPM in general. As for the bicubic method, it outperforms both the SPSAM and bilinear methods. While comparing the bicubic and Kriging methods, one can observe that the latter tends to provide more accurate SPM results. Focusing on the values in the last column, the proposed RBF method is found to be superior to the other four SPM methods in nearly all cases.

Table 4.6 Comparison between the five SPM methods for the three groups of images with four zoom factors (12 cases in all; A vs B: + means the PCC of A is higher while – means the PCC of A is smaller)

	Bicubic vs	SPSAM vs	Kriging vs	RBF vs
Bilinear	12+	8+ 4-	12+	12+
Bicubic		1+ 11-	9+ 3-	12+
SPSAM			12+	12+
Kriging				11+ 1-
RBF				

2) Influence of parameter a in the basis function. The parameter a in the basis function (see (4.6)) affects the non-linear modeling ability of RBF and, thus, plays an important role in RBF interpolation. This necessitates the analysis of the parameter for the proposed SPM method. The parameter a should take neither too large nor too small values. If a is too large, according to the properties of the Gaussian function, all elements in the matrix Φ will be very close to 1. In this case, Φ will be a singular matrix and (4.10) will not be uniquely solvable, which will lead to unacceptable SPM results consequently. On the other hand, if a is too small, all elements in Φ will be very close to 0 instead, which will also lead to a singular matrix.

We tested the influence of parameter a with 10 values: 0.1, 0.5, 1, 3, 5, 8, 10, 15, 20 and 30. The three groups of synthetic coarse images degraded with four different scales were used again for testing. Figure 4.13(a)-(c) shows the sensitivity of the proposed SPM method in relation to a. As shown in the three sub-figures, when a is less than 10, the PCC increases with an increase of a in all 12 cases. When a takes values between 10 and 30, the PCC in each case reaches a stable value.

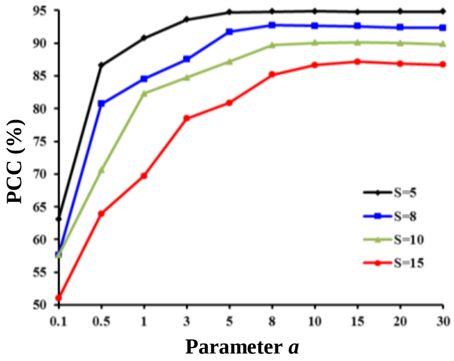

(a)

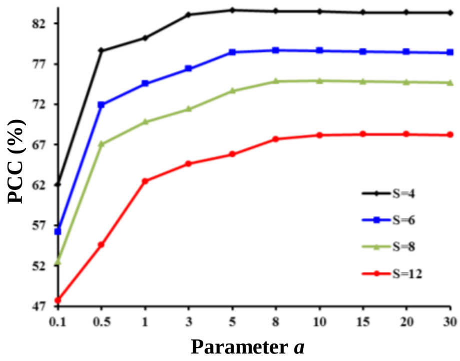

(b)

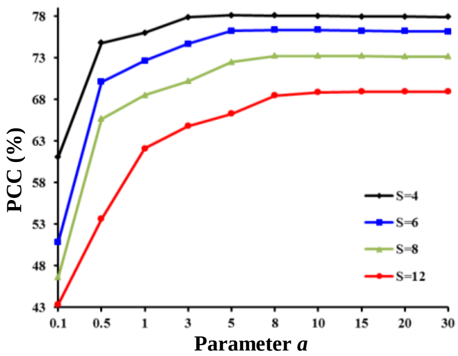

(c)

Figure 4.13. Influence of parameter *a* in the basis function of the proposed RBF interpolation-based SPM. (a) Aerial image. (b) ROSIS image. (c) QuickBird image.

3) Influence of window size N. Three window sizes, N=3, 5 and 7, were analyzed for the RBF-based SPM method. For each window size, parameter a with 10 values (i.e., 0.1, 0.5, 1, 3, 5, 8, 10, 15, 20 and 30) were considered and the largest PCC was selected from 10 values for comparison of different window sizes. Figure 4.14 shows the PCC for the three window sizes when the three groups of synthetic coarse images degraded with four different scales were tested. It is seen that when N increases from 3 to 5, the PCC increases obviously. When N increases to 7, however, the accuracy gains are relatively limited. In fact, larger N corresponds to larger size of matrix Φ and heavier computing burden in (4.10). Consequently, N=5 is recommended as a suitable window size for RBF-based SPM, when considering both SPM accuracy and computing efficiency.

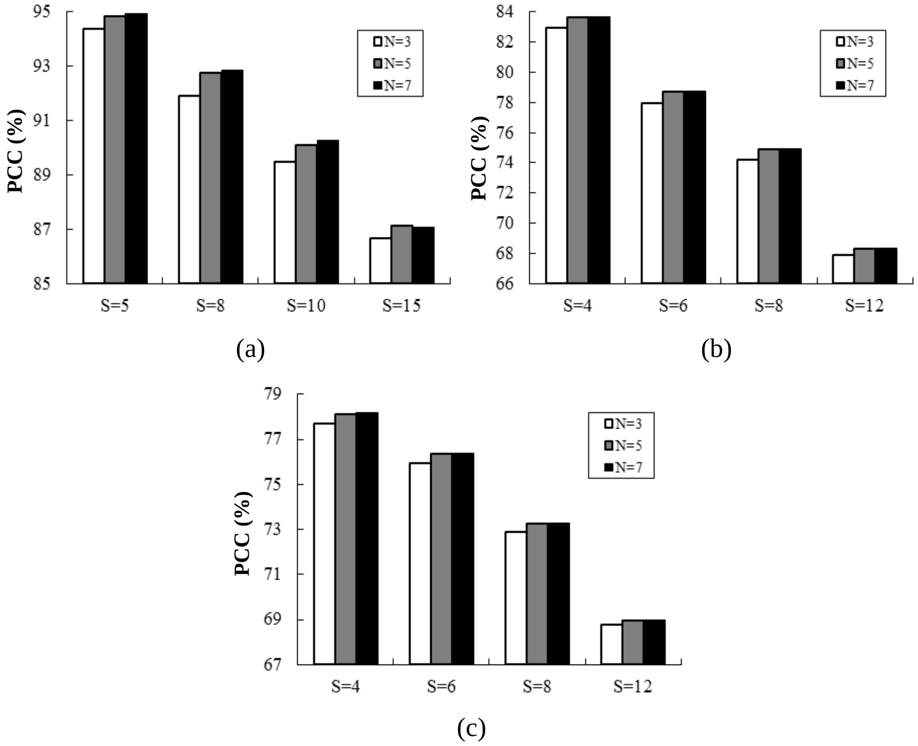

Figure 4.14. Influence of the window size in the proposed RBF interpolation-based SPM. (a) Aerial image. (b) ROSIS image. (c) QuickBird image.

4.5. Discussion

4.5.1. Computational efficiency

It is important to consider the computing efficiency of SPM methods, especially in real-time applications. The computing time of the five SPM methods at different zoom scales is given in Figure 4.15. The time required for the class allocation process (see Section 4.3.2) was not considered for each SPM method here. On the one hand, this process is very quick (needs less than 3 seconds in all cases in Figure 4.15), which has been demonstrated in Chapter 2. On the other hand, the class allocation process for all five SPM methods is the same, so can be ignored.

It is seen from the bar charts that the bilinear, bicubic and SPSAM are fast methods whereas the Kriging and RBF methods usually require more time. The geostatistics-based Kriging method considers the spatial covariance in the whole set of prediction data and calculates the contributions from each observed value. For the RBF method (N=5), the model in (4.10) is built and computed once for each visited mixed pixel. The processes of Kriging and RBF are more complex, thereby, consuming more time than the other three methods. As learned from Figure 4.12 and Table 4.6 previously, Kriging and RBF are capable of producing greater accuracy than the bilinear, bicubic and SPSAM methods. Therefore, the relatively long running time is the cost of enhancing SPM accuracy for Kriging and RBF. Both the Kriging and RBF methods, however, can still be viewed as real-time algorithms, as they took less than 1 minute in the experiments.

Comparing the values in the bar charts in Figure 4.15, it is found that for the aerial image with the smallest size among the three tested images, the computing time is the least, whilst for the QuickBird image with the largest size, the time is the most. Therefore, consistent with the other four SPM methods, the computation efficiency of RBF is related to the size of the study area (i.e., the number of mixed pixels). Furthermore, the computation time of RBF is also a function of the zoom factor.

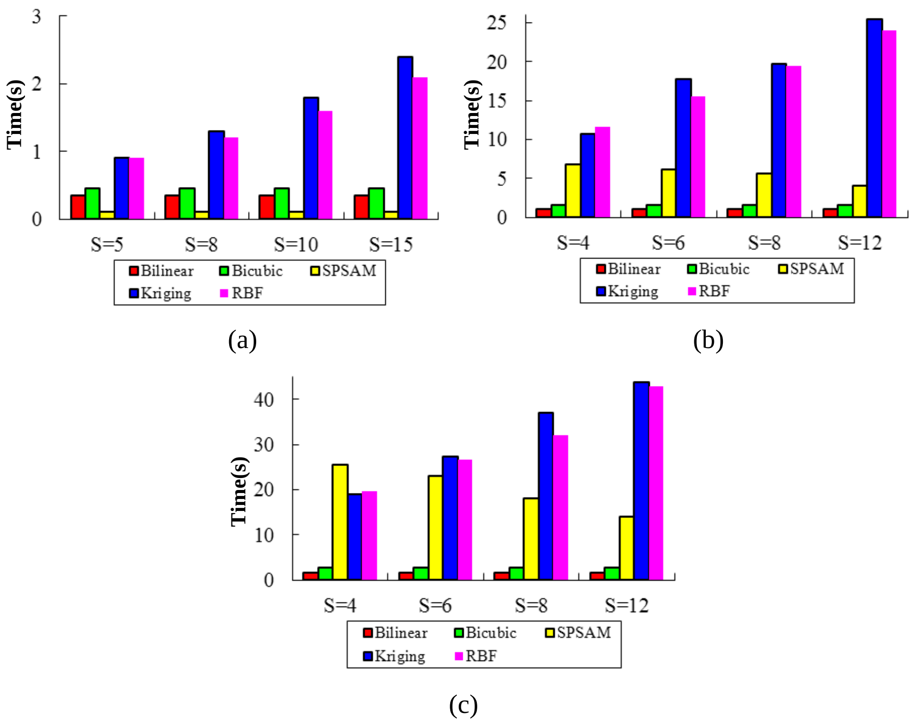

Figure 4.15. Computing time (seconds) of the five SPM methods. (a) Aerial image. (b) ROSIS image. (c) QuickBird image.

4.5.2. Characteristics and advantages of RBF-based SPM

The experimental results shown in Section 4.4.3-4.4.5 indicate that the RBF interpolation-based method presented in this chapter displays potential for SPM, irrespective of the complexity of land cover pattern in the studied images. In the first experiment, for the SPM of three coarse spatial resolution images with different types of land cover patterns, the new method provides consistently smoother and more continuous SPM results than do the bilinear, bicubic, SPSAM and Kriging methods. The PCC values indicate that the accuracy of the new method is higher than that of the bilinear, bicubic, SPSAM and Kriging methods. When applied to two degraded ROSIS hyperspectral images with different spatial resolutions in the second experiment, where inherent uncertainty exists in soft classification (i.e., LSMA), the new method also produces higher accuracy than the aforementioned four SPM methods. The good performance of the proposed method is also further confirmed by the results in Figure 4.12, where four different scales were tested for each image.

The advantage of the new method in terms of SPM accuracy can be attributed to the strong non-linear modeling ability of RBF. The core idea of SPM is to either maximize or match prior expectations about spatial dependence. In the proposed method, the spatial autocorrelation between any sub-pixel and its neighboring coarse pixels is characterized by the basis function in RBF interpolation. Meanwhile, the spatial autocorrelation between coarse pixels in the input proportion images is exploited fully to adaptively calculate the corresponding coefficients of the basis function values. The proposed SPM method, therefore, tries to capture and use as much of the available information about spatial dependence.

As described systematically in the introduction, for the post-processing of a soft classification, the STHSPM may be considered advantageous in terms of computing efficiency. The proposed SPM algorithm is a newly developed STHSPM algorithm. In all the experiments in this study, the proposed SPM method took less than 1 minute for each coarse spatial resolution image. Certainly, the computation time of RBF is related to the size of the study area and zoom factor. Unlike the back-propagation neural network and Indicator CoKriging, the proposed method does not require any prior class information on spatial structure. With respect to the other two SPM algorithms, SPSAM and Kriging, experimental results suggest that the new method is able to obtain more accurate SPM results. The proposed RBF interpolation-based method, therefore, provides a promising new and real-time SPM method for practical applications.

The difference between Kriging and the proposed RBF method is that the former is a global interpolation approach while the latter is a local interpolation strategy. The Kriging method is implemented based on the framework of geostatistical theory which takes the spatial configuration in the entire study area into consideration and estimates weights for each observed data point based on the global spatial covariance. The RBF method, however, builds a non-linear model for each coarse pixel, using proportions as well as the locations of its surrounding coarse pixels as observed data. In RBF interpolation, each coarse pixel has its unique set of observed data and RBF interpolation is spatially adaptive.

4.5.3. Influences of several factors on RBF-based SPM

Similar to the other SPM methods, the proposed SPM method is sensitive to the zoom scale factor, as shown in Figure 4.12. Its accuracy decreases when the zoom factor increases. One main reason is that the SPM problem increases in complexity with larger zoom factors, as for every coarse pixel the locations of more sub-pixels need to be predicted and uncertainty increases. Another reason is that in the coarse images produced with large degraded resolutions, pixels may be larger than some land cover objects, and some objects may fall within isolated coarse pixels. This is referred to as the L-resolution case in Atkinson (2009). In the L-resolution case, the spatial dependence-based SPM methods, including the proposed method, fail to locate objects accurately at fine spatial resolution.

We can observe further from Figure 4.12 that the PCC values of the proposed method decreases from Figure 4.12(a) to Figure 4.12(c). As an example, the PCC in Figure 4.12(a) is over 94% for S=5, but in Figure 4.12(b) and Figure 4.12(c) for a smaller scale S=4, the PCC declines to be less than 84% and 79%, respectively. This is because from Figure 4.12(a) to Figure 4.12(c), in the three groups of coarse images, the number of land cover classes increases from five to seven. On the other hand, the complexity of the land cover pattern also increases. From the corresponding three reference maps in Figure 4.3(b), Figure 4.4(b) and Figure 4.5(b), one can see that the aerial image is occupied by large and continuous objects, which can be well recreated by the new spatial dependence-based SPM method. In the ROSIS and QuickBird images, however, many small objects and elongated features exist, especially in the latter.

Comparing the resulting sub-pixel maps for the ROSIS image in the first experiment to those in the second experiment, it is seen that the errors from soft classification impose a considerably negative effect on the overall accuracy of SPM methods. This can be illustrated by the existence of isolated pixels in Figure 4.11(a)-(e), and the fact that some pixels of the shadow class in the reference map in Figure 4.11(f) were incorrectly assigned to the water class in Figure 4.11(a)-(e). Regarding the quantitative evaluation of the RBF results for the ROSIS image, the PCC (pure pixels were included for accuracy statistics) reached 91.87% and

81.99% for S=4 and S=8 in the first experiment, where no error exists in soft classification. In the second experiment, however, due to the errors in soft classification, the corresponding PCC decreased by around 17% and 12%, respectively.

As for the parameter a in the basis function, the proposed method tends to obtain highly accurate SPM results when it is set to values between 10 and 30 (see Figure 4.13). When a is too large (e.g., 50 in the experiments), it leads to a singular matrix Φ and poor SPM results.

4.5.4. Change of scale in RBF interpolation

The RBF interpolation is essentially an area-to-point prediction method and its outputs are continuous variables (in SPM these outputs are converted to categories by class allocation in Section 4.3.2). The challenge with area-to-point prediction is to account explicitly for the change of scale (Atkinson, 2013). More specifically, when predicting the values at an arbitrary sub-pixel (point), the information within any observed coarse pixel (area) needs to be expressed at a finer spatial resolution. This is not the case, however, in RBF interpolation as presented in this chapter. RBF interpolation deals with change of scale implicitly: Each observed coarse pixel is treated as a point at its centroid; when the scale factor S changes, the distance calculation in (4.7) and (4.8) changes correspondingly, leading to changes of Gaussian function values (see (4.6)) and matrix Φ (see (4.12)).

Here, we attempted to consider the change of scale in RBF interpolation in a more explicit way, in which the Gaussian function and matrix Φ are described at the sub-pixel scale

$$\phi(P_n, p_i) = \frac{1}{S^2}\sum_{m=1}^{S^2} e^{-d^2(p_m, p_i)/a^2} \tag{4.13}$$

$$\phi(P_n, P_v) = \frac{1}{S^4}\sum_{m=1}^{S^2}\sum_{t=1}^{S^2} e^{-d^2(p_m, p_t)/a^2} \tag{4.14}$$

where p_m denotes any sub-pixel within coarse pixel P_n, p_t denotes any sub-pixel within coarse pixel P_v, $d(p_m, p_i)$ is the distance between the centroid of sub-pixel p_i and the centroid of any sub-pixel p_m within pixel P_n and $d(p_m, p_t)$ is the distance between the centroid of any sub-pixel p_m within P_n and the centroid of any sub-pixel p_t within P_v.

A question is whether the scheme in (4.13) and (4.14) will impart benefits for

RBF interpolation. For simplicity, we denote the revised RBF that considers the change of scale with (4.13) and (4.14) as SRBF. The two interpolation algorithms, SRBF and RBF, were tested and compared using the three remote sensing images, with four scale factors for each image. The PCC of the SRBF and RBF-based SPM is shown in Figure 4.16. Values in the three bar charts indicate SRBF does not increase the accuracy of SPM. This suggests that SRBF will decrease the non-linear modeling ability of the original RBF. The computational burden of two versions of interpolation algorithms is exhibited in Table 4.7. Again, the time needed in class allocation is not taken into consideration. It is demonstrated that SRBF needs more computing time than RBF for the task of interpolation, due to the more complicated calculation process in (4.13) and (4.14). Consequently, SRBF is not an advisable scheme for SPM.

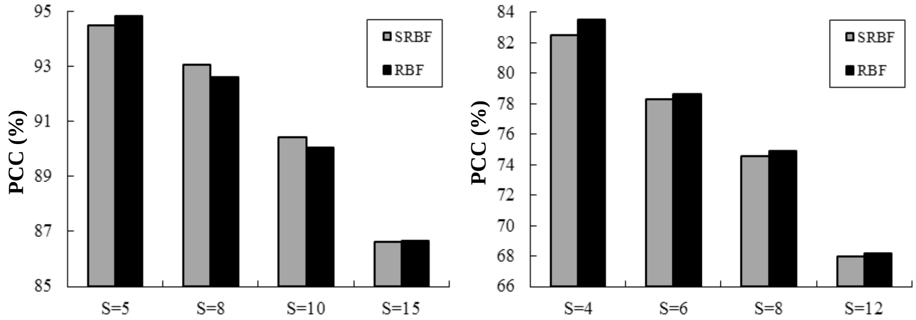

(a) (b)

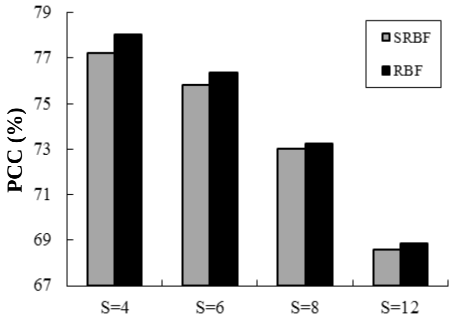

(c)

Figure 4.16. PCC (%) of the SRBF and RBF-based SPM methods. (a) Aerial image. (b) ROSIS image. (c) QuickBird image.

Table 4.7 Computing time (seconds) of the SRBF and RBF-based SPM methods

	Aerial image				ROSIS image				QuickBird image			
	S=5	*S*=8	*S*=10	*S*=15	*S*=4	*S*=6	*S*=8	*S*=12	*S*=4	*S*=6	*S*=8	*S*=12
SRBF	2.2	10.0	22.8	110.7	12.3	18.3	28.5	69.0	20.6	29.7	42.0	86.6
RBF	0.9	1.4	1.6	2.1	11.6	15.6	19.5	24.0	19.7	26.6	32.0	43.0

4.6. Summary

This chapter presents a new RBF interpolation-based SPM method for remote sensing images. The new method first utilizes RBF interpolation to predict the soft class values at each sub-pixel. Under the coherence constraint imposed by the coarse resolution land cover proportions, a sub-pixel map is then generated by hardening the soft class values. Based on the non-linear modeling ability of the RBF, the proposed method makes full use of the available spatial information to characterize spatial dependence, and does not need any prior information. The new method is also free of iteration and involves few parameters. Both visual and quantitative assessment on a range of experimental results reveals that the proposed method provides greater accuracy in comparison with bilinear-, bicubic-, SPSAM- and Kriging-based SPM methods. Moreover, the performance of the proposed SPM method is related to the quality of soft classification, the zoom factor, the number of classes required and the spatial complexity of the land cover pattern in the studied image.

5. Indicator cokriging-based STHSPM without prior spatial structure

(This chapter is based on Wang *et al.* (2015a))

5.1. Introduction

As introduced in Section 3.1, the ICK-based STHSPM algorithm needs prior knowledge from fine spatial resolution training images. It extracts the indicator semivariogram from the training image, to calculate conditional probabilities of class occurrence at each sub-pixel. In Boucher and Kyriakidis's (2006) as well as Sections 2.1 and 3.1, the geostatistics-based ICK model has been demonstrated to be competent for SPM, which is free of iteration and needs few parameters. ICK-based SPM is demanding in terms of its requirement for prior spatial structure information:

1) The spatial resolution of the prior structure information needs to be the same as the target fine spatial resolution for SPM.
2) The prior spatial structure information needs to be representative of the study area for SPM.

Jin et al. (2012) presented an interesting work to extract a fine spatial resolution indicator semivariogram from a small representative local area rather than the entire image for ICK-based SPM. The results demonstrated that ICK produces comparable accuracy with those using a globally-derived spatial structure. This method is still based on the existence of fine spatial resolution training images. Recently, attention has turned to ways to obtain training images, from which prior spatial structure information can be extracted for land cover mapping. The training images can be obtained by the following approaches (Atkinson, 2013; Ge, 2013).

1) Fine spatial resolution classified maps from other areas of similar spatial structure to the study area. For example, Boucher and Kyriakidis (2008) utilized a fine spatial resolution land cover map of a nearby city (Foshan) for ICK-based SPM of Guangzhou.
2) Fine spatial resolution images of the study area that are captured by previous airborne or satellite sensor observation. These images are then classified to

generate training images.

3) Manually drawn artificial training images associated with computer technology and the user's expert knowledge on the characteristics of land cover. In Ge and Bai (2011), a training image was drawn by hand according to the linear characteristics of roads for road extraction.
4) Other sources, such as land use maps, aerial photographs and Google Earth, can also be used to derive training images.

Uncertainties in the abovementioned approaches are unavoidable. For example, due to the differences between two cities, such as economic condition, environment, government planning, etc., the characteristics of the land cover in two neighboring cities may not be the same. The land cover of the same area in different periods may also have different spatial structures, considering human activities (e.g., building construction and vegetation harvesting, planting and regrowth) and natural changes (e.g., changes of rainfall and vegetation phenology) and so on. More importantly, the sources of training images are not always accessible or laborious work is needed to acquire training images even if access to them is available. Therefore, it is worthwhile to explore if some effective alternative can be provided for ICK-based SPM when such prior spatial structure information is unavailable.

For traditional ICK-based SPM, fine spatial resolution training images are used to extract semivariograms for each land cover class, to characterize their spatial pattern at the target fine spatial resolution. In this chapter, the fine spatial resolution semivariogram for ICK-based SPM was estimated using coarse spatial resolution land cover proportion images. This information is automatically available since the coarse spatial resolution image of proportions provides the input data for the SPM process. Although the proportion images are at a coarse spatial resolution, they provide information on the spatial characteristics of the land cover classes. For each class, the initially acquired coarse spatial resolution semivariogram was converted to the equivalent at the target spatial resolution by deconvolution.

Deconvolution is a technique for deriving a point support semivariogram from the experimental semivariogram of areal data (Journel and Huijbregts, 1978; Goovaerts, 2008). It is frequently used in mining, where all areas are considered to have the same size and shape of support (Collins and Woodcock, 1999; Truong et al., 2014). The technique has been extended to cases where only irregular geographical units are available. Kyriakidis (2004) discussed theoretically the deconvolution of semivariograms when areal data supports change from place-to-place. Goovaerts (2008) provided an example study to explore its practical implementation, by mapping lung cancer mortality rates in Indiana and the Western United States using units of different shape and size. This is also one of the few studies that present explicitly the deconvolution process.

In some fields, such as soil survey, disease mapping and population mapping, it is common to represent variables on a point support, as observations on quasi-point supports are much smaller than the support of interest. However, this is not the case for satellite remote sensing. Remote sensing images are normally composed of regularly sized pixels that cover a positive finite area, producing a given spatial resolution. In this chapter, by deconvolution, we mean the derivation of the fine spatial resolution semivariogram (via the point semivariogram) from the coarse spatial resolution semivariogram (areal semivariogram). In the deconvolution process, the coarse spatial resolution proportions are viewed as the available areal data, and the framework is based on regular geographical units. Dconvolution is an intermediate step towards ICK-based SPM. After deconvolution, the estimated fine spatial resolution semivariogram of each class is used for ICK to predict the probability of class occurrence at the sub-pixel levels. SPM is finally realized according to the ICK-derived probability and the proportions constraint from the input soft classification.

5.2. Methods

Suppose Y is the observed coarse spatial resolution image with N pixels and X is the sub-pixel map at the fine spatial resolution with M pixels. Here, $M/N=S^2$ and S is the zoom factor. Let v_m (m=1,2,…,M) be a sub-pixel, K be the number of classes in the study area, $\gamma_k(h)$ be fine spatial resolution semivariogram of the kth class that characterizes the spatial pattern of the kth class, and $F_k(V_n)$ be the kth (k=1,2,…,K) class proportion in a coarse pixel V_n (n=1,2,…,N).

5.2.1. ICK-based STHSPM

Details on ICK-based STHSPM can be found in Section 3.1.2.1. The ICK-derived probabilities are transferred to hard class labels using the UOC-based class allocation method proposed in Section 2.1.

5.2.2. Estimation of fine spatial resolution semivariogram without prior spatial structure

The critical issue for ICK-based SPM is to obtain the fine spatial resolution semivariogram for each class. In the traditional ICK-based SPM model, the semivariogram sets $\gamma_1(h), \gamma_2(h), ..., \gamma_K(h)$ are extracted from fine spatial resolution training images. Specifically, the training image of a study area covering *K* classes can be decomposed into *K* binary land cover maps. The semivariogram $\gamma_k(h)$ can be acquired from the binary land cover map of the *k*th class. In this section, the fine spatial resolution semivariogram sets are derived by deconvolution of the coarse spatial resolution semivariogram and the whole process does not require any training images.

5.2.2.1. Objective of deconvolution

Suppose $\gamma_k^V(h)$ is the coarse spatial resolution semivariogram calculated from the proportion image of the *k*th class

$$\gamma_k^V(h) = \frac{1}{2N(h)} \sum_{n=1}^{N(\mathbf{h})} [F_k(V_n) - F_k(V_n + h)]^2 \tag{5.1}$$

where *N*(*h*) is the number of paired pixels at a specific lag distance *h* (in coarse pixels) from the center pixel V_n. In this chapter, the isotropic semivariogram is considered and pixels at a specific distance from the center pixel in all directions are treated equally. With the scattered points, the continuous semivariogram function is fitted by the commonly used exponential model.

The fine spatial resolution semivariogram $\gamma_k(h)$ can be convolved to the coarse spatial resolution semivariogram $\gamma_k^{V-R}(h)$, also termed regularized semivariogram, by the well-known regularization (Journel and Huijbregts, 1978)

$$\gamma_k^{V-R}(h) = \gamma_k^{VV}(V_n, V_n + h) - \gamma_k^{VV}(V_n, V_n) \tag{5.2}$$

where $\gamma_k^{VV}(V_n, V_n + h)$ is the coarse-to-coarse spatial resolution semivariogram and $\gamma_k^{VV}(V_n, V_n)$, a constant for a given zoom factor *S*, is the average coarse spatial resolution semivariogram within a coarse pixel. Both of them are calculated using (3.4) in Chapter 3. Deconvolution aims to estimate the optimal fine spatial resolution semivariogram (denoted as $\gamma_k^{v-O}(h)$), the regularized semivariogram of which approximates $\gamma_k^V(h)$. The difference D between $\gamma_k^{V-R}(h)$ and $\gamma_k^V(h)$ is quantified by means of the root mean square error (RMSE)

$$D = \sqrt{\frac{\sum_{l=1}^{L}[\gamma_k^{V-R}(h_l) - \gamma_k^V(h_l)]^2}{L}} \tag{5.3}$$

where L is the number of lag distances. Consequently, the objective of deconvolution is specifically to minimize the difference D in (5.3). Strictly, deconvolution is an ill-posed problem. Even though one can obtain reassurance about regularizations (convolutions) of the fine spatial resolution semivariogram, one can never be sure that the estimated semivariogram is exactly the same as the true semivariogram of the study area (Atkinson, 2013). Deconvolution is employed in this chapter to provide reliable inputs of class probability estimation for ICK-based SPM, rather than restoring an ideal fine spatial resolution semivariogram.

5.2.2.2. Implementation of deconvolution

Deconvolution is an iterative process and contains two stages: initialization and update. Define I as an indicator whether update of $\gamma_k^{v-O}(h)$ is successful: 1 means successful update and 0 *vice versa*. In the whole process, the isotropic semivariogram is considered and the commonly used exponential model is applied to fit the continuous semivariogram function. The detailed implementation is given as follows.

Stage 1: Initialization. The task of this stage is to initialize the optimal fine spatial resolution semivariogram $\gamma_k^{v-O}(h)$, and obtain correspondingly the optimal regularized semivariogram $\gamma_k^{V-RO}(h)$ and optimal difference D^O.

1) Initialization of $\gamma_k^{v-O}(h)$. The starting range of $\gamma_k^{v-O}(h)$ was the same as for $\gamma_k^V(h)$, the starting sill was double that for $\gamma_k^V(h)$, and the starting nugget was an empirical value $S/200$.
2) Regularization of $\gamma_k^{v-O}(h)$. The fine spatial resolution semivariogram $\gamma_k^{v-O}(h)$ is convolved to the regularized semivariogram $\gamma_k^{V-RO}(h)$, see (5.2).

3) Calculation of the difference between $\gamma_k^{V-RO}(h)$ and $\gamma_k^{V}(h)$. The optimal difference D^O in the initialization stage can be quantified by the RMSE between the two coarse spatial resolution semivariograms.
4) Initialization of indicator *I*. *I* is initialized to 1.

Stage 2: Update. This stage is implemented to update $\gamma_k^{v-O}(h)$ and modify it iteratively to minimize D^O.

1) Update of $\gamma_k^{v-O}(h)$. Each lag of the new fine spatial resolution semivariogram, denoted as $\gamma_k^{v-N}(h)$, is generated by

$$\gamma_k^{v-N}(h_l) = \gamma_k^{v-O}(h_l) + \rho_l[\gamma_k^{V}(h_l) - \gamma_k^{V-RO}(h_l)] \tag{5.4}$$

where ρ_l is an adaptive weight related to the iteration number, $\gamma_k^{v-O}(h)$ and indicator *I*.

If the update of $\gamma_k^{v-O}(h)$ in the last iteration is successful (i.e., *I*=1), ρ_l is calculated as

$$\rho_l = \frac{\gamma_k^{v-O}(h_l)}{(C_1 + C_2)\sqrt{i}} \tag{5.5}$$

where C_1 and C_2 are the nugget and sill of $\gamma_k^{v-O}(h)$, and *i* is the number of current iteration. Take the first iteration as an example; ρ_l in (5.5) ranges from about 0 to 1 as *l* increases.

If the last update is unsuccessful (i.e., *I*=0), ρ_l takes a smaller value for small adjustment of $\gamma_k^{v-O}(h)$ (Goovaerts, 2008)

$$\rho_l = \frac{\gamma_k^{v-O}(h_l)}{2(C_1 + C_2)\sqrt{i}} \tag{5.6}$$

As the deconvolution proceeds iteratively, the weight ρ_l decreases gradually by dividing $\sqrt{i}$ and the adjustment of $\gamma_k^{v-O}(h)$ decreases. If the current optimal regularized semivariogram $\gamma_k^{V-RO}(h)$ is smaller than the target coarse spatial resolution semivariogram $\gamma_k^{V}(h)$, which indicates that the corresponding fine spatial resolution semivariogram $\gamma_k^{v-O}(h)$ is underestimated, an increase is produced in (5.4) for adjustment of $\gamma_k^{v-O}(h)$. In contrast, if $\gamma_k^{V-RO}(h)$ is greater than $\gamma_k^{v-O}(h)$, it indicates that $\gamma_k^{v-O}(h)$ is overestimated and a decrease is produced in (5.4) for $\gamma_k^{v-O}(h)$.

This flexible adjustment in (5.4) makes $\gamma_k^{V-RO}(h)$ approach the target $\gamma_k^{V}(h)$ gradually.

2) Regularization of $\gamma_k^{v-N}(h)$. The new fine spatial resolution semivariogram $\gamma_k^{v-N}(h)$ is convolved to the regularized semivariogram $\gamma_k^{V-RN}(h)$.

3) Calculation of the difference between $\gamma_k^{V-RN}(h)$ and $\gamma_k^{V}(h)$.The new difference D^N is obtained by calculating the RMSE between the two semivariograms.

4) Determination of a new indicator *I*. D^O and D^N are compared by $\Delta = D^N - D^O$.

   If $\Delta < 0$, it means the update of $\gamma_k^{v-O}(h)$ is successful. Correspondingly, $\gamma_k^{v-O}(h)$ is updated by $\gamma_k^{v-N}(h)$, $\gamma_k^{V-RO}(h)$ is updated by $\gamma_k^{V-RN}(h)$, and D^O is updated by D^N. Meanwhile, *I* is set to 1.

   If $\Delta \geq 0$, it means the update of $\gamma_k^{v-O}(h)$ is unsuccessful. In this case, $\gamma_k^{v-O}(h)$, $\gamma_k^{V-RO}(h)$ and D^O are not changed, and *I* is set to 0.

   The new indicator *I* is used to guide the update of $\gamma_k^{v-O}(h)$ in the next iteration (i.e., whether (5.5) or (5.6) is applied). By step 4), the optimal semivariogram from the initialization to current iteration is retained and the difference *D* is minimized as the deconvolution proceeds.

5) Termination of deconvolution. The deconvolution process is stopped when one of the following two conditions is met:

   i) The number of iterations exceeds the maximum number *H*. In this study, *H* was set to 20.

   ii)The change in D^N in comparison with D^O is less than a small threshold *T* (e.g., 0.1% in this paper) for a consecutive three times, i.e.,

$$\frac{|\Delta|}{D^O} \leq T \tag{5.7}$$

For all *K* classes, the abovementioned steps are carried out to produce the fine spatial resolution semivariogram sets $\gamma_1^{v-O}(h), \gamma_2^{v-O}(h), ..., \gamma_K^{v-O}(h)$, which are used as inputs to ICK-based SPM. Figure 5.1 summarizes the whole flowchart of deconvolution. As seen from the steps and Figure 5.1, the whole process of deconvolution needs no prior spatial structure information. The regularization process links the coarse spatial resolution semivariogram with the fine spatial resolution semivariogram, by involving the zoom factor *S* in (3.4). Therefore, the deconvolution approach is able to convert the coarse spatial resolution semivariogram to the desired target spatial resolution semivariogram.

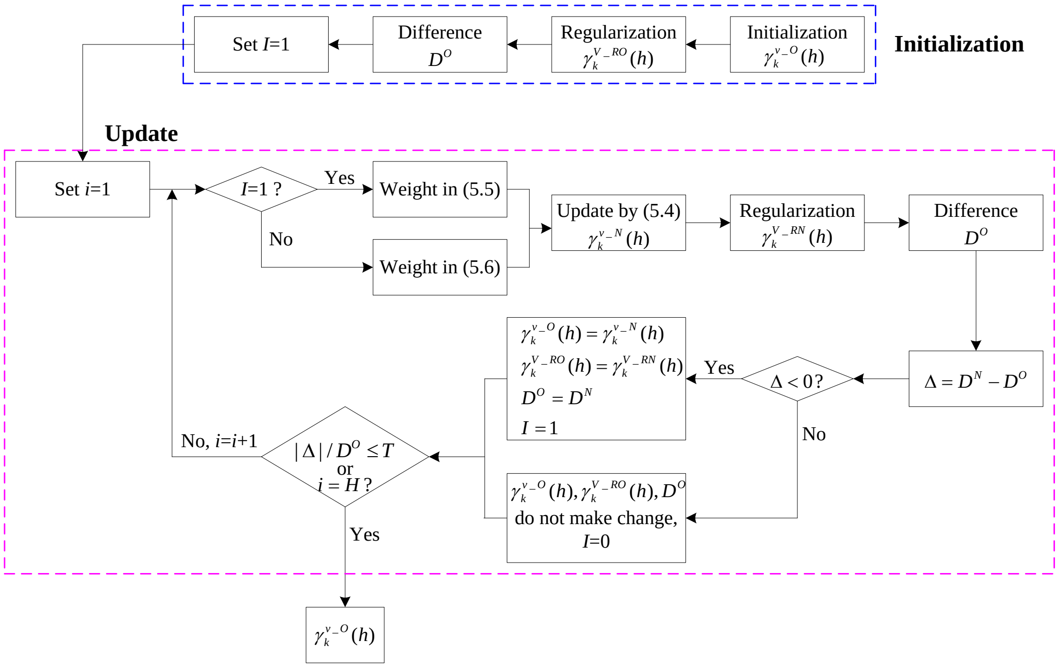

Figure 5.1. Flowchart describing the process of semivariogram deconvolution.

5.3. Experiments

In the first two experiments, to avoid errors from soft classification and some other processes (e.g., registration) (Xu et al., 2013), and focus solely on the performance of SPM, the soft classification results were simulated by degrading the fine spatial resolution map with a mean filter. In this way, every *S* by *S* fine pixels were degraded to a coarse pixel. The third experiment was designed to gain a more realistic simulation of the coarse spatial resolution image and consider the uncertainty in soft classification. Specifically, a 30 m spatial resolution Landsat image was degraded band by band with a degradation factor to generate a coarse spatial resolution multispectral image. Soft classification (i.e., spectral unmixing) was then implemented to obtain proportion images, which were used as inputs to SPM (including the deconvolution process in the proposed method). The hard classification result of the 30 m Landsat image was considered as reference for SPM evaluation (Atkinson, 2009).

The proposed ICK method that uses the semivariogram obtained by deconvolution was compared to the original ICK method using fine spatial resolution training images. For clarity, we call the proposed method naiive ICK (NICK). NICK was also compared with two well-known SPM algorithms, that is, PSA (Atkinson, 2005; Makido and Shortridge, 2007; Wang et al., 2012a) and SPSAM (Mertens et al., 2006), to validate its advantages in SPM. All experiments were tested on an Intel Core i7 Processor at 3.40-GHz with the MATLAB 7.1 version. PSA was implemented based on simulated annealing and the number of iterations was set to 3000. For both ICK and NICK, a neighborhood window with 5 by 5 coarse pixels was considered for each coarse pixel for reasons of computational efficiency, as was done in Boucher and Kyriakidis (2006).

5.3.1. Experiment 1

In the first experiment, two land cover maps from the National Land Cover Database 2001 (NLCD 2001) were tested. The NLCD 2001 is a raster-based land-cover classification with a medium spatial resolution of 30 m over all 50 US states and Puerto Rico, which was produced using a set of data layers, including multi-season Landsat 5 and Landsat 7 images mostly acquired in 2001, digital elevation model-based derivatives and other auxiliary datasets (Jin et al., 2012; Homer et al., 2004). Both land cover maps have a ground extent of 18 km by 18 km and a size of 600 by 600 pixels. Four land cover classes are presented in the two maps: water, urban, agriculture and forest. The first map covers an area in South Carolina while the second map an area in Ohio, as shown in Figure 5.2. It can be observed that the urban class in the two maps appears mainly as elongated features whereas the water class appears mainly as large objects. In the South Carolina map, the pixels of the water, urban, agriculture and forest classes occupy 9.74%, 16.27%, 26.76% and 47.23%, respectively, of the entire image and in the Ohio map, the corresponding proportions of the four classes are 6.33%, 23.32%, 45.88% and 24.47%, respectively.

The two 30 m spatial resolution maps were degraded with five mean filters, 4 by 4, 6 by 6, 8 by 8, 10 by 10 and 12 by 12, to simulate the 120 m, 180 m, 240 m, 300 m and 360 m coarse spatial resolution proportion images of the four classes. The five different spatial resolution proportion images were used as the input for SPM and the zoom factor S was correspondingly set to 4, 6, 8, 10 and 12, to restore the land cover map at 30 m spatial resolution.

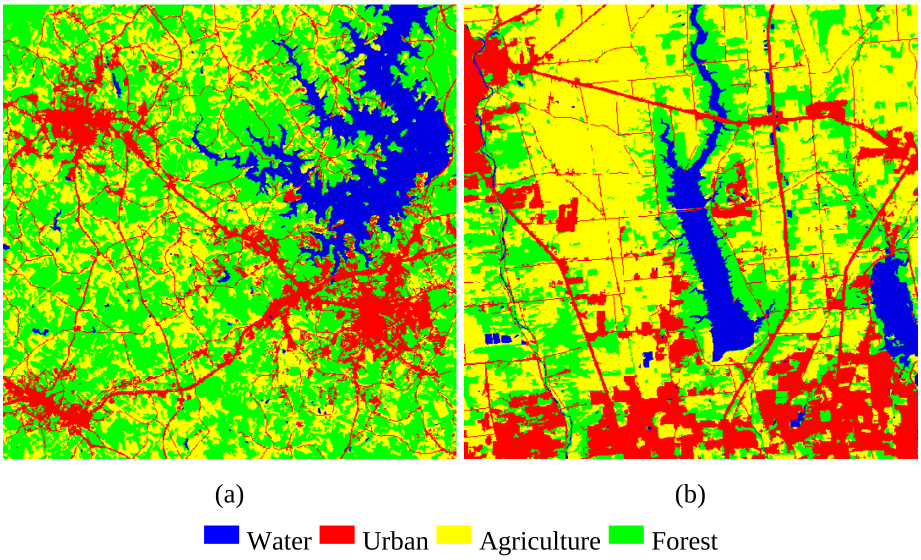

Figure 5.2. Reference land cover maps in the first experiment. (a) The South Carolina map. (b) The Ohio map.

We first take the 240 m spatial resolution image as an example for illustration and analysis. Figure 5.3 gives the 240 m spatial resolution proportion images created with a degradation factor of 8. It can be seen that the mixed pixels occur on the boundaries between classes and the commonly existing blurry boundaries necessitate SPM techniques. The 30 m fine spatial resolution semivariograms of the two areas, which are estimated by deconvolving the coarse spatial resolution semivariograms extracted from the proportion images, are shown in Figure 5.4. As can be observed from the semivariograms of each class in each coarse spatial resolution, the regularized coarse spatial resolution semivariogram (in green) and target coarse spatial resolution semivariogram (in blue) are highly similar and nearly coincide with each other in each case. This indicates the effectiveness of the deconvolution approach. It is worth noting that the nuggets of semivariograms at coarse spatial resolution (both regularized and target coarse semivariograms in Figure 5.4) are smaller than that of the fine spatial resolution semivariogram. Moreover, for several classes, there are slight differences between the nuggets of the regularized semivariogram and the corresponding target coarse semivariogram. This is because deconvolution is an ill-posed problem and the nugget of the fine spatial resolution semivariogram cannot be estimated from only the coarse spatial resolution semivariogram (Truong et al., 2014). Additional information or expert knowledge on the characteristics of land cover may be a feasible source to solve this problem.

(a)

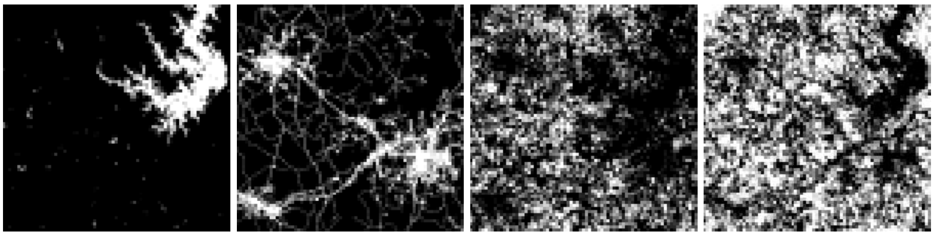

(b)

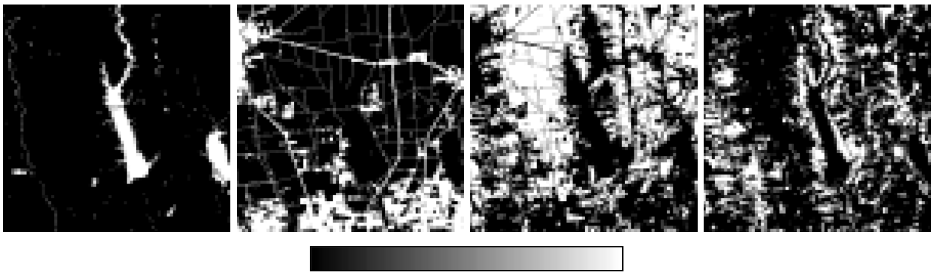

Figure 5.3. Proportion images of the four classes in the simulated 240 m coarse spatial resolution images in experiment 1. From left to right: water, urban, agriculture and forest. (a) South Carolina. (b) Ohio.

(a)

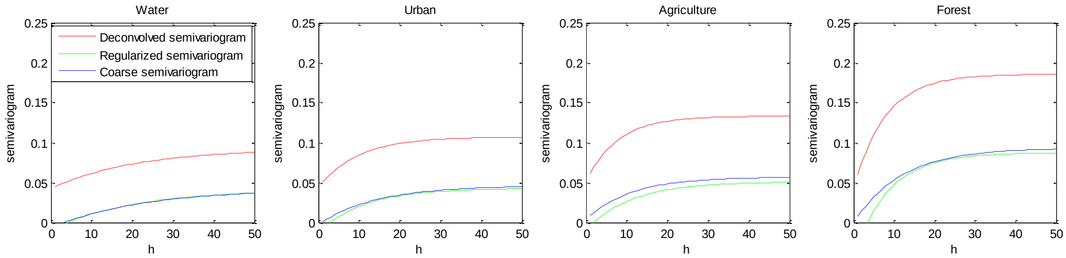

(b)

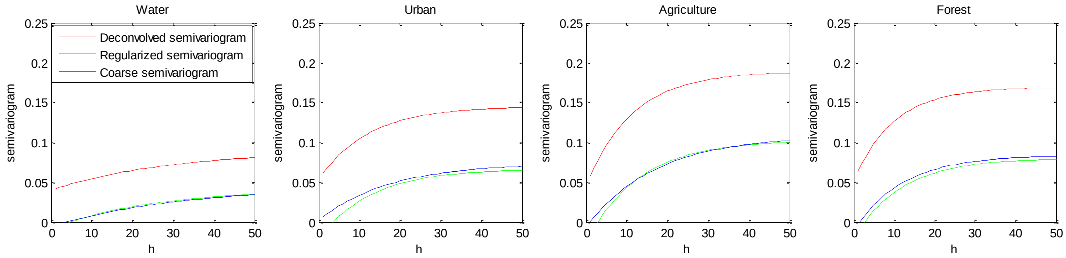

Figure 5.4. The fine spatial resolution semivariogram obtained by deconvolution in experiment 1 (S=8). The red, green and blue curves denote the fine spatial resolution semivariogram from deconvolution, regularized coarse spatial resolution semivariogram and coarse spatial resolution semivariogram extracted from the proportion image. (a) South Carolina. (b) Ohio.

Using the estimated fine spatial resolution semivariogram, the class probabilities for each sub-pixel were then estimated by the ICK method. Figure 5.5 exhibits the estimated ICK-derived probability maps of the four classses for the 240 m spatial resolution images in Figure 5.3, based on the fine spatial resolution semivariograms in Figure 5.4. Comparing the maps in Figure 5.5 with Figure 5.3, we can observe that the boundaries in Figure 5.5 are much clearer than those presented in Figure 5.3, suggesting that NICK is able to provide more detailed texture information than the proportion images.

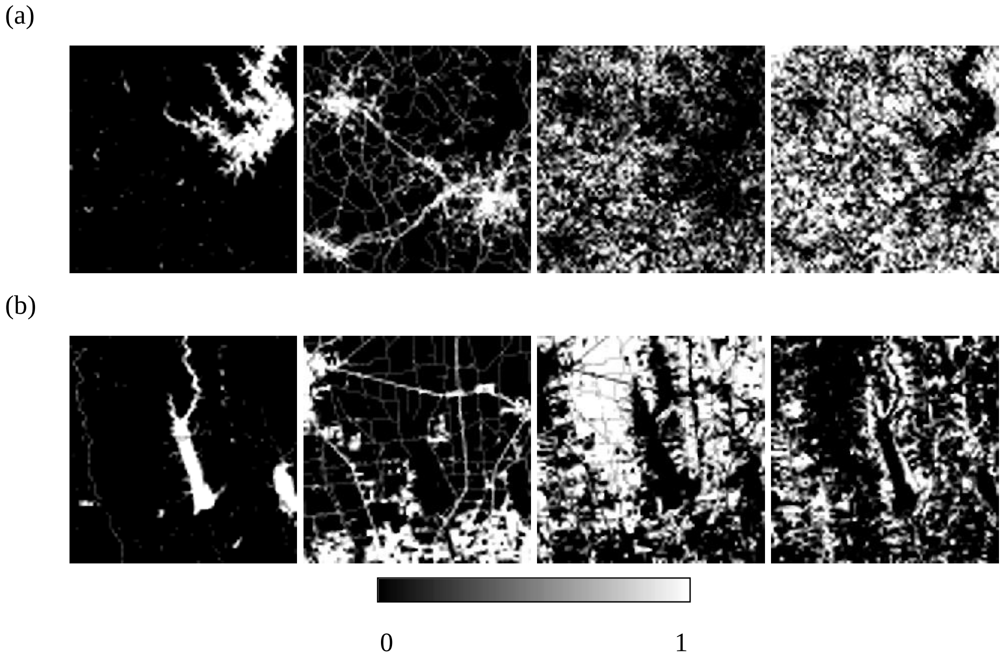

Figure 5.5. ICK-derived probability maps of the four classes in experiment 1 (S=8). From left to right: water, urban, agriculture and forest. (a) South Carolina. (b) Ohio.

The SPM results of the PSA, SPSAM, ICK and NICK methods for the 240 m spatial resolution images of two study areas are shown in Figure 5.6. For ICK-based SPM of the two areas, the reference land cover maps in Figure 5.2 were used as training images to extract the fine spatial resolution semivariogram. As shown in Figure 5.6(a) and Figure 5.6(e), although the distribution of land cover in PSA results are smooth, there exist many disconnected and hole-shaped patches, especially for the elongated urban class. Examining the SPSAM results, we can find many patches and linear artifacts in both resulting maps and this phenomenon is particularly obvious for the urban class. The results of NICK are highly similar to those of ICK. Compared to PSA and SPSAM, both of them produce more continuous SPM results, which are more in agreement with the reference maps in Figure 5.2. This can be illustrated well by the restoration of the urban class in the ICK and NICK results.

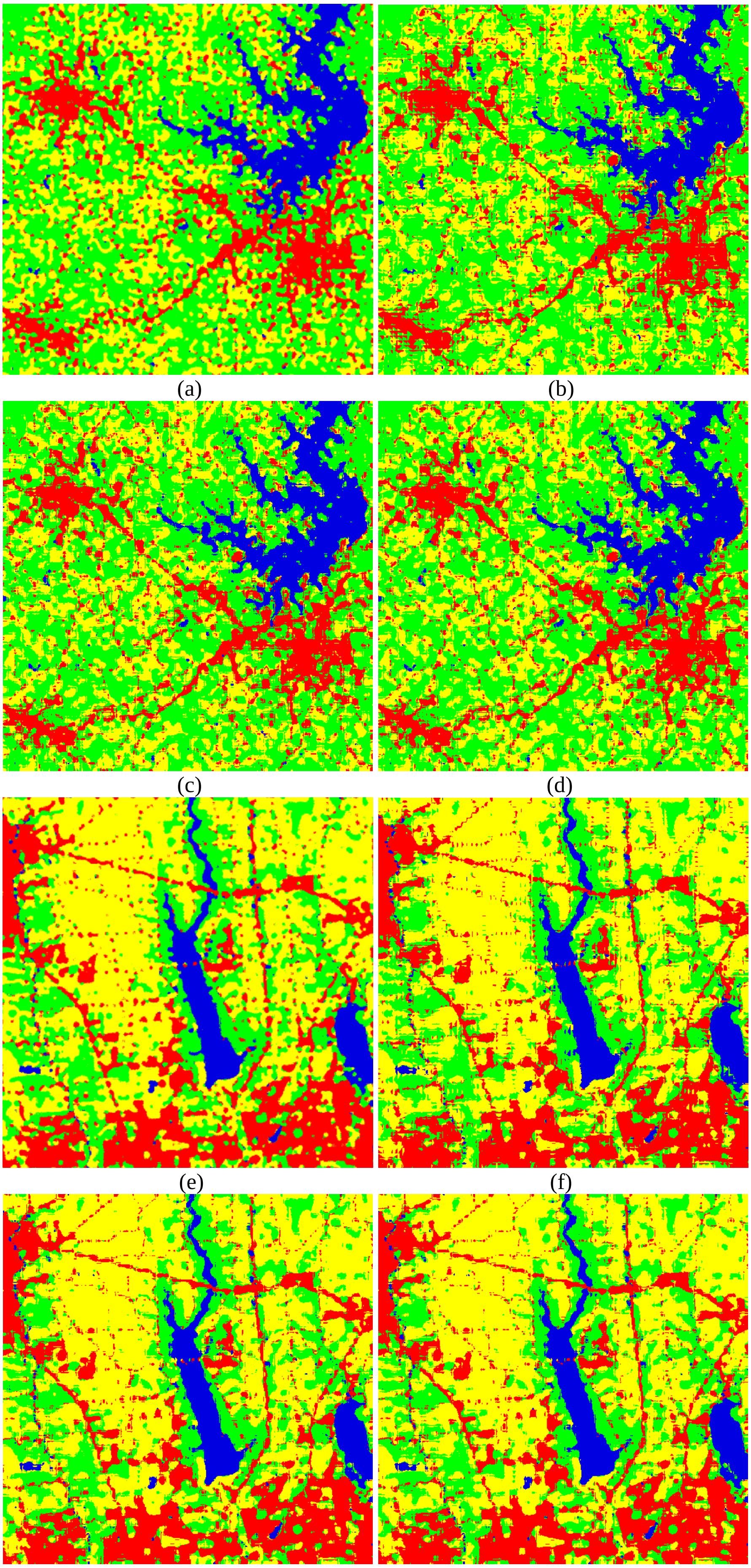

(a) (b) (c) (d) (e) (f) (g) (h)

Figure 5.6. SPM results in experiment 1 (*S*=8). (a) and (e) PSA results. (b) and (f) SPSAM results. (c) and (g) ICK results. (d) and (h) NICK results. (a)-(d) South Carolina results. (e)-(h) Ohio results.

The performances of three methods for the 240 m spatial resolution images of two areas are also evaluated quantitatively by the classification accuracy of each class and the overall accuracy in terms of the percentage of correctly classified pixels (PCC), as listed in Table 5.1. Note the non-mixed pixels were not considered in the accuracy statistics. Checking the accuracy for each area in Table 5.1, the accuracy of two geostatistics-based SPM approaches (i.e., ICK and NICK) is almost the same as well as the accuracy for each class and both of them are superior to PSA and SPSAM. In the South Carolina area, for NICK, the classification accuracy of the urban class is 62.02%, around 3% and 1% greater than that of PSA and SPSAM; The classification accuracy of the agriculture class is 63.34%, with gians of around 1.5% over PSA and SPSAM. With respect to the overall accuracy, PSA produces a PCC of 67.54% while SPSAM produces a PCC of 67.77%. NICK increases the PCC by 1.2%. Focusing the results for the Ohio area, ICK and the proposed NICK again achieve a similar accuracy for each class, which is higher than for PSA and SPSAM. The PCC of PSA and SPSAM increases from about 75.5% to76.41% for the two geostatistics-based SPM methods.

Table 5.1 Accuracy (%) of SPM methods for the South Carolina and Ohio areas in experiment 1 (*S*=8)

	South Carolina area				Ohio area			
	PSA	SPSAM	ICK	NICK	PSA	SPSAM	ICK	NICK
Water	80.16	80.34	81.06	81.07	75.58	76.60	77.22	77.20
Urban	59.15	61.05	62.02	62.02	72.68	72.84	73.30	73.31
Agriculture	61.69	61.90	63.30	63.34	79.32	79.52	80.33	80.33
Forest	72.54	72.19	73.40	73.42	72.14	71.77	72.93	72.94
PCC	67.54	67.77	68.97	68.99	75.52	75.58	76.41	76.41

In SPM, within each coarse pixel, the class labels of S^2 sub-pixels need to be predicted and the performance of NICK is affected by the zoom factor *S*. Likewise, the four SPM methods are tested for the other four zoom factors, 4, 6, 10 and 12. The PCC of the four methods for all five zoom factors is shown in the bar chart in Figure 5.7. It is worth noting that as *S* increases, the accuracy of all four methods decreases. Consistent with the results in Table 5.1, in ten cases, NICK produces almost identical accuracy to ICK and higher PCC than PSA and SPSAM, which further validates the effectiveness of deconvolution of coarse spatial resolution semivariograms from the proportion images for ICK-based SPM.

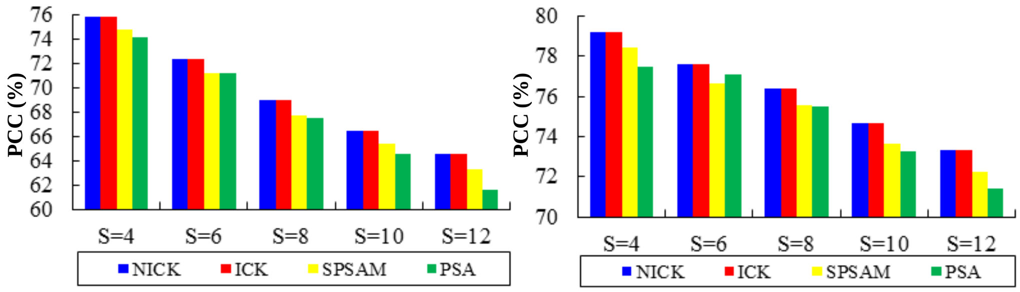

(a) (b)

Figure 5.7. PCC (%) of the four SPM methods in relation to zoom factor *S* in two areas. (a) South Carolina. (b) Ohio.

5.3.2. Experiment 2

In the second experiment, two fine spatial resolution (0.61 m) QuickBird images were used to test the NICK approach. The two QuickBird images contain 480 by 480 pixels and three multispectral bands (RGB), and were acquired in August 2005. One image covers the suburb of Xuzhou City, China while the other image covers the urban center area of that city (Zhang et al., 2014). The two images were classified with an algorithm that first integrated spatial features of pixel shape feature set, grey level co-occurrence matrix and Gabor transform with spectral information and then used a support vector machine for classification. Each generated land cover map contains seven classes: shadow, water, road, tree, grass, roof and bare soil. Figure 5.8 shows the two original QuickBird images and the corresponding classified land cover maps.

The land cover maps in Figure 5.8 were degraded with an 8 by 8 mean filter, producing two 5 m (relatively) coarse spatial resolution images, as shown in Figure 5.9. The task of SPM in this experiment was to reproduce the two 0.61 m land cover maps from the simulated 5 m proportion images of seven classes. Figure 5.10 shows the 0.61 m fine spatial resolution semivariograms of the two areas that were estimated by deconvolution. Likewise, the regularized coarse spatial resolution semivariogram and target coarse spatial resolution semivariogram are very similar to each other in each case. Figure 5.11 gives the SPM results of the PSA, SPSAM, ICK and NICK methods. The fine spatial resolution semivariograms for ICK were extracted from the reference maps in Figure 5.8. As can be observed from both PSA results, the land cover is generally over-compact, leading to locally smooth and hole-shaped artifacts. With respect to two SPSAM results, some disconnected and cone-shaped patches exist, which conflicts with the spatial characteristics in Figure 5.8. In the ICK and NICK results, this phenomenon is alleviated. As an example, in

Figure 5.11(c), Figure 5.11(d), Figure 5.11(g), and Figure 5.11(h), the road class is more continuous and the boundary of the roof class is smoother.

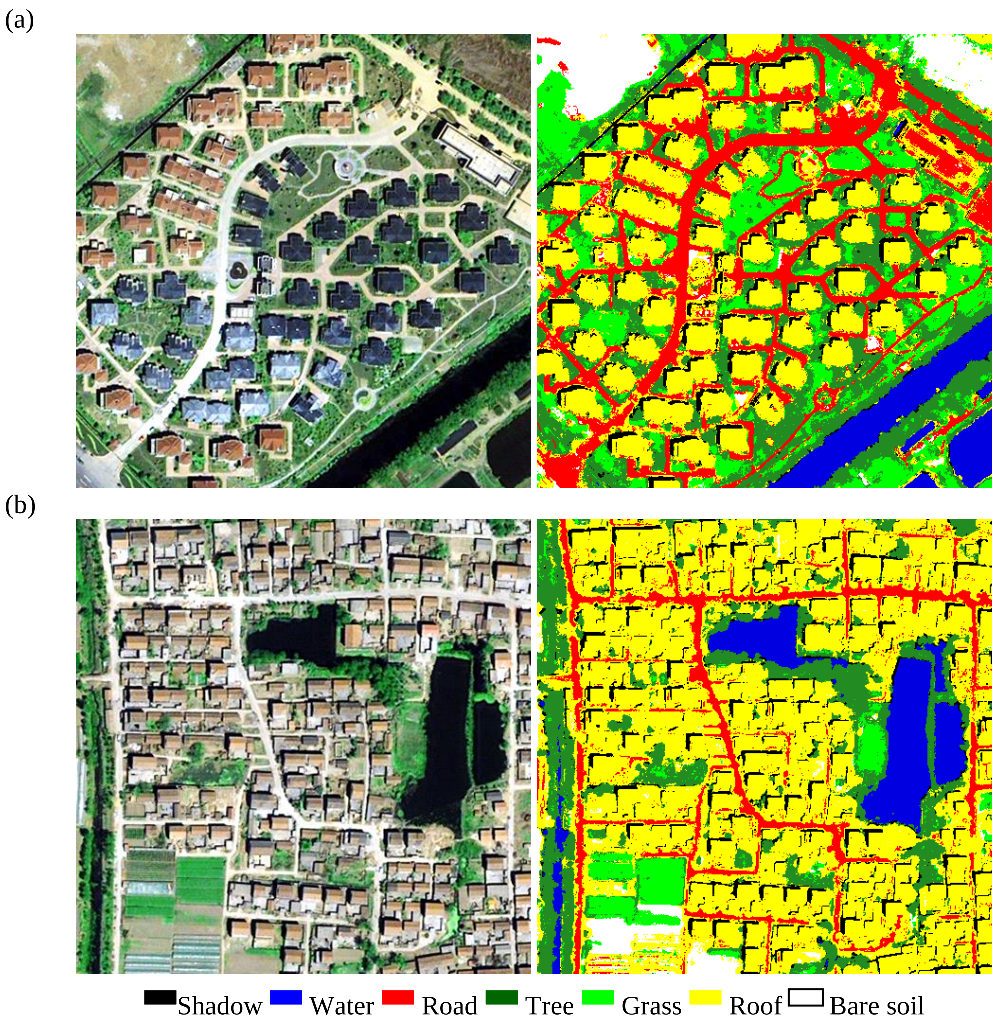

Figure 5.8. Two QuickBird images used in experiment 2. Left: Original images; Right: Classified land cover maps. (a) Xuzhou suburb area. (b) Xuzhou urban center area.

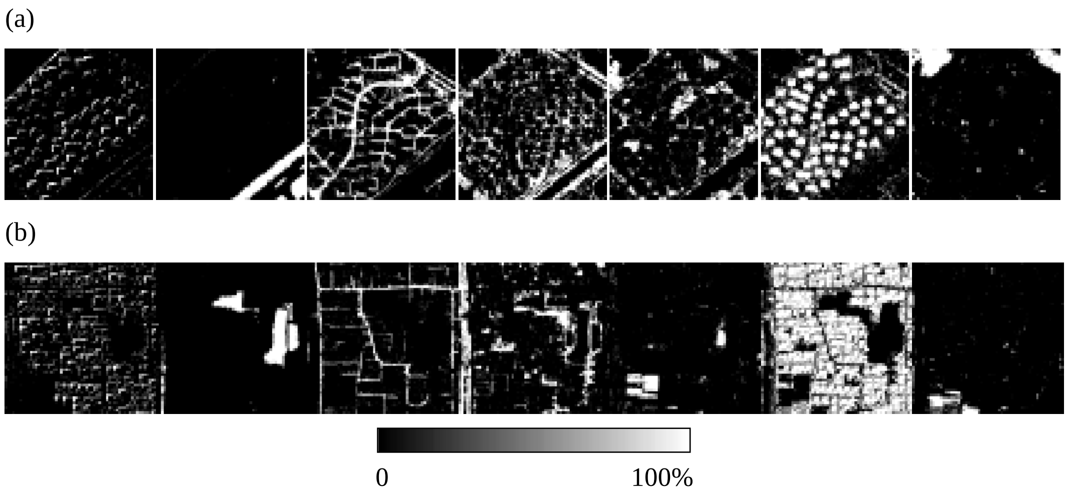

Figure 5.9. Proportion images of the seven classes in the simulated 5 m coarse spatial resolution images. From left to right: shadow, water, road, tree, grass, roof and bare soil. (a) Xuzhou suburb area. (b) Xuzhou urban center area.

Table 5.2 gives the classification accuracy of each class as well as the PCC for the four SPM methods. Again, the non-mixed pixels were not considered in the accuracy statistics. Regarding PSA, it produces higher accuracy for the shadow, road and tree classes and greater PCC than the ICK and NICK methods in the Xuzhou suburb area. In the Xuzhou urban center area, although PSA has higher accuracy for the water and road classes, the PCC of PSA is lower than for the ICK and NICK methods. Checking the values for SPSAM, it has higher accuracy for the bare soil class in the Xuzhou suburb area and the grass class in the Xuzhou urban center area than ICK and NICK, but the classification of the other six classes is less accurate. The overall accuracy of ICK and NICK is greater than that of SPSAM. Moreover, ICK and NICK have comparable accuracy for all seven classes.

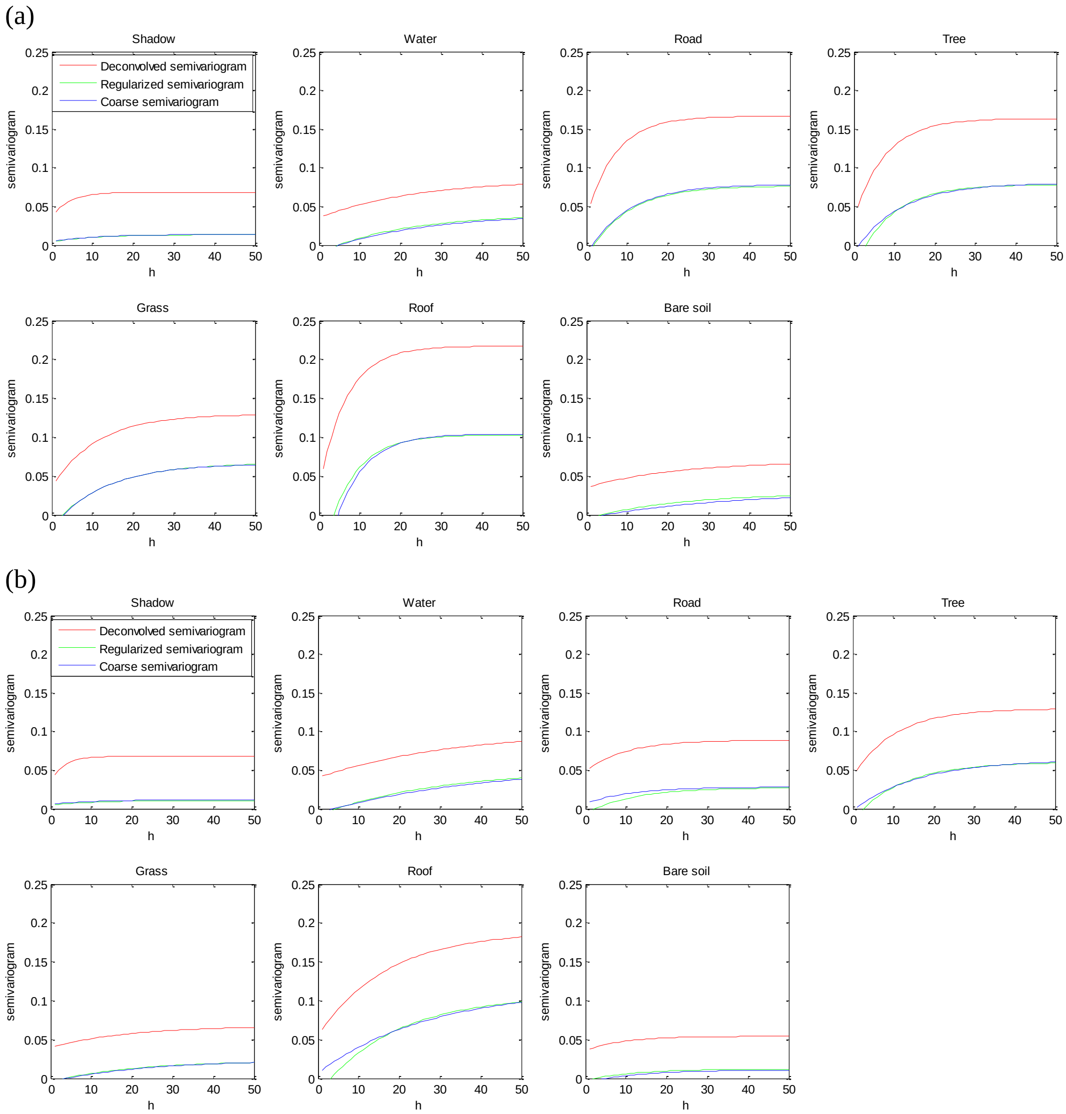

Figure 5.10. The fine spatial resolution semivariogram obtained by deconvolution in experiment 2 (S=8). The red, green and blue curves denote the fine spatial resolution semivariogram from deconvolution, regularized coarse spatial resolution semivariogram and coarse spatial resolution semivariogram extracted from the proportion image. (a) Xuzhou suburb area. (b) Xuzhou urban center area.

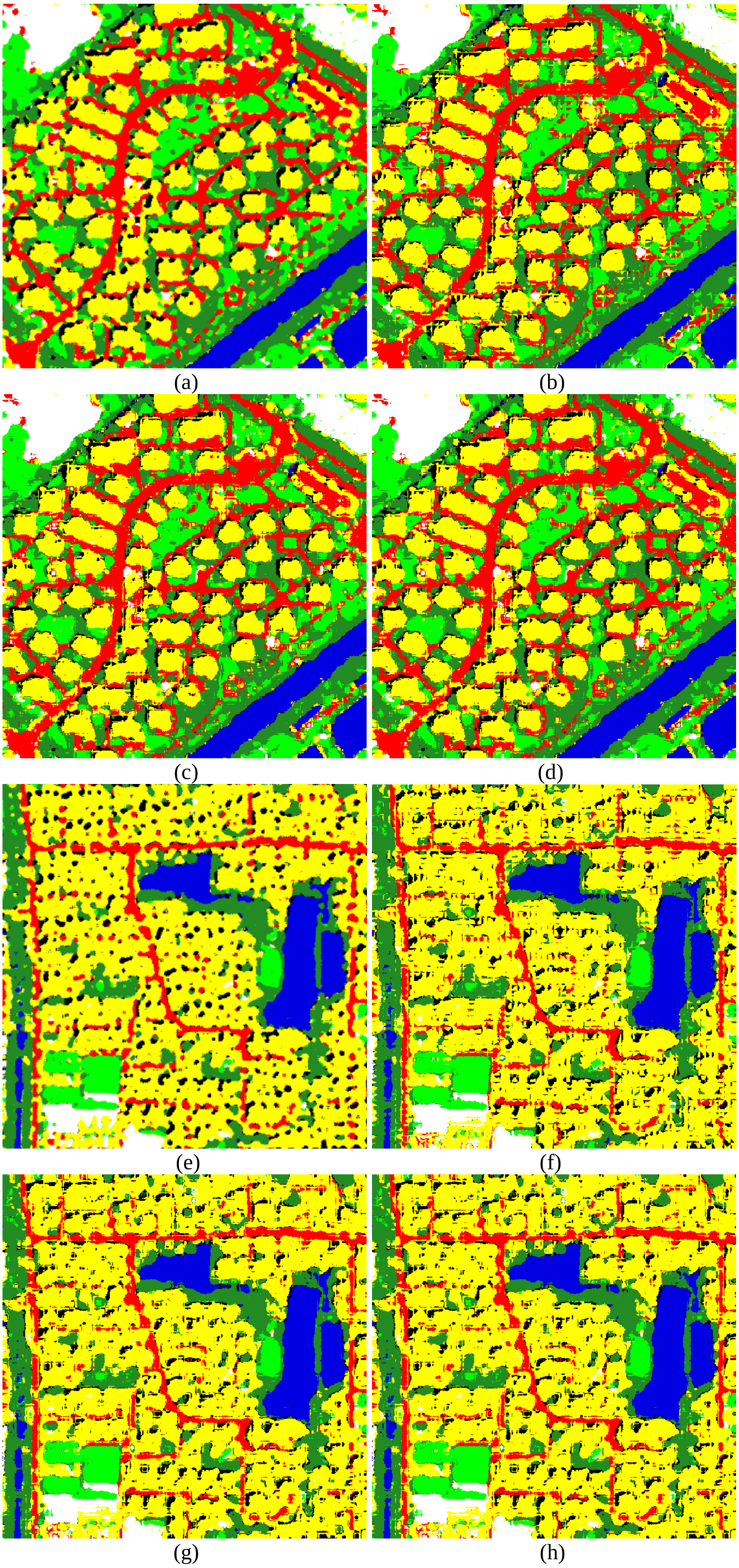

Figure 5.11. SPM results in experiment 2 (S=8). (a) and (e) PSA results. (b) and (f) SPSAM results. (c) and (g) ICK results. (d) and (h) NICK results. (a)-(d) Xuzhou suburb area results. (e)-(h) Xuzhou urban center area results.

Table 5.2 Accuracy (%) of SPM methods for the two Xuzhou areas in experiment 2 (S=8)

	Xuzhou suburb area				Xuzhou urban center area			
	PSA	SPSAM	ICK	NICK	PSA	SPSAM	ICK	NICK
Shadow	54.91	50.92	53.26	53.13	36.03	36.30	38.27	37.99
Water	90.90	91.04	91.20	91.25	85.93	85.34	85.26	85.29
Road	77.34	74.24	75.73	75.74	64.41	61.98	62.20	62.23
Tree	73.77	71.93	73.41	73.41	77.70	77.20	77.75	77.80
Grass	70.63	70.76	71.70	71.71	67.18	69.26	68.75	68.75
Roof	73.63	72.79	73.84	73.81	80.71	80.64	81.01	80.98
Bare soil	75.92	78.17	77.52	77.54	59.89	61.71	62.05	62.05
PCC	73.37	71.88	73.12	73.10	74.09	73.84	74.30	74.28

5.3.3. Experiment 3

A 30 m spatial resolution multispectral image acquired by the Landsat-7 enhanced thematic mapper plus (ETM+) sensor in August 2001 was used in this experiment. The image covers an area in the Liaoning Province, China and has a size of 400 by 400 pixels. Bands 1, 2, 3, 4, 5, and 7 of the Landsat image were used in the experiment. Four land cover classes were identified and we denote them as C1, C2, C3 and C4. The false color image is shown in Figure 5.12(a). The 30 m hard classified land cover map in Figure 5.12(b) was used as reference for SPM evaluation, which was generated by a maximum likelihood classification of the 30 m multispectral image (with an overall accuracy of over 90%).

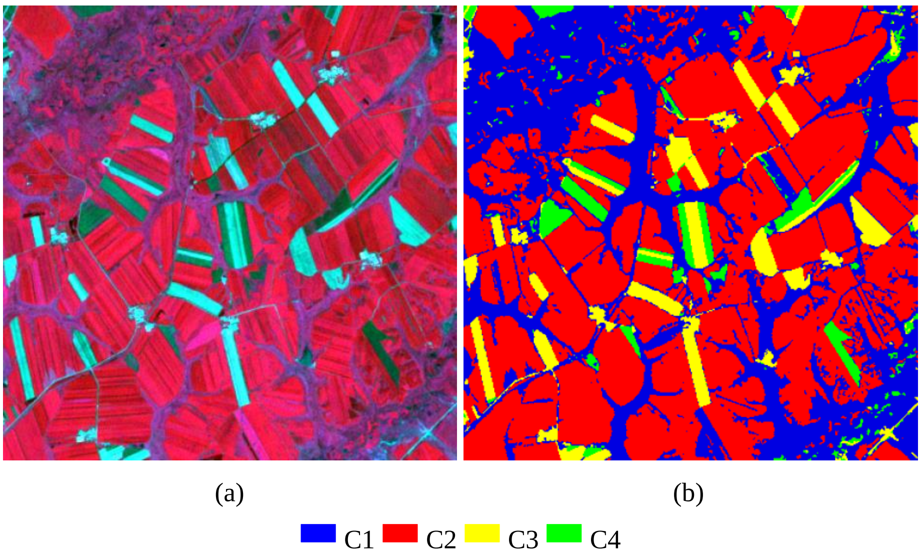

Figure 5.12. Landsat images used in experiment 3. (a) Original image (Bands 4, 3 and 2 as RGB). (b) Classified land cover map.

The 30 m multispectral image was degraded via an 8 by 8 pixel mean filter to simulate an image with coarse (240 m) spatial resolution, comparable to the spatial resolution of medium spatial resolution systems such as Moderate Resolution Imaging Spectroradiometer (MODIS). Fully constrained least squares linear spectral mixture analysis (Heinz and Chang, 2001; Wang et al., 2013) was employed for spectral unmixing. The predicted proportion images of the four classes are shown in Figure 5.13. Figure 5.13 is compared to the reference proportions (obtained by degrading Figure 5.12(b) with an 8 by 8 mean filter) by means of the RMSE. The values for C1, C2, C3 and C4 are 0.1930, 0.1551, 0.0555 and 0.1091, respectively, which are relatively small errors.

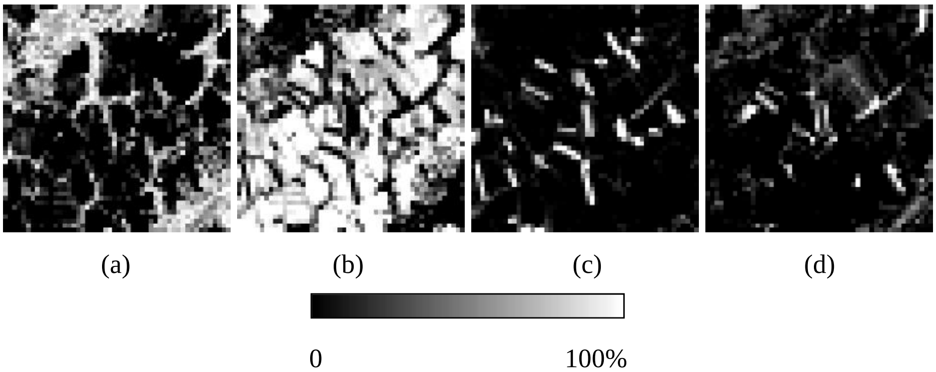

Figure 5.13. Proportion images of the four classes obtained by spectral unmixing of the 240 m coarse images in experiment 3. (a) C1. (b) C2. (c) C3. (d) C4.

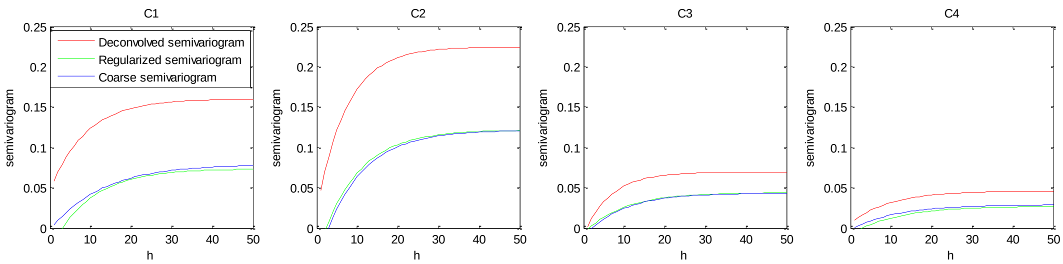

Figure 5.14. The fine spatial resolution semivariogram obtained by deconvolution in experiment 3 (S=8). The red, green and blue curves denote the fine spatial resolution semivariogram from deconvolution, regularized coarse spatial resolution semivariogram and coarse spatial resolution semivariogram extracted from the proportion image.

Figure 5.14 exhibits the deconvolved fine spatial resolution (30 m) semivariograms, along with the regularized coarse spatial resolution (240 m) semivariograms and target coarse semivariograms (240 m) extracted from Figure 5.13. For each class, the 240 m regularized semivariogram and target coarse semivariogram are very similar to each other. For the four classes, the differences between the deconvolved semivariograms and reference fine spatial resolution semivariograms extracted from Figure 5.12(b) are quantified by the RMSE, and the values are 0.0257, 0.0055, 0.0022 and 0.0046, suggesting that the deconvolved semivariograms are highly similar to the reference semivariograms. The high similarity is attributed mainly to the good semivariogram reconstruction ability of the deconvolution approach as well as the small errors in spectral unmixing in this experiment.

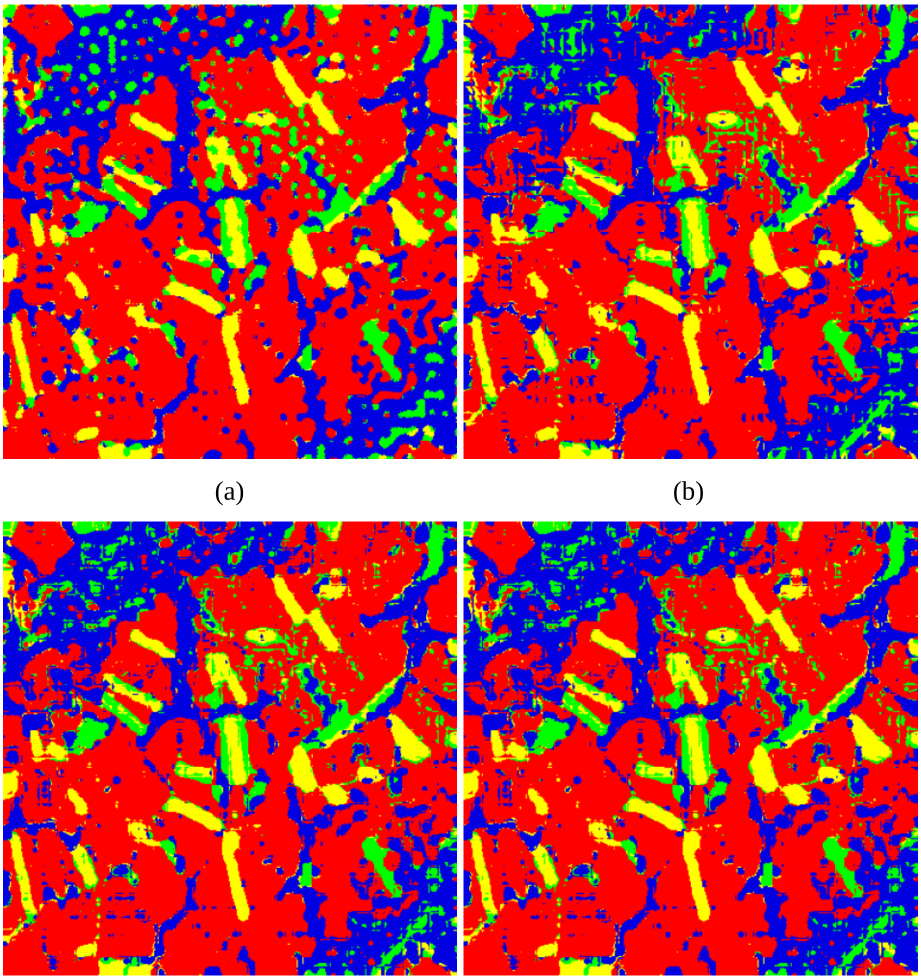

(a) (b) (c) (d)

Figure 5.15. SPM results in experiment 3 (*S*=8). (a) PSA result. (b) SPSAM result. (c) ICK result. (d) NICK result.

The SPM results of PSA, SPSAM, ICK and NICK methods (*S*=8) are provided in Figure 5.15. Again, ICK utilized the fine spatial resolution semivariograms extracted from the reference map in Figure 5.12(b). Similar to previous experiments, the PSA result appears to be locally smooth and the SPSAM result contains cone-shaped patches. Generally, the ICK and NICK results are visually more in agreement with the reference distribution of land cover in Figure 5.12(b). Table 5.3

lists the accuracy of the four SPM methods. Note that due to the inherent uncertainty in soft classification, in this experiment, all coarse pixels (including both mixed and non-mixed pixels) in Figure 5.13 were included in the accuracy statistics. PSA produces the greatest accuracy (i.e., 72.16%) for class C4 while SPSAM produces the greatest accuracy (i.e., 80.67%) for class C3. However, the overall accuracy in terms of PCC of ICK and NICK is greater than PSA and SPSAM.

Table 5.3 Accuracy (%) of SPM methods in experiment 3 (S=8)

	PSA	SPSAM	ICK	NICK
C1	61.85	61.71	62.01	62.00
C2	86.75	86.62	86.91	86.91
C3	80.17	80.67	80.43	80.38
C4	72.16	70.30	71.21	71.18
PCC	77.17	77.01	77.30	77.29

5.4. Discussion

5.4.1. Computing efficiency

The computing efficiency is an important factor for SPM algorithm evaluation. Table 5.4 lists the computing time of the four methods in each experiment. The computing burden of SPM algorithms is related to the image size and number of classes in the image. In the three experiments, SPSAM took the least time, as it is non-iterative and is based on simple multiplication. For PSA in each experiment, it took several minutes to converge to a satisfactory result. Both ICK and NICK are faster than PSA and need less than one minute in each experiment. Compared to ICK, NICK requires more time as it involves the extra deconvolution process.

Table 5.4 Computing time of SPM methods in experiments

	Size of coarse image	Zoom factor	Number of classes	PSA	SPSAM	ICK	NICK		
							Deconvolution	ICK	Total
Experiment 1	75×75	8	4	300s	15s	40s	17s	40s	57s
Experiment 2	60×60	8	7	210s	6s	50s	14s	50s	54s
Experiment 3	50×50	8	4	130s	2s	27s	16s	27s	43s

5.4.2. McNemar's test

In this section, McNemar's test was used to show the statistical significance in accuracy for different SPM methods. The McNemar's test results for the five test images are shown in Table 5.5, where f_{12} are the number of pixels that are correctly classified in result 1 but incorrectly classified in result 2 and f_{21} *vice versa*.. Using the 95% confidence level, the difference between two SPM results is considered to be statistically significant if $|Z|$>1.96. In each image, all pixels are included in the statistics for calculation of the *Z* values. As can be observed from the values, ICK and NICK are generally able to produce more statistically significant SPM results than PSA and SPSAM. As for the comparison between the ICK and NICK results, their differences are considered to be statistically insignificant in the experiments.

Table 5.5 McNemar's test for SPM methods in experiments

	Classifier 1	Classifier 2	f_{12}	f_{21}	Z_{12}
South Carolina	NICK	PSA	33309	28705	18.49
	NICK	SPSAM	25672	21799	17.78
	NICK	ICK	1249	1180	1.40
	ICK	PSA	33529	28994	18.14
	ICK	SPSAM	25785	21981	17.41
	SPSAM	PSA	34049	33318	2.82
Ohio	NICK	PSA	21487	19133	11.68
	NICK	SPSAM	16579	14386	12.46
	NICK	ICK	174	168	0.32
	ICK	PSA	21496	19148	11.65
	ICK	SPSAM	16634	14447	12.41
	SPSAM	PSA	21693	21532	0.77
Xuzhou suburb	NICK	PSA	15164	15653	-2.79
	NICK	SPSAM	12841	10561	14.90
	NICK	ICK	227	250	-1.05
	ICK	PSA	15139	15605	-2.66
	ICK	SPSAM	12825	10522	15.07
	SPSAM	PSA	15414	18183	-15.11
Xuzhou urban	NICK	PSA	16929	16569	1.97
	NICK	SPSAM	11918	11075	5.56
	NICK	ICK	611	655	-1.24
	ICK	PSA	16906	16502	2.21
	ICK	SPSAM	11923	11036	5.85
	SPSAM	PSA	17020	17503	-2.60
Liaoning	NICK	PSA	9342	9153	1.39
	NICK	SPSAM	7217	6777	3.72
	NICK	ICK	45	58	-1.28
	ICK	PSA	9344	9142	1.49
	ICK	SPSAM	7213	6760	3.83
	SPSAM	PSA	9651	9902	-1.80

5.4.3. Difference between the semivariograms used in NICK and ICK

NICK does not need training images and uses the semivariogram obtained by deconvolution, based on the input proportion images for SPM. As mentioned in the introduction, the spatial structure information used in ICK-based SPM should be defined at the target spatial resolution and be representative of the study area for SPM. In Section 5.2.2, it was demonstrated that deconvolution provides a suitable means of converting the coarse spatial resolution semivariogram to the desired fine spatial resolution semivariogram. Thus, in the example given, the mis-match between the desired spatial resolution of the target semivariogram and the coarse spatial resolution of the available data was addressed by NICK. This necessitates a discussion of how the spatial structure characterized by the deconvolved fine spatial resolution semivariogram matches that of the reference fine spatial resolution semivariogram. This was investigated by analyzing the differences between the two types of semivariograms, measured by the RMSE. In the experiments, the deconvolved semivariogram was used in NICK while the reference semivariogram was used in ICK.

The South Carolina and Ohio maps were used for the analysis. The RMSE values for five zoom factors (i.e., S=4, 6, 8, 10 and 12) and four classes in the two areas are shown in Figure 5.16. The RMSE between the two types of semivariograms increases in general as S increases, because the uncertainty in deconvolution increases correspondingly. Nevertheless, the RMSE values presented in the figure are not very large, and are very small for small zoom factors. For the South Carolina map, most of the values are less than 0.05 and for the Ohio map, the values are less than 0.02 for the urban, agriculture and forest classes. This indicates a relatively high degree of similarity between the two types of semivariograms. Hence, the spatial structure of classes characterized by the deconvolved fine spatial resolution semivariograms may be considered to be representative of the study area, especially for a small zoom factor in the experiment.

As can be found from the PCC of ICK and NICK, the two methods have similar accuracy. The accuracy of the two ICK-based SPM methods is related mainly to class probability estimation, which is determined by two parts: proportions and weights that are calculated based on the semivariogram. In ICK and NICK, the proportions are exactly the same, since they are performed on the same input coarse spatial resolution images. With respect to the two sets of weights in the ICK and NICK methods, they are derived from the semivariograms obtained by deconvolution and those extracted from the fine spatial resolution training images (reference land cover maps in the experiments), respectively. The two types of semivariograms used in ICK and NICK are close to each other, as can be found from Figure 5.16 and as discussed above. The similar accuracy of the two methods in the experiments is, thus, attributed to the same proportions and similar semivariograms used.

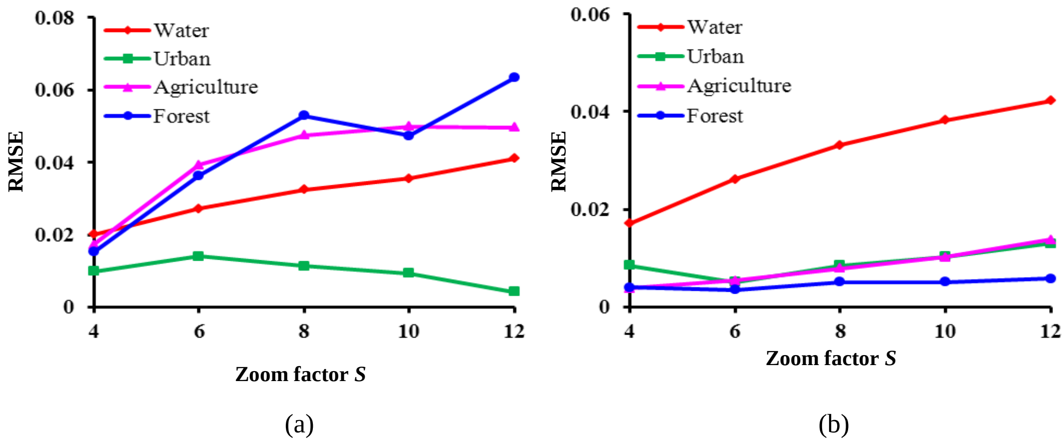

Figure 5.16. RMSE between the fine spatial resolution semivariogram estimated by deconvolution and that extracted from fine spatial resolution training images. (a) South Carolina. (b) Ohio.

5.4.4. Characteristics of NICK

In Section 3.1.1, it was mentioned that the ICK-based SPM method holds several advantages. Few parameters are involved in this model and it is non-iterative as the probabilities of class occurrence in sub-pixels are predicted by solving a system of equations via ICK. NICK has the same probability calculation process as ICK and, thus, the same benefits. The experimental results show that NICK consistently produces comparable SPM accuracy to ICK, and higher accuracy than the well-known SPSAM method. The difference between the original ICK and the proposed NICK method is the means of acquiring the required semivariogram. The acquisition of the semivariogram for NICK is realized by mining fully the available information in the coarse spatial resolution proportion images and does not require prior spatial structure information or training images. The deconvolution process in NICK is iterative and introduces several parameters, such as the number of iterations and threshold for the stopping condition. Therefore, the introduced iteration process and parameters are the cost of not using prior spatial structure information for NICK. Nevertheless, we can conclude that NICK inherits the advantage of ICK in terms of SPM accuracy, and more importantly, extends ICK to cases where the prior spatial structure information is unavailable. For these reasons, the newly developed geostatistics-based SPM method has great potential in real applications.

5.5. Summary

This chapter presents a NICK-based SPM method, in which the semivariogram used for ICK-derived probability prediction is obtained by deconvolving the semivariogram extracted from the input coarse spatial resolution proportion images, rather than additional fine spatial resolution training images as in the original ICK method. Experimental results reveal that it is feasible to estimate the fine spatial resolution semivariogram by deconvolution for ICK-based SPM. The semivariogram observed at a coarse spatial resolution can be converted to the one required at the target fine spatial resolution such as to characterize the spatial structure of land cover, representative of the study area. Tested with three groups of remote sensing images, the results of the new ICK method were found to have comparable SPM accuracy to the original ICK method. Thus, the proposed method enables the application of ICK in cases where no prior spatial structure information exists.

6. STHSPM for fast sub-pixel resolution change detection

(This chapter is based on Wang *et al.* (2015b))

6.1. Introduction

Due to rapid changes on the Earth's surface, it is important to perform CD at a fine spatial and fine temporal resolution. However, remote sensing images with both fine spatial and temporal resolution are commonly not available or where available, may be expensive to obtain. This chapter attempts to achieve fine spatial and temporal resolution land cover CD with a new computer technology based on SPM. The objective of this chapter was to develop fast SPM algorithms (i.e., STHSPM algorithms) for sub-pixel resolution CD. For the first time, five fast STHSPM algorithms, including bilinear interpolation-, bicubic interpolation-, SPSAM-, Kriging-, and radial basis function (RBF, see Chapter 4) interpolation-based SPM methods, are proposed for fine spatial and temporal resolution CD. Besides the low computational burden, these five algorithms also have the advantage of not requiring prior class information on spatial structure.

Similar to spatiotemporal fusion, in this chapter, the aforementioned five fast STHSPM algorithms for sub-pixel CD are developed based on the availability of fine spatial, but coarse temporal resolution information. Unlike spatiotemporal fusion, however, the objective of the five STHSPM algorithms was to generate fine spatial resolution sub-pixel land cover maps, which were then compared to monitor land cover changes at both fine spatial and temporal resolution. We consider borrowing information from the thematic land cover map of the known fine spatial resolution image, that is, FRM (Ling et al., 2011), to decrease the uncertainty in SPM of coarse resolution images and further increase the accuracy of CD.

The main contributions of this chapter are summarized as follows.

1) A framework of fast STHSPM algorithms is proposed for sub-pixel resolution CD. The fast STHSPM algorithm uses fine spatial resolution thematic information from an FRM for SPM of coarse images.
2) Different from Ling et al. (2011) that only used FRM in the "former FRM and

latter coarse image" case, the FRM is also considered in the "former coarse image and latter FRM" case and sub-pixel resolution CD between coarse images.

6.2. Methods

6.2.1. Incorporating an FRM in SPM and sub-pixel resolution CD

As was done in Foody and Doan (2007), the sub-pixel resolution CD can be realized straightforwardly by SPM of multitemporal coarse spatial resolution images of the same area first and then comparing the generated sub-pixel maps to monitor changes. However, the SPM problem is always under-determined, with many multiple plausible solutions that can lead to an equally coherent recreation of the input coarse proportion image. Applying SPM to CD without any auxiliary information will result in many errors in the form of noise. In fact, for SPM of a single date image, the accuracy can be enhanced by borrowing information from images before it and after it in time (Atkinson, 2013). Such a scheme would be helpful to separate real changes from noise. Some studies demonstrated how to borrow information from coarse spatial resolution time-series images to enhance SPM (Ling et al., 2010; Muad and Foody, 2012b; Wang and Wang, 2013). Those studies, however, focused on enhancing SPM and were conducted with the assumption that there are no changes between the utilized coarse spatial resolution images.

Ling et al. (2011) presented a method on using FRM to enhance sub-pixel resolution CD. In that study, however, only the historical FRM case was considered and also the sub-pixel resolution CD was implemented between different spatial resolution images (e.g., former Landsat and latter MODIS images). More importantly, different from the iterative PSA in Ling et al. (2011), non-iterative and fast sub-pixel resolution CD algorithms are proposed in this chapter.

This chapter extends the utilization of FRM to the following two cases.

1) The data acquisition date of the FRM is after that of the coarse spatial resolution image. Sometimes, users want to detect changes from a date earlier than that of the FRM and only a coarse spatial resolution image is available on that date. It is, therefore, necessary to develop methods for SPM of former coarse spatial resolution images with the aid of a latter FRM.

2) Sub-pixel resolution CD is implemented between images with the same coarse spatial resolution and the SPM results of both coarse images are obtained with the aid of the FRM. For CD during a certain period, on both the start and end days, there may be only coarse spatial resolution images. To detect changes at fine spatial resolution during that period necessitates the construction of SPM methods for those coarse resolution images.

The core idea of enhancing sub-pixel resolution CD with an FRM is to use the spatial distribution of sub-pixel classes in the FRM to modify the SPM results of coarse spatial resolution images on other dates. Specifically, the spectral unmixing-derived class proportion of each class within each coarse pixel is compared to the corresponding one (obtained by degradation) in the available FRM. According to the differences in the proportions, some locations at sub-pixel resolution are determined to be changed or unchanged for the class and correspondingly, some sub-pixels are considered to belong or not belong to the class.

Suppose P_j ($j=1,2,...,M$, M is the number of pixels in the coarse image) is a coarse pixel, and $F_k(P_j)$ is the coarse proportion of class k ($k=1,2,...,K$, K is the number of land cover classes in the study area) for pixel P_j. Let S (S>1) be the spatial resolution ratio between the coarse image and the FRM. The steps of incorporating the FRM in SPM are given below. Meanwhile, an example is provided in Figure 6.1 to facilitate the illustration. In Figure 6.1, a single coarse pixel and land cover information for class k is considered.

1) The FRM is degraded via an S by S mean filter (i.e., every S by S fine pixels are degraded to a coarse pixel) to synthesize the K coarse proportion images and the proportion for class k at pixel P_j, denoted as $F_{k\_H}(P_j)$.

2) The differences in proportions $\Delta_k(P_j)$ are calculated

$$\Delta_k(P_j) = F_k(P_j) - F_{k\_H}(P_j) \tag{6.1}$$

3) The changed and unchanged sub-pixel locations for each class are determined. The following three cases are taken into consideration.

a) If $\Delta_k(P_j)=0$, there is no change for class k, and the spatial distribution of class k within P_j in the coarse image is the same as that in FRM (e.g., the gray area in Figure 6.1).

b) If $\Delta_k(P_j)>0$, the locations of fine pixels for class k in the FRM (e.g., the gray area in Figure 6.1) are still assigned to class *k* in the coarse image, and some sub-pixels at the remaining locations are changed to class *k*.

c) If $\Delta_k(P_j) < 0$, all sub-pixels for class *k* in the coarse image are within the area for class *k* in the FRM, and some sub-pixels within that area are changed to other classes.

4) The abovementioned steps are implemented for all *M* coarse pixels and all *K* classes in the coarse image to generate the SPM result.

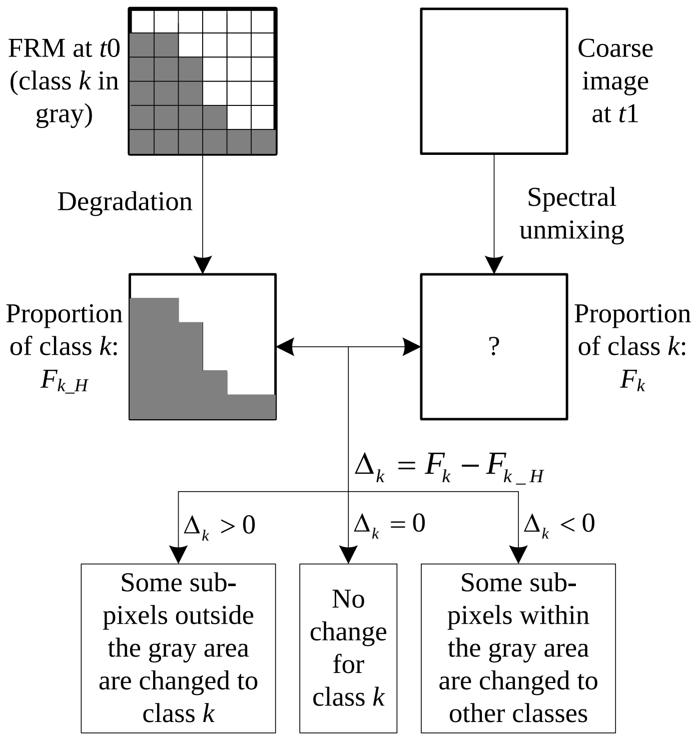

Figure 6.1. Illustration of incorporating an FRM in SPM, where a single coarse pixel and class *k* is considered.

As seen from Figure 6.1 and the steps mentioned above, the available FRM can be applied to SPM of the coarse image that is acquired either before or after the FRM. Moreover, the FRM can be used for SPM of multitemporal coarse images (see Figure 6.2). Finally, the generated SPM results can be compared for the purpose of fine spatial and temporal resolution CD.

The critical step in utilizing an FRM in SPM is to determine which sub-pixels at the remaining locations are changed to class *k* ($k = 1, 2, ..., K$) when $\Delta_k(P_j) > 0$, and which sub-pixels that are within the area for class *k* in the FRM are changed to other classes when $\Delta_k(P_j) < 0$. In this chapter, those sub-pixels are found using the five fast STHSPM algorithms.

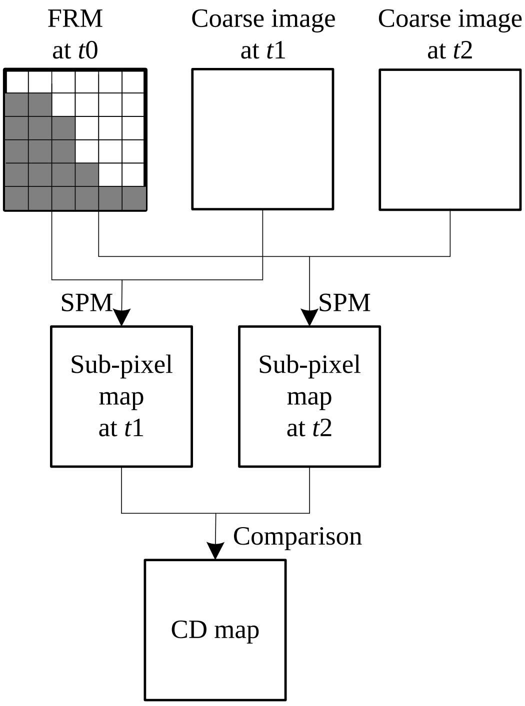

Figure 6.2. CD between multitemporal coarse images with FRM.

6.2.2. Fast STHSPM algorithms

The STHSPM algorithm is a type of SPM algorithm that first estimates the soft class values and then allocates a hard class to each sub-pixel. This chapter focuses on five non-iterative and fast STHSPM algorithms: bilinear interpolation, bicubic interpolation, SPSAM, Kriging and RBF interpolation methods.

Similar to Section 6.2.1, S denotes the zoom factor for SPM (i.e., each coarse pixel is divided into S by S sub-pixels). Suppose $p_{j,i}$ is the sub-pixel within coarse pixel P_j, and $F_k(p_{j,i})$ ($0 \le F_k(p_{j,i}) \le 1$) is the soft class value for class k at sub-pixel $p_{j,i}$. With the coarse proportion images as input, the task of soft class value estimation is to estimate $\left\{F_k(p_{j,i}) \middle| i=1,2,...,S^2; j=1,2,...,M; k=1,2,...,K\right\}$ at the target fine spatial resolution. The soft class values are estimated based on the assumption of spatial dependence as described above for the STHSPM algorithms. The preliminary soft attribute values obtained by each of the five STHSPM algorithms are normalized to fall within [0, 1].

Let $B_k(p_{j,i})$ be the binary class value

$$B_k(p_{j,i}) = \begin{cases} 1, \text{ if sub-pixel } p_{j,i} \text{ belongs to class } k \\ 0, \text{ otherwise} \end{cases} \tag{6.2}$$

For a particular coarse pixel, say P_j, the number of sub-pixels for class k, $E_k(P_j)$, is calculated by

$$E_k(P_j) = \text{round}(F_k(P_j)S^2) \tag{6.3}$$

where round(•) is a function that takes the integer nearest to •. The sum of the numbers of sub-pixels for all K classes is S^2. The hard class allocation step of the STHSPM algorithm aims to predict $\left\{B_k(p_{j,i}) \middle| i=1,2,...,S^2; j=1,2,...,M; k=1,2,...,K\right\}$, according to the soft class values and class proportions constraint in (6.3). The UOC approach proposed in Section 2.1 is employed.

6.2.3. STHSPM algorithm-based CD with an FRM

For the UOC-based class allocation method in the STHSPM algorithm, a sub-pixel map of each class is generated in turn and these maps are integrated to produce the SPM result. Suppose that the soft class values have already been estimated by any of the five STHSPM algorithms. Using an FRM as auxiliary information in STHSPM, for class k ($k = 1, 2, ..., K$), the sub-pixel map is predicted by comparison of the soft class values at the remaining locations (e.g., outside the gray area in Figure 6.1) when $\Delta_k(P_j) > 0$, and the soft class values within the area for class k in the FRM (e.g., the gray area in Figure 6.1) when $\Delta_k(P_j) < 0$. Sub-pixels with larger soft class values for class k are more likely to be allocated to class k. During the process, two constraints imposed inherently by the SPM problem need to be satisfied:

1) Each sub-pixel should be assigned to only one class.
2) The number of sub-pixels for each class should be consistent with the coarse proportion data (see (6.3)).

To meet the abovementioned constraints, two adjustments, both of which are essential for UOC-based class allocation when using an FRM, are presented.

Adjustment I. Within a coarse pixel, besides $\Delta_k(P_j) > 0$, sometimes there are other classes (e.g., class k') with $\Delta_{k'}(P_j) \geq 0$. Similarly, the corresponding locations in the FRM for class k' should still be assigned to this class in the coarse image. For the $\Delta_k(P_j) > 0$ case, at the remaining locations, the sub-pixels with the largest soft class values for class k may be those which should be assigned to class k'. Figure 6.3 gives an example to illustrate this issue. Let us consider two classes (i.e., red and blue) within a single coarse pixel, and $\Delta_{Red} = \frac{4}{36}$ and $\Delta_{Blue} > 0$. The red class is assumed to be visited before the blue class. Figure 6.3(a) is the FRM map for the two classes. By zooming with S=6, four sub-pixels should be allocated to the red class outside the red area when using the FRM. According to the soft class values in Figure 6.3(b), the four sub-pixels with the largest values (marked in red) are assigned to the red class. As $\Delta_{Blue} > 0$, however, all six blue sub-pixels should not change and should still be retained for the blue class during class allocation for the red class. In this case, the two sub-pixels with values 0.9 and 0.95 should not be assigned to the red class. To avoid such conflict, adjustment I is applied: the soft class values for the red class in the blue area need to be suppressed to be a very small value (any value less than 0) to ensure that the blue sub-pixels will not be allocated to the red class during class allocation. Meanwhile, the soft class values for the red class in the red area can also be modified to a very large value (any value greater than 1). After the adjustment, as seen in Figure 6.3(c), no blue pixels are allocated to the red class, but another two sub-pixels with values 0.65 and 0.6 (marked in red) are allocated instead.

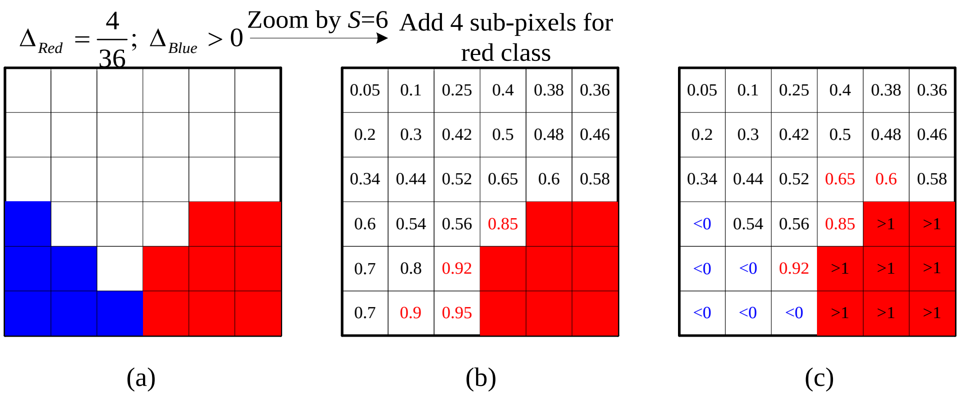

Figure 6.3. An example to illustrate the adjustment (adjustment I) of soft class values to avoid class allocation conflict between classes. (a) FRM map for the blue and red classes. (b) Class allocation result for the red class without adjustment I. (c) Class allocation result for the red class with adjustment I.

Adjustment II. Another example is provided in Figure 6.4 to facilitate description. Again, the red and blue classes within a single coarse pixel are considered, and $\Delta_{Red} = \frac{4}{36}$ and $\Delta_{Blue} = -\frac{1}{36}$. Assume that the calculated Moran index of the red class is larger than that of the blue class and the red class should be visited before the blue class. With S=6, four sub-pixels should be allocated to the red class outside the red area in Figure 6.4(a). Figure 6.4(b) marks the four soft class values of the four added sub-pixels for the red class. However, $\Delta_{Blue} = -\frac{1}{36}$ means that of the six blue sub-pixels, five of them should still belong to the blue class. Therefore, at least one of the two sub-pixels with values 0.9 and 0.95 should not be assigned to the red class. To address this issue, adjustment II is applied: any class (e.g., class k') with $\Delta_{k'}(P_j) < 0$ needs to be visited before the class (e.g., class k) with $\Delta_k(P_j) \geq 0$. Figure 6.4(c) shows the class allocation result for the red class, where the sub-pixel with value 0.95 is assumed not to belong to the blue class (according to the soft class values for the blue class) and the four added sub-pixels for the red class are marked in red.

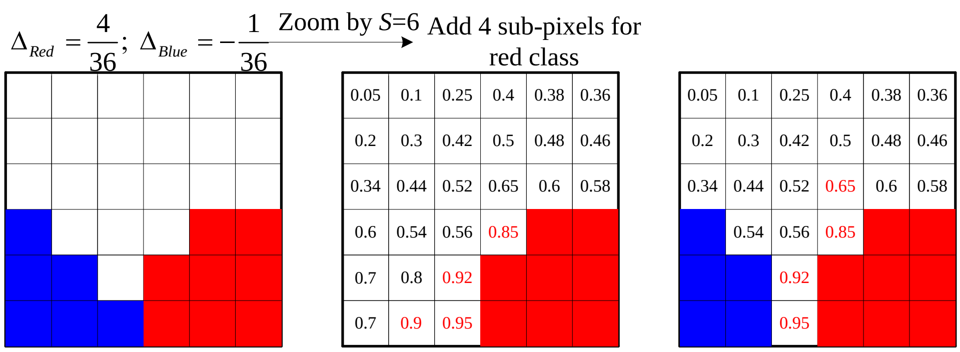

(a) (b) (c)

Figure 6.4. An example to illustrate the adjustment (adjustment II) of visiting order of classes. (a) FRM map for the blue and red classes. (b) Class allocation result for the red class without adjustment I. (c) Class allocation result for the red class with adjustment II.

6.2.4. Implementation of STHSPM algorithm-based CD with an FRM

The implementation steps of the proposed STHSPM-based algorithm for CD with an FRM are given here. Let us first take the former FRM (at $t0$) and latter coarse image (at $t1$) case as an example.

Step 1) Spectral unmixing is conducted on the coarse image at $t1$, and the outputs are a set of coarse proportion images of classes (i.e., $\{F_k(P_j) \mid j = 1, 2, ..., M; k = 1, 2, ..., K\}$).

Step 2) The coarse proportion images are downscaled with any of the five STHSPM algorithms, and the outputs are soft class values at the target fine spatial resolution (i.e.,

$$\{F_k(p_{j,i}) \mid i=1,2,...,S^2;\ j=1,2,...,M;\ k=1,2,...,K\}).$$

Step 3) Using the available FRM, UOC-based class allocation for the STHSPM algorithm is implemented to produce a SPM result at $t1$, where Adjustment I and Adjustment II are essential.

Step 4) The predicted SPM result at $t1$ is compared with the FRM at $t0$ in terms of class labels for CD analysis.

For the former coarse image (at $t0$) and latter FRM (at $t1$) case, the steps are the same as listed above. With respect to the sup-pixel resolution CD between coarse images at, say, $t1$ and $t2$, the FRM at another time (e.g., $t0$) is used for SPM of both coarse images independently, according to the abovementioned steps. The generated SPM results at $t1$ and $t2$ are finally compared for CD, as shown in Figure 6.2.

The pseudocode of UOC-based class allocation for STHSPM algorithm with an FRM is given below. Figure 6.5 exhibits an example of the whole flowchart of the proposed STHSPM algorithm with an FRM. The whole process does not involve any iteration.

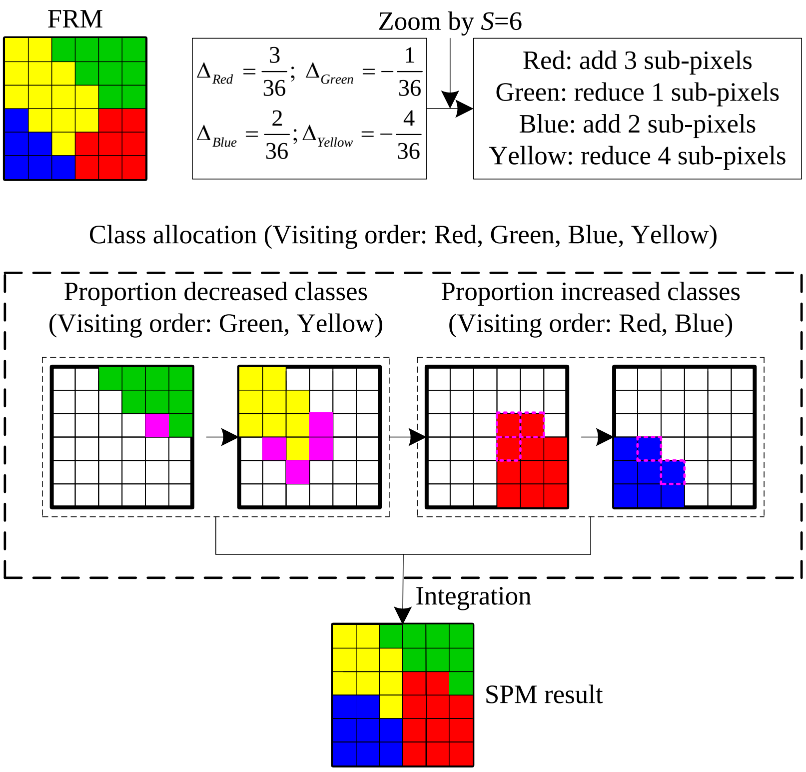

Figure 6.5. An example of the whole flowchart of incorporating an FRM in STHSPM, where the deep pink sub-pixels are those not allocated to the green or yellow class.

Algorithm: UOC-based class allocation for STHSPM algorithm with an FRM

Inputs: FRM; Class proportions $\left\{F_k(P_j)\middle| j=1,...,M; k=1,...,K\right\}$;

Soft class values $\left\{F_k(p_{j,i})\middle| i=1,...,S^2; j=1,...,M; k=1,...,K\right\}$

Define a visiting order of K classes $\boldsymbol{W}=[W_1, W_2, ..., W_K]$

for j = 1: M

for k = 1: K

Calculate $\Delta_k(P_j)$ using (6.1)

endfor

Find the classes with negative proportion differences (i.e., $\Delta < 0$) and find their visiting order from $\boldsymbol{W}$: $U_1, U_2, ..., U_m$

Find the classes with non-negative proportion differences (i.e., $\Delta \geq 0$) and find their visiting order from $\boldsymbol{W}$: $V_1, V_2, ..., V_l$

for k = 1: m

for i = 1: S^2

if in FRM $B_{U_k}(p_{j,i})=0$

$F_{U_k}(p_{j,i})$ is modified to be any value less than 0

endif

endfor

Find the $E_{U_k}(P_j)$ largest values among $F_{U_k}(p_{j,1}), F_{U_k}(p_{j,2}), ..., F_{U_k}(p_{j,S^2})$ and the corresponding sub-pixels are allocated to class U_k

endfor

Sub-pixels that have been allocated to any class of $U_1, U_2, ..., U_m$ are not considered for the remaining classes

for k = 1: l

for i = 1: S^2

if in FRM $B_{V_k}(p_{j,i})=1$

$F_{V_k}(p_{j,i})$ is modified to be any value greater than 1

endif

if in FRM $B_{V_{k'}\neq V_k}(p_{j,i})=1$

$F_{V_{k'}\neq V_k}(p_{j,i})$ is modified to be any value less than 0

endif

endfor

Find the $E_{V_k}(P_j)$ largest values among $F_{V_k}(p_{j,1}), F_{V_k}(p_{j,2}), ..., F_{V_k}(p_{j,S^2})$ and the corresponding sub-pixels are allocated to class V_k

Sub-pixels that have been allocated to class V_k are not considered for the remaining classes

endfor

endfor

Outputs: Binary class values $\left\{B_k(p_{j,i})\middle| i=1,...,S^2; j=1,...,M; k=1,...,K\right\}$

6.3. Experiments

Three datasets were used in three experiments for validation of the proposed five sub-pixel resolution CD methods. For the SPSAM and Kriging methods, the window sizes of the neighborhood were set to 3 and 5, as suggested by the repeated test. The parameters of the RBF method were set according to the parameter analysis in Chapter 4: the parameter in the basis function was set to 10 and the window size of the neighborhood was set to 5.

6.3.1. Experiment on synthetic coarse proportion images

1) Dataset

To control the analysis, a synthetic dataset was used in this experiment to test the proposed five STHSPM algorithm-based CD methods with an FRM. Specifically, three Landsat images with 30 m spatial resolution acquired on three different days were classified to produce three 30 m land cover maps. One of the maps was used as the FRM. The coarse proportion images were created by degrading the other two 30 m classified maps via an S by S mean filter. SPM methods were implemented to recreate the 30 m land cover maps, by zooming in the proportion images with a zoom factor S. The generated SPM results were compared to the FRM or they were compared mutually for CD analysis. The advantages of using synthetic coarse images are that the input proportions are error free and represent greater control in the test. Although this scheme does not represent a sufficiently real test of SPM and CD algorithms, the reference map is known perfectly and can be used to assess the accuracy of SPM prediction and CD. The test is directed at the SPM algorithm itself which is appropriate at the method development stage (Atkinson, 2009).

The three 30 m Landsat images cover an area in Shenzhen, China. Registration and relative radiometric correction were conducted on the Landsat images. The selected study area is a heterogeneous region with 250 by 250 pixels and covers mainly four land cover classes: vegetation, forest, urban and water. The three images were acquired on 20 Nov 2001 (t0), 7 Nov 2002 (t1) and 23 Nov 2005 (t2), respectively. The images were classified with a supervised neural network to generate the 30 m reference land cover maps. The classification accuracy for all t0, t1 and t2 reference maps was over 90%. Figure 6.6 shows the three images and their corresponding classified land cover maps used as reference. The reference change maps from t0 to t1 and t1 to t2 are shown in Figure 6.7, in which “CA to CB” means that the pixel belongs to class A at the former time but changes to class B at the latter time.

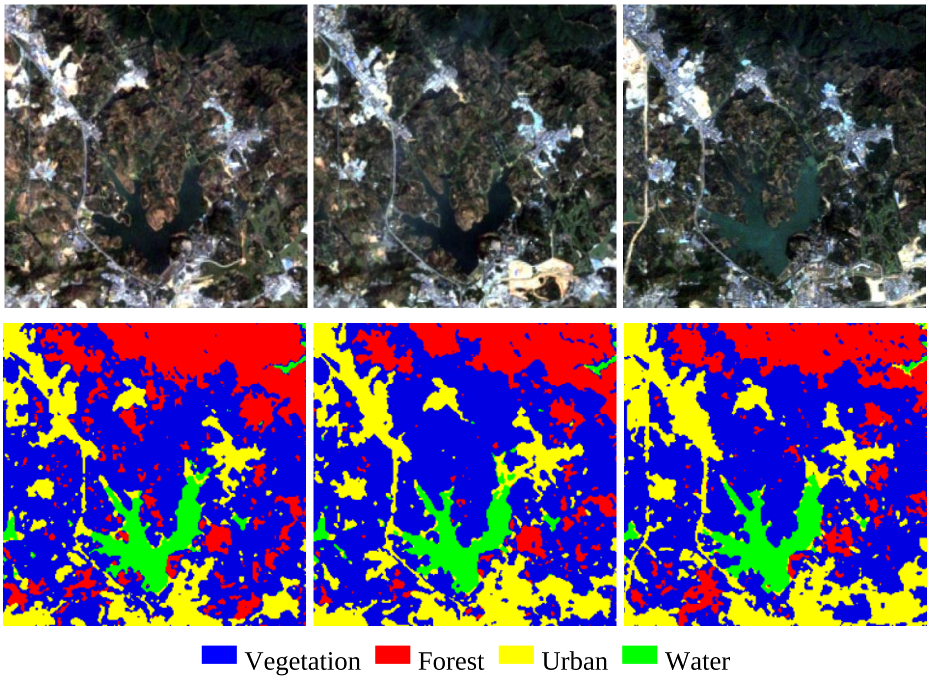

Figure 6.6. Three Landsat images in Shenzhen, China on three dates. From left to right: $t0$ on 20 Nov 2001, $t1$ on 7 Nov 2002, $t2$ on 23 Nov 2005. Line 1: Color image (Bands 3, 2 and 1 as RGB). Line 2: Hard classified land cover maps.

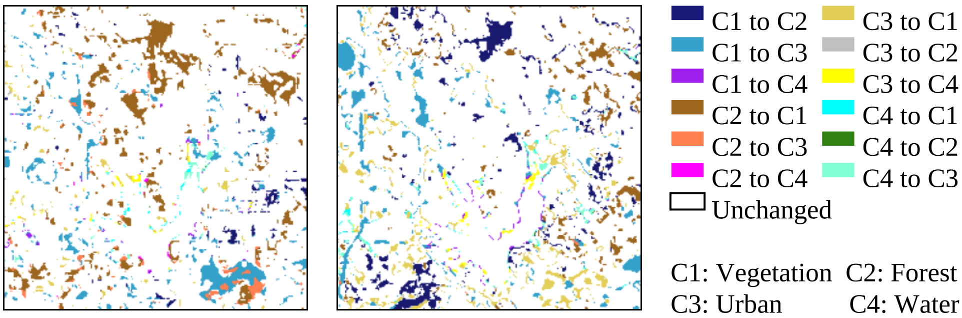

(a) (b)

Figure 6.7. Reference change maps. (a) From $t0$ to $t1$. (b) From $t1$ to $t2$.

2) Benefits of using an FRM in CD

The changes from $t0$ to $t1$ were tested in this subsection. The 30 m reference land cover map at $t0$ was used as an FRM and the reference map at $t1$ was degraded to synthesize coarse proportion images at $t1$. The 30 m map at $t1$ was degraded with five mean filters, 5 by 5, 8 by 8, 10 by 10, 12 by 12 and 15 by 15 pixels, to simulate proportion images with spatial resolutions of 150 m, 240 m, 300 m, 360 m and 450 m. The five STHSPM algorithms were applied to restore the 30 m land cover map, and then compared with the $t0$ reference map for CD.

Figure 6.8 shows the proportion images of four classes at 240 m spatial resolution, comparable to the spatial resolution of medium spatial resolution systems such as MODIS. As can be observed, the land cover information presented in these 240 m images is limited and insufficient for CD analysis. With these images as input and a zoom factor *S*=8, the five STHSPM algorithms were implemented. The results are given in Figure 6.9, where results of both the original version (i.e., without an FRM) and new version (i.e., with an FRM) algorithms are provided. The CD map for each method is also exhibited. For five original STHSPM algorithms without FRM, there are many linear artifacts and isolated pixels in the generated 30 m land cover maps, especially for the forest and urban classes. Consequently, many pixels are incorrectly identified as changed pixels when compared to the 30 m map at *t*0 time, as seen from the CD results in the second column in Figure 6.9. Focusing on the maps of the new version STHSPM algorithms in the third column, however, we can see with the aid of the FRM, the generated SPM results are much closer to the reference map at *t*1 in Figure 6.6. The elongated features of urban class are well restored and the boundaries of each class are smoother than those for the original STHSPM algorithms. Correspondingly, while referring to Figure 6.7(a), the CD maps of STHSPM algorithms with an FRM in the fourth column are found to be very close to the reference CD map (see, for example, the distribution of the “vegetation to urban” and “water to vegetation” classes). Visual comparison confirms the benefit of using an FRM in STHSPM algorithm-based CD.

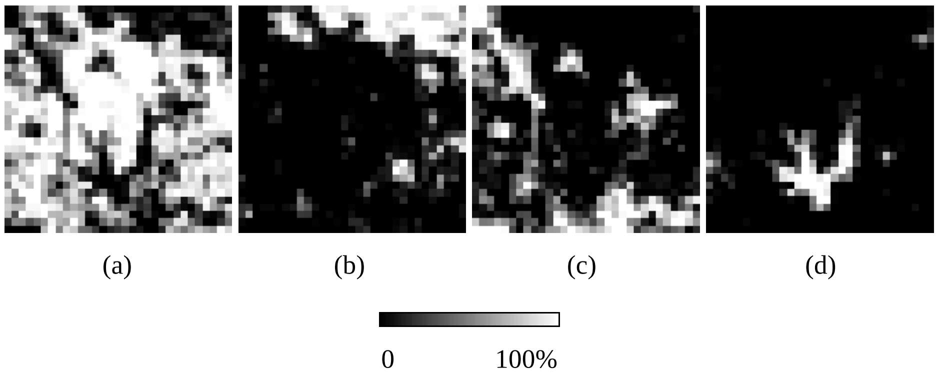

Figure 6.8. Proportion images of the four classes at *t*1. (a) Vegetation. (b) Forest. (c) Urban. (d) Water.

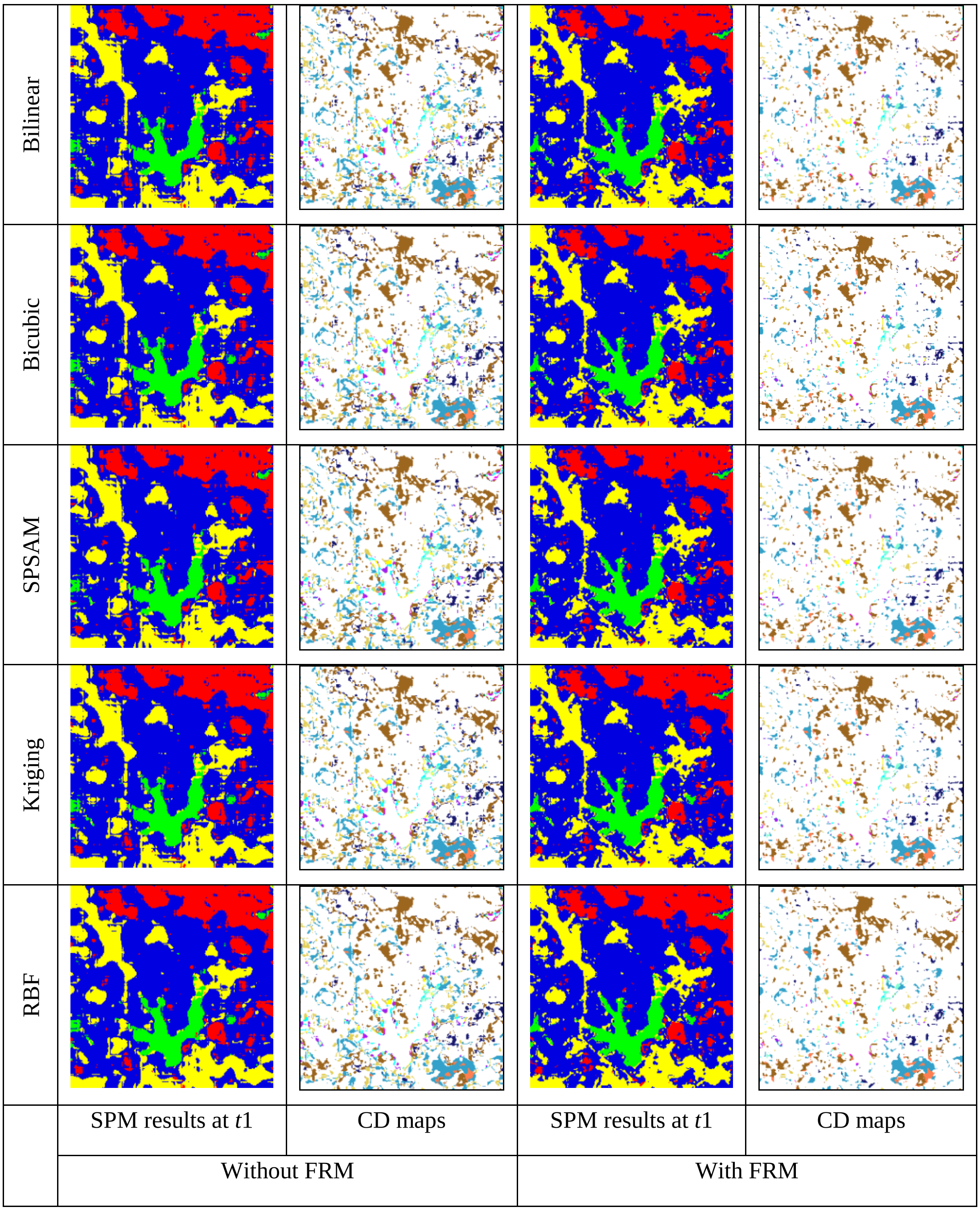

Figure 6.9. SPM and CD results of the five STHSPM algorithms (from $t0$ to $t1$, with the $t0$ reference map as the FRM (S=8)).

Table 6.1 gives the SPM accuracy of the five STHSPM algorithms for all five zoom factors. The pure coarse resolution pixels in Figure 6.8 were ignored in the accuracy statistics. As concluded from the table, using an FRM, the SPM accuracy increases noticeably. For example, the SPM accuracy of the five STHSPM algorithms increases by around 4% for S=5 and around 9% for S=15.

Table 6.1 SPM accuracy (%) of $t1$ image ($t0$ reference map as FRM) for the five STHSPM algorithms

	S=5		*S*=8		*S*=10		*S*=12		*S*=15	
	Without FRM	With FRM	Without FRM	With FRM	Without FRM	With FRM	Without FRM	With FRM	Without FRM	With FRM
Bilinear	81.99	86.33	80.07	86.49	79.74	86.36	78.39	86.18	76.63	85.90
Bicubic	82.67	86.50	80.61	86.55	80.02	86.42	78.67	86.26	77.15	86.00
SPSAM	81.90	86.24	79.37	86.18	78.95	86.10	77.93	85.95	76.02	85.81
Kriging	82.41	86.65	80.09	86.36	79.82	86.32	78.55	86.30	76.82	85.92
RBF	83.06	86.76	80.76	86.72	79.83	86.49	78.85	86.38	77.20	85.97

The overall accuracy (OA) of CD was calculated from the full transition error matrix and is provided in Figure 6.10. From this figure, three observations can be made. First, for all five zoom factors, greater CD accuracy is produced when the FRM is incorporated in the STHSPM algorithms. This is attributed to the fact that the FRM decreases the inherent uncertainty in SPM, as shown in Table 6.1. Second, as S increases, no matter whether the FRM is used or not, the CD accuracy of the five STHSPM algorithms decreases. This is because the complexity of the SPM task increases when S becomes larger, which propagates to the post CD analysis. Third, the accuracy gain of using the FRM increases as S increases. More precisely, the accuracy gain increases stably from 2% for S=5 to 8% for S=15. Through the above experiments, it was shown that using an FRM can increase SPM accuracy and, moreover, the sub-pixel CD accuracy for all five STHSPM algorithms.

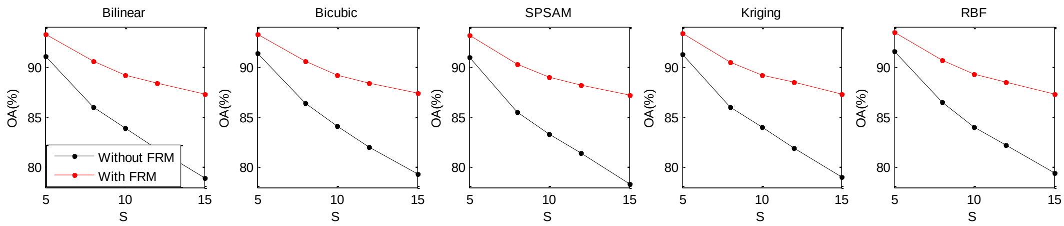

Figure 6.10. CD accuracy of the five STHSPM algorithms (from $t0$ to $t1$, $t0$ reference map as the FRM).

3) CD for a long period

In this subsection, the changes from $t0$ to $t2$ are tested for a longer period (i.e., four years) than from $t0$ to $t1$. The 30 m $t0$ reference map was used as the FRM and the coarse proportion images at $t2$ were synthesized by degrading the 30 m $t2$ reference map. Again, five zoom factors were analyzed: S= 5, 8, 10, 12 and 15. The CD accuracy of the five STHSPM algorithms without an FRM and with an FRM is shown in Figure 6.11. Similarly, with an FRM, the STHSPM algorithms were able to produce greater CD accuracy for all zoom factors. The accuracy of all ten methods decreases as *S* increases, but the five methods without an FRM decreases more rapidly. The accuracy gain by using an FRM in this experiment was compared to that in the last experiment. As shown in Figure 6.12, for each zoom factor, the accuracy gains for all five STHSPM algorithms from *t*0 to *t*2 are, as expected, smaller than for *t*0 to *t*1. For example, for *S*=5, with the aid of the FRM, for CD from *t*0 to *t*2, the accuracy increases by less than 1% while for CD from *t*0 to *t*1, the accuracy increases by over 2%. For larger zoom factors, the differences between the two periods are even larger, and when *S*=15, the differences are greater than 2%. As changes in land cover can be complicated, the uncertainty in CD increases for longer periods correspondingly. The results in this experiment reveal that the FRM imparts greater benefits for SPM of coarse images that are acquired on temporally proximate days.

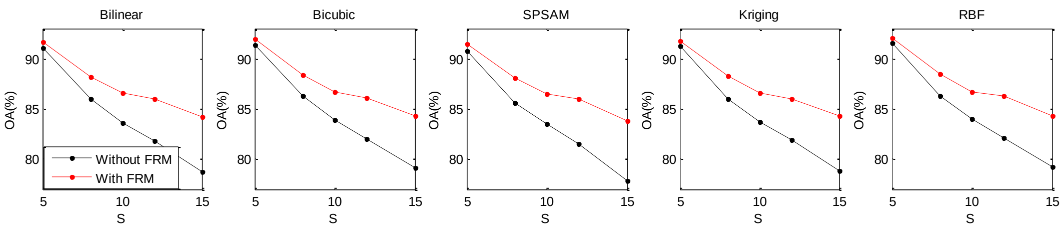

Figure 6.11. CD accuracy of the five STHSPM algorithms (from *t*0 to *t*2, t0 reference map as the FRM).

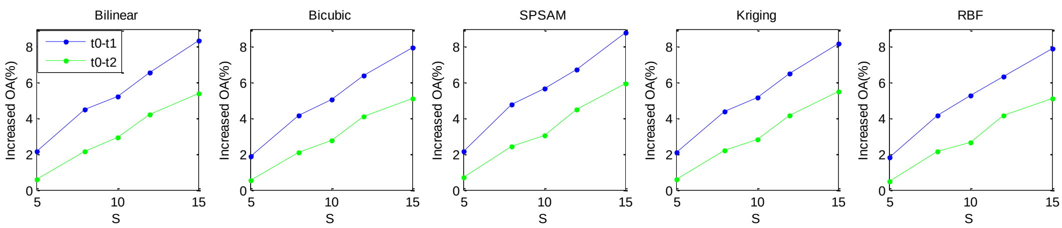

Figure 6.12. The CD accuracy gain by using FRM for *t*0 to *t*1 and *t*0 to *t*2 cases (*t*0 reference map as the FRM).

4) CD for the former coarse image and latter FRM case

In the previous two experiments, the acquisition date of the FRM precedes that of the coarse images. As mentioned in Section 6.2.1, it is necessary to develop SPM methods for a preceding coarse spatial resolution image (i.e., no fine spatial resolution images are available at the former time) with the aid of a latter FRM. In this experiment, we test the case where the FRM was acquired after the coarse images. The changes from *t*0 to *t*1 were tested in this experiment, but the 30 m *t*1 reference map was used as the FRM. The former coarse proportion images at *t*0 time were synthesized by degrading the 30 m *t*0 reference map. Five zoom factors, 5, 8, 10, 12 and 15, were tested. The generated SPM results of the five STHSPM algorithms were than compared to the latter 30 m *t*1 map for CD.

The CD accuracy for all cases (i.e., two versions of five STHSPM algorithms with five zoom factors) is given in Figure 6.13. It can be observed that for all STHSPM algorithms with the FRM at a latter time, greater accuracy can still be obtained for each zoom factor. This illustrates that the data acquisition date order of coarse images and the FRM is not restricted for enhancing sub-pixel resolution CD, and the proposed five STHSPM algorithm-based CD methods with an FRM are also applicable to an earlier coarse resolution image and latter FRM.

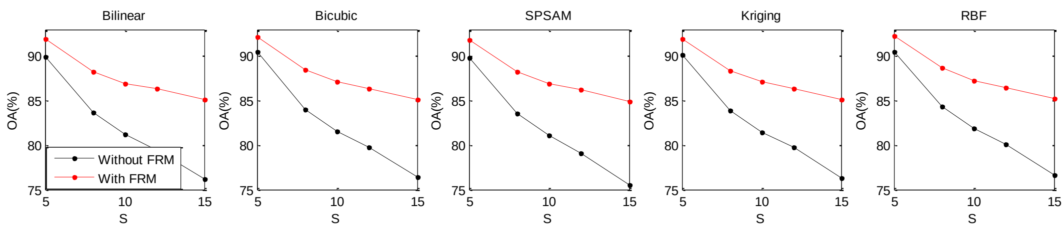

Figure 6.13. CD accuracy of the five STHSPM algorithms (from *t*0 to *t*1, *t*1 reference map as the FRM).

It is worth noting that the accuracy of all cases with FRM in Figure 6.13 is lower than the corresponding cases in Figure 6.10, where the CD accuracy from *t*0 to *t*1 is also presented. For S=5, with FRM, the accuracy of each STHSPM algorithm in Figure 6.13 is around 1.5% lower than that in Figure 6.10 while for S=15, the difference is around 2%. The reason for this phenomenon is that SPM of the *t*0 coarse images is conducted in Figure 6.13, whereas SPM of the *t*1 coarse images is conducted in Figure 6.10. As can be seen from the 30 m *t*0 and *t*1 reference maps in Figure 6.6, in some areas (such as the center area), there are small blocky features for the forest class in the *t*0 reference map, but they changed to vegetation pixels in the *t*1 reference map. In the *t*1 coarse image, coarse pixels in these areas are pure pixels, but mixed pixels in the *t*0 coarse image. Using the *t*1 map as the FRM for SPM of the *t*0 coarse images, the SPM results for the mixed pixels are still the same as those without the FRM. Therefore, pure pixels in the degraded FRM cannot help to increase the accuracy of SPM of the corresponding mixed pixels in other coarse resolution images.

5) CD between coarse images

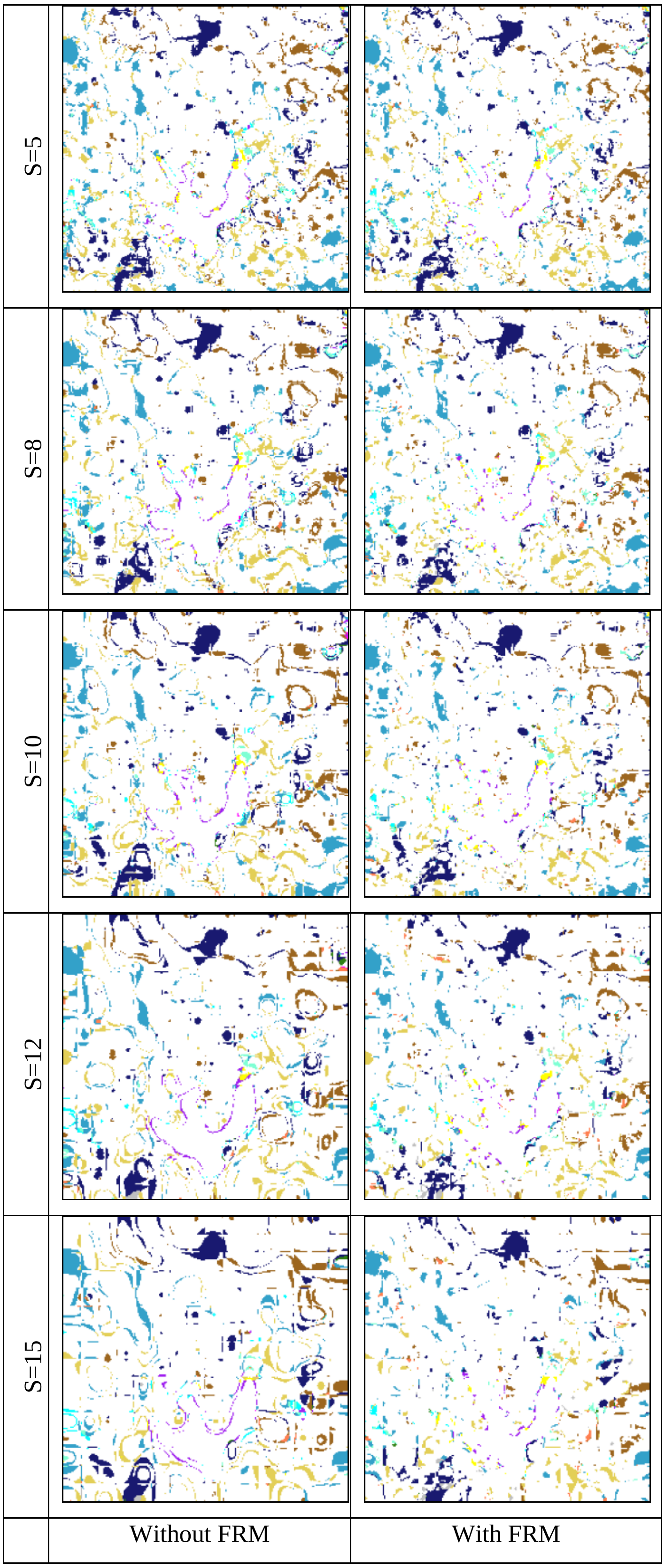

Figure 6.14. CD results of the RBF interpolation-based SPM algorithm (from *t*1 to *t*2, *t*0 reference map as the FRM).

From Section 6.3.1 2) to Section 6.3.1 4), CD was carried out between fine and coarse spatial resolution images, for the case where a fine spatial resolution image is available on either the start or end day during the studied period. Different from those three experiments, the sub-pixel resolution CD in this subsection was implemented between coarse resolution images, for the case where there is no fine spatial resolution on the start or end day during the studied period. Specifically, the 30 m *t*1 and *t*2 reference maps were degraded to synthesize the coarse proportion images at *t*1 and *t*2. Five zoom factors (i.e., *S*=5, 8, 10, 12 and 15) were considered. The *t*0 reference map was used as the FRM for SPM of both the *t*1 and *t*2 coarse resolution images. Finally, changes between *t*1 and *t*2 were detected.

Figure 6.14 shows the 30 m CD results of one of the five STHSPM algorithms (i.e., RBF interpolation-based SPM). Comparing the CD results in Figure 6.14 to the reference in Figure 6.7(b), we can observe clearly that without the FRM, the results contain many errors propagated from the SPM results of the *t*1 and *t*2 coarse images. Particularly, for a large zoom factor (e.g., *S*=12 or 15), many changed pixels in the CD result appear incorrectly as circular features. Using an FRM for both the *t*1 and *t*2 coarse images, the generated CD results seem more accurate while referring to Figure 6.7(b), and the advantages become more obvious as *S* increases. A quantitative evaluation for all five STHSPM algorithms is provided in Figure 6.15. Consistent with visual assessment, the FRM can help to increase the CD accuracy, and the increase is also obvious for the other four STHSPM algorithms. More precisely, the accuracy gain of using an FRM for the five STHSPM algorithms increases from about 2% for *S*=5 to 8% for *S*=15. This subsection, thus, demonstrates that it is helpful to use an FRM in CD between coarse images.

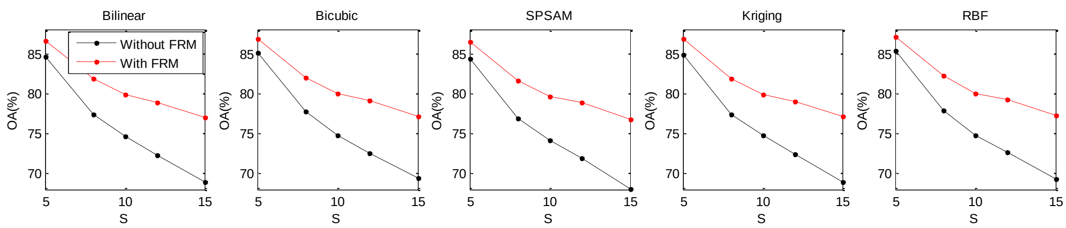

Figure 6.15. CD accuracy of the five STHSPM algorithms (from *t*1 to *t*2, *t*0 reference map as the FRM).

6) Comparison with other methods

The proposed five STHSPM algorithms with an FRM were compared to the PSA-based CD with an FRM (Ling et al., 2011) To illustrate the accuracy gain of sub-pixel resolution CD, a conventional pixel-based CD method was compared with the proposed algorithms, in which SPM results were produced by a pixel-based classification (HC) and CD was performed by comparing the former and latter fine spatial resolution maps. In the HC method, all sub-pixels within a coarse pixel were assigned to the class with the largest proportion. The changes from *t*0 to *t*1 (*t*0 reference map as FRM) and *t*1 to *t*2 (*t*0 reference map as FRM) were tested for comparison of the total of seven CD methods.

The CD accuracy of the seven methods is exhibited in Figure 6.16. Obviously, the accuracy of six SPM algorithms is higher than for the HC-based CD method. Generally, with an FRM, all five STHSPM algorithms were found to have very close accuracy for each zoom factor (see the two sub-figures). From the barcharts in Figure 6.16(a), it can be seen that PSA tends to achieve a higher accuracy than the five STHSPM algorithms for S=5, but for larger zoom factors, there are minor differences between the six methods. With respect to the CD accuracy for *t*1 to *t*2 in Figure 6.16(b), PSA produces slightly lower accuracy than the five STHSPM algorithms.

(a)

(b)

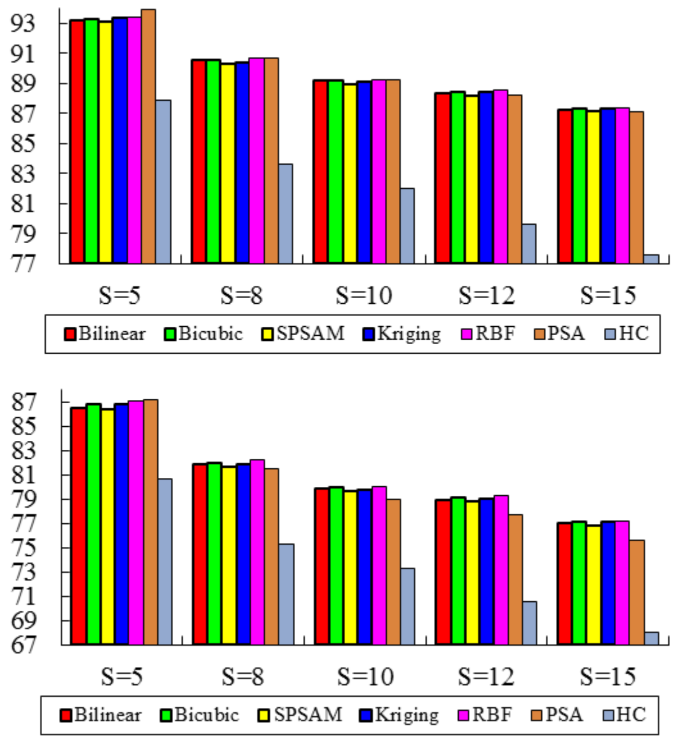

Figure 6.16. CD accuracy (%) of the six SPM algorithms with an FRM (*t*0 reference map as the FRM) and conventional pixel-based HC approach. (a) From *t*0 to *t*1. (b) From *t*1 to *t*2.

Figure 6.17 shows the computing time of the six SPM methods. All methods were tested on an Intel Core 2 Processor (1.80-GHz Duo central processing unit, 2.00-GB random access memory) with MATLAB version7.1. For CD from *t*0 to *t*1, SPM was conducted only on the $t1$ coarse images while from $t1$ to $t2$, SPM was conducted on both the $t1$ and $t2$ coarse images. Thus, the computing time in Figure 6.17(b) doubles that in Figure 6.17(a) in general. Note that the computing time of PSA decreases as S increases. This is because PSA swaps sub-pixels within the coarse pixel and it is implemented in units of coarse pixels. The computing efficiency of PSA is related mainly to the size of coarse image and not affected much by the number of sub-pixels within each coarse pixel. For S=5, 8, 10, 12 and 15 in the experiments, the size of the coarse images (by degradation of the 250 by 250 pixel reference maps) are 50 by 50, 31 by 31, 25 by 25, 20 by 20, 16 by 16, respectively. The decreasing size leads to the decreasing computing time of PSA as a result. Examining the results in Figure 6.17, we find that the five STHSPM algorithms are faster than PSA, and the bilinear, bicubic and SPSAM methods are much faster. All five STHSPM algorithms require less than 10 seconds for CD from $t0$ to $t1$ and less than 20 seconds for CD from $t1$ to $t2$. With respect to the bilinear, bicubic and SPSAM methods, less than 5 seconds is required in all cases in Figure 6.17. The high efficiency of the five STHSPM algorithms is attributed to their non-iterative character. This validates that the five STHSPM algorithms with an FRM are fast for sub-pixel CD applications.

(a)

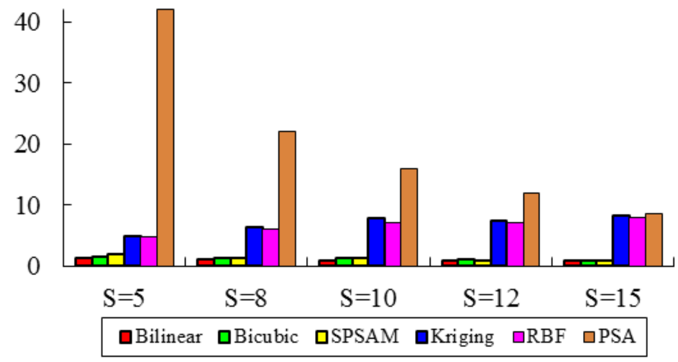

(b)

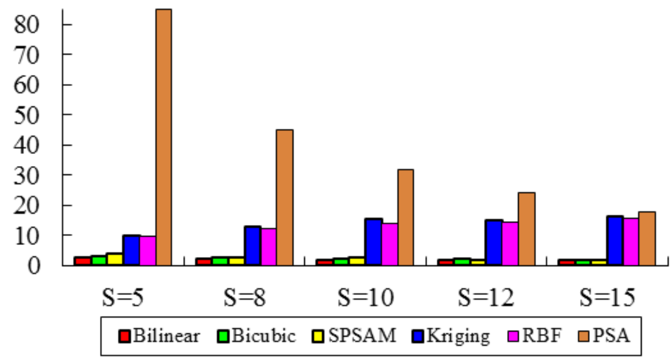

Figure 6.17. Computing time (in seconds) of the six SPM algorithms with an FRM ($t0$ reference map as FRM). (a) From $t0$ to $t1$. (b) From $t1$ to $t2$.

6.3.2. Experiment on degraded multispectral images

1) Dataset

The data used in this experiment are two 30 m multispectral Landsat images. This experiment is designed to consider the inevitable uncertainty in spectral unmixing, which can propagate to the post SPM and CD processes. One 30 m multispectral Landsat image was degraded band by band via an S by S mean filter to simulate a coarse multispectral image. Spectral unmixing was then conducted on the coarse images to generate proportion images, which were used as the input of SPM. With the zoom factor S, SPM was performed to predict the 30 m fine spatial resolution map. The hard classified land cover map of the other 30 m multispectral Landsat image was used as the FRM. With respect to the reference change map, it was obtained by comparison of the two hard classified maps of the corresponding 30 m multispectral images.

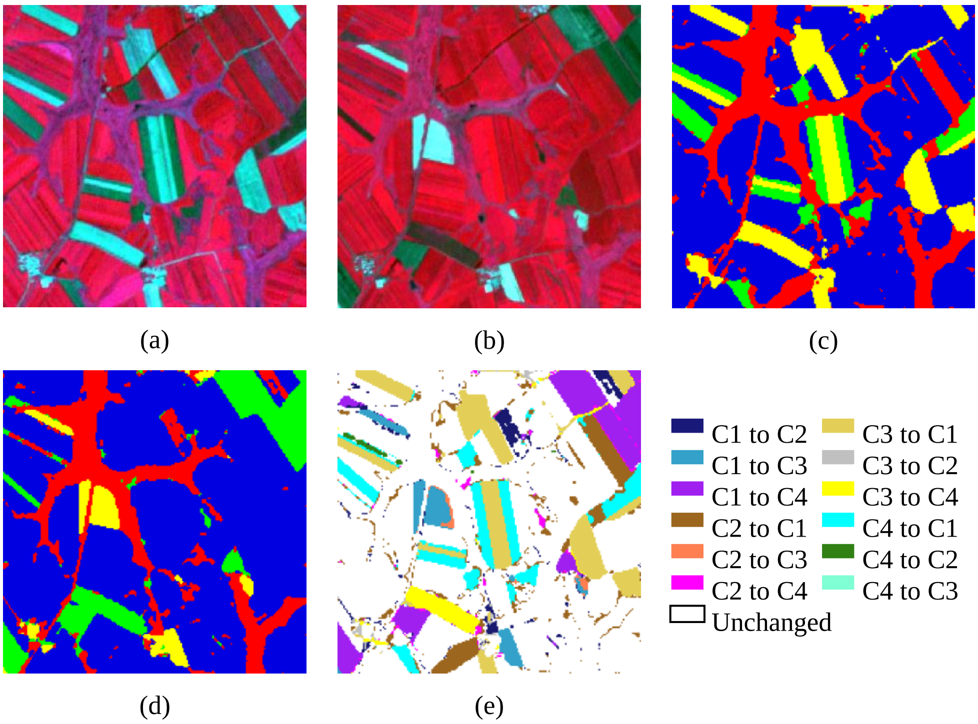

Figure 6.18. Two Landsat images covering the same area in Liaoning, China. (a) and (b) are false color images (Bands 4, 3 and 2 as RGB) in August 2001 ($t0$) and August 2002 ($t1$). (c) and (d) are hard classified land cover maps at $t0$ and $t1$ time, where blue, red, yellow and green denote classes C1, C2, C3 and C4, respectively. (e) CD reference map from $t0$ to $t1$.

The two 30 m multispectral images were acquired by the Landsat-7 enhanced thematic mapper plus sensor in August 2001 ($t0$) and August 2002 ($t1$) in the Liaoning Province, China. The $t0$ image was registered to the $t1$ image and then the histogram matching method was implemented for the relative radiometric correction (Hao et al., 2014). The study area covers 200 by 200 pixels and four land cover classes can be identified, which are denoted as C1, C2, C3 and C4. The two images are shown in Figure 6.18(a) and Figure 6.18(b), respectively. A supervised neural network was applied to the two Landsat images to generate the 30 m reference land cover maps. The classification accuracy for the two reference maps was over 90%. The *t*0 and *t*1 reference maps and the reference change map (produced by comparing *t*0 and *t*1 reference maps) are shown in Figure 6.18(c)-(e).

2) Results

The *t*1 30 m multispectral Landsat image was degraded with a 8 by 8 pixel mean filter to produce a 240 m MODIS-like image. Fully constrained least squares linear spectral mixture analysis (Heinz and Chang, 2001) was employed for spectral unmixing in the experiments. The generated proportion images of the four classes are exhibited in Figure 6.19. The five STHSPM algorithms were implemented to recreate the 30 m land cover map at *t*1. In the experiments, the *t*0 reference map in Figure 6.18(c) was used as the FRM.

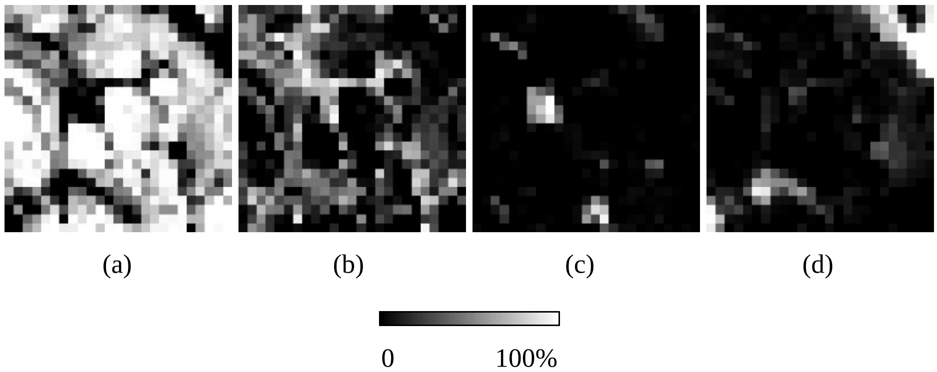

Figure 6.19. Proportion images of the four classes at *t*1. (a) C1. (b) C2. (c) C3. (d) C4.

Figure 6.20 gives the SPM and CD results of the RBF method. To illustrate the influence of spectral unmixing, the results for the degraded land cover map (the experimental procedure is the same as for Section 6.3.1) are also presented in Figure 6.20 for visual comparison. Checking the results in this figure, we see that due to the errors imposed by spectral unmixing, some scattering of pixels exists in the SPM results and the corresponding CD maps contain some noise. Using the FRM, for both cases, the produced SPM results seem more continuous and more linear features are restored, especially for class C2 (in red) and the CD results are closer to Figure 6.18(d).

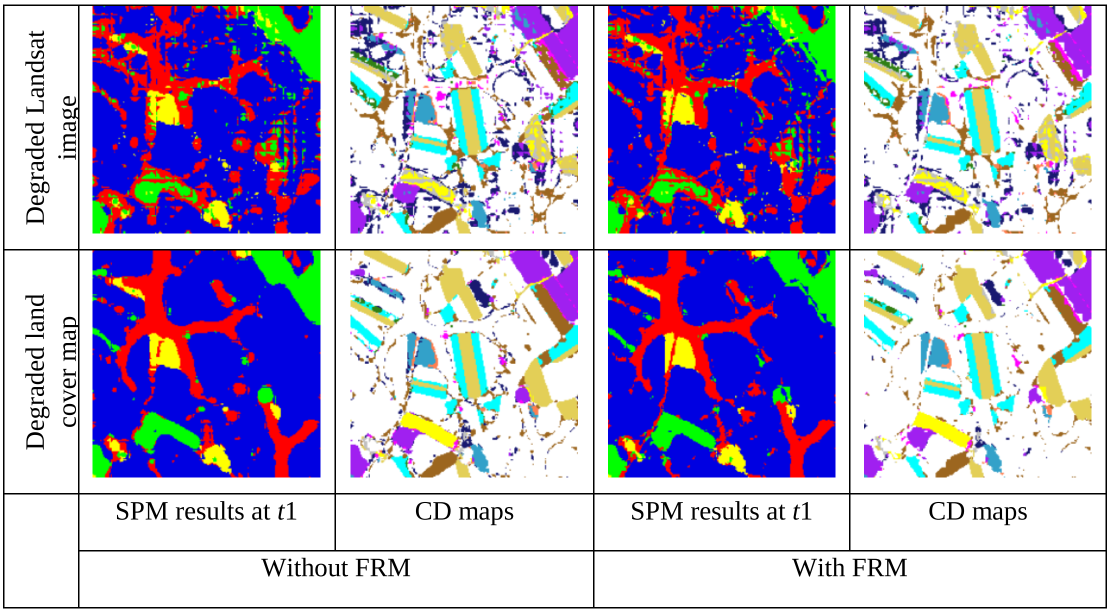

Figure 6.20. SPM and CD results of the RBF interpolation-based SPM algorithm.

Table 6.2 lists the OA of CD (calculated from the full transition error matrix) of all five STHSPM algorithms for both the degraded multispectral image and degraded land cover map cases. As shown in the table, because of the errors from spectral unmixing, when compared to the degraded land cover map case, the CD accuracy for the degraded multispectral image case decreases by around 15%. Nevertheless, for both cases, using the FRM, the proposed five STHSPM algorithms are able to produce greater CD accuracy. Particularly, for the degraded multispectral image case, the CD accuracy of five STHSPM algorithms increased from 77.1% to 78.1%. The experiment in this section suggests that FRM is also helpful for the sub-pixel resolution CD case where inherent uncertainty in spectral unmixing exists.

Table 6.2 CD accuracy (%) of *t*1 image (*t*0 reference map as the FRM) for the five STHSPM algorithms

	Degraded TM		Degraded Land cover map	
	Without FRM	With FRM	Without FRM	With FRM
Bilinear	77.06	78.13	91.47	93.01
Biubic	77.26	78.21	91.73	93.13
SPSAM	77.18	78.13	91.56	93.16
Kriging	77.17	78.14	91.75	93.10
RBF	77.18	78.18	92.21	93.26

6.3.3. Experiment on real Landsat-MODIS images

In this experiment, a set of Landsat-MODIS images, including two Landsat images and one MODIS image, were used to test the proposed sub-pixel resolution CD algorithms for a real case. The study area is a 67.5 km by 67.5 km tropical forest area in Brazil. One Landsat image acquired in July 1988 ($t0$) was used as the source of the FRM, and the other Landsat image acquired in July 2005 ($t1$) was used as reference. The five STHSPM algorithms were implemented on the one single eight-day surface reflectance MODIS image acquired in July 2005 to predict the SPM result with the Landsat spatial resolution (i.e., 30 m) at $t1$ time. The SPM result at $t1$ time was compared to the former FRM for CD from $t0$ to $t1$.

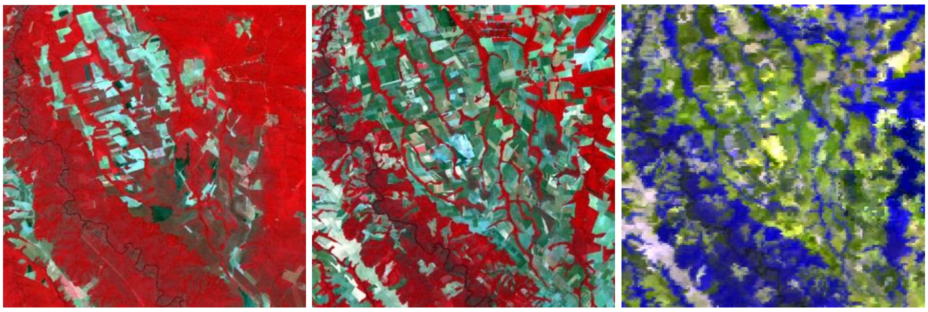

(a) (b) (c)

Figure 6.21. The Landsat-MODIS images (Bands 4, 3 and 2 as RGB). (a) The Landsat image acquired in July 1988. (b) The Landsat image acquired in July 2005. (c) The MODIS image acquired in July 2005.

The original MODIS image has a spatial resolution of 463 m and was re-projected into the Universal Transverse Mercator coordinate system and then resampled to a spatial resolution of 450 m using the nearest-neighbor algorithm (Lu et al., 2011). Registration was conducted on the two Landsat images and the errors were less than 0.5 pixel. The zoom factor of SPM for the MODIS image was set to 15 to predict a land cover map at 30 m spatial resolution. The spatial size of the MODIS image is 150 by 150 pixels and the Landsat image is 2250 by 2250 pixels. Figure 6.21 shows the three images.

The MODIS image was unmixed with fully constrained least squares linear spectral mixture analysis (Heinz and Chang, 2001). For the studied tropical forest area, proportion images of two main classes, forest and non-forest, were used as input to the SPM. For each 30 m Landsat image, the pixels were supposed to be pure materials, and an unsupervised *k*-means classifier was employed to generate the 30 m fine spatial resolution thematic map. The 30 m $t0$ map was used as the FRM in this experiment and the reference change map was produced by comparing the 30 m $t0$ and $t1$ reference maps.

Table 6.3 gives the CD accuracy for the five STHSPM algorithms. As seen from the table, without FRM, the CD accuracy of each STHSPM algorithm is around 72.2%. Incorporating FRM in SPM, all five algorithms produce greater accuracy and the accuracy gains are around 1.3%. To study the effect of errors from spectral unmixing and the reference, the 30 m $t1$ reference map was degraded with a factor of 15 to simulate the spectral unmixing result at 450 m spatial resolution. The CD accuracy of the five STHSPM algorithms resulting from such a design is over 95%, regardless of the use of FRM. For the test of real Landsat-MODIS images in this experiment, due to the uncertainty in spectral unmixing (originating from the point spread function of the MODIS sensor and unmixing algorithm itself, etc.) and the reference maps (both FRM and $t1$ reference map), the CD accuracy of the proposed algorithms decreases by 23%.

Table 6.3 CD accuracy (%) of the five STHSPM algorithms for the real Landsat-MODIS images

	Without FRM	With FRM
Bilinear	72.28	73.55
Bicubic	72.22	73.51
SPSAM	72.34	73.58
Kriging	72.27	73.54
RBF	72.22	73.51

6.4. Discussion

6.4.1. Differences between the proposed methods and spatiotemporal fusion techniques

As mentioned in the introduction, a major difference between the proposed methods and spatiotemporal fusion is that the five STHSPM algorithms yield sub-pixel maps, while spatiotemporal fusion yields images in units of reflectance. The objective of spatiotemporal fusion is to produce new multispectral images, which can be used for various goals, including monitoring changes in environmental variables and vegetation phenology, etc.. Some spatiotemporal fusion approaches were developed based on the strict assumption that there are no land cover changes during the studied period (Zurita-Milla et al., 2009).

Specifically, all coarse images (e.g., MERIS images) in the studied period are assumed to have the same land cover distribution, which can be obtained from an FRM (e.g., LGN5 or classified Landsat image). The FRM is degraded to provide the coarse proportions, and the ultimate task is to estimate the reflectance for each fine pixel, given the input MERIS reflectance. The reflectance of the fine spatial resolution, time-series images can be compared to monitor the vegetation dynamics, surface temperature and surface soil moisture, and other environmental variables. Some other spatiotemporal fusion approaches relax the strong assumption that there are zero land cover changes during the studied period. Alternatively, they extract correspondence between the known fine and the coarse spatial resolution images, to guide the prediction of fine spatial resolution images on other dates. It would be very promising to apply standard land cover CD techniques to the outputs of this type of spatiotemporal fusion, even though very few studies (to the best of our knowledge) have been directed at this problem. For simplicity, we denote the latter spatiotemporal fusion as image pair-based spatiotemporal fusion. Consequently, the proposed methods are constructed to detect land cover changes, while spatiotemporal fusion techniques (e.g., image pair-based spatiotemporal fusion) are capable of detecting changes of both land cover and reflectance of fine pixels.

The image pair-based spatiotemporal fusion has potential in sub-pixel resolution CD. This necessitates a discussion about the differences between it and the proposed methods. An important difference is the restriction on the acquisition date of the known fine spatial resolution image, as shown in Figure 6.22. For image pair-based spatiotemporal fusion, at least one pair of fine-coarse spatial resolution (e.g., Landsat-MODIS) images of the same area is required. They have to be acquired on very close dates to ensure that there are almost zero changes between the scene covered by the two different spatial resolution images. This is because image pair-based spatiotemporal fusion techniques need to exploit the correspondence between the known fine and the coarse spatial resolution images. For example, in the experiment in Section 6.3.3, if implementing image pair-based spatiotemporal fusion, the MODIS image acquired on a date closer to that of Figure 6.21(a) is required. However, due to cloud contamination, time inconsistency of image acquisitions and some other reasons (Song and Huang, 2013), high quality image pairs cannot always be guaranteed. By contrast, it is not the case for the five STHSPM algorithms using an FRM, as they do not necessarily need a pair of fine-coarse spatial resolution images.

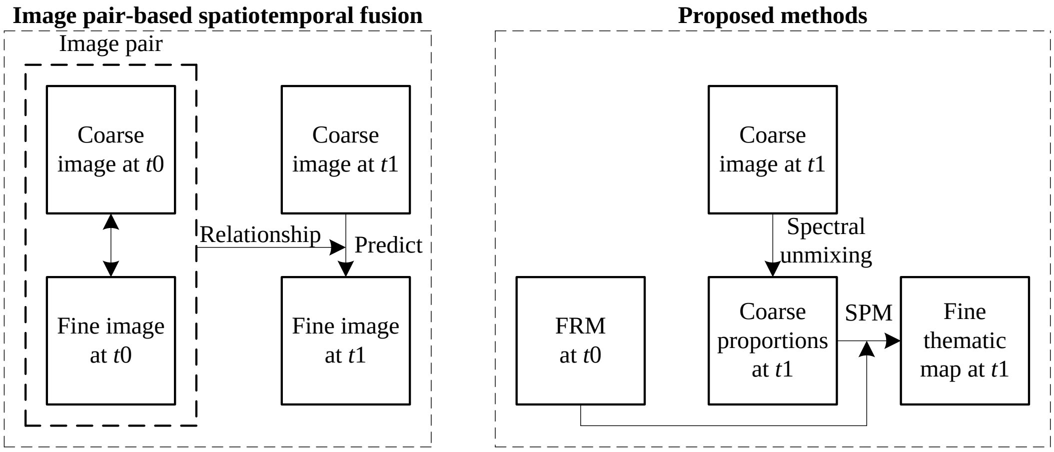

Figure 6.22. Differences between the proposed methods and image pair-based spatiotemporal fusion, where “coarse” and “fine” mean coarse and fine spatial resolution, respectively.

6.4.2. Uncertainties in FRM

An FRM is required in the proposed method to aid the SPM process applied to coarse resolution images and increase CD accuracy. It is necessary to consider the reliability of the FRM. In this study, the FRMs were obtained by hard classification of the fine spatial resolution multispectral image (i.e., Landsat images in the experiments). It is known that mixed pixels exist inevitably in remote sensing images (Fisher, 1997) and such a means of producing the FRM involves inherent uncertainties. Nevertheless, it should be noted that the source of FRM (i.e., fine spatial resolution multispectral image) is generally selected according to the desired spatial resolution (defined by investigators) for SPM and CD. For example, given a 250 m spatial resolution MODIS image at *t*1, if the desired spatial resolution of SPM and sub-pixel CD is 30 m (zoom factor *S*=8), we can seek a 30 m Landsat image for the source of FRM at *t*0; if the desired spatial resolution is 10 m (*S*=25), a 10 m SPOT image can be considered as the source of FRM at *t*0.

When defining 30 m as the desired target spatial resolution for SPM of a 250 m MODIS image at *t*1, if there are no 30 m Landsat images at *t*0, a finer spatial resolution image (if available), such as WorldView or QuickBird image, would be an effective alternative for the source of FRM at *t*0. In this case, the approximate 1 m FRM needs to be upscaled to 30 m to meet the required spatial resolution of SPM at *t*1. Since a 1 m FRM is available, an arising question is whether it is feasible to conduct SPM and sub-pixel resolution CD directly at a 1 m spatial resolution to obtain more detailed land cover information. For this issue, two factors are worth consideration: the zoom factor for SPM and the reliability of the FRM. First, it is suggested that the zoom factor S for SPM should not be too large, as within each coarse pixel the number of variables for SPM is S^2 and the uncertainty in SPM increases with increasing S. Second, classification accuracy often decreases with increasing spatial resolution, because smaller pixels may resolve within-class variation that leads to confusion between classes (Atkinson, 2006). For example, for soil patches within a field of cereals, investigators may wish the whole field to be classified as cereals (Atkinson, 2006). Therefore, by hard classification of very high spatial resolution (e.g., 1 m) images, the derived FRM at $t0$ may contain some scattering of pixels within large objects and result in a SPM result at $t1$ with significant noise.

In the proposed method, the FRM at $t0$ is upscaled to the same spatial resolution as for the coarse image at $t1$, and then the simulated proportions of the FRM need to be compared with the spectral unmixing-derived proportions (see expression (6.1) and Figure 6.1). Normally, due to the inconsistency of image acquisitions, the two types of proportion are not completely identical, even though there are strictly zero changes from $t0$ to $t1$. If the coarse image at $t0$ (acquired by the same sensor for the coarse image at $t1$) is available, it would be promising to use the spectral unmixing-derived proportions of the $t0$ coarse image directly to calculate the differences in proportions in expression (6.1). Such a scheme, however, may introduce additional uncertainties, which exist in spectral unmixing of the $t0$ coarse image.

6.4.3. Limitations to the method of using an FRM

There are several limitations to the method of using an FRM in this study. First, as indicated in Section 6.3.1 4), for SPM of the mixed pixels in coarse resolution images, the corresponding pure pixels in the degraded FRM cannot provide useful additional information. This case can occur where, for example, from the time of FRM to the time of the coarse image for SPM, there are new classes in those coarse pixels or even the whole study area. For example, we suppose there are four classes (i.e., vegetation, forest, urban and water) in the FRM at $t0$, and five classes (i.e., soil, vegetation, forest, urban and water) in the coarse image for SPM at $t1$. That is, the new class soil is produced from $t0$ to $t1$. As seen from Figure 6.1, no information can be borrowed from the FRM for SPM of the new class soil, because all coarse soil proportions in the FRM are zero (i.e., no "gray area" for the soil class in the FRM). Therefore, the proposed method of using an FRM cannot enhance SPM of the new classes during the studied period of CD, but can enhance SPM of the other classes.

Second, the results in Section 6.3.1 3) show that the FRM tends to be more helpful for CD during a short period. This is explained by an example in Figure 6.23. Suppose that in a coarse pixel, the proportion of the blue class during a long period from *t*0 to *t*n does not change (i.e., $\Delta=0$), but in the real world case the distribution of fine spatial resolution blue pixels evolves gradually. Eventually, at *t*n time, the distribution of those fine pixels is quite different from that at the beginning *t*0 time. This conflicts with the assumption that if for the blue class $\Delta=0$, there is no change for blue fine pixels and the spatial distribution of the blue class in the FRM can be copied directly to the coarse pixel at other times. Nevertheless, as observed from the changes (deep pink pixels) in Figure 6.23, for a time close to *t*0 (such as *t*1), the changes are very small when compared to *t*0. Therefore, we can conclude that the rules in Figure 6.1 and Section 6.2.1 of using FRM may be more appropriate for coarse images acquired on dates that are sufficiently close to that for the FRM. The sufficiently close dates can also ensure fewer new classes, as discussed above.

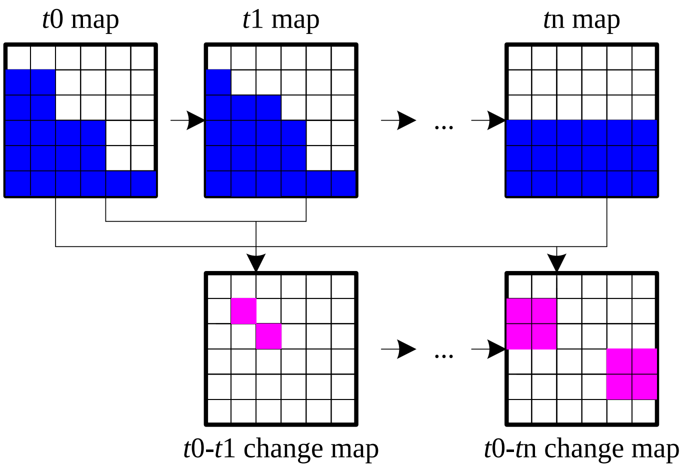

Figure 6.23. An example for illustration of the land cover changes (deep pink pixels) during a long period (*t*0 to *t*n), where the land cover proportion of the blue class is fixed from *t*0 to *t*n.

6.5. Summary

In this chapter, based on the availability of a land cover map obtained from an available fine spatial resolution image (i.e., the FRM), five non-iterative and fast STHSPM algorithms (i.e., bilinear-, bicubic-, SPSAM-, Kriging- and RBF-based SPM methods) were proposed for sub-pixel resolution land cover CD. The FRM was taken into account not only in the case of a former FRM and latter coarse image, but also the case of a former coarse image and latter FRM, as well as the case of CD between coarse images. The STHSPM algorithms determined the sub-pixels for each class by comparing the soft class values and referring to the hard class values (at the sub-pixel level) in the FRM. The FRM can help to reduce the solution space of SPM, and thus, decrease the uncertainty in SPM and increase the sub-pixel resolution CD accuracy. The proposed methods provide a promising avenue for fine spatial and temporal resolution CD. Experimental results demonstrated the five STHSPM algorithms to be effective in sub-pixel resolution CD, and with the information from the FRM, they can increase CD accuracy. Compared to the PSA-based sub-pixel resolution CD with an FRM, the proposed methods are able to achieve at least comparable CD accuracy, but need much less computing time, and hence provide new options for real-time applications.

7. Conclusion

Mixed pixels are a common phenomenon in remote sensing images. Sub-pixel mapping (SPM) is a technique for predicting the spatial distribution of land cover classes within mixed pixels at a finer spatial resolution level than that of the input coarse spatial resolution images. This thesis has been carried out on a typical SPM algorithm summarized in Section 1.3 for the first time: the soft-then-hard SPM (STHSPM) algorithm. STHSPM first estimates the soft class value at fine spatial resolution and then allocates hard class value for sub-pixels. The main works of this thesis and future research are summarized as follows.

7.1. Summary

In Chapter 2, a new class allocation approach UOC is proposed for the STHSPM algorithm in Section 2.1. Specifically, a visiting order for all classes is pre-determined and the number of sub-pixels belonging to each class is calculated using coarse fraction data. According to the visiting order, the sub-pixels belonging to the being visited class are determined by comparing the soft attribute values of this class and the remaining sub-pixels are used for the allocation of the next class. UOC was tested on three remote sensing images with five STHSPM algorithms: BPNN, HNN, SPSAM, Kriging and ICK. UOC was also compared to three existing allocation methods: LOT, UOS and HAVF. Results show that for all STHSPM algorithms, UOC is able to produce higher SPM accuracy than UOS and HAVF; compared to LOT, UOC is able to achieve at least comparable accuracy but needs much less computing time. Hence UOC provides an effective and a real-time class allocation method for STHSPM algorithms. Furthermore, in Section 2.2, UOC is extended with another new class allocation approach, named AUOC. In AUOC, the visiting order of classes within each coarse pixel is determined based on the local structure, rather than the global structure in UOC. Experiments on three remote sensing images show that AUOC is able to improve UOC in terms of SPM accuracy, especially for SPM with small zoom factors.

In Chapter 3, STHSPM is enhanced with additional information in terms of multiple shifted images (MSI). Each shifted image is downscaled to the target fine spatial resolution using the STHSPM algorithms, including ICK in Section 3.1 and image interpolation (i.e., bilinear and bicubic) methods in Section 3.2. ICK requires prior class information, while bilinear and bicubic do not require that. As a result, a set of sharpened (continuous) images for all classes are generated for each shifted image. According to the estimated sub-pixel shifts of MSI, the sharpened images for the same class are integrated, followed by the class allocation step finally. The experimental results showed that more accurate SPM results can be generated with MSI than with a single observed coarse image in the STHSPM algorithms.

In Chapter 4, a new STHSPM algorithm based on radial basis function (RBF) interpolation is proposed. In this STHSPM algorithm, the sub-pixel soft class values are calculated by RBF interpolation. Taking the coarse proportion images as input, an interpolation model is built for each visited coarse pixel. Three remote sensing images were tested and the new method was compared to bilinear-, bicubic-, sub-pixel/pixel spatial attraction model- and Kriging-based SPM methods. Results show that the proposed RBF interpolation-based SPM is more accurate. Hence the proposed method provides an effective new option for SPM.

In Chapter 5, in view of the limitation of ICK-based STHSPM that requires the semivariogram of land cover classes from prior information, a NICK-based STHSPM is proposed. In NICK, the fine spatial resolution semivariogram of each class is estimated by the deconvolution process, taking the coarse spatial resolution semivariogram extracted from the class proportion image as input. Experiments demonstrated the feasibility of the proposed NICK. It obtains comparable SPM accuracy to ICK that requires semivariogram estimated from fine spatial resolution training images. The proposed method extends ICK to cases where the prior spatial structure information is unavailable.

In Chapter 6, the STHSPM algorithms are proposed to achieve fast sub-pixel resolution CD. The fine spatial resolution land cover maps are first predicted through SPM of the coarse spatial but fine temporal resolution images, and then sub-pixel resolution CD is performed by comparison of class labels in the SPM results. For the first time, five fast SPM algorithms, including bilinear interpolation, bicubic interpolation, SPSAM, Kriging and RBF interpolation methods, are proposed for sub-pixel resolution CD. The auxiliary information from the known fine spatial resolution land cover map on one date, called the FRM, is incorporated in SPM of coarse images on other dates to increase the CD accuracy. Based on the five fast SPM algorithms and availability of the FRM, sub-pixels for each class are predicted by comparison of the estimated soft class values at the target fine spatial resolution and borrowing information from the FRM. Experiments demonstrate the feasibility of the five SPM algorithms using FRM in sub-pixel resolution CD. They are fast methods to achieve sub-pixel resolution CD.

7.2. Future research

Future research can be directed at the following aspects.

In the fields of image and signal processing, there are many available super-resolution algorithms, such as image interpolation, maximum *a posteriori*, iterative backward projection, projection onto convex sets, etc. These algorithms can potentially be developed to STHSPM algorithms, by employing them to downscale the available coarse proportion images first and then using the proposed UOC approach to transfer the downscaled proportion images to thematic maps (i.e., SPM results). UOC, therefore, builds a bridge between super-resolution reconstruction and SPM. The concept of STHSPM proposed in this thesis provides new insight into SPM and leaves the doors open to more potential options for SPM in future research. In this thesis, RBF interpolation and NICK have been proposed as new STHSPM algorithms following this framework. It is considerably promising to study the potential of other super-resolution reconstruction algorithms in SPM.

In this thesis, MSI were used as the additional information for the STHSPM algorithm. Additional information from other source images might also be applied. As presented in Section 1.5, various auxiliary information has been applied to enhance SPM in recent years, such as LIDAR data (Nguyen et al., 2005), panchromatic images (Atkinson, 2008; Ardila et al., 2011; Nguyen et al., 2011; Li et al., 2014a), high resolution color images (Mahmood et al., 2013) and shape information (Thornton et al., 2007; Ling et al., 2012b). It is expected that such auxiliary information will enable further improvement of STHSPM, particularly for reproduction of small objects in the L-resolution case. In the L-resolution case, many objects of interest fall within isolated, coarse pixels and the STHSPM algorithms may not be able to satisfactorily reproduce their spatial distribution due to the limited support from neighboring coarse pixels. Designing the appropriate way to incorporate the supplementary information to STHSPM would be an interesting challenge for the future.

STHSPM provides a promising new option for downscaling continua. It can predict continuous variables at a fine spatial resolution, given the input coarse spatial resolution image. Downscaling continua (Atkinson, 2013), such as downscaling surface temperature (Kallel et al., 2013) or surface soil moisture (Song et al., 2014), has gained increasing attention recently. Therefore, the STHSPM algorithm may be a promising choice for these applications. Furthermore, as illustrated in Li et al. (2009), there are other links between SPM and super-resolution reconstruction: after super-resolution reconstruction of a coarse multi-/hyperspectral remote sensing image, the finer spatial resolution image could then be classified by a standard hard classifier to achieve SPM. The STHSPM algorithm can also be employed for the purpose of super-resolution reconstruction.

As seen from Section 6.2.3, any STHSPM algorithm has potential for sub-pixel resolution CD by incorporating an FRM. It would be an interesting topic to develop new STHSPM algorithms for sub-pixel resolution CD. The FRM information can not only be derived directly from a multispectral image, but also from some other data. Aplin and Atkinson (2001) used Land-Line digital vector data to develop two per-field classification-based SPM approaches. One was designed to fill each polygon with the class within it that has the largest area in pixel-level hard classification, and the other was constructed to assign the class with the largest proportion inside a coarse pixel to the polygon occupying the largest area in the coarse pixel. Recently, Mahmood et al. (2013) developed another per-field classification-based SPM method, where a segmentation map generated from a fine spatial resolution color image was employed in the same way as the Land-Line digital vector data in Aplin and Atkinson (2001). However, in Mahmood et al. (2013), each polygon (i.e., parcel or object) was filled with the class within it that has the largest area in the pre-processing SPM result, rather than the pixel-level hard classification result in Aplin and Atkinson (2001). Robin et al. (2008) also utilized ancillary fine spatial resolution structural information in the form of a segmentation map for SPM, based on Bayes' rule and the maximum *a posteriori* criterion. All these types of fine spatial resolution boundary information associated with the coarse image are probably able to produce a reliable FRM for CD. How to acquire such information and convert it to a reliable FRM seems to be a promising avenue for future research.

References

Ai, B., Liu X., Hu, G., and Li, X., 2014. Improved sub-pixel mapping method coupling spatial dependence with directivity and connectivity. *IEEE Journal of Selected Topics in Applied Earth Observations and Remote Sensing*, 7(12), pp. 4887–4896.

Anderson, L. O., Shimabukuro, Y. E., and Arai, E., 2005. Multitemporal fraction images derived from Terra MODIS data for analysing land cover change over the Amazon region. *International Journal of Remote Sensing*, 26(11), pp. 2251–2257.

Aplin, P. and Atkinson, P. M., 2001. Sub-pixel land cover mapping for per-field classification. *International Journal of Remote Sensing*, 22(14), pp. 2853–2858.

Ardila, J. P., Tolpekin, V. A., Bijker, W., and Stein, A., 2011. Markov-random-field-based super-resolution mapping for identification of urban trees in VHR images. *ISPRS Journal of Photogrammetry and Remote Sensing*, 66, pp. 762–775.

Atkinson, P. M., 1997. Mapping sub-pixel boundaries from remotely sensed images. *Innovations in GIS*, 4, pp. 166–180.

Atkinson, P. M., 2004. Super-resolution land cover classification using the two-point histogram. In *GeoENV IV: Geostitistics for Environmental Applications*, pp. 15-28.

Atkinson, P. M., 2005. Sub-pixel target mapping from soft-classified, remotely sensed imagery. *Photogrammetric Engineering and Remote Sensing*, 71(7), pp. 839–846.

Atkinson, P. M., 2006. Resolution manipulation and sub-pixel mapping. In *Remote sensing image analysis: including the spatial domain*. S. M. de Jong and F. D. van der Meer (eds.). Dordrecht, The Netherlands, Kluwer, pp. 51-70.

Atkinson, P. M., 2008. Super-resolution mapping using the two-point histogram and multi-source imagery. In *GeoENV VI: Geostatistics for Environmental Applications*, pp. 307–321.

Atkinson, P. M., 2009. Issues of uncertainty in super-resolution mapping and their implications for the design of an inter-comparison study. *International Journal of Remote Sensing*, 30(20), pp. 5293–5308.

Atkinson, P. M., 2013. Downscaling in remote sensing. *International Journal of Applied Earth Observation and Geoinformation*, 22, pp. 106-114.

Bastin, L., 1997. Comparison of fuzzy c-means classification, linear mixture modeling and MLC probabilities as tools for unmixing coarse pixels. *International Journal of Remote Sensing*, 18, pp. 3629–3648.

Bioucas-Dias, J. M., Plaza, A., Dobigeon, N., Parente, M., Du, Q., Gader, P., Chanussot, J., 2012. Hyperspectral unmixing overview: Geometrical, statistical and sparse regression-based approaches. *IEEE Journal of Selected Topics in Applied Earth Observations and Remote Sensing*, 5(2), pp. 354-379.

Boucher, A. and Kyriakidis, P. C., 2006. Super-resolution land cover mapping with indicator geostatistics. *Remote Sensing of Environment*, 104(3), pp. 264–282.

Boucher, A. and Kyriakidis, P. C., 2008. Integrating fine scale information in super-resolution land-cover mapping. *Photogrammetric Engineering and Remote Sensing*, 73(8), pp. 913-921.

Boucher, A., Kyriakidis, P. C., and Cronkite-Ratcliff, C., 2008. Geostatistical solutions for super-resolution land cover mapping. *IEEE Transactions on Geoscience and Remote Sensing*, 46(1), pp. 272-283.

Boucher, A., 2009. Sub-pixel mapping of coarse satellite remote sensing images with stochastic simulations from training images. *Mathematical Geosciences*, 41, pp. 265-290.

Brown, M., Lewis, H., and Gunn, S., 2000. Linear spectral mixture models and Support Vector Machine for remote sensing. *IEEE Transactions on Geoscience and Remote Sensing*, 38(5), pp. 2346-2360.

Bruzzone, L. and Bovolo, F., 2013. A novel framework for the design of change-detection systems for very-high-resolution remote sensing images. *Proceedings of the IEEE*, 101(3), pp. 609–630.

Buhmann, M. D., 2003. Radial Basis Functions: Theory and Implementations. Cambridge, U.K.: Cambridge University Press.

Carpenter, G. M., Gopal, S., Macomber, S., Martens, S., and Woodcock, C. E., 1999. A neural network method for mixture estimation for vegetation mapping. *Remote Sensing of Environment*, 70, pp. 138–152.

Carr, J. C., Fright, W. R., Beatson, R. K., 1997. Surface interpolation with radial basis functions for medical imaging. *IEEE Transactions on Medical Imaging*, 16(1), pp. 96–107.

Carr, J. C., Beatson, R. K., Cherrie, J. B., Mitchell, T. J., Fright, W. R., McCallum, B. C., Evans, T. R., 2001. Reconstruction and representation of 3D objects with radial basis functions. In *Proceedings of the 28th annual conference on Computer Graphics and Interactive Techniques*, pp. 67–76.

Collins, J. B. and Woodcock, C. E., 1999. Geostatistical estimation of resolution-dependent variance in remotely sensed images. *Photogrammetric Engineering and Remote Sensing*, 65(1), pp. 41–50.

Collins, M. and Jong, M. De, 2004. Neuralizing target superresolution algorithms. *IEEE Geoscience and Remote Sensing Letters*, 1(4), pp. 318-321.

Coppin, P., Jonckheere, I., Nackaerts, K., and Muys, B., 2004. Digital change detection methods in ecosystem monitoring: a review. *International Journal of Remote Sensing*, 25(9), pp. 1565–1596.

Duda, R. O., Hart, P. E., and Stork, D. G., 2001. *Pattern Classification and Scene Analysis*, 2nded. John Wiley & Sons, New York.

Fisher, P., 1997. The pixel: A snare and a delusion. *International Journal of Remote Sensing*, 18(3), pp. 679-685.

Foody, G. M., 1998. Sharpening fuzzy classification output to refine the representation of sub-pixel land cover distribution. *International Journal of Remote Sensing*, 19(13), pp. 2593-2599.

Foody, G. M., 2000. Estimation of sub-pixel land cover composition in the presence of untrained classes. *Computers & Geosciences*, 26, pp. 469-478.

Foody, G. M., 2002. Status of land cover classification accuracy assessment. *Remote Sensing of Environment*, 80, pp. 185–201.

Foody, G. M., 2004. Thematic map comparison evaluating the statistical significance of differences in classification accuracy. *Photogrammetric Engineering and Remote Sensing*, 70(5), pp. 627–633.

Foody, G. M., Muslim, A. M., Atkinson, P. M., 2005. Super-resolution mapping of the waterline from remotely sensed data. *International Journal of Remote Sensing*, 26(24), pp. 5381–5392.

Foody, G. M., 2006. Sub-pixel methods in remote sensing. In S. M. de Jong and F. D. van der Meer (eds.) *Remote sensing image analysis: including the spatial domain*. Dordrecht, The Netherlands, Kluwer, pp. 37-49.

Foody, G. M. and Doan, H. T. X., 2007. Variability in soft classification prediction and its implications for sub-pixel resolution change detection and super-resolution mapping. *Photogrammetric Engineering and Remote Sensing*, 73(8), pp. 923-933.

Fuji, Y., Abe, Y., Iiguni, Y., 2012. Matching parameter estimation by using the radial basis function interpolation. *IET Image Processing*, 6(4), pp. 407–416.

Gao, F., Masek, J., Schwaller, M., and Hall, F., 2006. On the blending of the Landsat and MODIS surface reflectance: Predicting daily Landsat surface reflectance. *IEEE Transactions on Geoscience and remote sensing*, 44(8), pp. 2207–2218.

Ge, Y., Li, S., and Lakhan, V. C., 2009. Development and testing of a subpixel mapping algorithm. *IEEE Transactions on Geoscience and Remote Sensing*, 47(7), pp. 2155–2164.

Ge, Y. and Bai, H., 2011. Multiple-point simulation-based method for extraction of objects with spatial structure from remotely sensed imagery. *International Journal of Remote Sensing*, 32(8), pp. 2311–2335.

Ge, Y., 2013. Sub-pixel land-cover mapping with improved proportion images upon multiple-point simulation. International Journal of Applied Earth Observation and Geoinformation, 22, pp. 115-126.

Ge, Y., Chen, Y., Li, S., and Jiang, Y., 2014. Vectorial boundary-based sub-pixel mapping method for remote-sensing imagery. *International Journal of Remote Sensing*, 35(5), pp. 1756–1768.

González, J., Rojas, I., Ortega, J., Pomares, H., Fernández, F. J., Díaz, A. F., 2003. Multiobjective evolutionary optimization of the size, shape, and position parameters of radial basis function networks for function approximation. *IEEE Transactions on Neural Networks*, 14(6), pp. 1478–1495.

Goovaerts, P., 1997. Geostatistics for natural resources evaluation. Oxford University Press (ISBN 0-19-511538-4).

Goovaerts, P., 2008. Kriging and semivariogram deconvolution in presence of irregular geographical units. *Mathematical Geosciences*, 40(1), pp. 101–128.

Haertel, V., Shimabukuro, Y. E., and Almeida, R., 2004. Fraction images in multitemporal change detection. *International Journal of Remote Sensing*, 25(23), pp. 5473–5489.

Halimi, A., Altmann, Y., Dobigeon, N., and Tourneret, J. Y., 2011. Nonlinear unmixing of hyperspectral images using a generalized bilinear model. *IEEE Transactions on Geoscience and remote sensing*, 49(11), pp. 4153–4162.

Hao, M., Shi, W., Zhang H., and Li, C., 2014. Unsupervised change detection with expectation-maximization-based level set. *IEEE Geoscience and Remote Sensing Letters*, 11(1), pp. 210–214.

Heinz, D. C., Chang, C.-I., 2001. Fully constrained least squares linear spectral mixture analysis method for material quantification in hyperspectral imagery. *IEEE Transactions on Geoscience and Remote Sensing*, 39(3), pp. 529–545.

Hilker, T., Wulder, M. A., Coops, N. C., Linke, J., McDermid, J., G.Masek, J., Gao, F., and White, J. C., 2009. A new data fusion model for high spatial- and temporal-resolution mapping of forest based on Landsat and MODIS. *Remote Sensing of Environment*, 113(8), pp. 1613–1627.

Homer, C., Huang, C., Yang, L., Wylie, B., and Coan, M., 2004. Development of a 2001 National Land Cover Database for the United States. *Photogrammetric Engineering and Remote Sensing*, 70, pp. 829–840.

Huang, B. and Song, H., 2012. Spatiotemporal reflectance fusion via sparse representation. *IEEE Transactions on Geoscience and remote sensing*, 50(10), pp. 3707–3716.

Huang C., Chen, Y., and Wu, J., 2014. DEM-based modification of pixel-swapping algorithm for enhancing floodplain inundation mapping. *International Journal of Remote Sensing*, 35(1), pp. 365–381.

Hussain, M., Chen, D., Cheng, A., Wei, H., and Stanley, D., 2013. Change detection from remotely sensed images: From pixel-based to object-based approaches. *ISPRS Journal of Photogrammetry and Remote Sensing*, 80, pp. 91–106.

Jin, H., Mountrakis, G., Li, P., 2012. A super-resolution mapping method using local indicator variograms. *International Journal of Remote Sensing*, 33(24), pp. 7747-7773.

Journel, A. G. and Huijbregts, C. J., 1978. Mining geostatistics. Academic Press; London.

Kasetkasem, T., Arora, M. K., and Varshney, P. K., 2005. Super-resolution land-cover mapping using a Markov random field based approach. *Remote Sensing of Environment*, 96(3/4), pp. 302–314.

Kallel, A., Ottlé, C., Le Hégarat-Mascle, S., Maignan, F., and Courault, D., 2013. Surface temperature downscaling from multiresolution instruments based on Markov models. *IEEE Transactions on Geoscience and Remote Sensing*, 51(3), pp. 1588–1612.

Kolman, B. and Beck, R. E., 1995. Elementary linear programming with applications. Academic Press (ISBN 0-12-417910-X).

Kyriakidis, P. C., 2004. A geostatistical framework for area-to-point spatial interpolation. *Geographical Analysis*, 36(3), pp. 259–289.

Landgrebe, D., 2003. *Signal Theory Methods in Multispectral Remote Sensing*. New Jersey: Wiley.

Lee, Y. J., Yoon, J., 2010. Nonlinear image upsampling method based on radial basis function interpolation. *IEEE Transactions on Image Processing*, 19(10), pp. 2682–2692.

Li, F., Jia, X., Fraser, D., 2009. Superresolution reconstruction of multispectral data for improved image classification. *IEEE Geoscience and Remote Sensing Letters*, 6(4), pp. 689–693.

Li, X., Ling, F., and Du, Y., 2012a. Super-resolution mapping based on the supervised fuzzy c-means approach. *Remote Sensing Letters*, 3(6), pp. 501-510.

Li, X., Du, Y., and Ling, F., 2012b. Spatially adaptive smoothing parameter selection for Markov random field based sub-pixel mapping of remotely sensed images. *International Journal of Remote Sensing*, 33(24), pp. 7886-7901.

Li, X., Ling, F., Du, Y., Zhang, Y., 2014a. Spatially adaptive superresolution land cover mapping with multispectral and panchromatic images. *IEEE Transactions on Geoscience and Remote Sensing*, 52(5), pp. 2810-2823.

Li, X., Du, Y., and Ling, F., 2014b. Super-resolution mapping of forests with bitemporal different spatial resolution images based on the spatial-temporal Markov random field. *IEEE Journal of selected topics in applied earth observation and remote sensing*, 7(1), pp. 29-39.

Li, L., Chen Y., Yu, X., Liu, R., Huang, C., 2015. Sub-pixel flood inundation mapping from multispectral remotely sensed images based on discrete particle swarm optimization. *ISPRS Journal of Photogrammetry and Remote Sensing*, 101, pp. 10–21.

Lin, H., Bo, Y., Wang, J., and Jia, X., 2011. Landscape structure based super-resolution mapping from remotely sensed imagery. In *Proceedings of the International Geoscience and Remote Sensing Symposium*, pp. 79–82.

Ling, F., Xiao, F., Du, Y., Xue, H., and Ren, X., 2008. Waterline mapping at the subpixel scale from remote sensing imagery with high-resolution digital elevation models. *International Journal of Remote Sensing*, 29(6), pp. 1809–1815.

Ling, F., Du, Y., Xiao, F., Xue, H., and Wu, S., 2010. Super-resolution land-cover mapping using multiple sub-pixel shifted remotely sensed images. *International Journal of Remote Sensing*, 31(19), pp. 5023–5040.

Ling, F., Li, W., Du, Y., and Li, X., 2011. Land cover change mapping at the subpixel scale with different spatial-resolution remotely sensed imagery. *IEEE Geoscience and Remote Sensing Letters*. 8(1), pp. 182–186.

Ling, F., Du, Y., Xiao, F., Li, X., 2012a. Subpixel land cover mapping by integrating spectral and spatial information of remotely sensed imagery. *IEEE Geoscience and Remote Sensing Letters*, 9(3), pp. 408-412.

Ling, F., Li, X., Xiao, F., Fang, S., Du, Y., 2012b. Object-based sub-pixel mapping of buildings incorporating the prior shape information from remotely sensed imagery. *International Journal of Applied Earth Observation and Geoinformation*, 18, pp. 283–292.

Ling, F., Du, Y., Li, X., Li, W., Xiao, F., and Zhang, Y., 2013. Interpolation-based super-resolution land cover mapping. *Remote Sensing Letters*, 4(7), pp. 629-638.

Ling, F., Du, Y., Li X., Zhang, Y., Xiao, F., Fang, S., and Li W., 2014. Superresolution land cover mapping with multiscale information by fusing local smoothness prior and downscaled coarse fractions. *IEEE Transactions on Geoscience and Remote Sensing*, 52(9), pp. 5677-5692.

Lu, D., Mausel, P., Brondizio, E., andMoran, E., 2004a. Change detection techniques. *International Journal of Remote Sensing*, 25(12), pp. 2365–2407.

Lu, D., Batistella, M., and Moran, E., 2004b. Multitemporal spectral mixture analysis for Amazonian land-cover change detection. *Canadian Journal of Remote Sensing*, 30(1), pp. 87–100.

Lu, D., Batistella, M., Moran, E., Hetrick, S., Alves, D., and Brondizio, E., 2011. Fractional forest cover mapping in the Brazilian Amazon with a combination of MODIS and TM images. *International Journal of Remote Sensing*, 32(22), pp. 7131–7149.

Lu, Y., and Inamura, M., 2003. Spatial resolution improvement of remote sensing images by fusion of subpixel-shifted multi-observation images. *International Journal of Remote Sensing*, 24(23), pp. 4647–4660.

Magoules, F., Diago, L. A., Hagiwara, I., 2007. Efficient preconditioning for image reconstruction with radial basis functions. *Advances in Engineering Software*, 38, pp. 320–327.

Mahmood, Z., Akhter, M. A., Thoonen, G., Scheunders, P., 2013. Contextual subpixel mapping of hyperspectral images making use of a high resolution color image. *IEEE Journal of Selected Topics in Applied Earth Observations and Remote Sensing*, 6(2), pp. 779-791.

Makido, Y., Shortridge, A., Messina, J. P., 2007. Assessing alternatives for modeling the spatial distribution of multiple land-cover classes at sub-pixel scales. *Photogrammetric Engineering and Remote Sensing*, 73(8), pp. 935–943.

Makido Y. and Shortridge, A., 2007. Weighting function alternatives for a subpixel allocation model. *Photogrammetric Engineering and Remote Sensing*, 73(11), pp. 1233-1240.

Makido, Y., 2006. Land-cover mapping at sub-pixel scales. Ph.D. Dissertation, Michigan State University.

Manuel, G. S., Samuel, T. T., and James, R. F., 2008. Efficient subpixel image registration algorithms. *Optics Letters*, 33(2), pp. 156–158.

Mertens, K. C., Verbeke, L. P. C., Ducheyne, E. I., Wulf, R. De, 2003a. Using genetic algorithms in sub-pixel mapping. *International Journal of Remote Sensing*, 24(21), pp. 4241–4247.

Mertens, K. C., Verbeke, L. P. C., and Wulf, R. De, 2003b. Sub-pixel mapping with neural networks: Real-world spatial configurations learned from artificial shapes. In *Proceedings of 4th International Symposium on Remote Sensing of Urban Areas*, Regensburg, Germany, pp. 117–121.

Mertens, K. C., Verbeke, L. P. C., Westra, T., and Wulf, R. D, 2004. Sub-pixel mapping and sub-pixel sharpening using neural network predicted wavelet coefficients. *Remote Sensing of Environment*, 91, pp. 225–236.

Mertens, K. C., Basets, B. D., Verbeke, L. P. C., Wulf, R. De, 2006. A sub-pixel mapping algorithm based on sub-pixel/pixel spatial attraction models. *International Journal of Remote Sensing*, 27(15), pp. 3293–3310.

Muad, A. M. and Foody, G. M., 2010. Super-resolution analysis for accurate mapping of land cover and land cover pattern. In *Proceedings of International Geoscience and Remote Sensing Symposium*, pp. 502–505.

Muad, A. M., 2011. Super-resolution mapping. Ph.D. Dissertation, University of Nottingham, pp. 160-163.

Muad, A. M. and Foody, G. M., 2012a. Impact of land cover patch size on the accuracy of patch area representation in HNN-based super resolution mapping. *IEEE Journal of Selected Topics in Applied Earth Observations and Remote Sensing*, 5(5), pp. 1418–1427.

Muad, A. M. and Foody, G. M., 2012b. Super-resolution mapping of lakes from imagery with a coarse spatial and fine temporal resolution. *International Journal of Applied Earth Observation and Geoinformation*, 15, pp. 79–91.

Muslim, A. M., Foody, G. M., and Atkinson, P. M., 2007. Shoreline mapping from coarse-spatial resolution remote sensing imagery of Seberang Takir, Malaysia. *Journal of Coastal Research*, 23(6), pp. 1399-1408.

Nguyen, M. Q., Atkinson, P. M., Lewis, H. G., 2005. Superresolution mapping using a Hopfield neural network with LIDAR data. *IEEE Geoscience and Remote Sensing Letters*, 2(3), pp. 366–370.

Nguyen, M. Q., Atkinson, P. M., and Lewis, H. G., 2006. Superresolution mapping using a Hopfield neural network with fused images. *IEEE Transactions on Geoscience and Remote Sensing*, 44(3), pp. 736–749.

Nguyen, M. Q., Atkinson, P. M., Lewis, H. G., 2011. Super-resolution mapping using Hopfield neural network with panchromatic imagery. *International Journal of Remote Sensing*, 32(21), pp. 6149–6176.

Nigussie, D., Zurita-Milla, R., Clevers, J. G. P. W., 2011. Possibilities and limitations of artificial neural networks for subpixel mapping of land cover. *International Journal of Remote Sensing*, 32(22), pp. 7203–7226.

Park, S. C., Park, M. K., and Kang, M. G., 2003. Super-resolution image reconstruction: A technical overview. *IEEE Signal Processing Magazine*, 20(3), pp. 21–36.

Plaza, A., Martinez, P., Perez, R., and Plaza, J., 2004. A quantitative and comparative analysis of endmember extraction algorithms from hyperspectral data. *IEEE Transactions on Geoscience and Remote Sensing*, 42, pp. 650-663.

Pollandt, R., 1997. Solving nonlinear differential equations of mechanics with the boundary element method and radial basis functions. *International Journal for Numerical Methods in Engineering*, 40(1), pp. 61–73.

Robin A., Hegarat-Mascle, S. Le, and Moisan, L., 2008. Unsupervised subpixelic classification using coarse-resolution time series and structural information. *IEEE Transactions on Geoscience and remote sensing*, 46(5), pp. 1359–1374.

Schowengerdt, R. A., 1996. On the estimation of spatial-spectral mixing with classifier likelihood functions. *Pattern Recognition Letters*, 17(13), pp. 1379–1387.

Shen, Z., Qi, J., and Wang, K., 2009. Modification of pixel-swapping algorithm with initialization from a sub-pixel/pixel spatial attraction model. *Photogrammetric Engineering and Remote Sensing*, 75(5), pp. 557–567.

Singh, A., 1989. Digital change detection techniques using remotely-sensed data. *International Journal of Remote Sensing*, 10(6), pp. 989–1003.

Song, C., Jia, L., and Menenti, M., 2014. Retrieving high-resolution surface soil moisture by downscaling AMSR-E brightness temperature using MODIS LST and NDVI data. *IEEE Journal of Selected Topics in Applied Earth Observations and Remote Sensing*, 7(3), pp. 935–942.

Song, H. and Huang, B., 2013. Spatiotemporal satellite image fusion through one-pair image learning. *IEEE Transactions on Geoscience and remote sensing*, 51(4), pp. 1883–1896.

Su, Y. F., Foody, G. M., Muad, A. M., Cheng, K. S., 2012. Combining pixel swapping and contouring methods to enhance super-resolution mapping. *IEEE Journal of selected topics in applied earth observation and remote sensing*, 5(5), pp. 1428-1437.

Tatem, A. J., Lewis, H. G., Atkinson, P. M., Nixon, M. S., 2001a. Multi-class land cover mapping at the sub-pixel scale using a Hopfield neural network. *International Journal of Applied Earth Observation and Geoinformation*, 3(2), pp. 184–190.

Tatem, A. J., Lewis, H. G., Atkinson, P. M., and Nixon, M. S., 2001b. Super-resolution target identification from remotely sensed images using a Hopfield neural network. *IEEE Transactions on Geoscience and Remote Sensing*, 39(4), pp. 781–796.

Tatem, A. J., Lewis, H. G., Atkinson, P. M., and Nixon, M. S., 2001c. Super-resolution mapping of urban scenes from IKONOS imagery using a Hopfield neural network. In *Proceedings of the International Geoscience and Remote Sensing Symposium* (Sydney, Australia: IEEE), pp. 3200–3202.

Tatem, A. J., Lewis, H. G., Atkinson, P. M., and Nixon, M. S., 2002. Super-resolution land cover pattern prediction using a Hopfield neural network. *Remote Sensing of Environment*, 79, pp. 1–14.

Tatem, A. J., Lewis, H. G., Atkinson, P. M., and Nixon, M. S., 2003. Increasing the spatial resolution of agricultural land cover maps using a Hopfield neural network. *International Journal of Geographical Information Science*, 17(7), pp. 647–672.

Tatem, A. J., 2002. Super-resolution land cover mapping from remotely sensed imagery using a Hopfield neural network. Ph.D. Dissertation, University of Southampton.

Thornton, M. W., Atkinson, P.M., Holland, D.A., 2007. A linearised pixel-swapping method for mapping rural linear land cover features from fine spatial resolution remotely sensed imagery. *Computers & Geosciences*, 33, pp. 1261–1272.

Tolpekin, V. A. and Stein, A., 2009. Quantification of the effects of land-cover-class spectral separability on the accuracy of Markov-random-field based superresolution mapping. *IEEE Transactions on Geoscience and remote sensing*, 47(9), pp. 3283–3297.

Torres, C. E. and Barba, L. A., 2009. Fast radial basis function interpolation with Gaussians by localization and iteration. *Journal of Computational Physics*, 228, pp. 4976–4999.

Truong, P. N., Heuvelink, G. B. M., and Pebesma, E., 2014. Bayesian area-to-point kriging using expert knowledge as informative priors. *International Journal of Applied Earth Observation and Geoinformation*, 30, pp. 128–138.

Verhoeye, J., Wulf, R. De, 2002. Land-cover mapping at sub-pixel scales using linear optimization techniques. *Remote Sensing of Environment*, 79(1), pp. 96–104.

Villa, A., Chanussot, J., Benediktsson, J. A., Jutten, C., 2011. Spectral unmixing for the classifcation of hyperspectral images at a finer spatial resolution. *IEEE Journal of Selected Topics in Signal Processing*, 5(3), pp. 521–533.

Villa, A., Chanussot, J., Benediktsson, J. A., Jutten, C., and Dambreville, R., 2013. Unsupervised methods for the classification of hyperspectral images with low spatial resolution. *Pattern Recognition*, 46, pp. 1556–1568.

Wang, L., Zhang, Y., and Li, J., 2006. BP neural network based sub-pixel mapping method. In *International Conference on Intelligent Computing*, pp. 755–760.

Wang, L. and Jia, X., 2009. Integration of soft and hard classification using extended support vector machine. *IEEE Geoscience and Remote Sensing Letters*, 6(3), pp. 543–547.

Wang, L., Wang, Q., 2013. Subpixel mapping using Markov random field with multiple spectral constraints from subpixel shifted remote sensing images. *IEEE Geoscience and Remote Sensing Letters*, 10(3), pp. 598–602.

Wang, L., Liu, D., and Wang, Q., 2013. Geometric method of fully constrained least squares linear spectral mixture analysis. *IEEE Transactions on Geoscience and Remote Sensing*, 51(6), pp. 3558–3566.

Wang, Q., Wang, L., Liu, D., 2012a. Particle swarm optimization-based sub-pixel mapping for remote-sensing imagery. *International Journal of Remote Sensing*, 33(20), pp. 6480–6496.

Wang, Q., Wang, L., Liu, D., 2012b. Integration of spatial attractions between and within pixels for sub-pixel mapping, *Journal of Systems Engineering and Electronics*, 23(2), pp. 293–303, 2012.

Wang, Q. and Shi, W, 2014. Utilizing multiple subpixel shifted image in subpixel mapping with image interpolation. *IEEE Geoscience and Remote Sensing Letters*, 11(4), pp. 798–802.

Wang, Q., Shi, W., and Atkinson, P. M., 2014a. Sub-pixel mapping of remote sensing images based on radial basis function interpolation, *ISPRS Journal of Photogrammetry and Remote Sensing*, 92, pp. 1–15.

Wang, Q., Shi, W., and Wang, L., 2014b. Allocating classes for soft-then-hard subpixel mapping algorithms in units of class. *IEEE Transactions on Geoscience and Remote Sensing*, 52(5), pp. 2940–2959.

Wang, Q., Shi, W., Zhang, Hua, 2014c. Class allocation for soft-then-hard subpixel mapping algorithms with adaptive visiting order of classes. *IEEE Geoscience and Remote Sensing Letters*, 11(9), pp. 1494–1498.

Wang, Q., Shi, W., Wang, L., 2014d. Indicator cokriging-based subpixel land cover mapping with shifted images. *IEEE Journal of Selected Topics in Applied Earth Observation and Remote Sensing*, 7(1), pp. 327–339.

Wang Q., Atkinson P. M., and Shi W., 2015a. Indicator cokriging-based subpixel mapping without prior spatial structure information. *IEEE Transactions on Geoscience and Remote Sensing*, 53(1), pp. 309–323.

Wang Q., Atkinson P. M., and Shi W., 2015b. Fast sub-pixel mapping algorithms for sub-pixel resolution change detection. *IEEE Transactions on Geoscience and Remote Sensing*, 53(4), pp. 1692–1706.

Wang, S., Lim, K., Khoo, B., Wang, M., 2007. An extended level set method for shape and topology optimization. *Journal of Computational Physics*, 221(1), pp. 395–421.

Xu, X., Zhong, Y., Zhang, L., Zhang, H., 2013. Sub-pixel mapping based on a MAP model with multiple shifted hyperspectral imagery. *IEEE Journal of Selected Topics in Applied Earth Observations and Remote Sensing*, 6(2), pp. 580–593.

Xu, Y. and Huang, B., 2014. A spatio–temporal pixel-swapping algorithm for subpixel land cover mapping. *IEEE Geoscience and Remote Sensing Letters*, 11(2), pp. 474–478.

Zhang, L., Wu, K., Zhong, Y., and Li, P., 2008. A new sub-pixel mapping algorithm based on a BP neural network with an observation model. *Neurocomputing*, 71(10–12), pp. 2046–2054.

Zhang, L., Zhang, L., Tao, D., Huang, X., 2013. Tensor discriminative locality alignment for hyperspectral image spectral–spatial feature extraction. *IEEE Transactions on Geoscience and Remote Sensing*, 51(1), pp. 242–256.

Zhang, H., Shi, W., Wang, Y., Hao, M., and Miao, Z., 2014. Classification of very high spatial resolution imagery based on a new pixel shape feature set. *IEEE Geoscience and Remote Sensing Letters*, 11(5), pp. 940–944.

Zhong, Y., Zhang, L., 2012. Remote sensing image subpixel mapping based on adaptive differential evolution. *IEEE Transactions on Systerms, Man, and Cybernetics-Part B: Cybernetics*, 42(5), pp. 1306–1329.

Zhong, Y. and Zhang, L., 2013. Sub-pixel mapping based on artificial immune systems for remote sensing imagery. *Pattern Recognition*, 46(11), pp. 2902–2926.

Zhong, Y., Wu Y., Zhang, L., and Xu, X., 2014. Adaptive MAP sub-pixel mapping model based on regularization curve for multiple shifted hyperspectral imagery. *ISPRS Journal of Photogrammetry and Remote Sensing*, 96, pp, 134–148.

Zhu, X., Chen, J., Gao, F., Chen, X. H., and Masek, J. G., 2010. An enhanced spatial and temporal adaptive reflectance fusion model for complex heterogeneous regions. *Remote Sensing of Environment*, 114(11), pp. 2610–2623.

Zurita-Milla, R., Kaiser, G., Clevers, J. G. P. W., Schneider, W., and Schaepman, M. E., 2009. Downscaling time series of MERIS full resolution data to monitor vegetation seasonal dynamics. *Remote Sensing of Environment*, 113, pp. 1874–1885.